Université du Québec

INRS Institut national de la recherche scientifique

Énergie, Matériaux et Télécommunications

INVESTIGATION ON EFFECTS OF AROMATIC ORGANIC CATIONS IN HALIDE PEROVSKITES FOR SOLAR CELL APPLICATION

Par

Deepak Thrithamarassery Gangadharan

Thèse présentée pour l'obtention du grade de

Philosophiae Doctor (Ph.D.)

en sciences de l'énergie et des matériaux

Jury d'évaluation

Président du jury et examinateur interne	Emanuele Orgiu INRS-EMT
Examinateur externe	Joshua Byers Department of Chemistry UQAM - University of Quebec in Montreal
Examinateur externe	Timothy Kelly Department of Chemistry University of Saskatchewan
Directeur de recherche	Dongling Ma INRS-EMT
Codirecteur de recherche	Ricardo Izquierdo École de technologie supérieure (ETS)

ACKNOWLEDGEMENT

Firstly, I would like to express my sincere gratitude to my advisor Prof. Dongling Ma for the continuous support of my research, for her patience, motivation, and immense knowledge. Her guidance helped me in all the time of research and writing of this thesis. I could not have imagined having a better mentor for my Ph.D. journey.

Besides my advisor, I would like to extend my sincere appreciation to my co-supervisor Prof. Ricardo Izquierdo for his constant support during my Ph.D. study. I am grateful for his insightful comments, encouragement and letting me work in his laboratory.

My sincere thanks also go to Prof. Juan-Pablo Correa-Baena, Prof. Carlos Silva, and Dr. David A Valverde Chavez who provided me an opportunity to join their team as intern, and who gave access to the laboratory and research facilities.

I am grateful to my collaborators Prof. Qiquan Qiao, Prof. Baoquan Sun, Prof. Maurizia Palummo, Prof. Giacomo Giorgi, Dr. Ashish Dubey, Dr. Xinyu Gao, Yujie Han. Without their precious support it would not be possible to conduct this research.

I acknowledge Christophe Chabanier, Alexandre Robichaud and Gwenaël Chamoulaud for providing me training on state-of-the-art instruments, and their patience in helping me in solving technical problems came across in my research.

I thank administrative and technical staff at INRS-EMT, UQAM and Georgia Institute of Technology.

I thank my fellow colleagues and friends Qingzhe Zhang, Dr. Fan Yang, Dr. Long Tan, Pandeng Li, Ting Yu, for the stimulating discussions, and their support.

Last but not the least, I would like to thank my family: my parents and my brother for supporting me emotionally throughout my Ph.D. study and my life in general.

RÉSUMÉ

Avec leur efficacité exceptionnelle de conversion de l'énergie, de plus de 23 % actuellement, les pérovskites tridimensionnelles aux halogénures dominent la recherche sur les cellules solaires pouvant être traitées en solution. Toutefois, la présence dans ces dispositifs de pointe d'un élément toxique tel que le plomb ainsi que la stabilité chimique des pérovskites aux halogénures entravent la commercialisation de cette technologie. Des cellules solaires pérovskites halogénure sans plomb peuvent être réalisées en remplaçant complètement le plomb par des éléments tels que l'étain, le germanium, etc. Cependant, elles présentent une efficacité et une stabilité inférieures à celles des cellules contenant du plomb. À ce jour, les cellules solaires pérovskites à base d'étain sont celles qui sont les plus sûres du point de vue toxicologique et qui représentent donc le plus faible danger. Malheureusement, l'étain est sujet à l'oxydation, ce qui pose des problèmes de stabilité ainsi que des performances photovoltaïques plus faibles pour les cellules solaires en pérovskite à base d'étain. L'efficacité et la stabilité des cellules solaires pérovskites à base d'étain sont limitées par une recombinaison accrue des porteurs de charge induite par des lacunes d'étain qui sont activées par l'oxydation de l'étain d'un état d'oxydation 2^+ à un état d'oxydation 4^+ qui est plus stable. Alternativement, on peut remplacer partiellement le plomb par de l'étain ce qui permet de réduire la teneur en plomb (pérovskites alliées étain-plomb) sans perte significative d'efficacité. Dans le cas présent, les pérovskites d'alliage plomb-étain efficaces sont obtenues via une ingénierie de la composition qui comprends la substitution partielle des métaux et des halogénures dans les pérovskites en alliage. Aussi, la problématique de la stabilité chimique des pérovskites aux halogénures peut être résolue en utilisant des pérovskites en couches de faible dimensionnalité (pérovskites à deux dimensions) comme absorbeurs de soleil, mais ceci est réalisé au détriment des performances photovoltaïques. Les pérovskites en couches de faible dimensionnalité sont synthétisées par l'exfoliation de pérovskites à l'aide de cations d'ammonium organiques à grand volume. Les cellules solaires fabriquées avec ces pérovskites à faible dimensionnalité ont montré une amélioration significative de leur stabilité chimique contre l'humidité ainsi que contre l'élévation de la température par rapport à la structure d'origine. Dans cette thèse, nous avons d'abord étudié de manière approfondie les pérovskites à faible dimensionnalité synthétisées en utilisant un cation organique volumineux, le phényléthylammonium. Par la suite, nous avons exploré les effets des cations phényléthylammonium dans les pérovskites à base d'alliages étain-plomb afin d'améliorer leurs performances photovoltaïques ainsi que la stabilité des dispositifs. Il est intéressant de noter que

l'addition d'une petite quantité de cations volumineux d'ammonium organique dans les pérovskites peut passiver les défauts associés à l'oxydation de l'étain dans le matériau. Aussi nous avons optimisé la quantité de cations d'ammonium nécessaires pour améliorer simultanément l'efficacité et la stabilité. Cette thèse sert donc à paver la voie vers des cellules solaires à pérovskite sans plomb, ultra-stable et très efficace.

Mots-clés: cellules solaires pérovskites, pérovskites sans plomb, pérovskite à alliage étain-plomb, pérovskites moins toxiques, pérovskites stables, pérovskites bidimensionnelles, perovskites en couches, oxydation de l'étain, pile solaire de perovskite sans plomb, perovskites mixtes aux halogénures.

ABSTRACT

Three-dimensional halide perovskites have been dominating solution-processable solar cell research recently with outstanding power conversion efficiency of over 23%. The presence of toxic element “lead” in state-of-the-art devices and chemical stability of halide perovskites, however, hamper the commercialization of this technology. Although lead-free halide perovskite solar cells can be realized by completely replacing lead with other elements, such as tin, germanium, etc., they show inferior efficiency and stability. To date, tin-based perovskites are toxicologically safer, highest-performing lead-free perovskite solar cells. Unfortunately, tin is prone to oxidation causing critical stability issues as well as lower photovoltaic performance. The efficiency and stability of tin perovskites are limited by enhanced charge carrier recombination in the solar cell induced by tin vacancies activated by tin oxidation from the 2^+ oxidation state to more stable 4^+ oxidation state. Alternatively, partially replacing lead with tin helps to reduce the lead content (viz. tin-lead alloyed perovskites) in perovskite solar cells while without significant loss in efficiency. Here, efficeint lead-tin perovskites are achieved *via* compostional engineering. The compositional engineering was comprised of partially substituting metals and using mixed halides in alloyed perovskites. The issue of chemical stability of halide perovskites can be addressed by employing layered low-dimensional perovskite (known as two-dimensional perovskites) as solar absorbers, but at the expense of photovoltic performance. Layered low-dimensional perovskite structures are synthesized by exfoliating perovskite structure by bulky organic ammonium cations which have shown significant improvement on chemical stability against moisture and heat compared to the parent structure. In this thesis, layered perovskites using bulky organic cation, phenylethyl ammonium, are thoroughly studied. Subsequently, effects of phenylethyl ammonium cations in tin-lead peovskites are explored to improve photovoltic performance and device stability of tin-lead alloyed perovskites. Interestingly, a small amount of bulky organic ammonium cation addition in the perovskites showed various effects from passivating the Sn vacancy defects to homogenizing the metals and halides in the material. Here, the amount of phenylethyl ammonium cations is optimized to simultanously improve the efficiency and stability. The thesis proposes a recipe for a stable, highly efficient lead-less perovskite solar cell.

Keywords : perovskite solar cells, lead-free perovskites, tin-lead alloyed perovskite, less-toxic perovskites, stable perovskites, two-dimensional perovskites, layered perovskites, tin oxidation, efficeint less-lead perovskite solar cell, mixed-halide alloyed perovskites.

SYNOPSIS

INTRODUCTION

L'un des problèmes majeurs auquel l'humanité devra faire face au cours des 50 prochaines années est la crise de l'énergie. L'augmentation de la population, l'évolution rapide des modes de vie, l'industrialisation massive et l'évolution du paysage urbain ont considérablement accru la demande en énergie. Actuelement, la consommation annuelle mondiale d'électricité est de 12 TW et devrait passer à 24 TW d'ici 2050, ce qui laissera un déficit de 12 TW. Le scénario énergétique actuel consistant à utiliser des combustibles fossiles pour répondre à la demande en énergie ne permet pas de répondre efficacement à l'augmentation de la demande, car ces ressources en combustibles fossiles sont non renouvelables et limitées. En outre, ils causent des risques environnementaux importants, tels que le réchauffement de la planète et les problèmes climatiques associés. À l'heure actuelle, plus de 75% de la demande énergétique mondiale est satisfaite par des ressources énergétiques traditionnelles , notamment le charbon, le gaz naturel et le pétrole. Un rapport récent, publié par le Groupe d'experts intergouvernemental sur l'évolution du climat (GIEC) des Nations Unies (ONU), indique que si les ressources énergétiques « propres » ne sont pas largement utilisées, la planète atteindra le seuil critique de 1,5 avant les niveaux préindustriels d'ici 2030 Parmi les ressources énergétiques durables, l'énergie solaire est la plus propre, avec un coût en carbone zéro. Le photovoltaïque, qui convertit l'énergie solaire, la source d'énergie la plus abondante et la plus propre, en électricité est considérée comme l'une des technologies les plus prometteuses pour répondre à notre demande urgente d'énergie verte. Le silicium cristallin domine le marché des cellules solaires depuis des décennies, mais un nouveau matériau appelé « pérovskite aux halogénures » approche rapidement des niveaux d'efficacité identiques. Les pérovskites aux halogénures adoptent la structure cristalline ABX_3, où A = méthylammonium (MA), formamidinium (FA), césium (Cs) et / ou rubidium (Rb); B = plomb (Pb) et / ou étain (Sn); X = chlore (Cl), brome (Br) et / ou iode (I). Ces matériaux sont généralement décrits comme des pérovskites tridimensionnelles (3D). Les pérovskites aux halogénures sont attrayantes pour plusieurs raisons. Les ingrédients sont abondants et ils peuvent être mélangés facilement et à moindre coût. De plus, ils peuvent, à basse température, être mis en forme de couches minces contenant un matériau hautement cristallin comme celui des plaquettes de silicium après que celui-ci ait subi un traitement coûteux et à haute température. Cependant, la stabilité des cellules solaires pérovskites (PSC) et la présence de plomb métallique toxique dans les pérovskites sont sans doute les principaux

inconvénients qui limitent la commercialisation de cette technologie. Dans cette thèse, les préoccupations principales liées aux cellules solaires pérovskites sont abordées.

La présence de plomb dans les PSC les plus efficaces entrave l'application à grande échelle de cette technologie. En effet, des sous-produits toxiques du Pb hydrosolubles peuvent se former une fois les pérovskites d'halogénure de Pb au contact avec l'eau ou avec l'air humide, lesquels peuvent s'accumuler dans la chaîne alimentaire. Les directives de l'Union Européenne limitent à 0,1% en poids la concentration maximale de plomb dans chaque matériau homogène contenue dans des dispositifs électroniques, à savoir, le matériau pérovskite dans une cellule solaire pérovskite. L'Amérique du Nord impose également des restrictions similaires au contenu en plomb dans les appareils électroniques. Les matériaux hautement efficaces à base de pérovskite aux halogénures contiennent plus de 10% de plomb. Les candidats appropriés pour le remplacement du plomb sont des éléments du même groupe (groupe 4) que le plomb. Ainsi, le Sn et le germanium (Ge), qui ont tous deux plusieurs états d'oxydation (2+ et 4+), sont de bons candidats. Les simulations numériques montrent que la configuration électronique du Pb^{2+} dans la structure pérovskite ABX est cruciale pour ses remarquables propriétés photovoltaïques. Les pérovskites à base de Sn constituent la meilleure alternative aux pérovskites aux halogénures de plomb car ce sont des matériaux sans plomb plus sûrs sur le plan toxicologique. Cependant, les performances des meilleures PSC à base de Sn sont encore loin de celles des PSC aux halogénures de plomb. Une autre approche consiste à allier / remplacer le Pb par des métaux moins toxiques tels que Sn et Ge dans les pérovskites ABX_3, ce qui est une stratégie très prometteuse pour obtenir des cellules solaires stables et moins toxiques et ce sans compromettre les performances photovoltaïques. Ici, les pérovskites en alliage Sn-Pb sont utilisées pour résoudre le problème de la quantité élevée de Pb dans les pérovskites aux halogénures

Une autre préoccupation majeure est la stabilité chimique des pérovskites aux halogénures. Dans ces pérovskites, les petites molécules organiques volatiles telles que le MA et le FA peuvent être facilement évincées par l'eau en raison de la faible liaison entre la structure organique et la structure inorganique. En outre, l'exposition à la lumière des pérovskites halogénées peut entraîner la production de superoxyde O^{2-} qui peut à son tour déprotoner MA^+ pour former du $CH_3 NH_2$ et ainsi dégrader les pérovskites. L'introduction de certains cations organiques plus volumineux dans la structure de la pérovskite altère l'intégrité structurale de la structure de la pérovskite et conduit à la formation de pérovskites en couches de dimensionnalité inférieure (bidimensionnelle 2D). Les pérovskites 2D présentent une meilleure stabilité à l'humidité et à la chaleur. Les mécanismes exacts de cette stabilité supérieure sont encore en discussion.

Cependant, il a été affirmé que des cations organiques hydrophobes plus volumineux dans des pérovskites 2D pourraient tendre les liaisons Pb-I de surface et ainsi repousser les molécules d'eau des sites réactifs. Une autre hypothèse est la nanoencapsulation des couches de pérovskite par ces cations organiques volumineux. Cependat, les cellules solaires employant des pérovskites 2D présentent des performances photovoltaïques inférieures à celles des pérovskites 3D. Par ailleurs, l'incorporation de petites quantités de cations espaceurs volumineux dans des pérovskites 3D peut améliorer la stabilité et les performances photovoltaïques. Dans cette thèse, le phényléthylammonium (PEA), cation encombrant aromatique, a été exploré en tant que cation espaceur lors de la synthèse des pérovskites 2D. Aussi, les effets du PEA sur des pérovskites à alliage Sn-Pb sont étudiés afin d'améliorer les performances et la stabilité photovoltaïques.

Objectifs de recherche

L'objectif principal du projet est de développer des pérovskites stables et sans plomb. Les objectifs de la recherche sont divisés en deux parties tel qui suit.

Partie I: Synthèse et caractérisation de pérovskites 2D avec des cations espaceurs de phényléthylammonium (PEA) et leur application dans des cellules solaires

Les pérovskites 2D résistent à la dégradation en présence d'humidité, de chaleur et de lumière. Ici, les pérovskites 2D sont synthétisées en isolant des couches de pérovskite aux halogénures métalliques ($PbI_{6)}$ en utilisant des cations espaceurs aromatiques plus volumineux ($(C_6H_5(CH_2)_3NH_2)_2(CH_3NH_3)_{2)}$. Les cations espaceurs aromatiques devraient être meilleurs que les cations organiques aliphatiques pour conserver leurs performances dans des conditions d'humidité ambiante en raison de la propriété hydrophobe du cation espaceur. Des couches pérovskites de haute qualité $(PEA)_2(MA)_{n-1}Pb_{n-1}I_{3n-1}$ (n = 3, 4, 5) ont été préparés par un procédé à chaud sous pression pour l' application dans des cellules solaires. La stabilité supérieure de la pérovskite 2D à base de PEA a été étudiée grâce à une série de caractérisations, telles que l'analyse par diffraction des rayons X (DRX), les mesures d'absorption (utilisant la spectroscopie ultraviolet et visible), la durée de vie des porteurs (utilisant la photoluminescence résolue dans le temps), et analyse thermogravimétrique (TGA).

Partie II: Effets des cations PEA sur les pérovskites à alliage de Sn-Pb et amélioration des performances des cellules solaires

Bien que les pérovskites $I(PEA)_2(MA)_{n-1}Pb_{n-1}I_{3n-1}$ présentent une stabilité supérieure, la performance photovoltaïque semble être inférieure à celle des pérovskites 3D. De plus, la présence d'espèces de plomb solubles dans l'eau, qui entravent l'application réelle de cette

technologie, est une autre source de préoccupation. Le métal Sn s'avère être la meilleure alternative au Pb pour atteindre des performances photovoltaïques raisonnables, mais néanmoins inférieur aux Pb-pérovskites typiques. Alternativement, des alliages de Pb avec des pérovskites Sn semble être une stratégie prometteuse et équilibrée visant à obtenir des cellules solaires stables et moins toxiques sans trop compromettre les performances photovoltaïques. L'objectif principal était ici d'explorer les effets des cations PEA dans les pérovskites Sn-Pb afin d'améliorer simultanément les performances photovoltaïques et la stabilité du dispositif. L'expertise acquise avec les cations d'espacement PEA dans la conception de pérovskites 2D (dans la partie I) a été appliquée à la synthèse de pérovskites stables et efficaces à base de Sn-Pb incorporées dans du PEA. En outre, les pérovskites en alliage Sn-Pb présentent également l'avantage supplémentaire d'étendre l'absorption des photons au domaine spectral du proche infrarouge (NIR). Les effets de l'incorporation de cations organiques volumineux dans la réduction de la formation de défauts de Sn dans la pérovskite à base d'alliage Sn-Pb ont aussi été étudiés à l'aide de techniques expérimentales telles que : la spectroscopie par photoémission par rayons X (XPS), la diffraction des Rayons X, les mesures de potentiel de surface, les mesures d'absorption transitoire et la spectroscopie de photoluminescence (PL). De plus, la passivation du défaut de Sn par les molécules de PEA a été confirmée par des calculs de DFT.

Résultats

Utilisation des cations aromatiques alkylammonium pour produire des pérovskites à deux dimensions:

Les pérovskites 2D sont synthétisées en isolant des couches de pérovskite aux halogénures métalliques en utilisant un cation espaceur alkylammonium aliphatique ou aromatique, qui peut conserver ses performances dans des conditions d'humidité ambiante du fait de la propriété hydrophobe du cation espaceur. Cependant, la meilleure pérovskite 2D à ce jour, utilisant un cation espaceur à butylammonium court (BA), ne montre qu'une tolérance modeste à l'humidité et à la chaleur en raison de l'hydrophobie inférieure ainsi que de la taille relativement plus petite du cation BA. Ici, un phényléthylammonium aromatique (PEA) plus volumineux est utilisé comme cation espaceur pour la synthèse de la pérovskite 2D afin d'obtenir des cellules solaires très stables. Des couches pérovskites de haute qualité $(PEA)_2 (MA)_{n-1} Pb_n I_{3n+1}$ avec (n = 3, 4) sont préparés en modifiant le procédé de dépôt. Des matériaux conducteurs organiques ont été choisis comme couches sélectives de porteurs de charge dans une configuration de cellule solaire planaire qui peut être facilement mise à l'échelle pour la fabrication de cellules solaires d'un rouleau à l'autre. La nature excitonique des porteurs de charge dans la pérovskite 2D limite

l'épaisseur du film de $(PEA)_2(MA)_{n-1}Pb_nI_{3n+1}$ pour l'application de la cellule solaire. L'optimisation de l'épaisseur de la couche d'absorbeur solaire s'est avérée cruciale pour l'obtention de dispositifs de pérovskite 2D très efficaces avec une hystérésis très faible. La stabilité supérieure de la pérovskite 2D à base de PEA a été étudiée au moyen d'une série de caractérisations, telles que l'analyse par diffraction des rayons X (DRX), les mesures d'absorption, les mesures de la durée de vie des porteurs et l'analyse thermogravimétrique (TGA).

Les études précédentes ont montré qu'un simple revêtement par centrifugation en une étape du précurseur de pérovskite 3D à base de DMF ne donne pas une couche homogène de pérovskite. [11,12] La direction de cristallisation dépend en grande partie du type de cations organiques présents dans le précurseur ainsi que du solvant utilisé pour préparer la solution de précurseur. Par exemple, la présence d'IAM dans le précurseur de pérovskite préparé dans du diméthylformamide (DMF) favorise une croissance cristalline rapide le long de l'axe c-cristallographique, conduisant à la formation d'une couche inhomogène de pérovskite. Par contre, les pérovskites 2D (n = 1, 2, 3, 4) se cristallisent sous forme de plaques sur le dessus du substrat de verre avec une bonne couverture de surface car la cristallisation suivant les axes cristallographiques b se produit plus rapidement que celle suivant l'axe c, contrairement aux pérovskites 3D. En résumé, les espèces organiques de $(PEA)_2(MA)_4Pb_5I_{16}$ (n = 5) composées principalement d'AMI (MAI: 66% et PEAI: 34%) ont conduit à la formation d'une couche de pérovskite moins homogène, ce qui ressort clairement des images SEM et AFM (Figure 1.1 et Figure 1. S1). Avec le dépôt par centrifugation conventionnel à la température ambiante, des grains cristallins plus petits se forment en raison de l'évaporation rapide du DMF avant la cristallisation des pérovskites, ce qui entraîne également une couverture incomplète de la pérovskite sur le substrat. On a émis l'hypothèse que, lorsqu'un substrat est maintenu au-dessus de la température de cristallisation de la pérovskite pendant le revêtement par centrifugation, une croissance cristalline prolongée est favorisée en raison de la présence d'un excès de solvant pendant la cristallisation. Dans le revêtement par centrifugation classique, une phase pérovskite intermédiaire non entièrement cristallisée est déposée et une cristallisation complète de la pérovskite ne se produit que pendant l'étape de post-recuit. La croissance cristalline de pérovskite est ainsi limitée dans l'étape classique de post-recuit du film de pérovskite en raison de l'évaporation presque totale du solvant avant la cristallisation complète de la pérovskite. D'autre part, la présence d'un excès de solvant pendant la cristallisation offre plus de temps pour une plus grande croissance cristalline dans le procédé de coulée à chaud. Ici, le substrat a été maintenu à une température bien inférieure à la température d'ébullition du DMF pour éviter toute

évaporation significative du solvant, qui est cependant suffisamment élevée pour favoriser la croissance des cristaux de pérovskite.

La spectroscopie PL résolue dans le temps est utilisée pour étudier les porteurs de charge photo-excités et comprendre les processus de recombinaison de porteurs de charge (interbandes relaxation, recombinaison bimoléculaire radiatif et recombinaison assistée par piège) dans les couches de pérovskite 2D (Figure 3.3c). La durée de vie de la PL est significativement allongée pour tous les couches de pérovskite 2D coulés à chaud par rapport aux couches classiques déposées par centrifugation, ce qui peut être corrélé à la réduction des processus de recombinaison (figure 3.S3). L'allongement de la durée de vie de la PL peut être attribué à la réduction des défauts et du désordre aux joints de grain. Le rendement de conversion de puissance (PCE) des dispositifs à pérovskite de plus faible dimension est considérablement amélioré lorsque la méthode de coulée à chaud est utilisée. Le tableau 2.1 compare les paramètres photovoltaïques des dispositifs 2D à pérovskite fabriqués à la fois par la méthode de coulée à chaud et par la méthode de revêtement par centrifugation classique. La densité de courant en court-circuit (J_{sc}) a grandement augmentée pour tous les dispositifs en pérovskite 2D coulé à chaud à la suite de l'absorption accrue de photons et l'orientation des cristaux de pérovskite (n = 4, 5). Les gros cristaux ainsi que la bonne couverture de surface dans les couches coulées à chaud ont permis de réduire le piégeage des charges interfaciales et de réduire le nombre de défauts volumineux, entraînant une amélioration du facteur de remplissage (FF) et de la tension en circuit ouvert (V_{oc}) des cellules solaires. Parmi tous les pérovskites de plus basse dimension, les dispositifs $(PEA)_2$ $(MA)_3$ Pb_4 I_{13} ont présenté les meilleures performances photovoltaïques. Tous les paramètres photovoltaïques sont meilleurs dans les dispositifs déposés par coulée à chaud de $(PEA)_2$ $(MA)_3Pb_4$ $I_{13,}$ qui présentent un PCE moyen amélioré de 5,50% contre 3,92% pour le $PEA_2(MA)_3$ Pb_4I_{13} déposés par centrifugation classique. Des mesures de JV dans différentes directions de balayage (figure 3.4a) et des vitesses de balayage (figure 3.4b) sont effectuées et une hystérésis de JV faible a été observée pour les dispositifs $(PEA)_2(MA)_3Pb_4I_{13,}$ suggérant une fiabilité de fonctionnement photovoltaïque de ces dispositifs.

Pour étudier la stabilité à l'humidité, des dispositifs de pérovskite 2D non encapsulés ont été stockés dans l'obscurité à une humidité relative de 72 ± 2%. La demi-vie de ces dispositifs s'est avérée être de 90 heures (figure 3.5a). En revanche, la demi-vie des dispositifs de pérovskite 3D était beaucoup plus courte, environ 10 heures. Fait intéressant, le PCE des dispositifs de pérovskite 2D a initialement augmenté de 10% après une exposition à l'humidité. La figure 3.5b montre la stabilité thermique de dispositifs de pérovskite 3D et 2D maintenus dans une

atmosphère inerte (N_2). Dans le cas des dispositifs en pérovskite 3D, la chute de PCE est au moins de 20% au bout de 24 heures. Les cellules solaires 2D montrent une excellente stabilité thermique, conservant 65% de la PCE initiale au bout de 70 heures. La figure 3.5c démontre la photostabilité des dispositifs en pérovskite testés pendant 65 heures dans une atmosphère inerte et la PCE reste presque constante pour les pérovskites 2D en tandis que les dispositifs en pérovskites 3D conservent seulement 60% de la PCE initial. La figure 3.S5 montre l'évolution des paramètres photovoltaïques en fonction du temps dans différentes conditions environnementales difficiles. Pour comprendre la stabilité à l'humidité de la pérovskite 2D, nous avons analysé les modifications du diagramme de diffraction des rayons X des couches de pérovskite stockés à 72 ± 2% HR (figure 3.6a). Un pic correspondant à PbI_2 à 12,7 ° commence à apparaître dans la couche de pérovskite 2D après dix jours d'exposition à l'humidité. En revanche, la pérovskite 3D commence à montrer des signes de dégradation après seulement trois jours (figure 3.S6). De plus, il n'y a pas eu de baisse de l'absorbance de la couche de pérovskite 2D même après 23 jours avec une humidité relative de 72 ± 2% (Figure 3.6b). D'autre part, l'absorbance constante de la couche de pérovskite 3D est considérablement réduite, en particulier dans la région visible du spectre solaire après quatre jours à 72 ± 2% HR, ce qui indique une dégradation majeure du matériau (figure 3.S6). Les cations PEA intercalés entre les couches de pérovskite peuvent empêcher l'exposition directe des cations MA aux molécules d'eau; ainsi, les couches de pérovskite sont nanoencapsulées, ce qui contribue à l'amélioration de la stabilité. Néanmoins, même si les cations PEA sont moins hygroscopiques que les cations MA, ils restent sensibles aux molécules d'eau, ce qui finit par conduire à la lente dégradation des pérovskites 2D. Cela ressort clairement de l'émergence d'un pic, correspondant à PbI_2, dans le diagramme DRX après exposition à l'humidité.

La stabilité thermique exceptionnelle de la pérovskite 2D a été mise au jour en étudiant le comportement thermique des précurseurs et des pérovskites à l'aide du TGA. Les températures de sublimation (ΔH_{sous}) et de sublimation (T_{sub}) ont été déterminées pour les pérovskites à partir d'un ajustement linéaire des moindres carrés des données isothermes TGA (équation 1. S1). Les valeurs calculées ΔH_{sub} et T_{sub} du log ($m\ T^{1/2}$) par rapport au tracé 1 / T sont répertoriées dans le tableau 3.2, où m est la pente de la perte de masse obtenue à partir de chaque isotherme à température constante (T) (Figure 3.S7). La figure 3.7c montre les courbes TGA pour la poudre de pérovskite 3D et 2D. Les deux étapes de perte de masse observées dans la première dérivée des courbes TGA pour la pérovskite (Figure 3.7d) correspondent à la libération d'espèces organiques et inorganiques, respectivement. L'encadré de la figure 3.7c présente une comparaison des courbes de chauffage TGA d' espèces organiques (MAI et PEAI)

et de poudres de pérovskite, où l'étape de perte de masse de l'AMI se produit plus rapidement quand elle se trouve à l'intérieur de la matrice de pérovskite 3D. Mais en présence de PEAI dans la matrice de pérovskite, un retard notable a été observé dans la sublimation des espèces organiques. Les courbes TGA des pérovskites confirment que différentes voies de décomposition se produisent lorsque le cation PEA est incorporé à la structure de pérovskite, ce qui indique essentiellement le comportement thermique supérieur de la pérovskite 2D. Mais en présence de PEAI dans la matrice de pérovskite, un retard notable a été observé dans la sublimation des espèces organiques. Les courbes TGA des pérovskites confirment que différentes voies de décomposition se produisent lorsque le cation PEA est incorporé à la structure de pérovskite, ce qui indique essentiellement le comportement thermique supérieur de la pérovskite 2D.

Effet des cations d'espacement d'alkylammonium aromatiques sur les pérovskites halogénures avec alliage Sn- Pb:

Les pérovskites 2D employant des cations volumineux résistent à l'humidité et à l'oxygène, mais aux dépens du PCE de la cellule solaire. Dans cette thèse, le chapitre 4 explore les effets de la substitution d'une petite quantité de cations organiques du site A dans des pérovskites d'alliage Sn-Pb par des cations PEA. Actuellement, les PSC les plus efficaces contiennent des espèces de Pb solubles dans l'eau, ce qui entrave la commercialisation de cette technologie. [1]

Les pérovskites de Pb forment facilement des sous-produits solubles dans l'eau, qui peuvent s'accumuler dans la chaîne alimentaire et donc dans le corps humain. [3] Il est donc indispensable de limiter l'utilisation du Pb en le remplaçant partiellement ou totalement par des métaux moins toxiques ou, mieux encore, non toxiques. Très probablement, les candidats appropriés au remplacement du plomb sans trop compromettre les propriétés photovoltaïques sont des éléments du même groupe (groupe 4) que le plomb. Les candidats immédiats apparaissent alors comme le Sn et le Ge puisque tous les deux peuvent être facilement oxydées des états 2^+ 4^+ tout comme le Pb. Des simulations numériques ont montré que la configuration électronique du Pb^{2+} dans la structure pérovskite d' ABX_3 est cruciale pour son remarquable comportement photovoltaïque. Par conséquent, bien que les pérovskites à base de Sn forment les cellules solaires sans plomb les plus performantes en termes de PCE, le fait que Sn soit plus stable à l'état d'oxydation 4^+ pose des problèmes. Aussi, ils montrent des performances beaucoup plus faibles que les cellules solaires pérovskites Pb en raison de la formation de lacunes Sn associés à l'oxydation de Sn^{2+} à Sn^{4+}. Ces lacunes jouent le rôle de centres de recombinaison non radiative dans les pérovskites à base de Sn. Les PSC à base de Sn présentent ainsi une tension de circuit ouvert (V_{oc}) inférieure à la normale[23,24], principalement en raison d'une recombinaison assistée

par un piège profond généré par un dopage / défaut non intentionnel induit par une vacance de Sn. Différentes approches y compris le contrôle morphologique des pérovskites Sn, la minimisation de l'exposition à l'oxygène pendant la préparation du dispositif et l'addition de sels de Sn, ont été étudiés et se sont avérés utiles pour améliorer la performance des PSC à base de Sn. Récemment, Wang *et al.* ont rapporté des PSC de Sn avec une efficacité de 9,41% en utilisant des pérovskites de Sn quasi-dimensionnelles (2D), qui sont toutefois loin d'être équivalentes aux efficacités des PSC de Pb. En revanche. L'alliage du plomb à la pérovskite au Sn semble être une stratégie prometteuse et équilibrée visant à obtenir des cellules solaires stables et moins toxiques sans trop compromettre les performances photovoltaïques. En outre, les pérovskites en alliage Sn-Pb apportent un avantage supplémentaire, l'absorption étendue de photons dans le domaine spectral du proche infrarouge (NIR) (jusqu'à 1050 nm avec une largeur de bande interdite optique de 1,18 eV). En revanche, les pérovskites hybrides organiques-inorganiques hybrides typiques telles que $MAPbI_3$, $FAPbI_3$ et $FASnI_3$ ne présentent pas d'absorption dans la gamme NIR en raison de leurs bandes interdites optiques relativement plus élevées, de 1,55 eV (jusqu'à 800 nm), 1,48 eV (jusqu'à 838 nm).) et 1,30 eV (jusqu'à 950 nm), respectivement. [27] Malheureusement, la performance des pérovskites Sn-Pb est limitée par l'oxydation $Sn^{2+} \rightarrow Sn^{4+}$ tel que mentionnée précédemment. La stratégie la plus efficace pour inhiber ce processus préjudiciable a été l'incorporation de SnF_2 dans les pérovskites à base de Sn. Cependant, même avec une quantité optimale de SnF_2, le coefficient de recombinaison assisté par piège, défini comme une vitesse spécifique à laquelle les ions de charge opposée se combinent au niveau des pièges, est 70 fois plus élevé que celui des ions à base de Pb. Ceci suggère une perspective d'améliorer les performances des PSCs en alliage Sn-Pb en réduisant les défauts liés à l'oxydation de Sn^{2+} vers Sn^{4+} et / ou la formation de vacance Sn.

Plus récemment, plusieurs groupes, dont nous ont montré que les pérovskites 2D employant des cations encombrants sont résistants à l'humidité et de l'oxygène, mais au détriment du PCE de la cellule solaire. Ici, la suppression de la formation de défauts par la substitution de petits cations organiques dans des pérovskites en alliage par des cations organiques volumineux est explorée pour la première fois dans le but d'augmenter simultanément le PCE et la stabilité. Pour être plus spécifique, différentes compositions de pérovskites d'alliage Sn-Pb sont réalisées en mélangeant stoechiométriquement $FASnI_3$ et $MAPbI_3$ (identifiées comme pérovskites à alliage FA / MA).

Les absorptions optiques de $(FASnI_3)_x(MAPbI_3)_{1-x}$ et $(PEA)_y(FA_xMA_{1-x})_{1-y}Sn_xPb_{1-x}I_3$ (x = 0, 0,3, 0,5, 0,7 et 1) ont été déterminés à partir de mesures d'absorption ultraviolets et visibles (UV-Vis) (figures 4.1a et 4.S1). Les pérovskites mixtes Sn-Pb montrent un décalage du début de

l'absorption vers la région NIR par rapport aux pérovskites Pb (x = 0) ou Sn (x = 1) pures. Le plus bas était de 1,18 eV pour $(FASnI_3)_{0,7}(MAPbI_3)_{0,3}$, puis 1,22 eV pour $(FASnI_3)_{0,5}(MAPbI_3)_{0,5}$ et 1,26 eV pour $(FASnI_3)_{0,3}(MAPbI_3)_{0,7}$, comme indiqué par lignes pointillées à la figure 4.1a. La substitution de FA / MA par une petite quantité de PEA ne modifie pas considérablement le début de l'absorption optique (Figures 4.1b et 4.S1). Mais nous avons remarqué une modification de la forme du spectre d'absorption optique ainsi que de l'intensité de l'absorption optique. Fait intéressant, le pic situé à 1,85 eV (marqué d'une flèche dans le spectre d'absorption) de pérovskites en alliage FA / MA a disparu pour les pérovskites en alliage PEA-FA / MA. En général, le pic proche du bord d'absorption optique est attribué à l'état excitonique lié en raison de l'attraction Coulombienne des électrons et des trous (pic d'absorption hydrogénique). Dans notre cas, le pic est situé (à 1,85 eV) de manière significative par rapport aux débuts d'absorption (à 1,18 eV, 1,22 eV, 1,26 eV), ce qui exclut fondamentalement l'origine d'absorption hydrogénique du pic. La modification de la forme des spectres d'absorption pourrait être associée aux propriétés excitoniques des pérovskites en alliage PEA-FA/MA et des études plus détaillées portant sur les espèces photogénérées dans les zones à faible bande interdite sont nécessaires pour comprendre cette particularité.

La structure cristalline des pérovskites en alliage a été caractérisée par XRD. Comme le montre la figure 4.S5, le $FASnI_3$ n'a qu'un seul pic, compris dans l'intervalle entre 22 , et 25 , indexé sur le plan (113) dans le groupe d'espace orthorhombique de A*mm* 2, alors que $MAPbI_3$ présente deux pics du même intervalle indexés aux plans (211) et (202) du groupe spatial tétragonal (*14cm*). Les spectres XRD des pérovskites alliées (figures 4.3a à 4.3c) ne présentent qu'un seul pic dans la plage comprise entre 22 et 25 , ce qui suggère fortement que les pérovskites en alliage adoptent la structure cristalline orthorhombique. En outre, il semble que les atomes de Sn et Pb occupent de façon aléatoire les sites métalliques du coin de partage ($[Sn_{1-x}Pb_xI_6]^{-4}$) octaèdres. La structure cristalline est inchangée après le remplacement d'une petite quantité de cations FA / MA par des cations PEA dans des pérovskites en alliage PEA-FA / MA. Les cations organiques volumineux tels que le PEA sont généralement utilisés pour la synthèse de pérovskites 2D, les pics aux angles faibles (210) correspondant aux pérovskites de faible dimension ainsi que les débuts d'absorption étaient absents. L'intensité des pics XRD, en particulier le pic (110) à 14,1 , a notamment augmenté pour tous les pérovskites en alliage avec l'introduction du PEA, ce qui pourrait être dû à une cristallinité plus élevée de la pérovskite en alliage et / ou à une meilleure couverture de la couche sur substrat.

Le changement de la taille du cristal a été sondé en suivant la variation de la largeur totale du maximum à mi-hauteur (FWHM) du pic XRD situé en 14 correspondant au plan cristallin (110) (Figure 4.S6). Le FWHM est passé de 0,239 à 0,214 et de 0,246 à 0,230 po $(FASnI_3)_{0,3}(MAPbI_3)_{0,7}$ et $(FASnI_3)_{0,5}(MAPbI_3)_{0,5}$ lorsque FA / MA ont été remplacés par 5% de PEA, respectivement. Le changement de FWHM est corrélé à la déformation locale et à la cristallinité. La diminution de FWHM implique une augmentation de la cristallinité ainsi qu'une réduction de la déformation du réseau. En particulier, la réduction du FWHM du pic XRD situé en (110) signifie une diminution de la contrainte de réseau le long de la direction de liaison inorganique de I-Pb-I, I-Sn-I. Toutefois, une intégration plus poussée du PEA à 10% a entraîné une augmentation du FWHM, qui reste toutefois inférieure à celle de l'échantillon exempt de PEA. Il est clair qu'une intégration de 5% de PEA peut produire des pérovskites en alliage hautement cristallines parmi $(PEA)_y(FA_{0,3}MA_{0,7})_{1-y}Sn_{0,3}Pb_{0,7}I_3$, $(PEA)_y(FA_{0,5}MA_{0,5})_{1-y}Sn_{0,5}Pb_{0,5}I_3$ (y = 0%, 5% et 10%). Au contraire, la composition riche en Sn a montré une tendance différente. Le FWHM a augmenté progressivement avec la quantité de PEA (5 et 10%) dans $(FASnI_3)_{0,7}(MAPbI_3)_{0,3,}$ suggérant dans ce cas, l'introduction de PEA a conduit à une diminution de la cristallinité.

Pour étudier le rôle des cations PEA dans la prévention de l'oxydation de Sn^{2+} dans les pérovskites en alliage, des mesures XPS ont été effectuées (figure 4.S7, figures 4.4a et 4.4b). Pour le $(FASnI_3)_{0.3}(MAPbI_3)_{0.7,}$ le pic Sn $3d_{5/2}$ (situé à 486.08 eV) pourrait être bien déconvolué en deux pics situés à 485.75 eV et 486.3 eV, correspondant aux états d'oxydation Sn^{2+} et Sn^{4+} (figure 4.4a). De même, le pic Sn $3d_{3/2}$ (situé à 495,41 eV) est composé de deux pics situés à 494,27 eV et 494,71 eV, associés aux états d'oxydation Sn^{2+} et Sn^{4+}. En revanche, le $(PEA)_{0,05}(FA_{0,3}MA_{0,7})_{0,95}Sn_{0,3}Pb_{0,7}I_3$ ne montre que deux pics nets, non déconvoluables, sans aucun pic Sn^{4+}. Les spectres XPS des pérovskites $(PEA)_{0,05}(FA_{0,7}MA_{0,3})_{0,95}Sn_{0,7}Pb_{0,3}I_3$ ont également présenté un comportement similaire à celui de leurs échantillons témoins (figure 4.S7). L'oxydation de Sn^{2+} en Sn^{4+} est une indication forte de la formation de lacunes Sn dans les pérovskites à base de Sn, qui sont les principaux défauts des pérovskites à base de Sn en raison de leur faible énergie de formation de défauts parmi tous les défauts ponctuels.

Les premiers calculs de principe ont montré que la taille des cations organiques pouvait jouer un rôle vital dans la formation de l'énergie de formation des lacunes de Sn dans les pérovskites à base de Sn. [25] La taille ionique plus grande pourrait réduire le couplage antiliant Sn 5s – I 5p, entraînant des énergies de formation de vacance de Sn plus élevées. Pour prouver la tendance réduite de la formation de V_{Sn} dans les pérovskites mixtes PEA-FA/MA, l'énergie des défauts de pérovskite $(PEA_{1-x}FA_x)_2SnI_4$ (x = 0,056) a été calculée. La structure défectueuse $(PEA_{1-x}FA_x)_2$

SnI_4 est rapportée à la figure 4.5c. Les résultats montrent clairement une tendance réduite vers la formation de V_{Sn} pour le cas mixte (illustré à la figure 4.5f) ce qui correspond aux données expérimentales. Ainsi, l'introduction de cations organiques volumineux (PEA) augmente l'énergie de formation de lacunes dans Sn PEA contenant perovskites alliés dans nos conditions riches Sn. Moins de postes vacants dans les pérovskites PEA-FA / MA Sn-Pb sont très encourageants pour les applications photovoltaïques.

Les propriétés photovoltaïques des pérovskites en alliage de FA / MA et PEA-FA / MA ont été testés par emploi de l'architecture de cellule solaire suivante : oxyde indium dopé d'étain (ITO) / poly (3, 4-éthylène dioxythiophène) -poly (styrène sulfonate) (PEDOT : PSS) / pérovskite / p henyl-C61-butyrique ester méthylique (PCBM) / argent (Ag). Parmi les pérovskites en alliage FA / MA, $(FASnI_3)_{0,3}(MAPbI_3)_{0,7}$ affichait le PCE le plus élevé suivi de $(FASnI_3)_{0,5}$ $(MAPbI_3)_{0,5}$, puis $(FASnI_3)_{0,7}(MAPbI_3)_{0,3}$. Le V_{oc} et le facteur de remplissage (FF) diminuent avec l'augmentation de la teneur en Sn (tableau 4.1), les cellules riches en Sn ($(FASnI_3)_{0,7}(MAPbI_3)_{0,3}$) indiquant les plus faibles V_{oc} et FF de toutes les compositions. Étant donné que le V_{oc} et le FF dépendent fortement de la recombinaison des porteurs de charge dans la cellule solaire, les pérovskites riches en Sn contiennent très probablement un nombre plus élevé de défauts limitant le V_{oc} et le FF de leurs dispositifs. Plus précisément, les défauts de la bande interdite attireraient des électrons / trous et agiraient en tant que centres de recombinaison non radiative, ce qui aurait un impact important sur le V_{oc} des cellules solaires correspondantes. La dépendance de FF sur l'intensité de la lumière incidente annule la nature du processus de recombinaison dans la cellule solaire pendant le fonctionnement du dispositif. Dans le processus de recombinaison bimoléculaire pur, le taux de recombinaison est proportionnel au produit des densités de porteurs de charge. Par conséquent, à une faible intensité lumineuse (c'est-à-dire une faible densité de porteurs de charge), le taux de recombinaison diminue et un meilleur FF est obtenu. Ceci est essentiellement la tendance qui a été observée pour les PEA-PSCs FA allié / MA (Figure 4.7 c), ce qui est en ligne avec la prédominance de la recombinaison bimoléculaire dans ces dispositifs. D'autre part, le FF a nettement diminué avec la diminution de l'intensité lumineuse dans les dispositifs de pérovskite en alliage FA/MA, ce qui confirme sans ambiguïté la dominance de la recombinaison assistée par un piège dans ces dispositifs. Comme le nombre de pièges ne change pas avec la diminution de l'intensité lumineuse, on comprend aisément que le taux de recombinaison des porteurs de charge photo-générés avec des charges piégées augmente lorsque l'intensité lumineuse diminue, ce qui entraîne une diminution du FF. L'étude montre clairement que l'introduction du PEA a effectivement modifié le processus de recombinaison des porteurs de charge dominants dans nos PSC.

L'étude de la dégradation de la performance photovoltaïque de dispositifs de type pérovskite en alliage contenant 5% de PEA non encapsulés et offrant les meilleures performances (en termes de PCE) a été réalisé dans différentes conditions environnementales pour évaluer leur stabilité et la comparer à celle de leurs échantillons de contrôle. Ici, nous définissons $t_{1/2}$ comme un temps pour que le PCE du dispositif tombe à 50% de sa valeur initiale pour normaliser la comparaison entre différents dispositifs. La figure 4.8b illustre la dégradation des dispositifs sous illumination AM1.5G dans une atmosphère inerte. Les dispositifs $(PEA)_{0,05}$ $(FA_{0,3}$ $MA_{0,7})_{0,95}$ $Sn_{0,3}$ $Pb_{0,7}$ I_3 présentaient une meilleure photostabilité que les dispositifs FA / MA en pérovskite ($t_{1/2}$ = 30h vs $t_{1/2}$ = 15h). La lumière semble être plus nocive que l'humidité pour les dispositifs en alliage de pérovskite. La figure 4.8c montre que la dégradation des dispositifs en alliage de pérovskite est devenue plus rapide en présence d'humidité légère. Cependant, les dispositifs en pérovskite PEA-FA/MA étaient encore plus résistants à la dégradation, conservant 20% des performances initiales après 24h, alors que les dispositifs en pérovskite FA / MA étaient totalement dégradés au cours de la même période. Les défauts des pérovskites Sn-Pb induits par les lacunes du Sn jouent non seulement un rôle clé dans la détermination des performances photovoltaïques (hystérésis PCE et JV), mais également la stabilité des dispositifs. Les défauts des pérovskites sont vulnérables à l'infiltration de l'oxygène ou de l'humidité et accélèrent la dégradation des dispositifs dans des conditions ambiantes. [43] Sur la base de toutes les caractérisations décrites ci-dessus sur les matériaux (PL, AFM, SEM, XPS, XRD, GIWAXS) et les dispositifs (mesures JV et EQE, analyses dépendantes de l'intensité lumineuse des paramètres de performance de la cellule solaire), on peut tirer une conclusion raisonnable: i) plus de défauts sont présents dans les PSC en alliage FA / MA , et plus la recombinaison assistée par piège domine leurs performances et ii) en remplaçant les cations FA/MA par une petite quantité de cations PEA, le nombre de défauts peut être considérablement réduit et de ce fait, il y a une baisse significative de la recombinaison assistée par piège dans les pérovskites en alliage. Cette conclusion est en outre corroborée par une diminution importante de l'hystérésis de JV observée dans les dispositifs à pérovskite en alliage PEA-FA/MA par rapport à celle des dispositifs à pérovskite en alliage FA/MA (Figure 4.S12). Parmi les nombreuses raisons possibles suggérées pour le phénomène préjudiciable de l'hystérésis de la courbe de la coentreprise, la migration des défauts dans les PSC est considérée comme la principale responsable. Il a déjà été montré que des défauts chargés tels que des lacunes MA / FA et Pb / Sn proches des couches sélectives de charge gênent l'extraction de la charge au niveau des contacts sélectifs, provoquant l'hystérésis de la cellule solaire. En réduisant le nombre de défauts chargés, nous pensons que la migration des défauts a été considérablement réduite dans les pérovskites de Sn-Pb contenant du PEA,

réduisant ainsi l'hystérésis JV dans les dispositifs. Comme indiqué précédemment, les défauts proches de la région interfaciale entre les couches sélectives à la pérovskite et à la charge influencent principalement l'hystérésis de la JV.

Effets des cations espaceurs en alkylammonium aromatiques dans les pérovskites d'halogénures mixtes Sn-Pb

À ce jour, les pérovskites aux halogénures Sn-Pb avec 60% de Sn de la teneur totale en métal du site B offrent les meilleures performances photovoltaïques. La performance des pérovskites aux halogénures Sn-Pb contenant 60% de Sn est en partie limitée par leur faible bande interdite (1,18 eV-1,2 eV), qui réduit généralement le V_{oc} des PSC. Il est bien connu que la bande interdite de la pérovskite peut être ajustée en utilisant des mélanges fractionnels de I et de Br dans la composition, connus sous le nom de pérovskites mixtes aux halogénures. Cependant, on sait que la ségrégation des halogénures réduit les performances photovoltaïques et la stabilité des pérovskites à halogénures mixtes. Les couches minces de pérovskite en alliage d'halogénure mélangé Sn-Pb, $(FASnI_3)_{0,7}$ $(MAPbBr_3)_{0,3}$ (FA/MA/SnPb/I/Br) sont préparées en mélangeant des précurseurs de pérovskite $FASnI_3$ et $MAPbBr_3$. La bande interdite de 1,4 eV de FA/MA/SnPb/I/Br est très proche de la bande interdite idéale pour atteindre une efficacité théorique maximale dans une cellule solaire à simple jonction. Malheureusement, la bande interdite avantageuse de ce matériau ne s'est pas manifestée sur les performances de leur cellule solaire, principalement en raison d'un photocourant plus faible, malgré leur impressionnant V_{oc} pour un pérovskite allié riche en Sn. La ségrégation de l'halide est connue pour être la cause de la réduction du rendement photovoltaïque et de la stabilité des pérovskites d'halogénure mixte de Pb. Des chercheurs ont récemment découvert que la substitution partielle de cations de sites A par des cations inorganiques tels que Rb, Cs pouvait conduire à l'homogénéisation d'halogénures dans des pérovskites à halogénures mixtes. Dans cette thèse, nous avons étudié les effets de la substitution partielle des cations des sites A avec un cation volumineux PEA en homogénéisant des métaux et des halogénures en halogénure mixte Sn-Pb en alliage de pérovskites (FA/MA/SnPb/I/Br).

Nous avons mesuré l'absorption de ces films et extrait la bande interdite des pérovskites FA/MA (SnPb)I/Br et PEA/FA/MA(SnPb)I/Br, comme indiqué sur la figure 5. 1c et 5.1 d. En général, les pérovskites en alliage Sn-Pb sont des semi-conducteurs à bande interdite basse (1,2 eV). La présence à la fois de Pb et de Br dans les pérovskites mixtes aux halogénures Sn-Pb donne lieu à une bande interdite plus large de 1,4 eV. L'ajout de 5% de PEA à la solution de pérovskite FA/MA(SnPb)I/Br ne modifie pas la bande interdite de la couche mince de pérovskite (figure 5.

1d). Une augmentation significative de l'intensité du pic de diffraction des rayons X a été observée pour les échantillons de PEA / FA / MA (SnPb) I/Br par rapport à FA / MA (SnPb) I / Br montrant que PEA / FA / MA (SnPb I / Br pérovskites) expose plus fortement les cristaux orientés dans le plan (110) que ses homologues sans PEA (Figure 5.2a) . Une analyse plus poussée du profil des pics montre que l'incorporation de cations PEA conduit à une légère diminution de la largeur totale à mi-hauteur (FWHM) (figure 5. S1). La diminution du FWHM implique un réseau moins contraint lors de l'ajout de 5% de PEA. Plus précisément, la réduction de la FWHM des pics (110), (200) signifie une diminution de la contrainte de réseau le long de la direction de liaison inorganique de I -Pb (ou / et Sn)-I, Br-Pb (ou / et Sn) -Br ou I -Pb (ou / et Sn) -Br. La pérovskite orientée le long de la direction de liaison inorganique sur le substrat est avantageuse pour un transport efficace de la charge vers les contacts sélectifs de la charge dans une cellule solaire, car les porteurs de charge rencontrent des obstacles moins importants dans une couche de pérovskite avec un empilement parfait des cristaux. Les différences de composition chimique entre les échantillons ont été analysés par quantification des rapports d'intensité du signal XPS entre les différents éléments. Les ratios d'intensité estimés à partir de XPS comparés aux ratios obtenus à partir de la formule chimique permettent d'étudier les compositions chimiques des couches minces. Des surfaces riches en Sn et en Br ont été observées dans une couche de pérovskite FA/MA(SnPb)I/Br. Cela peut être dû à la distribution non homogène des éléments dans la couche mince de pérovskite FA/MA(SnPb) I/Br. L'ajout de PEA modifie la composition chimique précise de la couche de pérovskite. Les rapports Sn / Pb et I / Br pour PEA / FA / MA (SnPb) I / Br sont proches des valeurs théoriques, en accord avec sa formule chimique (tableau 5.1), qui suggère une distribution homogène des éléments dans l' ensemble du PEA / FA / Film de pérovskite MA (SnPb) I / Br. Nous nous attendons à ce que l'homogénéisation des halogénures et des métaux influence la recombinaison des porteurs de charge dans les pérovskites, car les zones riches en Br / I du film de pérovskite agissent en tant que centres de recombinaison. Une spectroscopie d'absorption transitoire (TAS) a été réalisée pour comprendre la dynamique de recombinaison dans les pérovskites en alliage d'halogénures mixtes (Figure 5.3). Les caractéristiques spectrales monter un étroitement quand on incorpore 5% PEA dans la structure (Figure 5.3a- 5.3c). Le rétrécissement de la caractéristique spectrale indique une diminution des événements de recombinaison dans le matériau. Le comportement dépendant du temps du signal GSB + SE à 1,5 eV est illustré à la figure 5. 3d. Le recouvrement GSB + SE de l'échantillon PEA/FA/MA (SnPb)I/Br est beaucoup plus lent que pour l'échantillon FA/MA(SnPb)I/Br, ce qui suggère un dépeuplement plus lent des porteurs de charge dans les échantillons contenant du PEA. La récupération du signal lent GSB + SE TAS implique la

population porteuse de charge à long terme. L'inhomogénéité de la composition et la déformation du réseau peuvent provoquer des pertes non radiatives dans les couches mixtes de pérovskite contenant des halogénures. Comme nous l'avons noté dans la discussion sur les résultats XPS et XRD, l'incorporation de molécules de PEA améliore la distribution des éléments en plus de réduire la contrainte de réseau dans les pérovskites aux halogénures mixtes Sn-Pb, ce qui entraîne une diminution des pertes de recombinaison non radiative dans les couches de PEA/FA /MA(SnPb)I/Br. Les propriétés photovoltaïques des pérovskites FA/MA (SnPb) I/Br et PEA / FA/MA(SnPb)I/Br ont été évaluées dans une architecture de cellules solaires planaires composées de ITO/ PEDOT: PSS /pérovskite/PCBM/Bathocuproine (BCP)/Ag (Figure 5. 4a).

Les courbes J-V des dispositifs les plus performants sont représentés sur la figure ure 5. 4b et 5. 4 c. FA /MA(SnPb)I/Br) et elles présentait une PCE moyenne de 7,03 ± 0,70%, une tension en circuit ouvert (V_{oc}) de 0,72 ± 0,03 V, une densité de courant en court-circuit (J_{sc}) de 15,03 ± 1,35 $mAcm^{-2}$ et un facteur de remplissage (FF) de 64,73 ± 1,36%. L'ajout de PEA améliore considérablement les performances globales du dispositif. PEA/FA /MA (SnPb)I/Br présentait une moyenne de PCE de 12,06 ± 0,62% avec un V_{oc} de 0,76 ± 0,01 V, un J_{sc} de 22,61 ± 1,06 mA/cm^2 et un FF de 69,42 ± 0,78%. Tous les paramètres photovoltaïques ont été améliorés dans le PEA/FA/MA(SnPb/I/Br) par rapport au FA/MA(SnPb/I/Br), le J_{sc} montre l'amélioration la plus importante. La forte augmentation de J_{sc} dans PEA/FA/MA(SnPb/I/Br) est expliquée par l'alignement de la bande des pérovskites, comme cela a été observé pour influencer fortement le photocourant de dispositifs. La spectroscopie par photoémission ultraviolette (UPS) a été réalisée sur les pérovskites FA/MA (SnPb)I/Br et PEA/FA/MA(SnPb)I/Br pour étudier l'énergie d'ionisation (par rapport au vide), et donc le maximum de la bande de valence (VBM) de ces composés (Figure 5. 5a - 5,5 d). Le PEA/FA/MA(SnPb)I/Br a montré une énergie d'ionisation inférieure à celle du FA/MA(SnPb)I/Br (-5,66 eV contre -6,04 eV, respectivement). Comme nous l'avons noté dans la discussion sur le XPS, la composition chimique précise peut être différente en PEA/ FA/MA(SnPb)I/Br par rapport à FA/MA(SnPb)I/Br, ce qui peut entraîner des modifications de la position VBM du matériau. Nous pensons que les surfaces de pérovskite riches en Br de FA/MA(SnPb)I/Br influence la position énergétique du VBM, car les Brutovskites présentent une énergie d'ionisation significativement plus élevée (et donc des VBM plus profondes). Pour produire une bande de conduction qui s'aligne avec le contact sélectif électronique on ajoute la bande interdite optique à l'énergie d'ionisation des composés. Les niveaux d'énergie connus de PCBM et PEDOT: PSS sont esquissés à la figure ure 5. 5c et 5.5 d. En raison d'un VBM plus profond, le CBM de FA/MA (SnPb)I/Br présente un alignement défavorable de la bande avec le PCBM, créant une barrière d'énergie de 0,34 eV pour le transport d'électrons à travers l'interface

pérovskite / PCBM. En revanche, le CBM de PEA/FA/MA(SnPb)I/Br s'aligne bien avec celui de PCBM sans barrière apparente à travers l'interface pérovskite/PCBM. Il a été démontré que les barrières énergétiques situées à l'interface contact / pérovskite / sélection d'électrons étaient à l'origine de faibles Jsc rencontrées dans les cellules solaires à pérovskite. Bien que l'alignement de la bande favorable pour pérovskite / PCBM accroisse la J_{sc} dans les cellules solaires PEA/FA/MA(SnPb)I/Br, le défaut d'alignement de CB avec PCBM inhibe le transfert de charge interfaciale dans les cellules solaires FA/MA(SnPb)I/Br qui à son tour réduit la J_{sc} dans les dispositifs. Dans ce travail, nous avons constaté que l'alignement des bandes défavorable au niveau de l'interface pérovskite/PCBM est le principalt responsable de la baisse des performances des pérovskites en alliage halogéné mixte Sn-Pb. Les résultats XPS suggèrent que l'alignement défavorable de la bande provient de la surface riche en Sn et Br des couches de pérovskite en alliage d'halogénure mélangé Sn-Pb.

En résumé, cette thèse explore les divers effets du cation organique aromatique, PEA dans les pérovskites hybrides pour améliorer la performance photovoltaïque et la stabilité. L'utilisation de PEA comme cation d'espacement dans les pérovskites est connue pour produire des pérovskites 2D avec une excellente stabilité face à l'humidité et à la chaleur. L'étude sur les pérovskites 2D utilisant le PEA comme cations espaceurs nous a incités à étudier d'autres effets des cations organiques espaceurs dans les pérovskites sans plomb. La substitution partielle au site A avec PEA a été explorée dans les pérovskites en alliage Sn-Pb, ce qui conduit à la passivation de défauts et à l'homogénéisation des pérovskites halogénures ce qui améliore le rendement photovoltaïque et de la stabilité.

TABLE OF CONTENTS

LIST OF FIGURES

LIST OF TABLES

LIST OF ABBREVIATIONS

2D	Two-dimensional
3AMP	3-(aminomethyl) piperidinium
3D	Three-dimensional
4AMP	4-(aminomethyl) piperidinium
AFM	Atomic Force Microscopy
BA	Butylammonium
BdA	Butanediammonium
BZA	Benzylammonium
DJ	Dion-Jacobson
EDS	Energy Dispersive X-ray Spectroscopy
EQE	External Quantum Efficiency
FA	Formamidnium
FF	Fill Factor
FWHM	Full Width at Half Maximum
GISAXS	Glazing Incident Small Angle X-ray Scattering
GIWAXS	Glazing Incident Wide Angle X-ray Scattering
GIXS	Glazing Incident X-ray Scattering
HA	Histammonium
HTL	Hole Transporting Layer
ITO	Indium Tin Oxide
J-V	Current Density-Voltage
MA	Methylammonium
NIR	Near Infrared
PA	Propylammonium

PEA	Phenylethylammonium
PCBM	Phenyl-C61-Butyric acid methyl ester
PCE	Power Conversion Efficiency
PEDOT: PSS	Poly(3,4-ethylenedioxythiophene): polystyrene sulfonate
PL	Photoluminescence
PSC(s)	Perovskite Solar Cell(s)
PV	Photovoltaic
RMS	Root-mean-square Roughness
RP	Ruddlesden-Popper
SPO	Stabilized Power Output
ThMA	Thiophenemethylammonium
UV	Ultraviolet
Vis	Visible
XPS	X-ray Photoelectron Spectroscopy
XRD	X-ray Diffraction
ZnPc	Tetra-ammonium zinc phthalocyanine

LIST OF PEER-REVIEWED PUBLICATIONS

1. Bulky cations improve band alignment and stability in Sn-based perovskite solar cells, **Deepak Thrithamarassery Gangadharan**, David A Valverde-Chávez, Ricardo Izquierdo, Carlos Silva, Dongling Ma, Juan-Pablo Correa-Baena, (Manuscript in preparation).

2. Reducing non-radiative recombination in Pb-less halide perovskite films by incorporating bulky phenylethylammonium cations**, Deepak Thrithamarassery Gangadharan**, Pandeng Li, Qingzhe Zhang, Fan Yang Ricardo Izquierdo, Baoquan Sun, Maurizia Palummo, Giacomo Giorgi, Dongling Ma, (Under review in ACS Appl. Mater. Interfaces)

3. Searching for stability at lower dimensions: current trends and future prospects of layered perovskite solar cells, **Deepak Thrithamarassery Gangadharan** and Dongling Ma, Energy Environ. Sci., 2019,12, 2860-2889.

4. Aromatic Alkylammonium Spacer Cations for Efficient Two-Dimensional Perovskite Solar Cells with Enhanced Moisture and Thermal Stability, **Deepak Thrithamarassery** Gangadharan, Yujie Han, Ashish Dubey, Xinyu Gao, Baoquan Sun, Qiquan Qiao, Ricardo Izquierdo, Dongling Ma, Solar RRL,2018, 2 (4), 1700215.

5. Ice-Assisted Synthesis of Black Phosphorus Nanosheets as a Metal-Free Photocatalyst: 2D/2D Heterostructure for Broadband H_2 Evolution, Q Zhang, S Huang, J Deng, **DT Gangadharan**, F Yang, Z Xu, G Giorgi, Maurizia Palummo, Mohamed Chaker, Dongling Ma, Advanced Functional Materials, 1902486.

6. Recent advancements in plasmon-enhanced promising third-generation solar cells, **Deepak Thrithamarassery Gangadharan**, Zhenhe Xu, Yanlong Liu, Ricardo Izquierdo, Dongling Ma, Nanophotonics, 2017, 6, 153-175.

7. Enhanced Long-term and Thermal Stability of Polymer Solar Cells in Air at High Humidity with the Formation of Unusual Quantum Dot Networks, Long Tan, Fan Yang, Mee Rahn Kim, Pandeng Li, **Deepak Thrithamarassery Gangadharan**, Joëlle Margot, Ricardo

Izquierdo, Mohamed Chaker, Dongling Ma, ACS applied materials & interfaces 2017, 9, 26257-26267.

8. Recent advancements in plasmon-enhanced visible light-driven water splitting, Qingzhe Zhang, **Deepak Thrithamarassery Gangadharan**, Yanlong Liu, Zhenhe Xu, Mohamed Chaker, Dongling Ma, Journal of Materiomics, 2017, 3 (1), 33-50.

1 INTRODUCTION

One of the major problems that humanity must face in the next 50 years is the energy crisis. The rising population, rapidly changing lifestyles of people, massive industrialization and evolving landscape of cities have enormously increased energy demands. The present annual worldwide electricity consumption is 12 TW and is expected to become 24 TW by 2050, leaving a challenging increase of 12 TW.[1] The current energy scenario based on the use of fossil fuels is unable to meet that largely increased energy demand, as these fossil fuel resources are non-renewable and limited. Also, they cause significant environmental hazards, like global warming and the associated climatic issues. Major energy sources like hydroelectricity, nuclear power, and coal have their own drawbacks.[2] For example, hydropower facilities can have significant environmental impacts by changing the environment and affecting land use, homes, and natural habitats in the dam area. On the other hand, solar energy is a clean, safe, and inexhaustible energy source. A recent report suggests that wind and solar will produce almost 50% of world electricity by 2050.[3] Photovoltaic (PV) is considered as one of the most suited technology for solar energy conversion. Increased awareness about human-made climatic changes along with steadfastly falling prices of solar technologies will soon make solar PVs as one of the lowest-cost options for future electricity supply. Interestingly, solar panels have recorded a cost-decline of 85% since 2010 with solar module retailer prices as low as 0.56 US$ / Watt.[4]

Before going into details about solar photovoltaic materials, a brief description of the working principle of solar cells is provided in the next section.

1.1 Theory of solar cells

A solar cell is a device that converts light energy into electrical energy by the photovoltaic effect.[5] A semiconductor is used as solar cell material. The energy conversion involves absorption of light, production of electron-hole pairs in a semiconductor and charge carrier separation. Typically, p–n junction is used for efficient charge carrier separation. It is necessary to understand the working principle of p–n junction solar cells, to comprehend and develop new-type of solar cells.

The generation of current in a solar cell involves three fundamental processes, which determine the overall efficiency of the solar cell, (1) absorption of incident photons to create electron-hole pairs, (2) charge separation and (3) collection of photo-generated charge carriers by the p-n junction. In the first process, electron-hole pairs will be generated in the semiconductor provided that the incident photon has an energy greater than that of the band gap of the semiconductor.

However, electrons and holes will only exist, on average, for a duration of time equal to the minority carrier lifetime before they recombine. The light-generated electron-hole pair is lost, or no power can be generated in a solar cell if the charge-carrier recombines. In the second process, the recombination is prevented by spatially separating electrons and holes by using a p-n junction. In third process, the electrons can also flow through the external wire; there will be effectively no voltage across the solar cell if external wire has very low electrical resistance, but current can flow, which is called the short-circuit current (I_{sc}). To generate power in a solar cell, both voltage and current should be produced simultaneously. If photo-generated carriers are prevented from leaving solar cells, both the number of electrons on the n-type side and the number of holes on the p-type side increase and this separation of charges creates an electric field opposed to already existing electric field at the p-n junction. This will reduce the electric field, which leads to the increase of the forward bias diffusion current. The voltage required to balance out photogenerated current and diffusion current is called the open-circuit voltage (V_{oc}). In an operating solar cell, an optimal current and voltage are generated across the load, leading to the maximum power to do useful work.

The solar cell performance can be characterized by current-voltage (I-V) measurements. A typical I-V graph is shown in Figure 1.1.[6] The I_{sc} is the maximum current (I_{max}), and V_{oc} is the maximum voltage (V_{max}) can be obtained from a solar cell. The maximum power point (MPP) is a point on an I-V curve corresponding to the highest power generated in a solar cell. MPP is a product of I_{mp} (current at maximum power) and V_{mp} (voltage at maximum power). The fill factor (FF) is figure of merit provided by the ratio between $I_{mp} \times V_{mp}$ and $I_{max} \times V_{max}$ ($FF = I_{mp} \times V_{mp} / I_{max} \times V_{max}$).

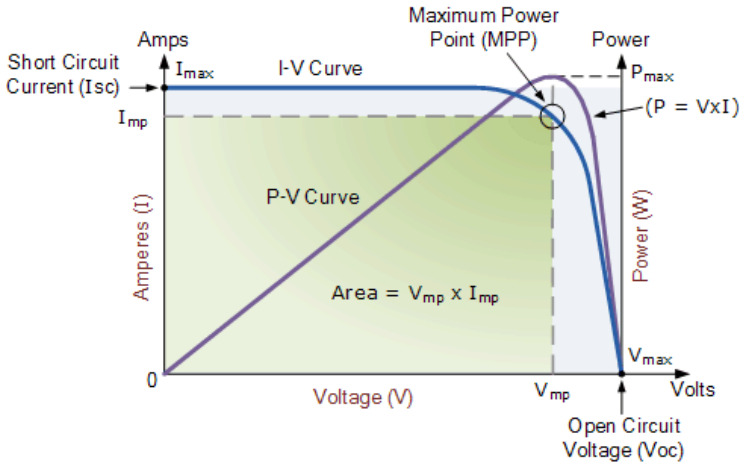

Figure 1.1 I-V curve of a solar cell. Reprinted from ref. 6 with permission from the Alternative Energy Tutorials.

1.2 Halide perovskite solar cell

To date, silicon solar panels dominate the renewable energy market, being most matured semiconductor technology. However, the silicon solar cells are relatively expensive due to the high-temperature processing of material and solar panel installation costs.[7,8] The cost associated with silicon wafer technology has forced to search for new materials and technology for solar energy conversion. Thin-film solar cells based on cadmium telluride (CdTe) and copper indium gallium selenide (CuInGaSe) offer good efficiencies around 20%; however, they have serious disposal problems.[9] Unfortunately, more environmentally friendly solar technologies such as dye/quantum dot (QD) solar cells have subpar performance compared to silicon wafer and/or thin film solar technologies.[10,11] On the other hand, hybrid halide perovskite solar cells (PSCs) are an emerging solar technology that may have the potential to outperform established solar technologies at cheaper costs than silicon because high-quality halide perovskite semiconductor can be made at much lower temperatures.[12–15] Halide perovskites are enticing for several reasons. The ingredients are abundant, and researchers can blend them easily and inexpensively, at low temperature, into thin films that have high crystallinity like that accomplished in silicon wafers while after costly, high-temperature processing.

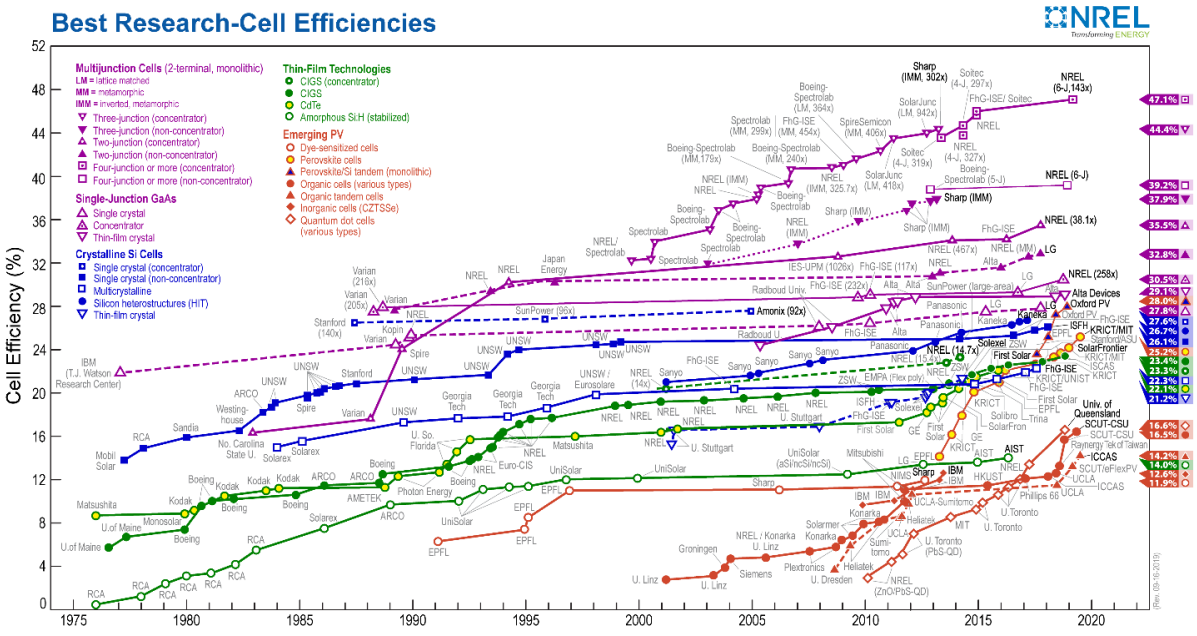

Figure 1.2 National Renewable Energy Laboratory (NREL) chart of the highest confirmed power conversion efficiencies for research cells for a range of photovoltaic technologies. Reprinted from ref. 16 with permission from the NREL.

PSCs have achieved an impressive certified power conversion efficiency (PCE) of 25.2% within a decade of their development due to their high absorption coefficient, high carrier mobility and, long diffusion length (Figure 1.2).[16]

In the next section, the structural and optoelectronic properties of halide perovskites are described, which make them a unique solar material in providing an excellent alternative option to silicon wafer solar technology.

1.2.1 Structure and properties of halide perovskites

Halide perovskites adopt ABX_3 crystal structure (Figure 1.3), where A = methylammonium (MA), formamidinium (FA), cesium (Cs) and/or rubidium (Rb); B= lead (Pb) and/or tin (Sn); X= chlorine (Cl), bromine (Br) and/or iodine (I), which are typically described as three-dimensional (3D) halide perovskites. ABX_3 perovskite structure consists of an extended 3D network of corner-sharing BX_6 octahedra, where B is generally a divalent metal cation, and X is halide anion. The A cations fill the 12-fold coordinated cubo-octahedral cavity formed by adjacent octahedra. Goldschmidt's tolerance factor (t) dictates the formation of ABX_3 perovskite structure,

$$t = \frac{(R_A+R_X)}{\sqrt{2}(R_B+R_X)}, \qquad (1.1)$$

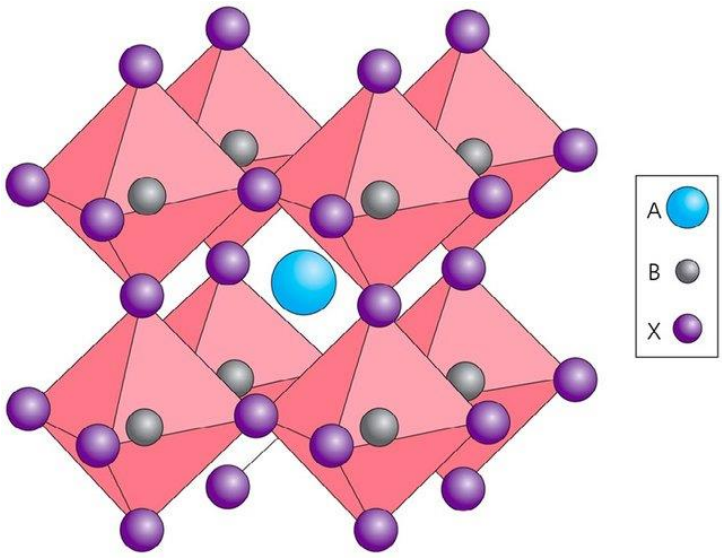

Figure 1.3 Crystal structure of ABX_3 perovskites. Reprinted from ref. 14 with permission from the Springer Nature Springer Nature Limited.

where R_A, R_B, and R_X denote the ionic radii for the A, B, X ions, respectively, and the tolerance factor must satisfy t ≈1 for 3D ABX_3 perovskite formation. The ability to change components in a number of permutations within the limit of tolerance factor provides a room for engineering perovskite materials with tunable physical, chemical, optical, and electronic properties.[17] Figure 1.4a shows the tunability of bandgap of halide perovskites by compositional engineering.[18]

3D perovskites have a direct bandgap nature with relatively large absorption coefficient, which produces high photocurrent in submicron films used in optoelectronic applications. A strong optical absorption in halide perovskites originates from the halide-p → metal-p band edge transition. Here, we should take note of that the direct gap nature of halide perovskites is a standard generalization, but there may be subtle nevertheless crucial exceptions in noncentrosymmetric perovskite compounds due to Rashba, Rashba/Dresselhaus splitting.[19,20] The absorption coefficient of typical halide perovskite, $MAPbI_3$ is presented in Figure 1.4b along with $MAPbBr_3$ and a number of other semiconductors which are widely used as solar absorbers in a variety of PV systems.

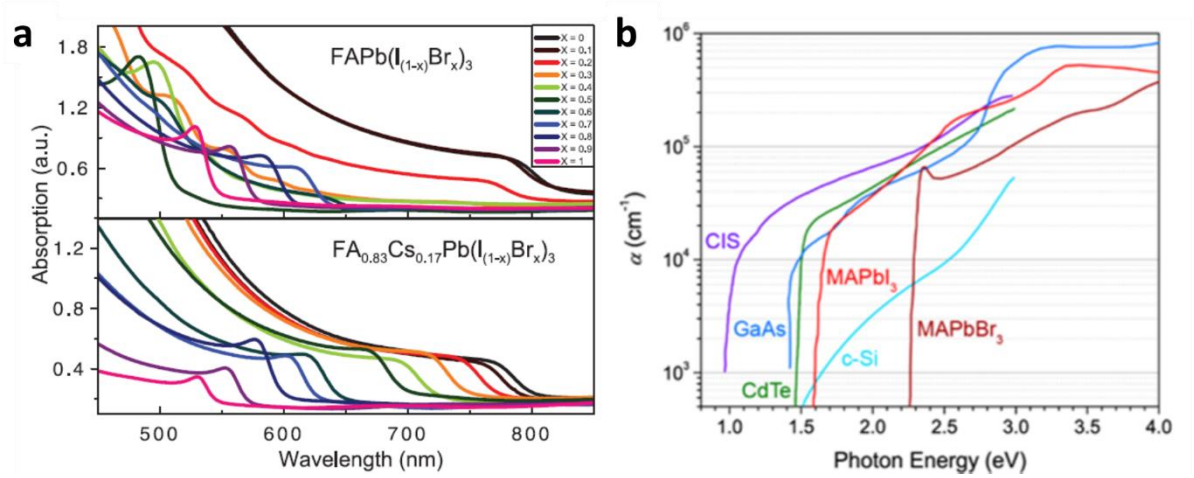

Figure 1.4 a) Bandgap tunability of $FAPb(I_{1-x}\ Br_x)_3$ perovskite (Br composition increasing from x = 0 to 1). Reprinted from ref. 18 with permission from the American Association for the Advancement of Science. b) Experimentally determined the absorption coefficient of variety of solar absorbers. Reprinted from ref. 17 with permission from the American Chemical Society.

In addition to the superior optical properties of halide perovskites, underlying photophysics has been found critical in achieving efficient thin-film PV devices. For example, photoexcited charge carriers in 3D perovskites exist as free charge carriers at room temperature which allows fabricating planar thin-film solar cells. The temperature dependent photoluminescence (PL) and magneto-absorption measurements have revealed that 3D perovskites have exciton binding

energies ranging from 19 to 50 meV, which are comparable to the thermal energies at room temperature of k_bT ~25 meV. One of the greatest advantages of PSCs is their low potential loss between bandgap and V_{oc}, due to low density of sub gap defect states. The exciton dynamics and low defect densities contribute to much longer charge carrier recombination lifetime in halide perovskites which results in longer charge carrier diffusion lengths (>1 μm).

A more comprehensive discussion on material and optoelectronic properties of halide perovskites can be found in chapter 2. In the next section, major concerns with state-of-the-art Pb-based 3D perovskites are discussed.

1.2.2 Toxicity and stability of halide perovskites

The state-of-the-art PSCs involve water-soluble Pb species, which hinder the wide application of this technology.[21] Pb halide perovskites in contact with water or humid air form water-soluble by-products of Pb, which can accumulate within the food chain and so human body.[22,23] Countries around the world adhere to lead-free directives which set a maximum amount of lead in electronic devices. For example, the European Union adheres to the ''Directive on the restriction of the use of certain hazardous substances in electrical and electronic equipment,'' RoHS1 in 2003 and the subsequent RoHS2 in 2011. These Directives restrict to 0.1% in weight the maximum concentration of lead in each homogeneous material contained in any electronic devices, i.e., the perovskite material within a perovskite solar cell. North America also makes similar restriction to the content of lead in the electronic devices. Meanwhile, it should be noted that highly efficient halide perovskites materials contain more than 10% lead in weight. Suitable candidates for Pb replacement, without much tradeoff in photovoltaic performance, are elements in the same group (group 4) as Pb. The Sn and germanium (Ge), both of which have multiple oxidation states (2+ and 4+) are good candidates. The computational studies show that the electronic configuration of Pb^{2+} in the ABX_3 perovskite structure is crucial for its remarkable photovoltaic properties.[24,25] To date, Sn-based perovskites are toxicologically safer, highest-performing lead-free perovskite solar cells.[26,27] However, the performance of the best Sn-based PSC is still falling far short of Pb halide PSCs, reporting the highest efficiency of 9.41%.[28] Another approach is alloying/replacing Pb with less toxic metals such as Sn and Ge in ABX_3 perovskites which is a very promising strategy towards achieving stable, less toxic solar cells without compromising the photovoltaic performance.

Another major concern is stability of halide perovskites. The effect of moisture on PSCs has received substantial attention on the account of presence of water (from rain and humid air) in

real-world applications of solar cells.[29,30] The volatile small organic molecules (A-site cations) such as MA and FA can be expelled by water due to the weak non-covalent bond between organic and inorganic framework. For example, $MAPbI_3$ perovskite can easily hydrolyze in the presence of water due to deprotonation of MA^+ by H_2O.[31] Even though a complete understanding of decomposition of 3D perovskites upon exposure to water is not yet fully formed, there is a consensus on organic cations being a susceptible component to the H_2O molecules. Also, organic cations have low enthalpies of formation making them unstable even at moderate temperatures.[32] The halide perovskite upon exposure to light can generate superoxide O^{2-} formed which acts as a Lewis base to deprotonate MA^+ to form CH_3NH_2 and degrade the perovskites.[33,34]

1.2.3 Layered halide perovskites

As described in last section **1.2.2**, the small organic molecules in halide perovskite are the weakest component as far as their stability is concerned. Therefore, replacement of these unstable small hygroscopic organic cations with bulkier hydrophobic organic cations is expected to help prolong the lifetime of the perovskites under ambient conditions.[35,36] As we discussed in section **1.2.1**, the introduction of bulkier organic cations in perovskite structure distorts the structural integrity of the perovskite framework. The introduction of bulkier organic cations leads to the formation of lower dimensional (two-dimensional (2D)) or layered perovskites.[37–39] The bulky organic cations in 2D perovskites provide steric hindrance for the surface water absorption which is the initial step of halide perovskite decomposition. Therefore, hydrophobic bulky organic cations in 2D perovskite structure can effectively impede moisture infiltration.[39] The 2D perovskites can be formed along different crystallographic directions, specifically, <100>-oriented, <110>-oriented, and <111>-oriented.[41] The <100>-oriented perovskites are most commonly used layered perovskite, further they can be categorized into Ruddlesden−Popper (RP) phases, Dion−Jacobson (DJ) phases, and alternating cation in the interlayer space (ACI) phases. RP phases are most ideal for optoelectronic applications. The RP perovskites have generic formula of $(RNH_3)_2(A)_{n-1}BX_{3n-1}$ (n is an integer which represents the number of perovskite layers), where RNH_3 is a primary aromatic or aliphatic alkylammonium cation serving as a spacer between the perovskite layers. The number of perovskite layers can be tuned by changing ratios between RNH_3 and A-site cations (Figure 1.5).[40]

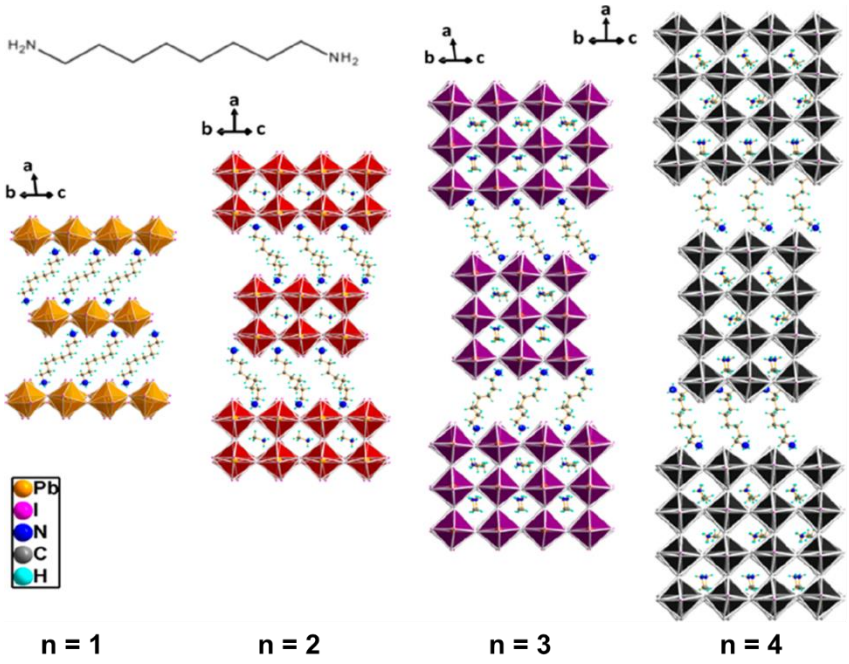

Figure 1.5 Crystal structures for $(NH_3C_8H_{16}NH_3)$ $(CH_3NH_3)_{n-1}Pb_nI_{3n+1}$ (n = 1−4) from solution method. Reprinted from ref. 40 with permission from the American Chemical Society.

Phase-pure compounds of layered perovskites are difficult to synthesize, only up to n = 7 have been successfully synthesized. Generally, attempts to obtain thin films of 2D perovskites with n>4 do not really produce a phase-pure n-member of layered perovskites but a mixture of different n-members of lower dimensional perovskites. Optoelectronic properties of 2D perovskites are significantly different from that of 3D perovskites due to dielectric and quantum confinement of charge carriers[42]. In chapter 2, we explore structural and optoelectronic properties of 2D perovskites in detail. Due to the different optoelectronic properties of phase-pure 2D perovskites, such as wider optical band gaps and limited charge transport, the 2D perovskites are not ideal for photovoltaic applications. In summary, use of stable 2D perovskites in solar cells comes with major trade-off in photovoltaic performance.

1.2.4 Bulky organic cations as additives or/and A-site substituents in halide perovskites

The optoelectronic properties of the layered perovskites can be tuned by varying the number of perovskite layers. For instance, change in optical band gap with varying “n” is shown in Figure 1.6. The layered perovskites with n>10, can be considered as mixture of lower dimensions and 3D perovskites. The mixed-dimensional perovskites show better photovoltaic performance

compared to phase-pure 2D perovskites and improved device stability compared to 3D perovskites. Even though, mixed-dimensional perovskites show better stability compared to 3D perovskites, they exhibit comparatively lower photovoltaic performance to that of 3D perovskites.

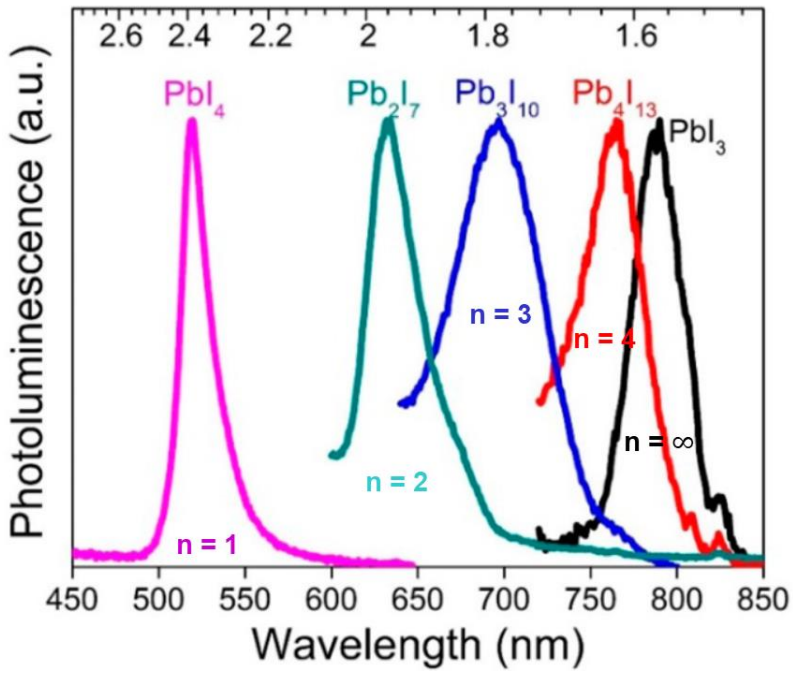

Figure 1.6 PL spectra of perovskite thin films of the $MAPbI_3$ (n=∞) and $(BA)_2(MA)_{n-1}Pb_nI_{3n+1}$ compounds showing change in the optical band gap with varying number of perovskite layers. Reprinted from ref. 37 with permission from the American Chemical Society.

In another class of materials, namely 2D/3D perovskites, a very small amount of 2D perovskites are incorporated on the top surface of the 3D perovskite film (*via* spin coating 2D perovskite precursor solution on the top of 3D perovskite film) or in the bulk 3D perovskites (substituting a small amount of A-site cations with bulky organic cations in the perovskite precursor). 2D/3D perovskites predominantly show bulk 3D perovskite characteristics (optoelectronic and structural properties), but with some additional benefits, such as improved stability and fewer defects.

1.3 Thesis Objectives and Organization

1.3.1 Objectives

Part I: Synthesis and characterization of 2D perovskites with phenylethyl ammonium (PEA) spacer cations and their solar cell application

2D perovskites are resistant to degradation in the presence of moisture, heat, and light. Here, 2D perovskites are synthesized by isolating metal halide perovskite layers (PbI_6) using bulkier aromatic PEA ($(C_6H_5(CH_2)_2NH_3)_2(CH_3NH_3)_2$) spacer cations. The aromatic spacer cations are expected to be better compared to aliphatic organic cations in retaining their performance under ambient humidity levels due to the hydrophobic property of the spacer cation. High quality $(PEA)_2(MA)_{n-1}Pb_{n-1}I_{3n-1}$ perovskite films (n=3, 4, 5) were prepared by hot-cast method for solar cell application. The superior stability of PEA-based 2D perovskite through a series of characterizations, such as X-ray diffraction (XRD) analysis, absorption measurements (using ultraviolet–visible spectroscopy), charge-carrier lifetime measurements (using time-resolved photoluminescence (PL)), and thermogravimetric analysis (TGA).

Part II: Effects of PEA cations in Sn-Pb alloyed perovskites and performance enhancement of solar cells

Though, $(PEA)_2(MA)_{n-1}Pb_{n-1}I_{3n-1}$ perovskite exhibit superior stability, the photovoltaic performance seems to be inferior to that of 3D perovskites. Another concern is involvement of water-soluble Pb species, which hinder the real-world application of this technology. The Sn metal is found to be best alternative for Pb in achieving reasonable photovoltaic performance, but still inferior to typical Pb-perovskites. Alternatively, alloying Pb with Sn perovskites seems to be a promising, balanced strategy towards achieving stable, less toxic solar cells without much compromising the photovoltaic performance. The major objective was here to explore the effects of PEA cations in Sn-Pb perovskites to simultaneously improve photovoltaic performance and device stability. The expertise and familiarity with PEA spacer cations in designing 2D perovskites (in Part I) applied to synthesize stable and efficient PEA-incorporated Sn-Pb perovskites. Additionally, alloyed Sn-Pb perovskites also fetch an added benefit of extending absorption of photons to the near-infrared (NIR) spectral range. Effects of incorporating bulky organic cations in reducing Sn defect formation in iodide-based Sn-Pb based perovskite investigated through experimental results such as X-ray photoemission spectroscopy (XPS), XRD, surface potential measurements, transient absorption measurements and PL spectroscopy. Furthermore, Sn defect passivation by PEA molecules was confirmed by DFT calculations. Further, bandgap of Sn-Pb perovskites was tuned by partial substitution of I with Br and a value of 1.4 eV was obtained, which is close to ideal bandgap for a single-junction solar cell according to the Shockley–Queisser limit. In the case of mixed halide Sn-Pb perovskites, addition of optimized amount of PEA led to halide homogenization in the perovskite film surface which resulted in favorable band alignment of

perovskite with electron transport layer. The photovoltaic properties and recombination dynamics of mixed halide Sn-Pb perovskites were studied.

1.3.2 Thesis organization

The thesis organized into five chapters as follows:

Chapter 1 Introduction: This chapter briefly introduces theory of solar cells and halide perovskite solar cells.

Chapter 2 Literature Review: Structural and optoelectronic properties of 2D layered perovskites and 2D/3D perovskites and their application as solar cell absorbers.

Results: The experimental results are discussed in next three chapters.

Chapter 3 This chapter presents synthesis of 2D perovskites using aromatic alkylammonium spacer cations, PEA, and their characterization. Also, modified thin film fabrication and their application for solar cells are provided.

Chapter 4 In the fourth chapter, use of PEA in Sn-Pb alloyed perovskites and characterization of Sn-Pb thin films are described. Furthermore, the improvement of photovoltaic performance and stability in PEA-containing Sn-Pb perovskites is rationalized through series of characterizations.

Chapter 5 deals with fine-tuning the performance of Sn-rich alloyed perovskites. Here, optical properties of Sn-rich alloyed perovskites are tuned by partially substituting iodine with bromine. Further, optimized amount of PEA incorporated in these mixed halide Sn-rich alloyed perovskites to yield improved performance and stability.

Chapter 6 General discussion and conclusion: General comments and main conclusions are presented based on the experimental results, theoretical calculations and their analysis. Also, future prospects in this research direction are proposed.

2 LITERATURE REVIEW ON 2D PEROVSKITES AND 2D/3D PEROVSKITES

Title of the article: Searching for stability at lower dimensions: current trends and future prospects of layered perovskite solar cells

French translation: À la recherche de la stabilité à des dimensionalités inférieures: les tendances actuelles et les perspectives futures des cellules solaires pérovskites en couches

Authors:

Authors' names: Deepak Thrithamarassery Gangadharan and Dongling Ma

Professional affiliations: Institut National de la Recherche Scientifique, Centre-Energie Materiaux et Telecommunications, Universite du Quebec, Varennes, QC, J3X 1S2, Canada.

Title of the journal or book:

Energy & Environmental Science, submitted on 16th May 2019, Accepted on 15th July 2019, DOI: 10.1039/c9ee01591d.

Contribution of the authors:

The manuscript was written by Deepak Thrithamarassery Gangadharan. Dongling Ma supervised and made necessary corrections.

2.1 Introduction

In search of cheap, solution-processable solar conversion technologies to replace Silicon (Si) wafer technology, halide perovskite solar cells (PSCs) have become a leading contender within a decade of their development.[12,43–45] PSCs employing a three-dimensional (3D) structure achieved a certified efficiency of 23.7%.[16] Unfortunately, the issue associated with the long-term stability of 3D perovskites against moisture, heat, and light is still a huge hurdle for their real-world applications.[29,30] The effect of moisture on PSCs has received substantial attention on the account of presence of water (from rain and humid air) in realistic operating conditions of solar cells. A small amount of Lewis base, such as water, can readily disrupt the 3D perovskite structure through hydrogen bonding. The volatile small organic molecules (such as methylammonium (MA) and formamidinium (FA)) can be ejected by water due to the weak non-covalent bond between organic and inorganic framework. For instance, a typical 3D perovskite methylammonium lead triiodide ($MAPbI_3$) readily hydrolyzes in the presence of water due to deprotonation of $CH_3NH_3^+$ (MA^+) by H_2O, and degrades into products, such as CH_3NH_2, HI, and PbI_2.[31,46,47] Some researchers suggested that the degradation of $MAPbI_3$ in ambient environments may produce $PbCO_3$ and α-PbO rather than PbI_2.[48,49] Formation of unstable intermediate phases like monohydrated $CH_3NH_3PbI_3.H_2O$ or dihydrated $(CH_3NH_3)_4PbI_6.2H_2O$ has also been observed.[50–52] First-principles calculations have recently predicted that intermediate degradation products could reduce the activation energies for vacancy-mediated ion migration.[48] Ion migration is also detrimental to the photovoltaic performance and stability of PSCs. Even though a comprehensive understanding of water-induced decomposition of 3D perovskites is not yet fully established, there is a resounding consensus on small organic cations being an extremely vulnerable component to the water molecules. In addition, organic cations having low enthalpies of formation can also be easily liberated at moderate temperatures.[32] As well, superoxide O_2^- formed in halide perovskites under illumination acts as a Lewis base to deprotonate MA^+ to form CH_3NH_2.[33,34] Therefore, replacement of these unstable small hygroscopic organic cations with bulkier hydrophobic organic cations expected to help prolong the lifetime of the perovskites under ambient conditions. The introduction of certain bulkier organic cations in perovskite structure distorts the structural integrity of the perovskite framework and lead to the formation of lower dimensional (two-dimensional (2D)) layered perovskites but in some cases, they passivate the defects in 3D perovskites. We are well aware of ongoing debate over the

semantics of “layered perovskites” as well as definition of a “perovskite-type structure”, but we label the materials that contains disconnected perovskite layers as “layered perovskite” in this review, following the widely held perception.[35,53] Nevertheless, it has been asserted that bulkier, hydrophobic organic cations in 2D perovskites could strain the surface Pb-I bonds and repel the water molecules from reactive sites.[54,55] Karunadasa *et al.* reported the first application of 2D halide perovskite as a promising, stable solar absorber layer, although the power conversion efficiency (PCE) of 4.73% was relative low even at that time.[36] An over 10% efficiency reported by Mohite and co-authors in 2016 revived interest in layered perovskite materials.[56] This led to a number of seminal fundamental and experimental studies in 2017-2018, including but not limited to structure-property relationships, excitonic properties of charge carriers, synthetic chemistry aspects and solar cell application, *etc*.[57–60] Recently, a mixed composite of 3D and 2D perovskite phases, known as 2D/3D perovskites emerged as a class of excellent photovoltaic material with long-term stability. In this review, considering an invigorated appeal to 2D perovskites, we discuss their structural and optoelectronic properties. We also summarize the progress of 2D and 2D/3D PSCs extensively in this article. Further, we assess the design principles for efficient layered PSCs.

2.2 Structural characteristics

ABX_3 perovskite structure consists of an extended 3D network of corner-sharing BX_6 octahedra, where B is generally a divalent metal cation, and X is halide anion. The A cations fill the 12-fold coordinated cubo-octahedral space created by adjacent octahedra.[61] The ABX_3 perovskite structure formation is dictated by the Goldschmidt’s tolerance factor,

$$t = \frac{(R_A+R_X)}{\sqrt{2(R_B+R_X)}}, \qquad (2.1)$$

The ABX_3 perovskites known as 3D perovskites have rigid structural constrains, which limit their structural tunability. But they can be cut into slices from the 3D structure to lower dimensional layered configuration, all the way down to eventually zero-dimensional (0D) BX_6 octahedra clusters.

Dimensional reduction gradually removes the size constrains imposed by the tolerance factor. The layered 2D derivatives of the 3D perovskites can be conceptualized by slicing the 3D structure

into well-defined 2D inorganic or perovskite layers (Figure 2.1).[37,39,41,62] The layered perovskites can accommodate considerably larger and more complex organic cations as compared to 3D perovskites. There are two central guiding principles to be followed in designing and synthesizing new 2D layered perovskites.

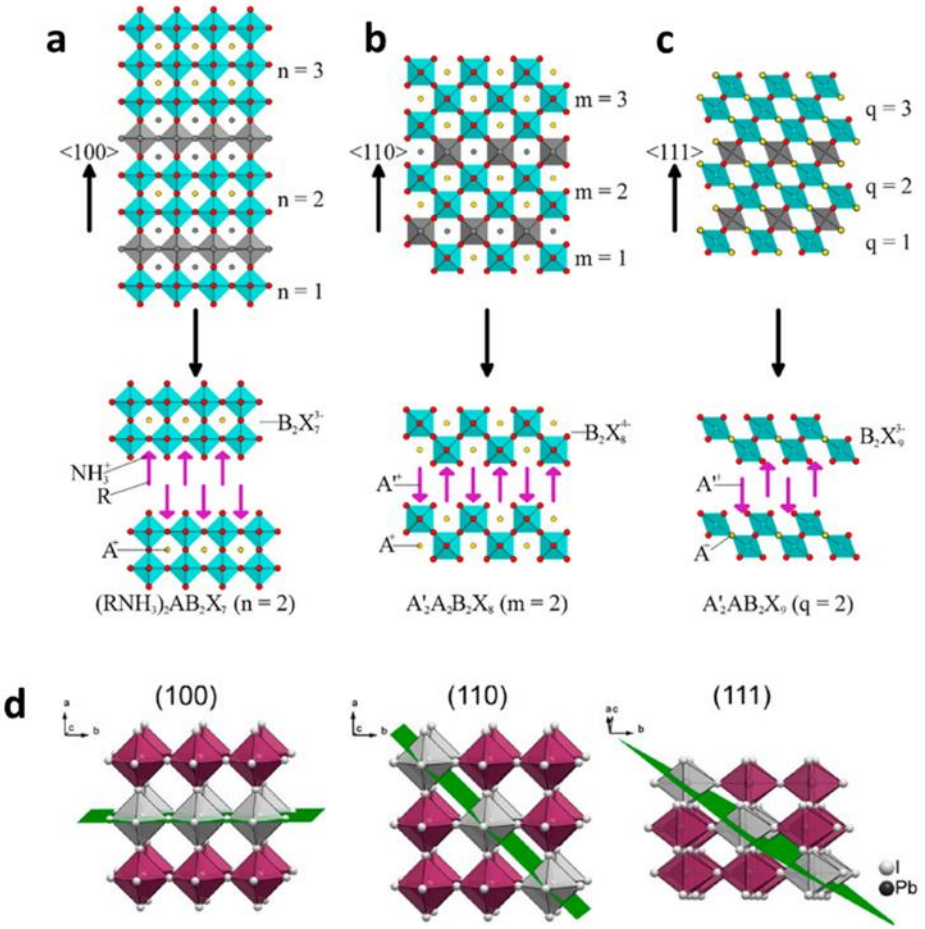

Figure 2.1 Schematic representation of different families of layered perovskites: (a) family of <100>-oriented layered 2D perovskites with a general formula of $(RNH_3)_2A_{n-1}B_nX_{3n+1}$, (b) (<110>-oriented, $A'_2A_mB_mX_{3m+2}$ layered 2D perovskites (c) and < 111>-oriented, $A'_2A_{q-1}B_qX_{3q+3}$ layered 2D perovskites. Reprinted from ref. 41 with permission from the American Chemical Society. d) Derivation of 2D halide perovskites from the parental cubic perovskite lattice of 3D LHPs by cutting the latter along typical crystallographic planes: (100), (110), and (111). Reprinted from ref. 63 with permission from the American Chemical Society.

Foremost, the organic molecule must contain one or two terminal functional groups that can interact with the inorganic anion via hydrogen bonds. It is important to note that the rest of the organic molecule should not interfere with the "B" and "X". Secondly, the width of the organic molecule is regulated by a space specified by adjacent corner-sharing BX_6 octahedra.

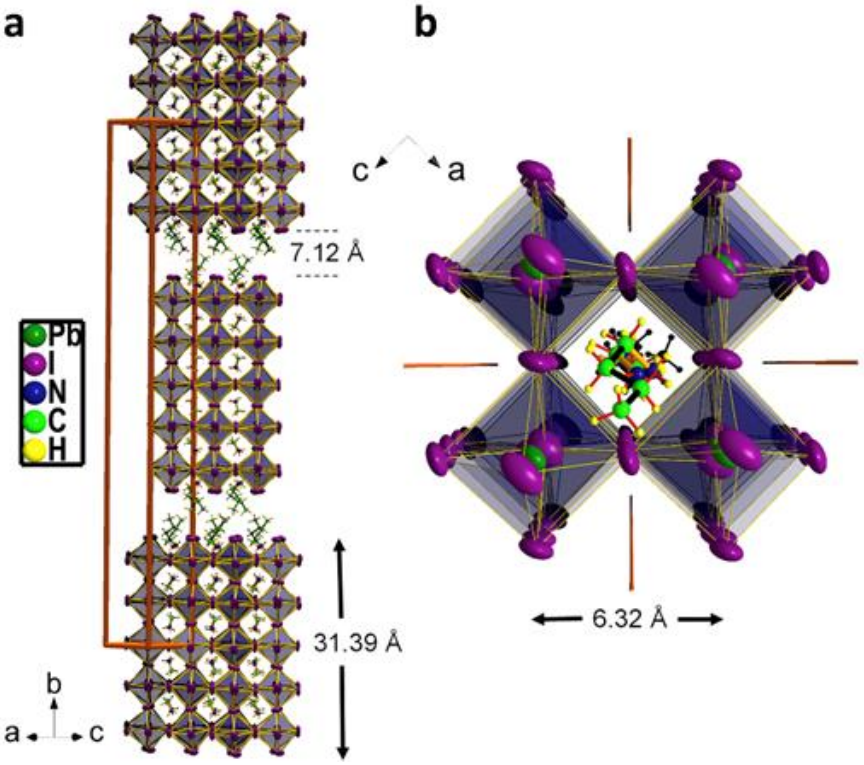

Figure 2.2 (a) Unit cell of $BA_2MA_4Pb_5I_{16}$ (n=5), where layers are separated by a distance ~ 7.12Å. (b) A View of a single perovskite slab along the b axis. Reprinted from ref. 77 with permission from the Cell press.

If the width of the organic molecule is too large, it can cause steric hindrance to neighboring organic molecules, leading to difficulty in fitting the required number of organic cations into the perovskite framework for the charge balance. The formation of layered 2D derivatives may be along different crystallographic directions, producing different families of layered perovskites, namely <100>-oriented, (<110>-oriented), and <111>-oriented perovskites (Figure 2.1). Out of the three classifications, <100>-oriented perovskites are by far the most commonly found 2D layered perovskite structure. Further, the number or thickness of perovskite (or inorganic) layer in layered 2D perovskites can be synthetically controlled by tuning the stochoimetric ratio between A-site cations and larger spacer cations. The layer thickness is denoted by 'n' in <100>- oriented layered perovskites, 'm' in <110>-oriented layered perovskites and 'q' in <111>- oriented layered perovskites. Following the classification of layered oxide perovskites (such as Sr_2TiO_4, Ca_2MnO_4 and $SrLaAlO_4$), the <100>-oriented 2D halide perovskites can be further categorized to Ruddlesden−Popper (RP),[64,65] Dion−Jacobson (DJ),[66] and Aurivillius (AV) perovskites.[67–69] Among these three types, RP phase perovskites are the most commonly used in optoelectronic applications. In contrast, we are aware of only few reports on the DJ phase in halide

perovskites,[70,71] while the AV phase can only be found in oxide perovskite families. In this section, our discussion primarily focuses on the <100>-oriented RP phase halide perovskite.

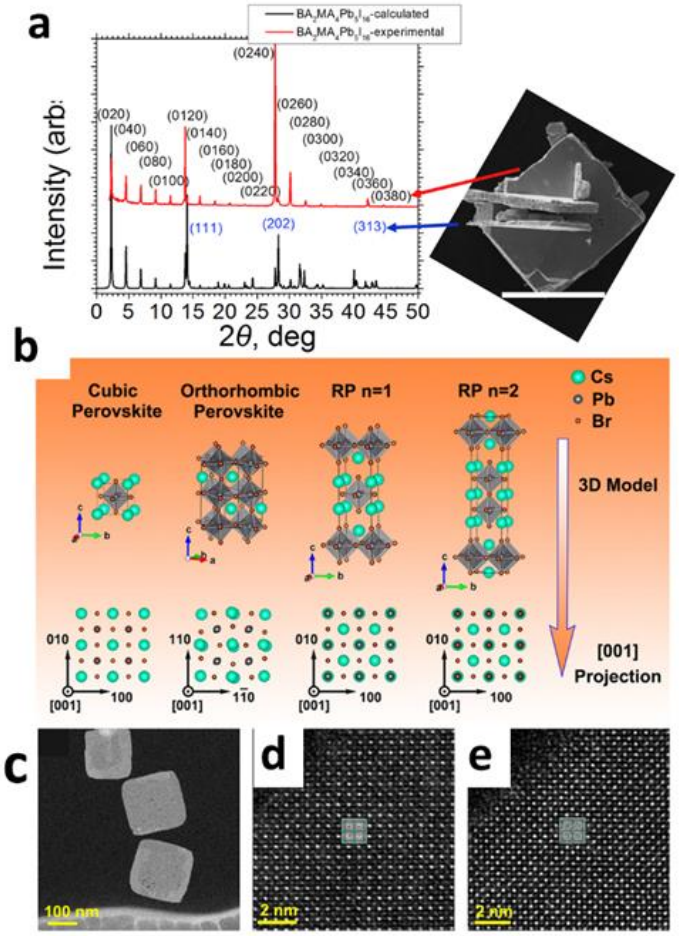

Figure 2.3 a) XRD pattern and scanning electron microscopy (SEM) image of $BA_2MA_4Pb_5I_{16}$ crystals. Reprinted from ref. 77 with permission from Cell press. (b) Representations of the crystal structures of conventional $CsPbBr_3$ perovskite phases (cubic and orthorhombic) and RP phases (n = 1, 2) and (c) STEM image of $CsPbBr_3$ nanosheets (d) Atomic-scale AC-STEM image of conventional perovskite phase within a $CsPbBr_3$ nanosheet and (e) [001] projections are overlaid in an unusual phase region in $CsPbBr_3$ nanosheet, where an in-plane (½, ½) shift between two adjacent $CsPbBr_3$ observed. Reprinted from ref. 80 with permission from the American Chemical Society.

2.2.1 RP phase perovskites

RP perovskites with a general formula $(RNH_3)_2\ A_{n-1}B_nX_{3n+1}$ can be imagined as intergrowth compounds formed from the 3D ABX_3 and 2D layered $(RNH_3)_2BX_4$. The RNH_3 is an organic cation spacer. From a crystallography point of view, RP perovskites can be produced by methodically

removing the B-component from the inorganic framework along the <100> crystallographic axis in the ABX_3 structure.

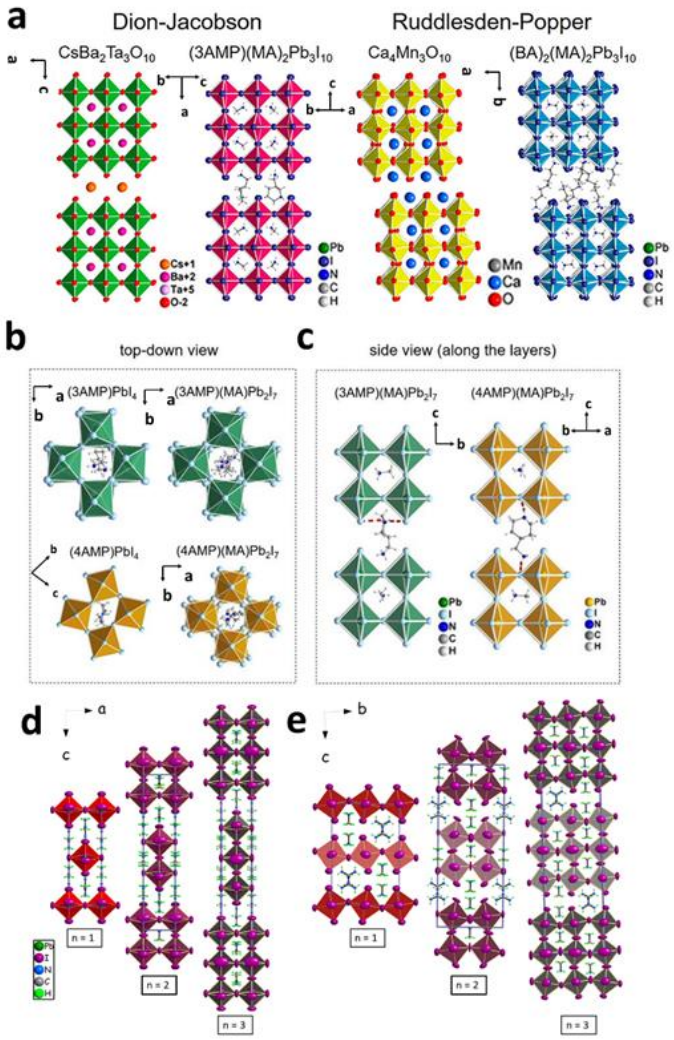

Figure 2.4 a) Difference in crystal structures between DJ phase and RP phase of both oxide and halide perovskite. (b) Top-view of DJ phase 2D perovskites, and (c) side-view of DJ phase 2D perovskites. Reprinted from ref. 70 with permission from the American Chemical Society. Unit cells of ACI perovskites $(GA)(MA)_nPb_nI_{3n+1}$ (n = 1−3) along (d) the crystallographic b-axis and (e) the crystallographic a-axis. Reprinted from ref. 85 with permission from the American Chemical Society.

In the RP phase, inorganic layers are offset by one octahedral unit, showing a (½, ½) displacement along the ab-plane (i.e. a half unit cell shift in both a and b crystallographic axes). As a result, the layers are to slide in a staggered configuration (where inorganic layers are not stacked perfectly on top of each other). The structure of $(RNH_3)_2BX_4$ compounds generally

matches that of the distorted K_2NiF_4-type. The unit cell in the layered $(RNH_3)_2BX_4$ perovskites features two inorganic layers and two organic bilayers. In contrast to the 3D structure, the lattice constant values in layered perovskites are increased due to the incorporation of larger spacer cations. For example, Butylammonium (BA) spacers need an accommodating space of ~7.12 Å between the perovskite layers and one perovskite layer has a thickness ~6.32 Å, which is about two Pb−I bond lengths (Figure 2.2). As the perovskite slab gets thicker by introducing smaller cations (*e.g.*, MA) in the crystal structure, the unit cell expands. The low angle reflections in X-ray diffraction (XRD) reveal the number of perovskite layers in a 2D perovskite. Both the calculated and experimental XRD spectra (Figure 2.3a) of $BA_2MA_4Pb_5I_{16}$ (n=5) show five distinct reflections below $2\theta \approx 14°$, indicating the number of perovskite layers in the compound. The positions of heavy atoms in layered perovskites govern the crystal symmetry, but the exact space group changes with the nature of the organic spacer and thereby indirectly affects the details of crystal symmetry. The organic spacer provides the structure more freedom and prompts a relative rotation and tilting of the $[BX^6]^{4-}$ octahedra with respect to small A-site cations in the cuboctahedral cages. All A-site cations in 2D layered RP perovskites are oriented in the same direction, which is implied by noncentrosymmetric configurations in the 2D perovskite crystal structure.[36,72–76] The $(BA)_2(MA)_{n-1}Pb_nI_{3n+1}$ layered perovskite compounds are one of the well-studied (100)-oriented RP phase.[39,77] BA is a monovalent organic spacer molecule. All $(BA)_2(MA)_{n-1}Pb_nI_{3n+1}$ (n=1,2,3,4,5,6,7) perovskites crystallize in orthorhombic space groups, of which $(BA)_2PbI_4$ (n=1) crystallizes in the primitive centrosymmetric *Pbca* space group, the $(BA)_2(MA)Pb_2I_7$ (n=2) in Cc2m, the $(BA)_2(MA)_2Pb_3I_{10}$ (n=3) in C2cb, the $(BA)_2(MA)_3Pb_4I_{13}$ (n=4) in *Cc2m*, the $(BA)_2(MA)_4Pb_5I_{16}$ (n=5) in *Acam*, the $BA_2MA_5Pb_6I_{19}$ (n=6) in *Cc2m* and the $(BA)_2(MA)_6Pb_7I_{22}$ (n=7) in *C2cb*. It is important to note that compounds with n > 5 is synthetically challenging to be isolated in a phase pure form due to unfavorable enthalpies of formation (ΔH_f). The higher-n members tend to transform to the n = 3 and n = ∞ members. Recently, Kanatzidis *et al.* reported first and only structurally characterized high members of layered perovskites (n=6,7) using kinetically controlled chemical synthesis.[78] In contrast to monovalent organic spacer cations like BA, the divalent organic cations bring the inorganic layers closer. For example, the interlayer terminal iodide−iodide distance was decreased from 9.14 Å to 4.37 Å to when benzylammonium (BZA), a monovalent organic cation was replaced with histammonium (HA), a divalent organic cation in 2D perovskites.[79] The variation of the interlayer distance strongly affects the lattice constants, therefore the crystal structure of 2D perovskites. Crystallographic data of 2D layered perovskites explored in solar cell applications are listed in **Table 2.1.**

Interestingly, RP phase was observed in $CsPbBr_3$ nanosheets.[80] Aberration-corrected scanning transmission electron microscopy (AC-STEM) revealed the structural details of plausible coexistence of RP domains and conventional perovskite phases (such as cubic and orthorhombic).[81] The [001]-projected atom columns in conventional perovskite phases are pure Cs and Pb−Br columns. On the other hand, all the [001]-projected atom columns are Cs−Pb−Br in RP phases. Figure 2.3b shows the crystal structures of different phases, where the [001] structural projection is also depicted. AC-STEM image of $CsPbBr_3$ is shown in Figure 2.3d. Yu *et al.* observed an unusual phase region in the AC-STEM image of $CsPbBr_3$ nanosheets along with conventional perovskite phase (Figure 2.3e).[80] They overlaid the [001]-projection of conventional phase on the unusual phase region to identify the unusual phase observed in the $CsPbBr_3$ nanosheets with atomic resolution. An in-plane (½, ½) shift corresponding to the RP phase was observed between two adjacent $CsPbBr_3$ units. Therefore, all the [001]-projected atom columns were Cs−Pb−Br columns in the unknown phase region confirming the coexistence of RP and conventional perovskite phases. It also shows that RP domains and conventional perovskite domains are well-connected, and all the domain boundaries are positioned in the $<100>$ crystallographic directions on the atomic scale. Very recently, Li *et al*. synthesized all-inorganic 2D RP perovskites, $Cs_2PbI_2Cl_2$ and $Cs_2Sn_2I_2Cl_2$ with the optoelectronic response for the first time.[82,83] The RP compound $Cs_2PbI_2Cl_2$, with n = 1, is formed by corner-sharing of elongated $[PbI_2Cl_4]$ octahedral units. The $Cs_2PbI_2Cl_2$ synthesized by a solid-state method crystallizes in the tetragonal space group of *I4*/*mmm*. All-inorganic layered compounds, $Cs_2SnI_2Cl_2$ and $Cs_2PbI_2Cl_2$, and hybrid layered compound $(MA)_2PbI_2(SCN)_2$[84] have distinctive structure compared to the rest of hybrid layered perovskite RP phases. In these structures, the separation between the layers occurs without the use of bulky organic spacers, while as a result of the ionic-size mismatch of the two heteroatoms (I^- and SCN^- in $(MA)_2PbI_2(SCN)_2$ compound and I^- and Cl^- in $Cs_2SnI_2Cl_2$ and $Cs_2PbI_2Cl_2$ compounds).

2.2.2 DJ phase perovskites

Recently Mao et al. reported the first complete homologous series of DJ hybrid layered perovskites, which adopt a general formula of $A'A_{n-1}Pb_nI_{3n+1}$.[70] In comparison to the RP phase which features two monovalent spacer cations, the DJ structure contains single divalent (2^+) interlayer spacer cation. In a crystallographic standpoint, the DJ phases are supplemented relative (1/2, 0) shift of the layers along the ab-plane or no shift (0,0) at all.

Table 2.1 Crystallographic parameters of 2D perovskites explored in PSCs.

Compound	Spacer cation	Crystal system	Space group	Unit cell dimensions (Å)		
				a	b	c
RP Phase						
$(BA)_2PbI_4$	n-Butylammonium (C_4NH_{11})	orthorhombic	*Pbca*	8.876	8.692	27.601
$(BA)_2(MA)Pb_2I_7$	n-Butylammonium (C_4NH_{11})	orthorhombic	*Cc2m*	8.947	39.347	8.858
$(BA)_2(MA)_2Pb_3I_{10}$	n-Butylammonium (C_4NH_{11})	orthorhombic	*C2cb*	8.927	51.959	8.877
$(BA)_2(MA)_3Pb_4I_{13}$	n-Butylammonium (C_4NH_{11})	orthorhombic	*Cc2m*	8.927	64.383	8.881
$BA_2MA_4Pb_5I_{16}$	n-Butylammonium (C4NH11)	orthorhombic	*C2cb*	8.905	77.013	8.931
$(PEA)_2(MA)Pb_2I_7$	Phenylethylammonium ($C_{18}N_8H_{36}$)	-	*P1*	-	-	-
$(PEA)_2(MA)_2Pb_3I_{10}$	Phenylethylammonium ($C_{18}N_8H_{36}$)	Triclinic	*P1*	8.728	8.733	28.80
$(HA)PbI_4$	Histammonium ($C_5N_3H_{11}$)	monoclinic	*$P2_1/n$*	8.915	20.033	8.992
(HA)SnI4	Histammonium ($C_5N_3H_{11}$)	monoclinic	*$P2_1/n$*	8.741	20.044	8.984
$(BZA)_2PbI_4$	Benzylammonium ($C_{14}N_2H_{20}$)	orthorhombic	*Pbca*	9.1561	8.689	28.776
$(BZA)_2SnI_4$	Benzylammonium ($C_{14}N_2H_{20}$)	orthorhombic	*Pbca*	9.0944	8.6613	28.764
$(PA)_2MA_4Pb_5I_{16}$	n-Propylammonium (C_3NH_{11})	orthorhombic	-	8.624	72.53	9.297
$(Gu)_2PbI_4$	Guanidinium (CN_3H_5)	orthorhombic	*Pnnm*	27.033	9.310	12.917
$(Gu)_2SnI_4$	Guanidinium (CN_3H_5)	monoclinic	*$P2_1/n$*	9.2784	26.95	12.814
$BdAPbI_4$	1,4-Butanediammonium	Triclinic	*P1*	8.4815	8.847	11.202
$Cs_2PbI_2Cl_2$	Cesium (Cs)	Tetragonal	*I4/mmm*	5.6385	5.638	18.879
DJ Phase						
(3AMP) PbI_4	3-(aminomethyl) piperidinium	Monoclinic	*$P2_1/c$*	8.6732	18.426	20.4522
(3AMP) (MA) $Pb_2 I_7$	3-(aminomethyl) piperidinium	-	*Ia*	8.8581	8.8607	33.4749
(3AMP) $(MA)_2Pb_3I_{10}$	3-(aminomethyl) piperidinium	-	*Pa*	8.8616	8.8624	23.0316
(3AMP) $(MA)_3Pb_4I_{13}$	3-(aminomethyl) piperidinium	-	*Ia*	8.8627	8.8689	58.842
(4AMP) PbI_4	4-(aminomethyl) piperidinium	monoclinic	*Pc*	10.4999	12.542	12.5289

Table 2.1 Crystallographic parameters of 2D perovskites explored in PSCs. (Continued)

Compound	Spacer cation	Crystal system	Space group	Unit cell dimensions (Å)		
				a	b	c
(4AMP) $(MA)Pb_2I_7$	4-(aminomethyl) piperidinium	-	*Ia*	8.841	8.843	33.604
(4AMP) $(MA)_2Pb_3I_{10}$	4-(aminomethyl) piperidinium	-	*Pc*	23.133	8.836	8.8354
(4AMP) $(MA)_3Pb_4I_{13}$	4-(aminomethyl) piperidinium	-	*Ia*	8.858	8.857	58.915

In DJ oxide perovskites, the size of the spacer cations determines the shift in the unit cell; the (0,0) shift (*P4*/*mmm* space group) was observed with large cations, whereas (½,0) shift (*I4*/*mmm* space group) was observed with smaller cations. However, it has been perceived that this particular rule does not apply to halide perovskites.[85] The layers in DJ halide perovskites do not display any significant shift (with (0,0) displacement, where layers are stacked perfectly on top of each other). Figure 2.4a shows the comparison of crystal structures between the DJ and RP phases of both oxide and halide perovskites. The DJ halide perovskites were formed by employing 3AMP (3AMP = 3-(aminomethyl) piperidinium) and 4AMP (4AMP = 4 (aminomethyl) piperidinium) cations as spacer cations in between inorganic layers. The multilayered perovskites (n>1) were synthesized employing MA as the A-site cation. From the top-view of the DJ phase structure, the inorganic layers in (3AMP) PbI_4 exhibited a small mismatch owing to an out-of-plane octahedral tilting (Figure 2.4b&2.4c). Conversely, a large in-plane tilting was observed in (4AMP) PbI_4, which resulted in perfect stacking of the inorganic layers. As observed in the RP phase, the hydrogen bond between spacer cation and the inorganic layer has a significant effect on the octahedral tilting (or Pb−I−Pb angles) in DJ phases. For example, in (3AMP) $(MA)Pb_2I_7$, the 3AMP cation forms a weak hydrogen bond (red dotted line) with the terminal I^-, which has a small effect on the in-plane Pb−I−Pb angles since the terminal I^- does not directly impact the in-plane distortion. In the case of (4AMP) analogue, the hydrogen bonds are formed with the bridging I^- anions which are located inside the layers, which can strengthen the in-plane distortion.

(3AMP)PbI_4 has one of the shortest interlayer distance of ~ 4.0 Å among all the Pb-based 2D perovskites, which impacts the electronic properties of these materials.[70] The use of propane-1,3-diammonium (PDA) as spacer was also found to produce DJ hybrid perovskites with the shortest interlayer distance of 2Å in 2D perovskites.[86] The short interlayer distance in DJ hybrid perovskites is favorable for solar cell applications due to its beneficial effect on optoelectronic properties. The relationship between the interlayer distance and optoelectronic properties will be discussed in the next section.

By introducing two types of spacer cations, guanidinium (Gu) and MA, simultaneously into the interlayer space produce a unique type of structure , named as alternating cations in the interlayer space (ACI), was formed.[85] ACI perovskites exhibited the structural features of the DJ phase with the chemical formula of the RP phase. To be more specific, in the ACI phase, inorganic layers exhibit a (½, 0) shift along ab-plane similar to the DJ phase structure, but at the same time differ in the position of the interlayer sites due to charge balance restrictions, thus leading to different centering of the unit cell (Figure 2.4d and 2.4e).

2.2.3 Functional spacer cations and structural ordering

Widely used spacer cations (like aromatic and aliphatic ammoniums) in synthesizing layered perovskites are electrically insulating without any active functionalities, such as light absorbing.[87,88] Replacing aliphatic and aromatic spacer cations with functional organic cations has attracted great interest. For example, conjugated oligomers can absorb a complementary portion of the solar spectrum to that of the inorganic layer and conductive polymers can improve charge carrier transport in the layered perovskite solar absorber.[89–92] The layered perovskites with functional spacer cations are especially relevant to optoelectronic applications. For instance, improved light absorption of layered perovskites with conjugated oligomers and dye molecules as spacer cations potentially could boost the current of derived solar cells and enhance their efficiency.[93] Dye molecules like 5,5'''-bis(aminoethyl)-2,2':5',2'':5'',2'''-quaterthiophene (AEQT) can strongly influence optical properties of layered perovskites.[88] In the case of AEQT molecule, it has an appropriate molecular shape and two aminoethyl groups to bond to the inorganic framework. Recently, Vanderzande et. al. introduced charge-transfer complexes (combination of pyrene-butylammonium, a donor molecule with the strong acceptor molecules tetracyanoquinodimethane (TCNQ) and tetracyanobenzene (TCNB)).[94] The incorporation of charge-transfer complexes has a significant influence on the absorption in the visible wavelength region.

Interestingly, subtle structural alterations induced by the organic spacer cation substitutions can change the properties of layered perovskites. This opens new opportunities in materials design. One of the simple structural tailoring of layered perovskites is selectively fluorinating PEA spacer cation at different positions of aromatic benzene ring.[95] The position of the fluorine atom on the aromatic moiety (ortho, meta, para) leads to changes in the ordering of the organic spacer cations in the interlayer gallery (two organic cations in the spacing for RP phase) relative to one another with varying degrees of structural disorder. For instance, para-$FPEA_2PbI_4$ and para-$FPEA_2SnI_4$ (with fluorine atom located at para-position) have cations within the interlayer gallery facing the same direction in a co-aligned fashion, whereas, ortho-$FPEA_2PbI_4$ has the most orientation disorder among other positions.[95–97] Custom-synthesized, more complicated organic cations are also used to tune structural ordering of the cation within the interlayer space to alter the properties of layered perovskites. For example, a series of layered perovskites, (aromatic-O-linker-$NH_3)_2PbI_4$ (where the aromatic moiety is naphthalene, pyrene, or perylene and the linker is ethyl, propyl, or butyl) showed better energy level matching between the inorganic and organic layers, resulting from ordering of organic cations.[91]

2.2.4 Synthetic aspects and layer thickness limitations

Typically, thin films of halide perovskites are used for optoelectronic applications and good quality 3D perovskite thin film can be easily fabricated through spin coating perovskite precursor solutions onto substrates. Nonetheless, synthesis of phase-pure layered perovskites by this approach is not viable and such obtained layered perovskite thin films may contain multiple lower dimensional perovskite phases.[77] The best approach to produce phase-pure layered perovskites is by synthesizing single crystals through a wet chemistry route. Even though numerous synthesis protocols exist for the n = 1 member of a homologous series (a single inorganic $[BX_6]$ layer), few report the synthesis of higher-n members.[39,77,98,99] Phase-pure compounds of layered perovskites up to n = 7 have been successfully synthesized by using the n-BA, as the limiting reagent.[78] In this synthetic protocol, the use of BA is essential in achieving the layered perovskites in the pure form, avoiding precipitation of unwanted n= "∞" (3D perovskite phase). Other synthetic protocols like slow evaporation of solvent, precipitation of compounds using antisolvent etc. are only successful in producing low-n members of layered perovskites (up to n=3).[36,100,101]

A recent study on enthalpies of formation (ΔH_f) of the RP phase suggest that, high-n members (n>7) of layered perovskites are thermodynamically unstable and challenging to be synthesized.[78] The ΔH_f values are negative for low-n-member compounds (n = 1–5) but positive for the

compounds with a higher n (n= 6 and 7). For a favourable reaction, the ΔH_f must be negative to achieve the negative Gibbs free energy (ΔG). The attempt to grow high-n-member ($n > 7$) compounds can lead to the formation of mixture of 3D perovskites with a lower-n compound or randomly or coherently intergrown 2D perovskites. These materials consistently show a blue shift of the band gap compared to the 3D analogues and can be termed as "quasi-2D perovskites". In wake of growing number of publications on lower dimensional perovskites, researchers are advised to term the synthesized compounds as "2D perovskites" or "quasi-2D perovskites" only based on the rigorous analysis of optical and structural characterizations. As we mentioned in the beginning of this section, most of the optoelectronic applications of layered perovskites have been reported using thin films. The fundamental properties of the films are significantly different from those of the grown single crystals. Primarily, thin films do not produce phase-pure n-member of layered perovskites but a mixture of different n-members of lower dimensional perovskites. Evidently, almost all the reports on 2D perovskite based solar cells are effectively employing quasi-2D perovskites in their devices. In another class of materials, called 2D/3D perovskites, 2D perovskites are incorporated on the top surface of the 3D perovskite film or inside the bulk 3D perovskites.

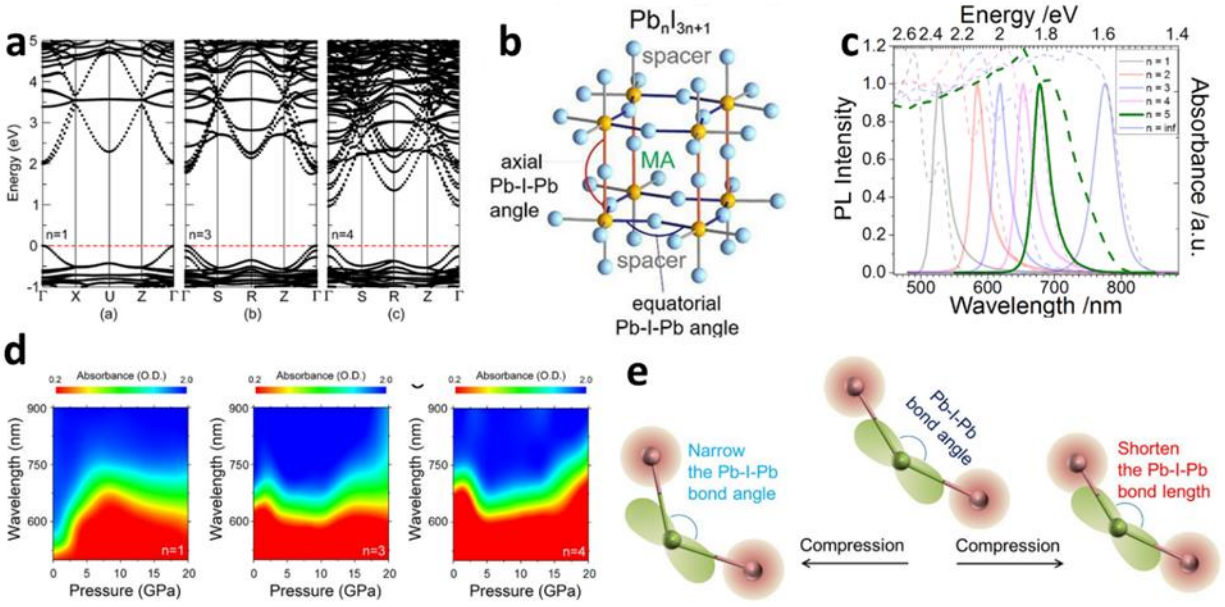

Figure 2.5 a) Band structure of $(BA)_2(MA)_{n-1}Pb_nI_{3n+1}$ perovskites. Reprinted from ref. 63 with permission from the American Chemical Society. (b) Schematic of axial and equatorial Pb−I−Pb angles. Reprinted from ref. 69 with permission from the American Chemical Society. (c) Experimental optical absorption and emission spectra of $(BA)_2(MA)_{n-1}Pb_nI_{3n+1}$ perovskites. Reprinted from ref. 77 with permission from Cell press. (d) Contour plots of pressure-dependent absorbance of (BA) PbI_4, $(BA)_2(MA)_2Pb_3I_{10}$ and $(BA)_2(MA)_3Pb_4I_{13}$, and (e) illustration

of Pb−I−Pb bonds in $(BA)_2PbI_4$ under compression. Reprinted from ref. 110 with permission from the United States National Academy of Sciences.

2D/3D perovskites predominately show bulk 3D perovskite characteristics (optoelectronic and structural properties), even though, they have some additional benefits, such as improved stability and fewer defects.

In summary, the structural characteristics of 2D perovskites can be vastly tuned by means of changing interlayer spacing, number of perovskite layers, octahedral tilting *etc.* through employing different organic/inorganic spacers. The recent advancement in the unexplored, 2D perovskite structures has shown that there are profuse opportunities for new material discovery. Also, structural properties of 2D perovskites strongly affect their optoelectronic properties. So even a slight change in structure may lead to significant modification of optoelectronic features of 2D perovskites. In the next section, we discuss current fundamental understanding of optoelectronic properties of the 2D layered halide perovskites.

2.3 Optoelectronic properties

Halide perovskites are fundamentally different from other direct band gap inorganic semiconductors explored in solar cell applications, such as GaAs and CdTe *etc*. (known as p-s semiconductors), due to the presence of lone-pair Pb s electrons. In 3D Pb perovskites, the conduction band minimum (CBM) comes from Pb p orbitals, and the valence band maximum (VBM) derives from a mixture of Pb s and I p orbitals (called as a s-p semiconductor). The hole effective mass is balanced with electron effective mass due to strong s-p antibonding coupling in VBM, which leads to ambipolar conductivity in halide perovskites that leads to high charge carrier mobilities. Also, the superior optical absorption observed in halide perovskites is closely associated with their electronic structure. In addition to direct band gap absorption,the intense optical absorption also partially originates from the halide-p to metal-p transition at the band edge. Because the electronic band structure of the 2D perovskites is very different from that of 3D perovskites, it can be expected that they exhibit significantly different optoelectronic properties. In this section, we describe and discuss the band structure, confinement effects of 2D perovskites and their effects on optical properties and charge carrier dynamics.

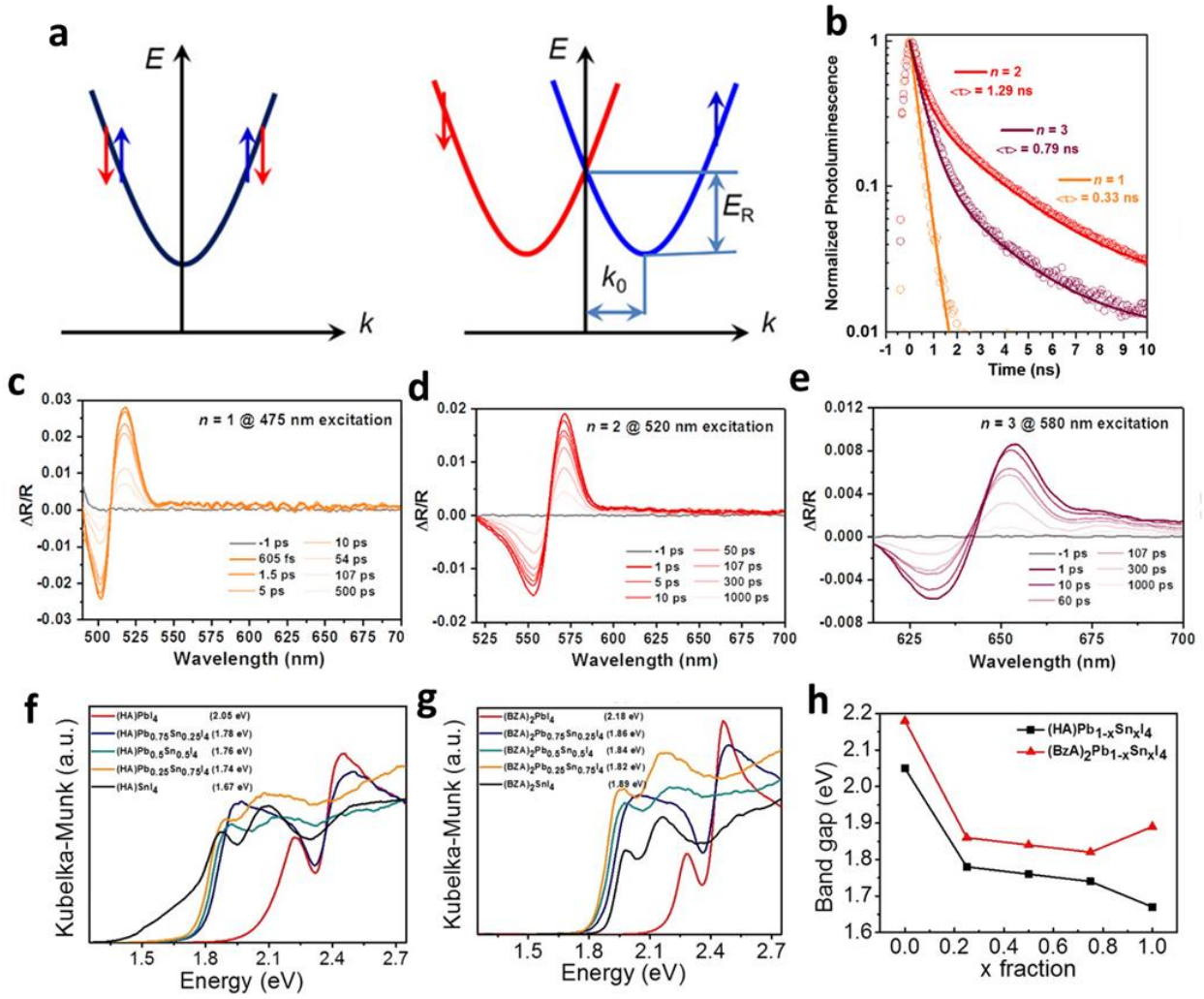

Figure 2.6 a) Dispersion relation of a CB showing a doubly spin-degenerate parabolic band having a single minimum at k = 0 (on right side) and two parabolic branches with opposite spin (subjected to Rashba splitting). Reproduced from ref. 118 with permission from the American Association for the Advancement of Science. (b) Time-resolved photoluminescence spectra (TRPL) of 2D perovskites, ground-state bleaching (GSB) peaks of (c) $(PEA)_2PbI_4$, (d) $(PEA)_2MAPb_2I_7$, and (e) $(PEA)_2MA_2Pb_3I_{10}$. Reprinted from ref. 119 with permission from the American Chemical Society. Optical absorption of (f) $(HA)Pb_xSn_{1-x}I_4$ and (g) $(BZA)Pb_xSn_{1-x}I_4$, and (h) band gap variation of 2D perovskites with different content of Pb and Sn. Reprinted from ref. 79 with permission from the American Chemical Society.

2.3.1 Band structure and optical properties

A detailed understanding of materials' band structure provides insights into their optical and electronic properties from a fundamental viewpoint. First principle calculations, such as density functional theory (DFT), can predict consistent structures and stabilities of perovskites.[102–105]

The calculations showed that organic molecules are not directly involved in determining the electronic structure of organic-inorganic halide perovskites. For instance, density of states (DOS) of $MAPbI_3$ suggest that the contribution from the states of MA cations is insignificant around band edges (Figure 2.5a). The organic molecule in halide perovskites primarily functions as a counterion for stabilizing the perovskite structure and charge balance. However, the size and nature of organic cations influence the B-X-B bond angle and equatorial B-X bond length, which strongly affects the optical properties of these materials. For instance, the differences in hydrogen bonding between organic spacer cations and halide ions have an impact on the B−X−B angles, thereby their optoelectronic properties. 2D perovskite compounds having similar crystal structures while different spacer cations, the B−X−B bond angles are the dominant factor in influencing the band gap. An undistorted octahedra networks have a B−X−B bond angle of 180°. In the case of Pb-based perovskites, larger Pb−I−Pb bond angles (close to 180°) mean greater overlap of Pb s and I p orbitals, which instigates larger bandwidths and consequently lowers the band gap.[106] The B−X−B bond angles can be classified into two categories, equatorial along the inorganic plane and axial along the stacking axis. Equatorial B−X−B bonds are more relevant to the band gap because the charges transport across the inorganic layer (Figure 2.5b).

Axial Pb−I−Pb bonds mainly impact the excitonic behavior. Therefore, 2D perovskites prepared with different types of organic spacer cations can have the same band gap if they have similar crystal structures and equatorial Pb-I-Pb bond angles. For example, $(NH_3C_8H_{16}NH_3)(MA)_2Pb_3I_{10}$ (where $NH_3C_8H_{16}NH_3$ is diammonium ion) and $(BA)_2(MA)_2Pb_3I_{10}$ with the same structure of the RP phase) and the similar equatorial Pb-I-Pb bond angles of 168.7° and 169.4° respectively, have the same band gap at ~2 eV. For 2D layered perovskites with different structures, the interlayer spacing between inorganic layers is the determinant factor for the band gap rather than the Pb−I−Pb bond angle. (3AMP) $(MA)_2Pb_3I_{10}$ (with the equatorial Pb-I-Pb angle of 163.5°) and (4AMP) $(MA)Pb_3I_{10}$ (with the equatorial Pb-I-Pb angle of 157.4°) are more distorted than $(BA)_2(MA)_2Pb_3I_{10}$ (with the equatorial Pb-I-Pb angle 169.4°) and still have similar band gaps (1.90-1.97 eV *vs.* 2 eV) due to the shorter interlayer spacing in (3AMP) $(MA)_2Pb_3I_{10}$ and (4AMP) $(MA)Pb_3I_{10}$.[107,108] Figure 2.5c shows the variation of absorption and emission, *i.e.*, the optical band gap, with the change of layer thickness. The 2D perovskites show a change in optical properties when they are subjected to external pressure.[109,110] An unprecedented 8.2% decrease in band gap was observed in $(BA)_2(MA)_2Pb_3I_{10}$ after compression to 26 GPa and then decompression back to ambient pressure (Figure 2.5d).[110] The $(BA)_2(MA)_{n-1}Pb_nI3_{n+1}$ series exhibit a characteristic structural change upon compression, specifically reflecting the narrowing in the Pb-I-Pb angle

and shortening in the Pb-I bond length (Figure 2.5e), leading to the increased electronic wave function overlap between Pb and I, and thereby accounting for the narrowed optical band gap.

The calculated electronic band structures exhibit a quasi-direct band gap at the Γ point for 2D perovskites (Figure 5a).[97,111] The electronic structure shows no dispersion along the Γ-Z direction as a direct consequence of a dielectric mismatch between inorganic (PbI_4 anionic component in the case of Pb-perovskite) and organic layers. The absence of dispersion along the Γ-Z direction results in nearly infinite effective masses in the direction perpendicular to the perovskite layers, demonstrating the reduced charge carrier mobility across the perovskite layers. On the other hand, 2D perovskites exhibit light electron and hole effective masses parallel to the perovskite layers. For example, the $(BA)_2SnI_4$ displays electron and hole effective masses of $0.15m_0$ and $0.13m_0$ respectively parallel to the 2D perovskite sheets, comparable to the effective masses of 3D $MASnI_3$ ($0.28\ m_0$ and $0.13m_0$).[112] Also, the 2D perovskites exhibit larger band gaps compared to 3D analogs because of the reduced dimensionality. Figure 2.5c displays increase in optical absorption edge with decreasing n value, from 1.50eV ($n = \infty$) to 2.43eV ($n = 1$) in the $(BA)_2(MA)_{n-1}Pb_nI_{3n+1}$ series.[39] DFT calculations agree with the general trend of decreasing band gap with increasing number of perovskite layers, although, DFT calculations consistently underestimate the band gap of materials. For accurate determination of band gaps, spin−orbit interactions or spin−orbit coupling (SOC) should be included in the calculations. A strong SOC is indeed generally observed in halide perovskites that can contribute formidably to the character of band gaps.[113–115] A Rashba band splitting, arising from the SOC effect, has been recently explored as a possible origin for the reduced electron−hole recombination observed in $MAPbI_3$.[116,117] In particular, a large Rashba splitting was observed in 2D perovskites where the spin degenerate parabolic band splits into two branches with opposite spin-aligned electronic states.[118] Figure 2.6a shows a schematic of the Rashba splitting of conduction band (CB) to two parabolic CB branches with opposite spins from a doubly spin-degenerate parabolic band having a single minimum at k = 0. DFT calculations yield an estimated Rashba parameter of (1.6 ± 0.1) eV·Å for the Rashba splitting in the plane perpendicular to the organic spacer barrier of $(PEA)_2PbI_4$. The experimental measurements by means of electroabsorption spectroscopy and photoinduced absorption spectroscopy confirmed the Rashba splitting in this compound, with the splitting energy of (40 ± 5) meV. Yin *et al*. observed perovskite layer thickness-dependence of the Rashba splitting in 2D perovskites.[119] Theoretical calculations predicted the larger Rashba splitting for n=2 among n= 1, 2, 3 systems, which was supported by the longer PL (Figure 2.6b) and ground-state bleaching recovery lifetimes for the n=2 system (Figure 2.6c-2.6e).

The band gap is also dependent on the size and electronegativity of metal and halide ions; as their size decreases, the band gap increases. For example, Sn-based 2D perovskites show a smaller band gap compared to Pb-based system at the same perovskite layer thickness. (HA)SnI_4 and $(BZA)_2SnI_4$ have much smaller band gaps compared to their Pb analogs (Figure 2.6f-2.6h). Sn-Pb alloyed 2D perovskites show an anomalous band gap behavior, where Sn-Pb perovskites display much narrower band gaps compared to both pure Pb and Sn systems (Figure 2.6h). It is linked to the SOC effects arising from alloying of heavier Pb atoms and lighter Sn atoms and accordingly structural distortion.[79,120]

2.3.2 Dielectric and quantum confinement effects in 2D perovskites

Quantum and dielectric confinement effects in 2D layered perovskites increase the band gap and the exciton binding energy compared to their 3D counterparts. The 2D perovskites, viewed as type-I quantum-well (QW), are composed of organic barriers separating inorganic wells.[121,122] Such scenario arises from a wider band gap of organic spacer molecules with respect to that of inorganic perovskite layers. As the thickness of the perovskite layer decreases, pronounced quantum confinement in the direction perpendicular to the plane of the inorganic layer leads to broadening of the band gap. The quantum confinement also increases the exciton binding energy. The exciton binding energy is given by

$$E_b = \left(\frac{2}{\alpha-1}\right)^2 E_{b,3D}, \qquad (2.2)$$

$$E_{b,3D} = \left(\frac{1}{\varepsilon_1}\right)^2 \left(\frac{m_{ex}}{m_0}\right) R_H, \qquad (2.3)$$

where E_b is the binding energy of 1s exciton, α is the dimensionality of the system, $E_{b,3D}$ is the exciton energy of the bulk system, ε_1 is the dielectric constant of the inorganic layer, m_0 is the free electron mass, and R_H is the Rydberg constant.[123,124] m_{ex} is the reduced exciton mass and can be calculated from:

$$m_{ex} = \left(\frac{1}{m_e} + \frac{1}{m_h}\right)^{-1}, \qquad (2.4)$$

Where m_e and m_h are mass of electron and hole, respectively. The value of α increases from 2 (for a perfect 2D system) to 3 (for the bulk, nonconfined system), as the thickness of the quantum well increases.

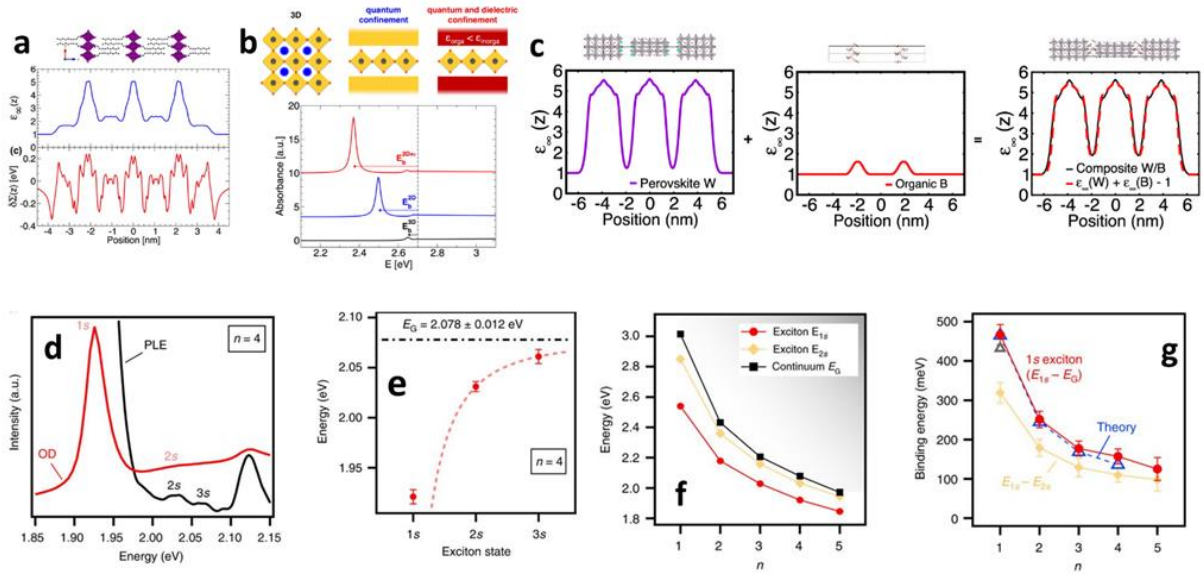

Figure 2.7 (a) Dielectric profile of 2D perovskite and (b) optical absorption computed using the k·p/ (Bethe−Salpeter equation) BSE approach. Reprinted from ref. 128 with permission from the American Chemical Society. (c) Composite approach to dielectric profiles for $(BA)_2(MA)_4Pb_5I_{16}$. Reprinted from ref. 131 with permission from the American Chemical Society. (d) Optical density and PL excitation spectra of the RP phase for $(BA)_2(MA)_3Pb_4I_{13}$, (e) energy of the exciton Rydberg states for $(BA)_2(MA)_3Pb_4I_{13}$, (f) evolution of exciton states and continuum energies with the 2D perovskite layer thickness, and (g) evolution of exciton energy with the 2D perovskite layer thickness. Reprinted from ref. 137 with permission from Springer Nature Publishing AG.

Moreover, the organic barrier has a much smaller dielectric constant than the inorganic perovskite layer. Dielectric confinement occurs when the inorganic layer with a high dielectric constant ε_1 is surrounded by organic molecules with a lower dielectric constant ε_2. In this scenario, the electric field generated by charges in the high dielectric constant material increases due to a less effective screening of the field by the low dielectric constant material. A stronger dielectric confinement steers to larger excitonic binding energies (100 meV-500 meV) in 2D perovskites.[111,125–127] Analysis of dielectric constants in 2D perovskites by classical models relies on a crude continuum modeling of the dielectric heterostructures with abrupt interfaces.[128–130] Atomic description of dielectric profiles for 2D perovskites built upon periodic supercells can provide a more accurate account of the dielectric confinement without any empirical input.[125] Pedesseau *et al*. treated 2D perovskite as a composite to analyze its dielectric profiles.[128] Figure 2.7a&2.7b shows the atomic level description of dielectric profiles of a composite 2D perovskite. With this approach, authors were able to accurately model the quantum and dielectric confinements and calculate CB and VB alignments in the 2D heterostructure.[131] Figure 2.7c shows the high frequency dielectric profile of 2D perovskites. A clear dielectric contrast between the organic part (with a low dielectric constant,

ca. 2.2) and the inorganic part (with a higher dielectric constant, *ca.* 5) is present in 2D perovskites. It may be noted that the dielectric constant of the inorganic part (ε_∞ = 4-5) in 2D perovskites is lower than the bulk value of 3D analogues (ε_∞ = 5.6), but greater than that of the single layer (ε_∞ = 4). It is worth mentioning that 2D perovskites differ from other 2D materials, where electron and hole wave functions are confined in a 2D plane.[132–135] In the case of 2D perovskites, exciton wave function is not confined to the 2D plane since the exciton size is comparable to the thickness of the perovskite layer. Generally, two types of excitons are observed in semiconductors, namely Wannier and Frenkel excitons.[17] The Wannier excitons are stretched over the host by numerous lattice constants with small binding energies <100 meV, whereas the Frenkel excitons have large binding energies ~500 meV, which are tightly bound to a single unit cell.[41,89,136] Most of the reports suggest the presence of the Wannier-type exciton in 2D perovskites, although no consensus on the nature of excitons in 2D perovskites has been reached. A direct measurement yielded a large excitonic energy of about 470 meV for BA_2PbI_4.[137] It was derived from optical transitions corresponding to the exciton Rydberg series and the continuum. The binding energy of excitons in perovskite wells steadily decreases as the number of perovskite layer is increased due to reduced quantum and dielectric confinements. An exciton energy of 125 meV was reported for the 2D perovskites with n=5 ($(BA)_2$ $(MA)_4Pb_5I_{16}$).

Magneto-absorption spectroscopy measurements confirmed the similar trend for reduced exciton masses, decreasing from 0.221 m_0 to 0.186 m_0 with increasing the perovskite layer thickness from n=1 to n=5. Blancon *et al*. proposed a scaling law to calculate exciton binding energy of excitons in 2D perovskites based on the Keldysh theory,[132] which was well corroborated by optical density (OD) and photoluminescence excitation (PLE) spectra.[137] Figure 2.7d shows OD and PLE spectra of $(BA)_2(MA)_3Pb_4I_{13}$ (n=4). The spectral features in these measurements can be assigned to the Rydberg series of Wannier-Mott excitons. The experimental spectra provide energies corresponding to 1s, 2s and 3s exciton states (Figure 2.7e). The difference $|E_{1s} - E_G|$, provides the binding energy of the 1s exciton ground state. The continuum energy E_G was calculated from fitting 2s, 3s Rydberg series with the 2D hydrogen model. Figure 2.7f displays the exciton ground state (1s), first excited state (2s), and continuum (E_G) energies for 2D perovskites with different layer thickness. Figure 2.7g compares experimentally obtained binding energies to theoretical values. Both optical and Magneto-absorption spectroscopy measurements suggested strongly bound excitons with energies >120 meV in the RP phase 2D perovskite with n=5.

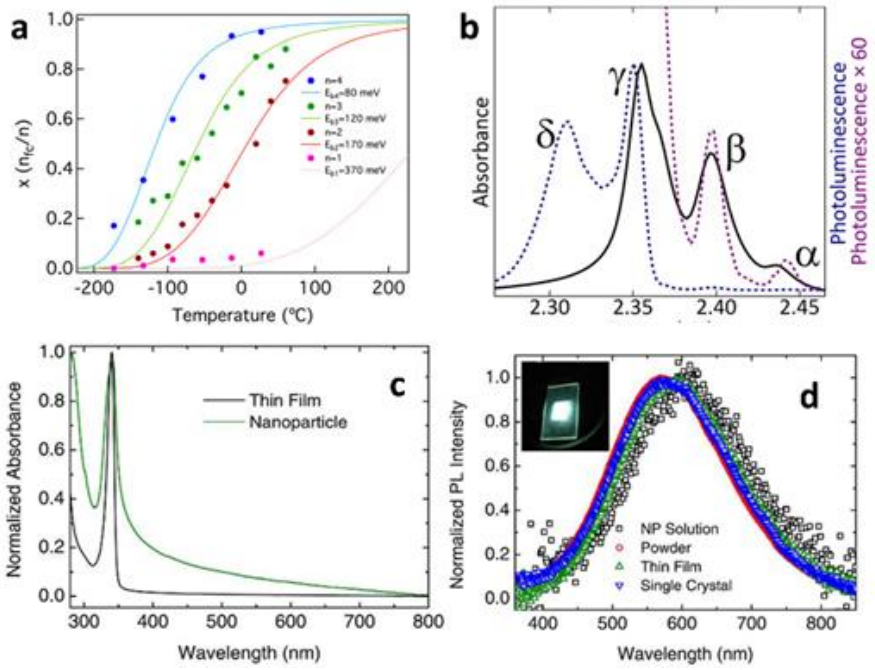

Figure 2.8 (a) Fraction of free charges in 2D perovskites as a function of temperature. The full lines are modeled using the Saha equation with an excitation density of 5 × 10^{14} cm^{-3}. The symbols indicate the experimental estimates. Reprinted from ref. 138 with permission from the American Chemical Society. (b) Excitonic absorption and PL spectra of PEA_2PbI_4. Reprinted from ref. 153 with permission from the American Chemical Society. (c) Absorption spectra of $(PEA)_2PbCl_4$ thin film and a nanoparticle solution in toluene. (d) PL spectra of $(PEA)_2PbCl_4$ thin film and a nanoparticle solution. Reprinted from ref. 157 with permission from the American Chemical Society.

The proposed scaling law for excitons predicts free carrier like behavior for layered 2D perovskites with $n \geq 20$.[137] On the contrary, the photoconductivity study and the Saha equation yielded significantly lower exciton energies, as low as 80 meV for n=4 ($(BA)_2(MA)_3Pb_4I_{13}$) (Figure 2.8a).[138] The excitonic properties are tunable, varied with the physical and chemical properties of the organic and inorganic cations.[139] For instance, by employing an aromatic organic cation of PEA (dielectric constant: 2.9) instead of the aliphatic cation of decylammonium, $C_{10}H_{21}NH_3$ (dielectric constant: 2.1) in 2D perovskites the exciton binding energy was significantly decreased from 320 meV for $(C_{10}H_{21}NH_3)_2PbI_4$ to 220 meV for $(PEA)_2PbI_4$.[140] The exciton energy can be further tuned by mixing organic cations that differ in their dielectric constants in 2D perovskites. For example, by stoichiometrically mixing organic cations A = 2,3,4,5,6-pentafluorophenethylammonium (5FPEA) and B = 2-naphthyleneethylammonium (NEA) cations in $(A_xB_{1-x})_2$ SnI_4 2D perovskites, the exciton energy was tuned from 572 nm (pure 5FPEA) to 602 nm (pure NEA).[141] An unusual, efficient generation of triplet excitons was observed in $(MA)_2Pb(SCN)_2I_2$ 2D perovskites, where MA is an organic spacer cation.[142] These triplet excitons showed extremely long diffusion length

of 152 nm. Alternatively, mixing halides can also modify the excitonic properties of 2D perovskites since the exciton binding energy is inversely proportional to the square of the dielectric constant. In 3D perovskites, $MAPbI_3$ showed a lower exciton energy than $MAPbBr_3$ due to the higher dielectric constant exhibited by $MAPbI_3$. Even though quantitative studies on halide-dependent changes of the excitonic energy in 2D perovskites are not available, a similar trend to that in 3D perovskites is expected. Also, when iodide is replaced by bromide and then by chloride, carrier effective masses tend to increase in perovskites.[143–146]

Polaron formation has also been observed in 2D perovskites.[147–149] The charge carriers in 2D perovskites were mainly scattered via deformation potential by acoustic and homopolar optical phonons, which is indicative of polaron formation in the material.[150] Formation of polarons limits the carrier mobilities, modulates the cooling process of hot charge carriers and broadens the width of radiative transitions.[151] Larger carrier effective masses due to the dielectric confinement in 2D perovskites strengthen the electron-phonon coupling and enables the polaron formation even at room temperature.[152] The splitting of excitonic absorption spectra (Figure 2.8b) of PEA_2PbI_4 into three transitions (α at 2.438 eV, β at 2.398 eV, and γ at 2.355 eV) with spacing of ~40 meV is an indication of the electron-phonon coupling.[153] Due to the strong electron-phonon coupling, free excitons are transformed to self-trapped excitons.[154] Self-trapped excitons are qualitatively similar to small polarons.[155] The calculation showed a large binding energy ($E_{polaron} \approx 0.4-1.2$ eV) for polarons, which are tightly localized at specific Pb-X positions (in $(EDBE)PbCl_4$). In contrast, a broadband emission (white-light emission) was found to deviate from the self-trapped excitons mostly in the organic lattice of $(PEA)_2PbCl_4$.[126,156] Interestingly, the $(PEA)_2PbBr_4$ and $(PEA)_2PbI_4$ (bromide and iodide analogues of $(PEA)_2PbCl_4$) exhibit narrower excitonic emission. All these observations together suggest that organic layers are more than just an inert spacer. $(PEA)_2PbCl_4$ showed a remarkably high color rendering index and photostability, rendering its high-quality material for white LED applications. Figure 2.8c&2.8d show strong excitonic absorption and intrinsic broad emission from $(PEA)_2PbCl_4$.[157]

2.3.3 Charge carrier dynamics

An increase in the charge mobility and a decrease in the effective masses of holes and electrons were observed as the thickness of the 3D perovskite layer was increased, as a result of easier disassociation of excitons into free charges.[138]

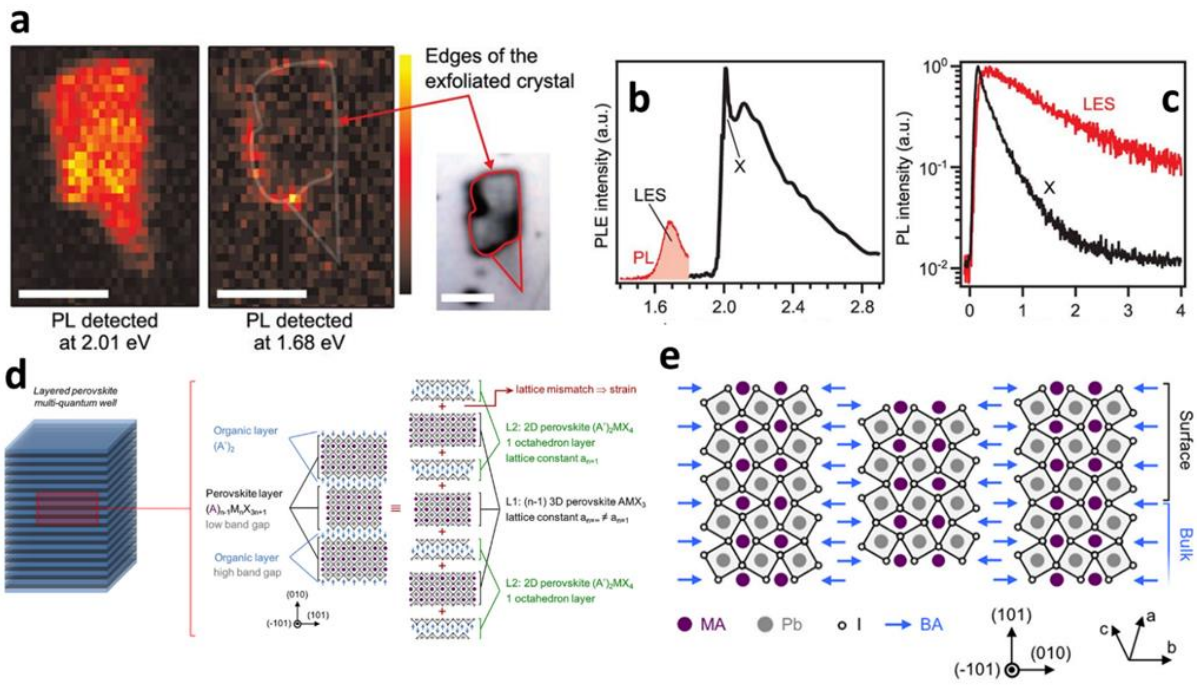

Figure 2.9 (a) Microscopic PL map of a single exfoliated crystal, probed at 2.010 and 1.680 eV, (b) PLE signal of the LES measured by locally exciting the exfoliated-crystal edges, and (c) TRPL of the PL of higher energy state, X state and LES. Reprinted from ref. 158 with permission from the American Association for the Advancement of Science. d) Illustration of layered perovskite viewed as heterostructures, and (e) schematic of (101) surface of the $(BA)_2(MA)_3Pb_3I_{10}$. Reprinted from ref. 158 with permission from the American Chemical Society.

On the other hand, charge carrier mobility in 2D perovskite film is inherently related to the exciton binding energy and defects in the material. The recombination in 2D perovskites falls into the Langevin-Type regime due to excitonic nature of charge carriers, limiting the overall thickness of absorber layer in 2D perovskite-based solar cells. Interestingly, the 2D perovskites with n >2 exhibit a unique, intrinsic dissociation of the photogenerated excitons to free carrier–like states through layer edge states.[158] For the n=3 2D perovskites, energy corresponding to the layer edge state was observed at 1.68 eV, lower than the exciton emission energy at 2.01 eV (Figure 2.9a). The charge carriers are thus trapped in the edge states and remain protected from nonradiative processes like electron-phonon coupling. Moreover, long-lived free carriers provided by lower energy edge states (LES) can contribute to photocurrent in a solar cell (Figure 2.9b&2.9c). This distinct behavior has been observed in both thin-films and their exfoliated crystal counterparts. Also, the presence of the edge states extends the perovskite absorption to the visible and even to near infrared regions (Figure 2.9b). Kepenekian *et al*. suggested LES might originate from the surface

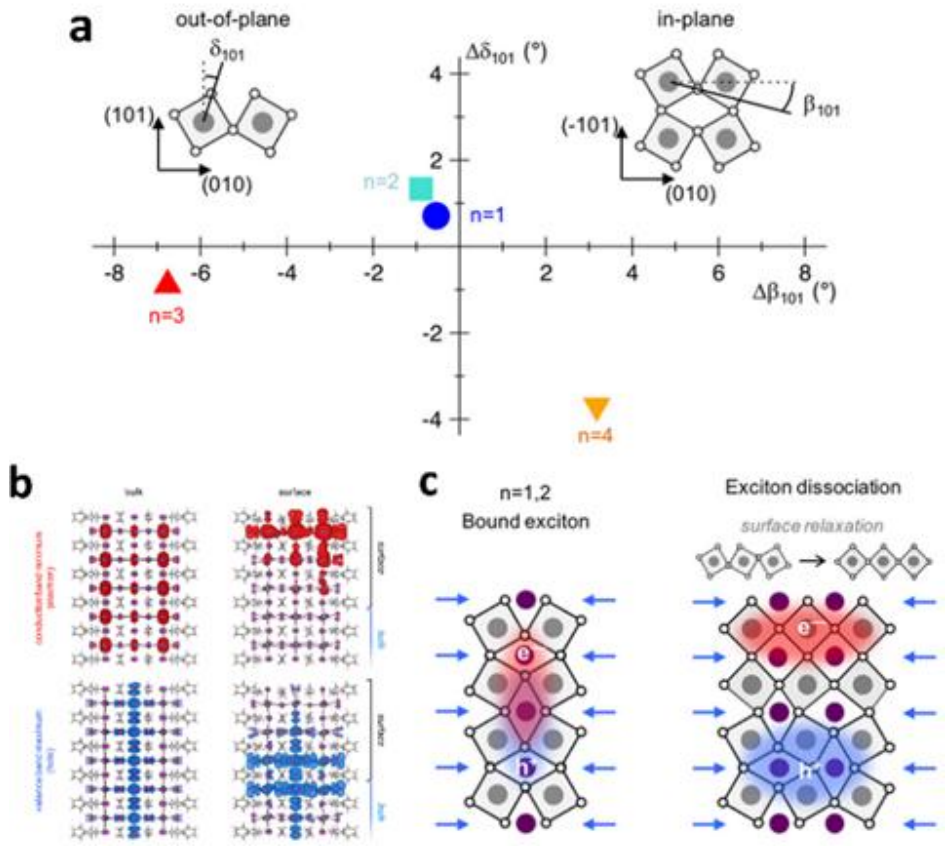

Figure 2.10 (a) Variation of in-plane and out-of-plane tilting of surface octahedra due to the (101) surface relaxation, (b) calculated partial charge densities at the VBM and CBM in bulk and relaxed surface for $(BA)_2(MA)_3Pb_3I_{10}$, and (c) illustrations of the surface-induced exciton dissociation. Reprinted from ref. 159 with permission from the American Chemical Society.

states in 2D perovskites as a result of lattice mismatch.[159] In this model, authors treated 2D perovskites as a composite system/heterostructure with coherent interface.[122] Figure 2.9d shows layered perovskites as a heterostructure with alternating stacking of 3D perovskite layers L1 (of thickness n−1) and of 2D perovskite monolayers L2 (single octahedron, n = 1). Classic theory of elasticity predicts that, for a heterostructure L1/L2 with a large lattice mismatch between L1 and L2, the structure may undergo a reorganization for a critical layer thickness Figure 2.9e).[160] Consequently, the internal elastic energy may accumulate inside the material. The surface octahedra in n= 1,2 have no rotational degrees of freedom, while those for n> 2 exhibit significantly larger in-plane and out-of-plane tilting (Figure 2.10a). Thus, the mechanical energy is more efficiently relaxed in n>2 compounds due to additional rotational degrees of freedom through surface relaxation (i.e., through in-plane and out-of-plane tilting of surface octahedra).

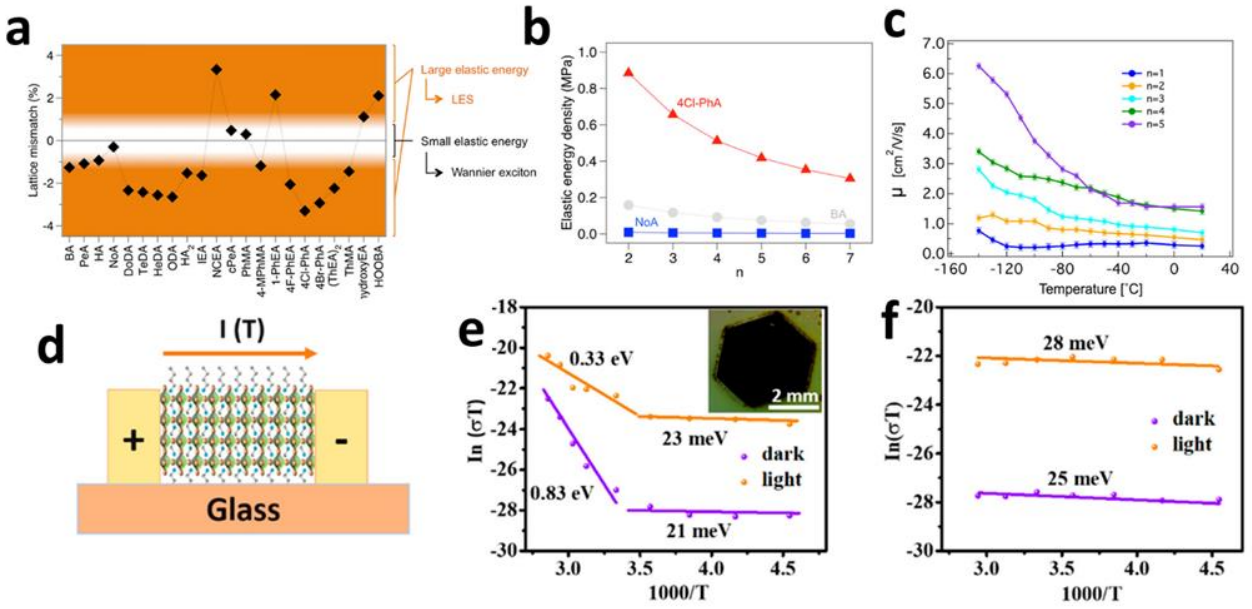

Figure 2.11 (a) Lattice mismatch between various 2D perovskites (n = 1) and $MAPbI_3$ and, (b) calculated elastic energy density for 2D different perovskite heterostructures. Reprinted from ref. 159 with permission from the American Chemical Society. (c) Mobility of 2D perovskites: $(BA)_2PbI_4$ (n = 1), $(BA)_2(MA)Pb_2I_7$ (n = 2), $(BA)_2(MA)_2Pb_3I_{10}$ (n = 3), $(BA)_2(MA)_3Pb_4I_{13}$ (n = 4) and $(BA)_2(MA)_4Pb_5I_{16}$ (n = 5) at different temperatures. Reprinted from ref. 138 with permission from the American Chemical Society. (d) Scheme for the in-plane temperature-dependent conductivity of a quasi-2D $(BA)_2(MA)_2Pb_3I_{10}$ perovskite; (e, f) results of temperature-dependent conductivity measurement of 3D and quasi-2D perovskite single crystals, respectively. The inset in (e) is a photo of a MAPbI3 single crystal. Reprinted from ref. 165 with permission from the American Chemical Society.

As a consequence, the band gap blueshifts by 70 and 150 meV for n = 1 and 2, respectively, and redshifts by 120 and 70 meV for n = 3 and 4, respectively (Figure 2.10b) compared to the calculated band gaps of these materials without taking account surface relaxation. The small octahedral tilting leads to lattice expansion at the (101) surface, which results in the blue shift of band gap, whereas a significant octahedral distortion in subsurface yields lattice compression that induces a band gap redshift. Importantly, the LES originating from surface relaxation can strongly localize the electron at the surface and enable the dissociation of the strongly bound excitons to long-lived free carriers. Schematic of the LES mechanism is shown in Figure 2.10c. For a broader picture, lattice mismatch in the layered perovskites employing different, a wide variety of spacer cations is shown Figure 2.11a. Clearly, spacer cations can largely impact lattice mismatch and influence the internal elastic energy density accumulated in the bulk of layered perovskites (Figure 2.11b). For instance, $(4Cl{-}C_6H_4NH_3)_2PbI_4$ (4Cl-PhA) displays a larger lattice mismatch, therefore a greater elastic density than other materials in Figure 2.11b. This would favor surface relaxation

and sequentially the formation of LES in $(4Cl{-}C_6H_4NH_3)_2PbI_4$. On the other hand, layered perovskites employing $C_9H_{19}NH_3$ (NoA) cation have an appreciably smaller lattice mismatch, resulting in a lower elastic energy density that effectively prevents the formation of LES. In summary, LES stems from the release of the strain-induced elastic energy at the heterostructured L1/L2 interface and fine-tuning the layered perovskite structure and composition can promote efficient exciton disassociation in 2D perovskites.

Understanding of defects and scattering processes in 2D perovskites is vital to realize their optoelectronic applications. The transient photoconductivity experiments using terahertz (THz) have asserted that photoconductivity is significantly higher along the inorganic or perovskite layers than across the layers in a 2D perovskite film.[161] Temperature-dependence of carrier mobility (Figure 2.11c) reveals the occurrence of electron−phonon scattering in 2D systems.[138] It also discloses the increase of the mobility and lifetime of charge carriers with the thickness of the perovskite layer. The charge transport properties in 2D perovskites are also related to the orientation of the inorganic layers within the perovskite film. The perovskite layers are called preferentially oriented if they are aligned perpendicular to the surface of the substrate, enabling smooth charge transport.[162] First principle studies have shown that defects in 2D perovskites are different from those in 3D perovskites. The point defects with surplus cations/deficient anions can easily n-dope the 3D perovskite. In comparison, the formation energy for point defects in 2D perovskites is higher.[58] The grain boundaries in halide perovskite films are very vulnerable as the form of edge and line defects due to misorientation crystal grains.[163,164] The defects such as anion and cation vacancies at grain boundaries create pathways for ion migration in halide perovskites. Huang and co-authors showed that the long-chain organic spacer cations could form a barrier suppressing ion migration along the out-of-plane and in-plane direction in single crystal layered perovskites compared to their 3D counterparts.[165,166] The ion migration is detrimental to the perovskite-based electronic devices by means of monomolecular recombination, photocurrent hysteresis and accelerated degradation *etc.*[167–169] Authors calculated the ion activation energy from fitting temperature-dependent electrical conductivity (Figure 2.11d-2.11f) using the Nernst−Einstein relation (from the slope of $\ln(\sigma T)$ −1/kT, where σ is the electric conductivity, k is Boltzmann's constant and T is the temperature in Kelvin).[165,170] The 2D perovskite exhibited only electronic conductivity at both low and high-temperature region without any transition from electronic conduction to ionic (Figure 2.11f), which implies ion migration is negligible in layered perovskites. Nonetheless, 3D $MAPbI_3$ showed ionic conductivity in the high-temperature region ($T > 280$ K) (Figure 2.11e). DFT calculations also estimated considerably higher formation energies of vacancy defects in 2D perovskites compared to their 3D analogs.

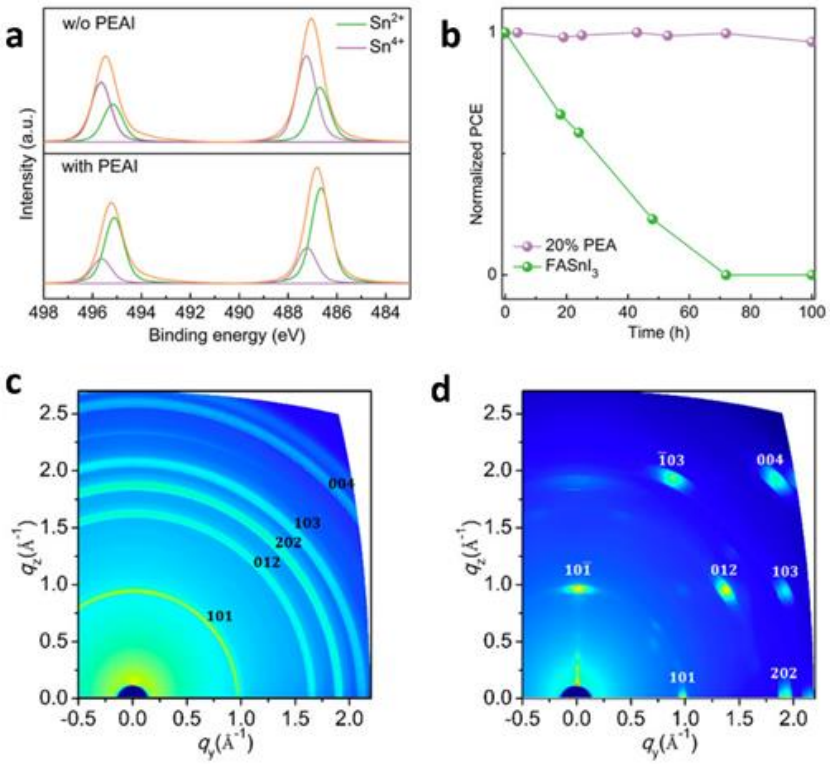

Figure 2.12 (a) XPS Sn 3d spectra of 3D (without PEAI) and 2D perovskite (with PEAI) films, (b) normalized PCE of the unencapsulated 3D and 2D perovskite device, and GIWAXS of (c) 3D perovskite and (d) 2D perovskite films. Reprinted from ref. 180 with permission from the American Chemical Society.

2.4 Solar cell application

In this section, we review the most recent and relevant reports on 2D/quasi-2D and 2D/3D PSCs. For 2D/quasi-2D RP perovskites, mainly those employing PEA and BA organic spacer cations are used in solar cell application. The diversification of spacer cations in RP phases for optoelectronic applications as well as employing hybrid DJ phase in solar cells have been main research focus in recent years. So, we divide this section into four subsections, with the first three subsections focusing on different organic spacer molecules in RP phase while the last subsection primarily discussing the emergence of hybrid DJ phase-based PSCs.

2.4.1 PEA cations as organic spacer in RP phase

In the first report on 2D PSCs, $(PEA)_2(MA)_2Pb_3I_{10}$ was employed as a solar absorber in a n-i-p planar device configuration.[36] These first generation devices displayed a high open-circuit voltage (V_{oc}) of 1.18 V with a PCE of 4.73%. The $(PEA)_2(MA)_2Pb_3I_{10}$ films also exhibited remarkable stability under humid air.

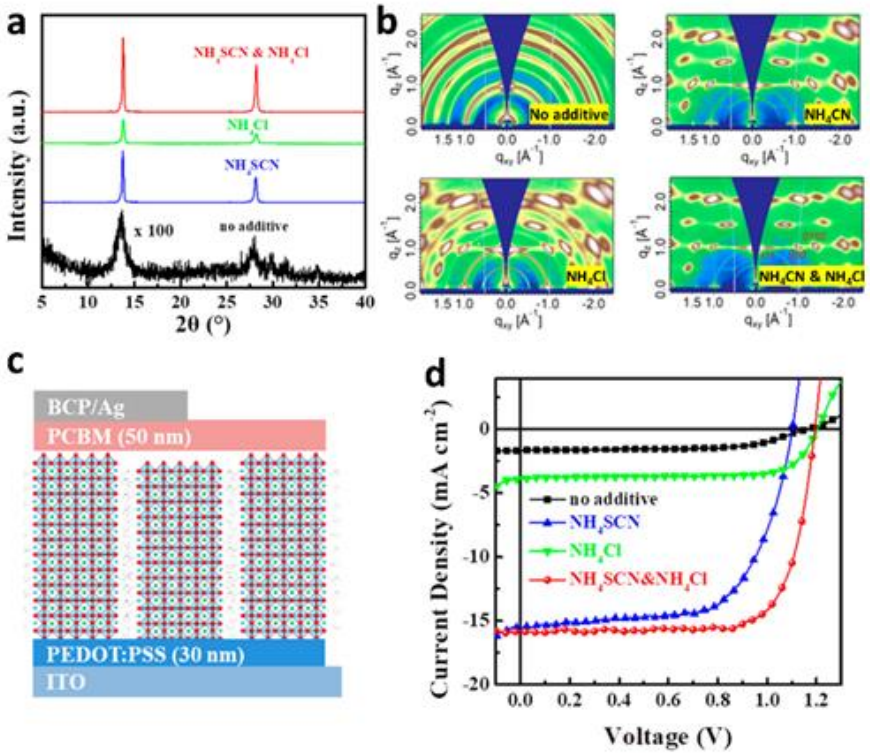

Figure 2.13 (a) XRD and (b) GIWAXS patterns of the perovskite films with additives, (c) scheme of a typical 2D perovskite device structure, and (d) J-V curves of devices employing 2D perovskite films with additives. Reprinted from ref. 184 with permission from the American Chemical Society.

Recently, we showed that optimization of film thickness and thin-film deposition can lead to a better PCE in $(PEA)_2(MA)_{n-1}Pb_nI_{3n+1}$ devices with significant less current density-voltage (J-V) hysteresis.[171] Depositing the 2D perovskite film at elevated temperature (known as hot-cast method) is a good practice to obtain highly crystalline, oriented 2D perovskite film. One of the major concerns with the Pb-based PSCs is the toxicity of water-soluble Pb component in the material.[172–174] So far, Tin (Sn) is the best replacement for Pb although the performance falls far short for Sn-based solar cells.[174–179] Moreover, the stability of Sn-based solar cells represents another concern for their practical use. The promise may lie in 2D engineering. Sn-based quasi-2D perovskite $(PEA)_2(FA)_8Sn_9I_{28}$ (n=9) devices were found to exhibit significantly improved stability compared to 3D $FASnI_3$ devices.[180] Importantly, $(PEA)_2(FA)_8Sn_9I_{28}$ also showed an impressive PCE of 5.94% with fill factor (FF) of 0.69 and V_{oc} of 0.59V. Notably, Sn-based quasi-2D perovskites showed a significant improvement in V_{oc} compared to 3D $FASnI_3$, which routinely exhibited a lower V_{oc} of less than 0.50 V.[181–183] The improvement in V_{oc} in the quasi-2D perovskites was ascribed to lower defect density as a result of lower chance of Sn^{2+} oxidation.

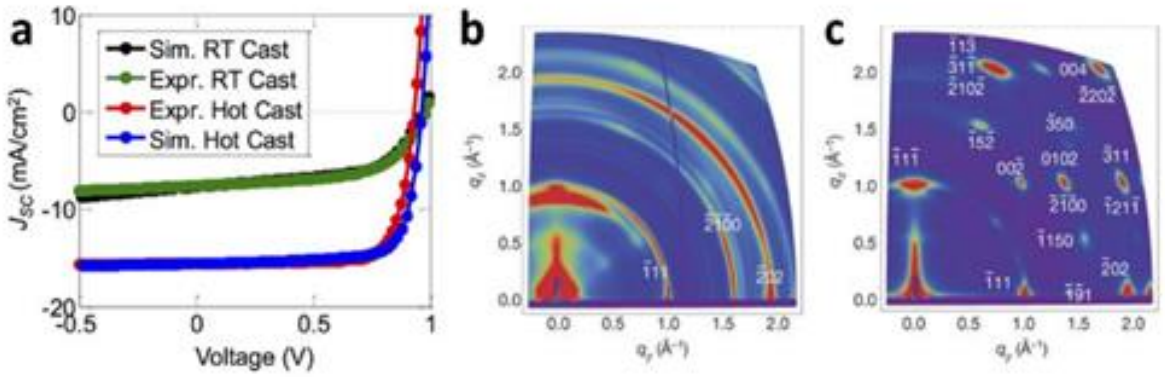

Figure 2.14 (a) J–V characteristics of room-temperature-cast and hot-cast methods (with simulated J-V curves), and (b) GIWAXS for (b) room-temperature-cast and (c) hot-cast films. Reprinted from ref. 56 with permission from John Wiley & Sons, Inc.

The Sn^{2+} in 3D perovskites can easily be oxidized into Sn^{4+} even if Sn-thin films are prepared under inert atmosphere, which greatly hampers the performance of Sn-perovskite devices. A comparison of X-ray photoelectron spectroscopy (XPS) measurements (Figure 2.12a) revealed that PEA molecule could retard the oxidation of Sn^{2+}. It also helped to improve the moisture stability of Sn-PSCs (Figure 2.12b). Additionally, crystal grains of quasi-2D perovskites were found to be highly oriented on the substrate, as revealed by sharp and discrete Bragg spots in Grazing-Incidence Wide-Angle X-ray Scattering (GIWAXS), whereas perovskite grains are randomly oriented in 3D perovskite films (Figure 2.12 c&2.12d). Highly oriented crystal grains in the perovskite film play a critical role in yielding well-balanced carrier charge transport in solar cell devices. A detailed discussion on the crystal orientation and GIWAXS characterization can be found in **Section 5** of this review. Recently, Fu *et al.* reported a PCE of 14.1% for n≤5 quasi-2D perovskites processed with ammonium salts additives.[184] In that work, they used NH_4SCN and NH_4Cl as additives in perovskite precursor solution with molar ratios of $PEAI/MAI/PbI_2/NH_4SCN/NH_4Cl$ at 2:4:5:1:1. It has been observed that NH_4SCN additive can regulate the orientation of crystal grains in the perovskite layer as well as enhance its crystallinity (Figure 2.13a-2.13c).[184,185] While, NH_4Cl can passivate the electron traps at PEDOT: PSS/perovskite interface. The effects of ammonium salts were unmistakably observed in solar cell performance.

The devices with NH_4SCN as an additive showed a high short-circuit current density (J_{sc}) as a result of highly oriented crystal grains and enhanced crystallinity. The better passivation of electron traps by Cl- with the use of NH_4Cl additive improved the Voc of the device. The

simultaneous incorporation of NH_4SCN and NH_4Cl as binary additives into 2D perovskite films led to both high V_{oc} (1.21 V) and J_{sc} (15.2 mA/cm^2) with an average efficiency of 12.9% (Figure 2.13d).

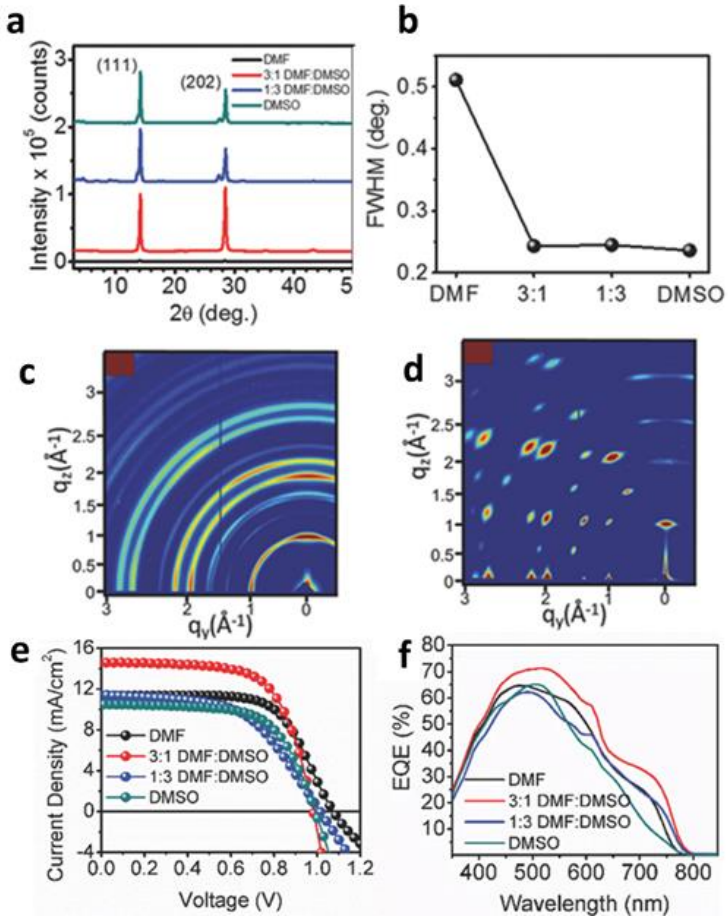

Figure 2.15 (a) XRD of $BA_2(MA)_4Pb_5I_{16}$ 2D perovskite films from different precursor solutions, (b) full width at half-maximum (FWHM) of the (111) reflection of 2D perovskite films from different precursor solutions, GIWAXS of $BA_2(MA)_4Pb_5I_{16}$ 2D perovskite films formed from (c) DMF precursor and (d) 3:1 DMF: DMSO mixed precursor, (e) J–V curves, and (f) External quantum efficiency (EQE)% of the devices employing the $BA_2(MA)_4Pb_5I_{16}$ films from different precursor solutions.[195]

Incredibly, these $(PEA)_2(MA)_4Pb_5I_{16}$ devices with ammonium salt additives displayed a record low nonradiative Voc loss of only 0.14−0.16 V in 2D PSCs.[39,56,186,187] As we have discussed in structural properties section, fluorine substitution on aromatic spacer molecule like PEA can induce structural ordering of spacer molecules in layered perovskites.[95] Zhang et. al. demonstrated that by fluorine substitution on the para position in PEA, the average phenyl ring centroid distances in the organic layer become shorter with better aligned packing of perovskite sheets.[188] The $(F\text{-}PEA)_2MA_4Pb_5I_{16}$ solar cells demonstrated an improved PCE of 13.64% compared to $(PEA)_2MA_4Pb_5I_{16}$ (9.66%) due to increased carrier lifetime and reduced trap density

in the solar absorber layer. The out-of-plane (or interlayer) microwave mobility of (F-PEA)2PbI4 (n=1) was found to be ~7 times higher than that of PEA analogue.

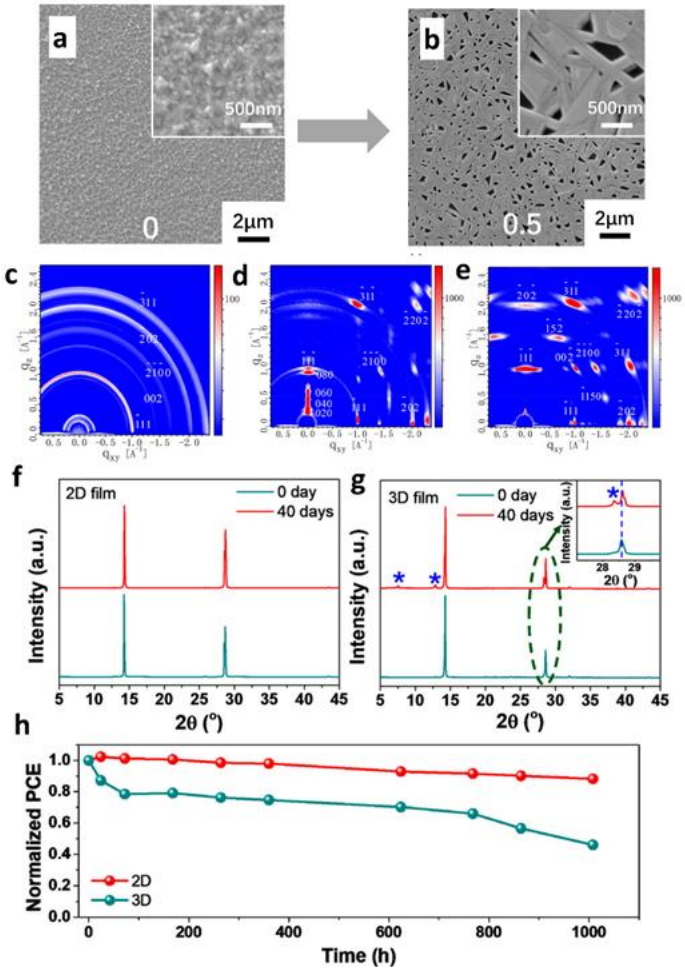

Figure 2.16 SEM images of perovskite films formed (a) with and (b) without MACl treatment, GIWAXS for 2D perovskite films formed with MACl/MAI weight ratios of (c) 0, (d) 0.3, (e) 0.5, (f), XRD patterns of (f) 2D perovskite and (g) 3D perovskite film after storage in air for 0 day and 40 days, and (h) degradation of 2D $(ThMA)_2(MA)_2Pb_3I_{10}$ and 3D $MAPbI_3$ devices. Reprinted from ref. 212 with permission from the American Chemical Society.

The increase in microwave mobility was probably due to better energetic alignment of the organic cations with the perovskite band structure rather than difference in perovskite interlayer distance since the F-PEA film happens to be slightly longer than the PEA film (smaller interlayer distance is supposed to be better for out-of-plane charge transport). On the other hand, the real-world devices employing $(F\text{-}PEA)_2MA_4Pb_5I_{16}$ (n=5) or $(F\text{-}PEA)_2MA_3Pb_4I_{13}$ (n=4), where films contain mixed dimensional phases (n=2, 3, 4, 5 and ∞) can benefit from ordered phase distribution depending on position of fluorine at on PEA,[95,189]

2.4.2 BA cations as organic spacer in RP phase

In their seminal paper, Tsai *et al.* reported the achievement of a high efficiency of 12.52% by employing hot-cast $(BA)_2(MA)_3Pb_4I_{13}$ film in the p-i-n device configuration (Figure 2.14a).[56] In the hot-cast process, PEDOT: PSS coated substrate is pre-heated at 150 ℃ for 10 min and immediately a perovskite precursor solution is spin coated. GIWAXS of hot cast films (shown in Figure 2.14b & 2.14c) exhibited sharp, discrete Bragg spots indicative of highly oriented crystal grains in contrast to randomly oriented crystal grains in room-temperature-cast 2D perovskite films. The nearly perfect oriented perovskite layers or $[(MA)_{n-1}Pb_nI_{3n+1}]^{2-}$ in hot cast films enabled charge transport across the device electrodes without any hindrance by the organic spacer layers, which resulted in a high J_{SC} of 16.76 mA cm^{-2} and FF of 0.74. In a separate study, the use of iso-BA as a spacer cation alone was found to produce highly oriented and crystalline 2D perovskites.[190] But the devices employing $(iso\text{-}BA)_2(MA)_3Pb_4I_{13}$ showed a large J-V hysteresis in FTO/C60/perovskite/Spiro-OMeTAD/Au configuration. Interestingly, the devices employing hot-cast $(BA)_2(MA)_4Pb_5I_{16}$ (n=5) films has shown relatively less PCE of 8.71% compared to its lower member, n=4 because of lower crystallinity of the film.[77] It was previously proved that in the 3D perovskite DMSO (Lewis base) has a high affinity for PbI_2 (or metal halides in general), and forms an intermediate phase retards the crystallization rate.[191–194] Soe *et al*. controlled the degree of crystallinity and crystal grain orientation by tuning the DMSO concentration in the DMF solution, producing highly oriented $(BA)_2(MA)_4Pb_5I_{16}$ thin films.[195] XRD analysis of $(BA)_2(MA)_4Pb_5I_{16}$ films fabricated from precursor solution with 3:1 DMF: DMSO concentration exhibited better crystallinity (Figure 2.15a).[195] To that account, the full width at half-maximum (FWHM) of the (111) XRD reflection peak was found to be lowest for the film grown from 3:1 DMF: DMSO precursor concentration, indicating the optimum DMSO concentration for obtaining high crystallinity (Figure 2.15b). Most of the perovskite layers were perpendicular to the substrate in the film fabricated from a precursor containing optimum DMSO concentration, as evidenced by the Bragg spots in the GIWAXS map (Figure 2.15c & 2.15d). The devices employing hot-cast films fabricated using 3:1 DMF: DMSO precursor solution displayed a PCE of 10% (Figure 2.15e). External Quantum Efficiency (EQE) measurements (Figure 2.15f) revealed an enhanced photoresponse for the devices with film fabricated using 3:1 DMF: DMSO precursor solution. The photocurrent enhancement correlates well with enhanced crystallinity and preferentially oriented microstructures in the perovskite film. Introduction of inorganic cations such as Cs and Rb into the halide perovskites is also beneficial for improving the stability.[44,45,196–199] It was found that the introduction of 5% Cs^+ in $(BA)_2(MA)_3Pb_4I_{13}$ film improved the stability.[200] The Cs-doped $(BA)_2(MA)_3Pb_4I_{13}$ devices also exhibited a superior PCE of 13.7% compared to reference solar

cells. Moreover, Cs-doped 2D perovskite devices retained 89% of the initial performance after 1400h storage in 30% RH environment vs. 79% for the devices made of pristine 2D perovskites. The addition of NH_4SCN was found beneficial in $(BA)_2(MA)_{n-1}Pb_nI_{3n+1}$ (n=3,4) 2D perovskite system likewise in PEA-based 2D systems.[184,185,201]

Yan *et al*. synthesized a low band gap 2D perovskite system by using FA as the A-site cation.[202] In 3D perovskite systems, FA-based perovskites exhibit relatively lower band gaps compared to MA-based perovskites.[194,203,204] A FA-based 2D perovskite, $(BA)_2(FA)_2Pb_3I_{10}$ film, exhibited a suitable band gap of 1.51 eV for single junction solar cell application, while $(BA)_2(MA)_2Pb_3I_{10}$ displayed a larger band gap of 1.87 eV. Nevertheless, $(BA)_2(FA)_2Pb_3I_{10}$ devices showed a low PCE of 1.19% mainly because of the random orientation of perovskite grains. Later, it was found that addition of 0.5 molar thiourea in the precursor was able to help with preferential orientation of grains in the $(BA)_2(FA)_2Pb_3I_{10}$ perovskite film. Basically thiourea, a Lewis-base, can coordinate with PbI_2 to produce large perovskite crystal grains with better orientation.[205,206] Consequently, the devices showed an enhanced average PCE of 5.27%. The unencapsulated devices stored in the air with 25% RH maintained 80% of their initial performance after 25 days. Further, the orientation can be controlled by mixing FA with MA in the 2D perovskite composition.[207] The perovskite crystals were aligned perfectly to the substrate when 20% MA cations were replaced with FA cations. The $(BA)_2(MA_{0.8}FA_{0.2})_3Pb_4I_{13}$ devices displayed a superior PCE of 12.81% vs. 10.7% for $(BA)_2(MA)_3Pb_4I_{13}$.

The 2D Sn-perovskites, such as $(BA)_2(MA)_2Sn_3I_{10}$ and $(BA)_2(MA)_3Sn_4I_{13}$, have nearly ideal band gaps of 1.50 and 1.42 eV, respectively for single junction solar cells. However, the derived devices displayed very low PCE due to the instability of Sn, as mentioned in the previous section. Cao *et al*. observed the formation of perovskite aggregates in $(BA)_2(MA)_2Sn_3I_{10}$ and $(BA)_2(MA)_3Sn_4I_{13}$ films when 0.2 mol SnF_2 was added to the precursor solution, which is a common additive used in 3D Sn-perovskites to suppress the oxidation of Sn^{2+} to Sn^{4+}.[208] The introduction of triethylphosphine (TEP), a weakly coordinating ligand for Sn^{2+} species, into 2D Sn-perovskite precursor solution avoids the perovskite aggregate formation. The devices employing TEP coordinated $(BA)_2(MA)_2Sn_3I_{10}$ displayed an average PCE of 1.75% with J_{sc} of 8.64 mA/cm^2, V_{oc} of 0.37 V and FF of 53.7%, and the $(BA)_2(MA)_3Sn_4I_{13}$ devices obtained an average PCE of 2.43% with high J_{sc} of 23.7 mA/cm^2, V_{oc} of 0.23 V and FF of 44.6%. Unencapsulated 3D Sn-perovskite ($MASnI_3$) devices displayed poor air stability, completely degrading within 3 min under ambient atmosphere. On the other hand, 2D $BA_2MA_3Sn_4I_{13}$ devices retained more than 20% of initial performance after 20 min. Encapsulated $BA_2MA_3Sn_4I_{13}$ devices maintained more than 50% of

their initial performance after 4 months. Ramirez *et al.* developed a quasi-2D Pb−Sn mixed perovskites using t-butylammonium (t-BA) as spacer cations with a low band gap of ~1.24 eV.[209] The resultant $(t\text{-}BA)_2(FA_{0.85}Cs_{0.15})_4(Pb_{0.6}Sn_{0.4})_5I_{16}$ devices exhibited an average PCE of 9.3%. Recently, a record-high PCE of 18.20% was reported for solar cells by using 3-bromobenzylammonium iodide (3BBAI) based quasi-2D perovskites.[210] The precursor solution with a weight concentration of 20% was prepared by mixing 3BBAI, MACl and PbI_2 at the molar ratio of 1.8:2.5:3 in DMF. These devices exhibited impressive, robust stability, retaining 82% of their initial performance after 2400 h storage in a chamber at room temperature with an RH of 40%.

2.4.3 Other spacer cations in RP phase

Recent progress in 2D perovskite research strongly suggests that organic spacer cations other than BA and PEA can also be interesting choices for solar cell applications because by tuning the nature of the spacer molecules the optoelectronic properties and orientation of the perovskite crystal grains can be tailored. Quasi-2D perovskites (n=5) using n-propylammonium (PA) spacer cations showed PCE up to 10.42%.[211] These $PA_2MA_4Pb_5I_{16}$ devices showed an excellent J_{sc} of 18.89 mA/cm^2 and V_{oc} of 1.11 V, with a FF of 49.53%. Also, they demonstrated commendable stability: retaining ~98% of initial performance after 500h under 60% RH. Lai *et al*. successfully synthesized 2D perovskites using 2-thiophenemethylammonium (ThMA) cations as a spacer. The resulting $(ThMA)_2(MA)_2Pb_3I_{10}$ devices displayed an impressive efficiency of 15.42%.[212] Incorporation of MACl in 2D perovskite precursor solution produced a nanorod-like morphology (Figure 2.16a & 2.16b) where perovskite layers were highly oriented on the substrate. Figure 2.16 c- 2.16e shows GIWAXS images, which depict crystal grain orientation as a function of the amount of MACl. In contrast, the GIWAXS map of pristine $(ThMA)_2(MA)_2Pb_3I_{10}$ film showed smooth diffraction rings, suggesting random orientation of perovskite layers in the film. Consequently, pristine $(ThMA)_2(MA)_2Pb_3I_{10}$ devices displayed a very low efficiency of 1.74%. Notably, the addition of MACl enhanced J_{sc} from 3.27 mA/cm^2 to 18.89 mA/cm^2, V_{oc} from 0.99 V to 1.07 V and FF from 53.9% to 76.3%. Such improvements were attributed to balanced hole and electron mobilities as well as considerably reduced defect density as supported by longer PL lifetime. Even better, MACl-treated $(ThMA)_2(MA)_2Pb_3I_{10}$ devices could keep more than 80% of the initial efficiency after being stored in the air with humidity of 30±10% RH for 250h. Polyethylenimine (PEI), a polymeric ammonium cation, was also successfully used as a spacer cation in producing 2D/quasi-2D perovskites, which were highly resistant against moisture even allowing the fabrication of efficient solar cells under the ambient humidity.[213] Polymeric ammonium cation

enables electronic interaction between inorganic layers unlike other organic cations mentioned above, which helps charge transport in 2D perovskites.[213,214] $(PEI)_2(MA)_6Pb_7I_{22}$ devices displayed an average efficiency of 9.39% in small area (0.04 cm^2) and still demonstrated a decent efficiency of 8.06% in larger area (2.32 cm^2). The devices fabricated with lower n-members of $(PEI)_2(MA)_{n-1}Pb_nI_{3n+1}$ (n= 3, 5) also exhibited good photovoltaic response.

2.4.4 Emergence of DJ phase and other new type of layered perovskites

To date, most of reports on 2D PSCs are based on RP phase 2D perovskites. Very recently, Kanatzidis *et al*. explored the use of DJ perovskites as light absorbers in solar cells.[70] They demonstrated photovoltaic response from two different DJ perovskites synthesized using organic cations stemming from a piperidinium organic backbone and the efficiency of resultant devices varied depending on the 3- and 4-positions of the $-CH_2NH_3^+$ group with respect to the piperidine nitrogen. Specifically, devices fabricated using 3AMP-based homologous series of perovskites showed a higher performance (a PCE of 7.32% for n=4) relative to 4AMP homologous series (a PCE of 4.24 % for n=4) due to the lower band gap of the former compound. The Pb−I−Pb angles for 3AMP-based perovskites are larger than those for the 4AMP. As explained in the optoelectronics section, larger the Pb−I−Pb bond angles (closer to 180°), narrower the bandgap due to more overlap between the Pb s and I p orbitals overlap. (3AMP) $(MA)_3Pb_4I_{13}$ exhibited the lowest band gap of 1.87 eV among 3AMP and 4AMP based homologous series (n=1-4) of DJ perovskites and led to a broader EQE response in the derived devices. The J-V curves and EQE spectra of DJ perovskite-based devices are presented in Figure 2.17a & 2.17b. By employing the mixture of MA and FA cations in the cuboctahedral/perovskite cages, $(3AMP)(MA_{0.75}FA_{0.25})PbI_{13}$ devices displayed a better performance with a champion PCE of 12.04%.[215] $(3AMP)(MA_{0.75}FA_{0.25})_3Pb_4I_{13}$ perovskite has a narrower band gap (1.48 eV) possibly due to less distorted inorganic framework than the $(3AMP)(MA)_3Pb_4I_{13}$. Also, the first Sn-based hybrid DJ perovskite used 4AMP as spacer cations, where the $(4AMP)(FA)_3Sn_4I_{13}$ devices showed a promising PCE of 4.22%.[216] Ma *et al.* used small PDA cations as spacer layer to synthesize DJ phase perovskites and (PDA) $(MA)_3Pb_4I_{13}$ -based solar cells showed PCE over 13%.[86,217] The unencapsulated solar cells employing $(PDA)(MA)_3Pb_4I_{13}$ demonstrated outstanding stability under various harsh stresses. They retained 95% of their initial efficiency under ambient air with 40%–70% RH for 4000 h, humid heat of 85℃ and 85% RH for 168 h, and constant 1-sun illumination for 3000 h.[71] It has been proposed that DJ phase 2D perovskites are more stable than RP phase perovskites under harsh humidity, heat and light conditions.

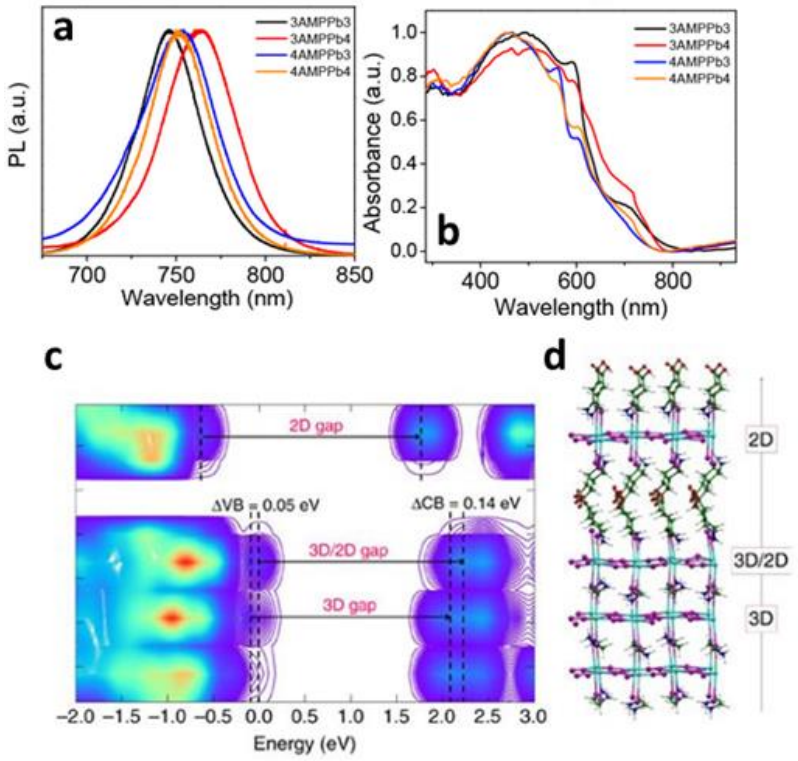

Figure 2.17 a) J-V curves and b) EQE spectra of DJ perovskite-based solar cell devices. Reprinted from ref. 70 with permission from the American Chemical Society. (c) DOS of the 3D/2D interface and (d) 2D phase/TiO_2 interface. Reprinted from ref. 222 with permission from Springer Nature Publishing AG.

It is because that the RP phase has a Van der Waals gap between adjacent monoammonium spacer cations, leading to a weak interaction between the perovskite layers, that affects the structural stability of the 2D perovskite framework upon exposure to external harsh stresses. On the other hand, diamine molecules with two amino groups in the DJ phase perovskites can produce hydrogen bonds with the inorganic slabs without any Van der Waal gaps, resulting in their enhanced stability. The incorporation of 1,4-benzenedimethanamonium iodide (BzDAI) as spacer cation in the perovskite framework was also found to produce DJ phase perovskites.[218] The Hall mobility measurements suggest that (BzDA) $(Cs_{0.05}MA_{0.15}FA_{0.8})_9Pb_{10}(I_{0.93}Br_{0.07})_{31}$ (n = 10) has similar carrier mobility as 3D perovskites. The (BzDA) $(Cs_{0.05}MA_{0.15}FA_{0.8})_9Pb_{10}(I_{0.93}Br_{0.07})_{31}$ devices showed a champion PCE 15.6%. DJ phase, $(PDMA)(FA)_2Pb_3I_{10}$ based solar cells (where PDMA is 1,4-phenylenedimethanammonium) also showed a good PCE of 7.11%. Interestingly, electron mobilities for PDMA-based 2D perovskite films deposited without using hot casing or antisolvent engineering are comparable to those reported for the most recent record performing 2D perovskites. The preliminary studies revealed that PDMA spacer molecule in combination with FA cations can greatly influence the orientation and crystallization of perovskite layers, which

resulted in better charge carrier mobilities in these systems. Unencapsulated (PDMA) $(FA)_2Pb_3I_{10}$ devices maintained >85% of the initial performance after 60 days upon storage at ambient air with RH of 30−50%.

The newly discovered ACI 2D perovskite structures also exhibited excellent photovoltaic response and stability. $(GA)(MA)_3Pb_3I_{10}$, a member of 2D ACI perovskite family, was applied as a light absorber in FTO/c-TiO_2/perovskite/PCBM/Ag solar cells and produced an average efficiency of 14.1 %.[219] The devices retained 88% of initial performance after kept under ambient environment for 240 days. The DJ phase and ACI phase perovskites exhibit better optoelectronic properties for solar cell applications as compared to RP phase perovskites. For instance, I···I interlayer distance of the 3AMP-based DJ perovskite is ∼4.0 Å, much shorter than that of BA-based perovskites (I···I ≈8). The smaller 3AMP-organic barrier is advantageous for better out-of-plane charge carrier transport, which results in better performance in solar cells.

The most relevant works on 2D/quasi-2D PSCs are listed in **Table 2.2**. Some major points can be briefly summarized as follows. Basically, the 2D/quasi-2D PSCs are mainly based on the RP phase perovskites containing either BA or PEA cations. A record PCE of 18.2% was reported for 2D perovskites employing a BA-derivative as spacer cations. But the most recent reports suggest a shift towards diversifying; different types of organic cations are being explored to improve the performance (efficiency and /or stability) of the solar cells. For instance, DJ phase $(PDA)(MA)_3Pb_4I_{13}$-based devices with 13% PCE showed impressive stability maintaining 95% of initial efficiency for 4000h under ambient air. Also, designing new types of 2D halide perovskites like ACI phase and reduction of Van der Waals gap in the layered perovskites are promising new research directions. A systemic study on the relationship between adjacent perovskite layer interaction and stability may lead to development of ultra-stable 2D PSCs. Also, the post-treatment of 2D perovskite film and the use of additives in the perovskite precursor solution were found to be beneficial to improve the crystallinity and orientation of perovskites, thereby contributing to the improvement of device efficiency. We strongly believe that an over 20% efficiency can be achieved in ultra-stable 2D perovskite-based solar cells by combining material design and post-treatment/additives approaches.

2.4.5 2D/3D perovskite solar cells

Due to the different optoelectronic properties of phase-pure 2D perovskites, such as wider optical band gaps and limited charge transport, the related devices do not deliver as high photovoltaic performance as their 3D perovskites.

Table 2.2 Photovoltaic performance and stability of 2D/quasi-2D PSCs.

Compound	Device configuration	Average PCE (%) *	Notes	Stability
$(PEA)_2(MA)_3Pb_4I_{13}$	ITO/PEDOT: PSS/perovskite/PCBM/Ag[171]	5.50	Active area of 0.06 cm^2	Unencapsulated devices stored in the dark at 72% RH retained 50% of initial performance after 90 h.
$(PEA)_2(MA)_5Pb_6I_{19}$	FTO/c-TiO_2/perovskite/spiro-OMeTAD/Au[186]	9.22	Active area of 0.049 cm^2	N/A
$(PEA)_2(MA)_4Pb_5I_{16}$	ITO/PEDOT: PSS/perovskite/PCBM/BCP/ Ag[184]	12.90 (14.1)	Active area of 0.12 cm^2/NH_4SCN and NH_4Cl additives	N/A
$(F\text{-}PEA)_2MA_4Pb_5I_{16}$	FTO/c-TiO_2/perovskite/spiro-OMeTAD/Au[188]	(13.64)	Active area of 0.12 cm^2/no additives and room temperature spin coating	Devices maintained 65% of their initial PCE after 576 h under an ambient environment at 70℃
$(BA)_2(MA)_3Pb_4I_{13}$	ITO/PEDOT: PSS/perovskite/PCBM/Al[56]	12.51	Active area of 0.05 cm^2/hot-cast method	Unencapsulated devices retained 20% of their original PCE after 60h stored in 65% RH.
$(BA)_2(MA)_3Sn_4I_{13}$	FTO/meso-TiO_2/perovskite/PTAA/Au[208]	2.43 (2.53)	Active area of 0.14 cm^2	Encapsulated devices maintained more than 50% of their initial performance after 4 months stored in the ambient atmosphere.
$(tBA)_2(FA_{0.85}Cs_{0.15})_4(Pb_{0.6}Sn_{0.4})_5I_{16}$	ITO/PEDOT: PSS/perovskite/ PCBM/BCP/Ag[209]	9.3 (10.6)	Active area of 0.09 cm^2	Devices retained 30% of initial efficiency after exposed to 1 Sun illumination and 65 ℃ temperature under an ambient atmosphere.
$(PA)_2(MA)_4Pb_5I_{16}$	FTO/TiO_2/perovskite/Spiro-OMeTAD/Au[211]	10.05 (10.42)	Active area of 0.09 cm^2/Solvent engineering with DMF: DMSO 1:1	Devices reported only 2% loss of efficiency after 500 h exposure to Air with 60% RH

Table 2.2 Photovoltaic performance and stability of 2D/quasi-2D PSCs. (Continued)

Compound	Device configuration	Average PCE (%) *	Notes	Stability
$(ThMA)_2(MA)_2Pb_3I_{10}$	ITO/PEDOT: PSS/perovskite/PCBM/BCP/Ag[212]	14.88 (15.42)	Active area of 0.1 cm^2/MACl-assisted film formation	Devices retained more than 80% of initial efficiency after 250h stored in the air with a humidity of 30±10% RH
$(PEI)_2(MA)_4Pb_5I_{16}$	ITO/PEDOT: PSS/perovskite/PCBM/LiF/Ag[213]	6.29 (6.99)	Large area of 2.32 cm^2	Devices maintained~ 95% of their initial value after 500 h under AM 1.5 light.
$(PEI)_2(MA)_6Pb_7I_{22}$	ITO/PEDOT: PSS/perovskite/PCBM/LiF/Ag[213]	8.06 (8.77)	Large area (2.32 cm^2)	Devices maintained ~90% of their initial value after 500 h under AM 1.5 light.

On the contrary, 3D/2D perovskites, a mixture of 3D and 2D perovskite phases, have recently surfaced as a promising photovoltaic material that can better balance long-term stability and high efficiency. Typically, 2D/3D perovskites are designed by replacing small amounts of organic cations with bulkier organic spacer cations in the precursor solution. To our best of our knowledge, only RP phase is used to design 2D/3D perovskites.

Though layered perovskites with n≥10 were reported in the literature, most likely they were indeed composed of both 2D and 3D perovskite phases. Sargent and co-authors conducted the theoretical and experimental investigations of multilayered-perovskites.[186] Based on their theoretical calculations, as the perovskites transitioned from the 2D to 3D phase, the formation energy decreased. The lack of long-term stability of 3D perovskites attributed to the lower formation energy of the material.[220] $(PEA)_2(MA)_{59}Pb_{60}I_{181}$ (n = 60) solar cells exhibited a PCE of 15.3% and could retain ~75% of initial performance after the storage in humid air (RH 55%) for 14 days. 2D/3D perovskites employing Br-containing organic cation spacers had higher optical band gaps, resulting in higher V_{oc} in corresponding solar cells than I-containing cells.[221] As an example, $(BA)_2(MA)_{49}Pb_{50}Br_{151}$ solar cells displayed an average efficiency of 8.8 % with a high

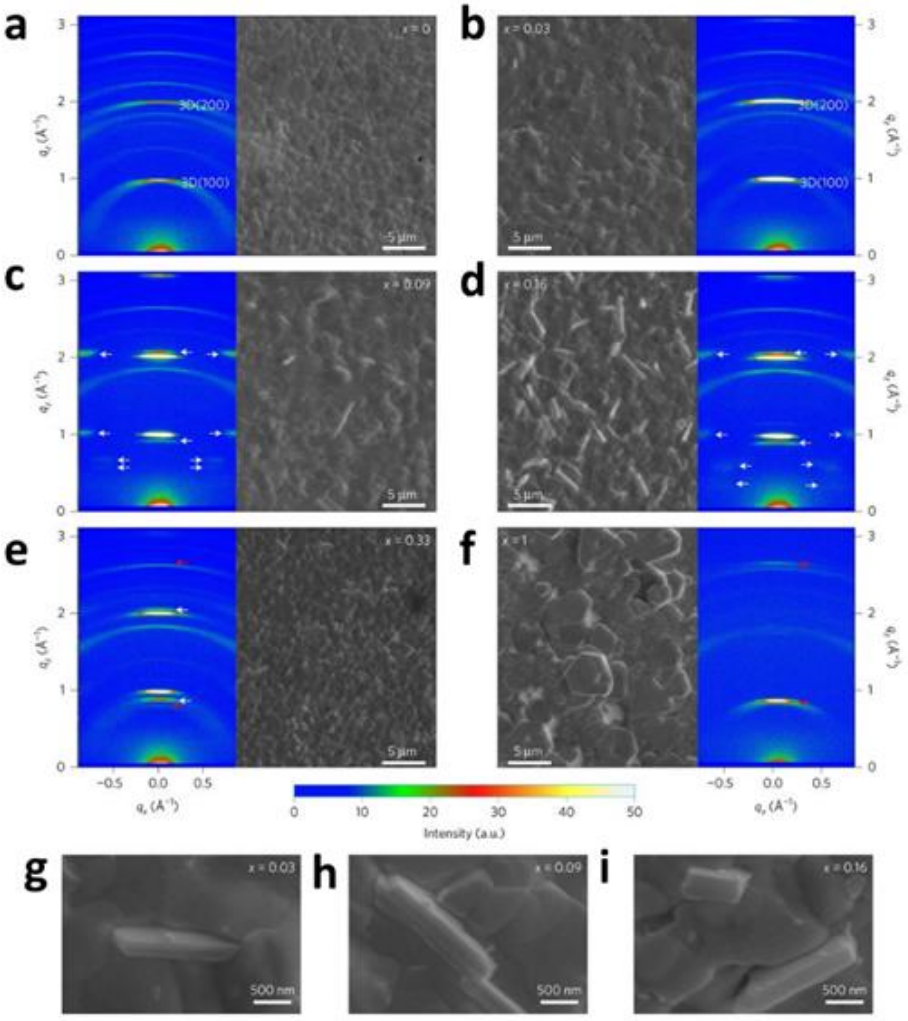

Figure 2.18 (a-e) SEM images and GIWAXS of 2D/3D perovskite films with different BA concentrations, and (f-h) enlarged SEM images of 2D/3D perovskite films with different BA concentrations. Reprinted from ref. 223 with permission from Springer Nature Publishing AG.

V_{oc} of 1.35 V. An even higher V_{oc} of 1.45 V was observed for $(PEA)_2(MA)_{49}Pb_{50}Br_{151}$ devices, representing one of the highest values among all the PSCs. These devices were also capable of delivering good efficiency without a hole transporting layer (HTL), with only 17% reduction in performance compared to the HTL-containing devices. Nazeeruddin and co-authors reported impressive one-year stability for HTL-free, 2D/3D engineered $(AVA)_{0.3}(MA)_{0.7}PbI_3$ perovskite solar modules, without any obvious loss in efficiency under ambient air with 1 Sun illumination at 55°C.[222] The $(AVA)_{0.3}(MA)_{0.7}PbI_3$ solar module produced 10.1% efficiency in FTO/c-TiO_2/meso-TiO_2/perovskite/meso-ZrO_2/Carbon device configuration. Small-sized $(AVA)_{0.3}(MA)_{0.7}PbI_3$ PSCs with SpiroOMeTAD/Au as HTL delivered a champion efficiency of 14.6% vs. 15.95% for 3D perovskites. First principle calculations suggested the widening of band gap at the 2D/3D interface

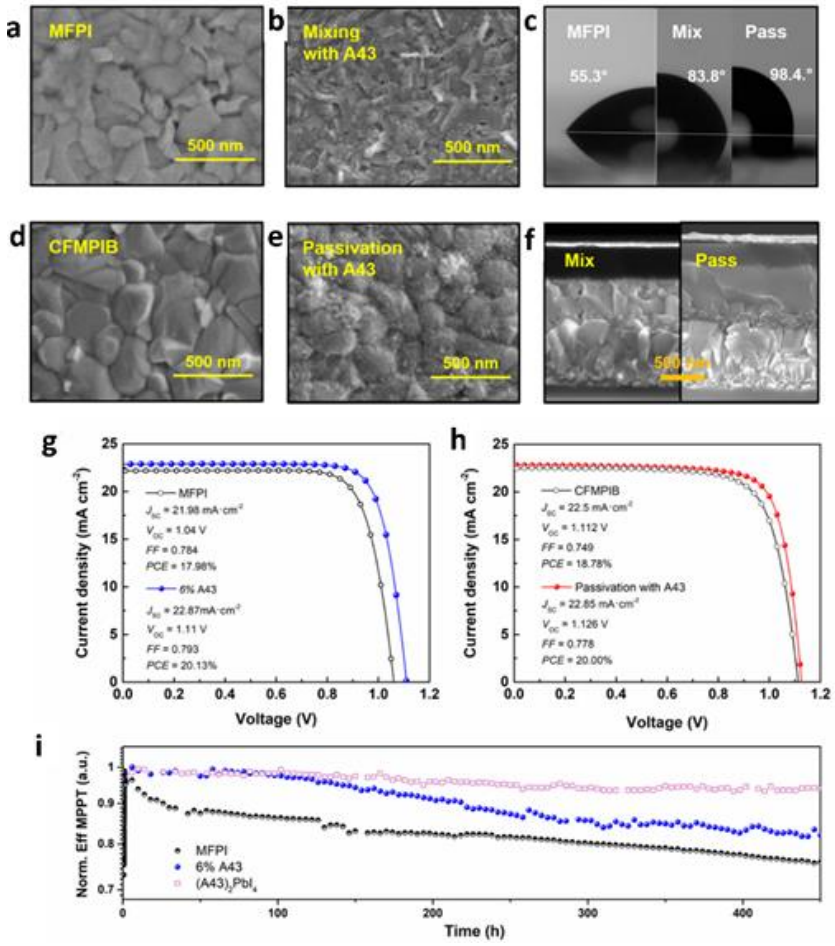

Figure 2.19 SEM top view of (a) MFPI, (b) MFPI/6% A43, (c) contact angle image of the pristine MFPI, MFPI containing 6%A43 and the CFMPIB/A43 perovskite films, and SEM top view of (d) CFMPIB, (e) CFMPIB /6% A43, (f) cross-sectional SEM images of devices, J-V characteristics of devices employing (g) MFPI and MFPI containing 6% A43 and (h) CFMPIB and CFMPIB/A43, and (i) stability of $(A43)_2PbI_4$, 3D MFPI, and MFPI containing 6%A43 devices. Reprinted from ref. 224 with permission from the American Chemical Society.

region of the $(AVA)_{0.3}(MA)_{0.7}PbI_3$ perovskite (Figure 2.17c & 2.17d). In this case, widening of band gap at the interface does not prevent electron injection to TiO_2 (an electron selective layer), rather it acts as a barrier to the electron recombination as a result of lower-lying CB of 2D perovskite versus that of 3D phase (Figure 2.17d). Consequently, efficiency of 2D/3D perovskite devices was largely unaffected, while retaining the stability features of the 2D phase. Snaith *et al*. designed "low" and "wide" band gap 2D/3D perovskites involving mixed A-site cations and halides.[223] They tuned BA-to-FA/Cs ratio in $FA_{0.83}Cs_{0.17}$ $Pb(I_{0.6}$ $Br_{0.4})_3$ (wide band gap perovskite) and $FA_{0.83}$ $Cs_{0.17}$ $Pb(I_{0.8}Br_{0.2})_3$ (low band gap perovskite) by replacing a small percentage of FA/Cs with BA spacer cations. $BA_{0.05}(FA_{0.83}Cs_{0.17})_{0.95}Pb(I_{0.8}Br_{0.2})_3$, a low band gap ($E_g$ = 1.61 eV) 2D/3D perovskite, yielded an average PCE as high as 18.1% with a stabilized power output (SPO) of 17.5%. Devices

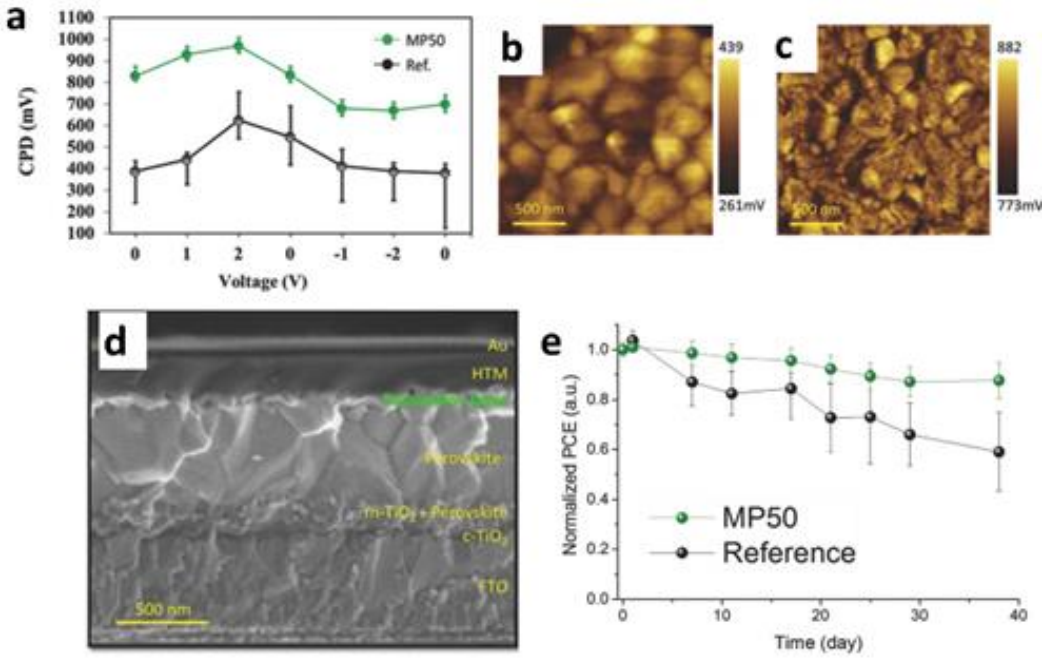

Figure 2.20 (a) Average CPD values as a function of bias voltage for the reference and passivated samples measured in the dark, and (b-c) corresponding KPFM surface images, d) cross-sectional SEM image of a solar cell employing perovskite film containing passivated layer, and (e) stability of the solar cells employing reference and passivated samples. Reprinted from ref. 226 with permission from John Wiley & Sons, Inc.

employing a wide band gap 2D/3D perovskite active layer ($BA_{0.09}(FA_{0.83}Cs_{0.17})_{0.91}Pb(I_{0.6}Br_{0.4})_3$) displayed an average efficiency of 15.5% with a SPO of 15.8%. When a lower percentage of BA was incorporated into the 3D perovskite structure, crystallinity was found to increase, as evidenced by GIWAXS analysis (Figure 2.18a-2.18f). Also, powder diffraction rings disappeared in GIWAXS of 2D/3D perovskite films indicative of orientation of crystals on the substrate. The 2D $(BA)_2(FA_{0.83}Cs_{0.17})_{n-1}Pb_n(I_{0.6}Br_{0.4})_{3n+1}$ phase emerged as plate-like structures at the grain boundaries of 2D/3D perovskite films as shown Figure 2.18g-2.18i. In general, devices using 2D/3D perovskites as a photoactive layer show less J-V hysteresis in comparison to devices using their 3D analogues. It was proposed that the formation of 2D-3D heterostructure at the grain boundaries contributed to the elimination of the hysteresis in PSC devices. The encapsulated $BA_{0.09}(FA_{0.83}Cs_{0.17})_{0.91}Pb(I_{0.6}Br_{0.4})_3$ devices exhibited superior stability with a lifetime of 1650h, maintaining 80% of original SPO whereas the SPO of devices employing 3D perovskites dropped to the similar level in a much shorter time of 970h. By employing 2D/3D Sn-perovskites, $PEA_2FA_{49}Sn_{50}I_{151}$ solar cells achieved a record high efficiency of 9% for Sn-based perovskite devices, much high than 6% in their 3D version, $FASnI_3$ devices.[182] Recently, we observed that defects associated with Sn vacancies can be reduced in Sn-Pb alloyed perovskites by designing

2D/3D perovskite composites. DFT calculations suggested higher formation energy for Sn vacancies in 2D Sn-perovskites ($(PEA)_2SnI_4$), which discloses the reason for the reduction of number of defects in the 2D/3D Sn-Pb perovskites. Nazeeruddin and co-authors observed the formation of a separate water-repellent 2D perovskite layer on the top surface of 3D perovskite film when fluorous spacer cation, $(CF_3)_3CO(CH_2)_3NH_3^+$ (coded as A43), was incorporated into perovskite film (Figure 2.19).[224] In their work, authors explored two different methods to incorporate 2D perovskites, $(A43)_2PbI_4$ (n = 1) and $(A43)_2MAPb_2I_7$ (n =2), into the perovskite film. In the first approach, they added A43 in $MA_{0.9}FA_{0.1}PbI_3$ (coded as (MFPI) precursor solution, so a 2D/3D composite formed in the entire film including on the film surface (Figure 2.19 a & 2.19b). In the second approach, a solution of A43 spin-coated on the top of the $Cs_{0.1}FA_{0.74}MA_{0.13}PbI_{2.48}Br_{0.39}$ (coded as CFMPIB) perovskite film, which led to the formation of a 2D phase at the top surface (Figure 2.19 d & 2.19e). In both cases, the presence of A43 spacer cation made the film surface waterproof as evidenced by the increase of contact angle from 55° to 80°-100° (Figure 2.19c). $(A43)_2PbI_4$ (n = 1) and $(A43)_2MAPb_2I_7$ (n =2), 2D perovskites at the film surface improved the moisture stability of the devices by blocking water infiltration and slowing down the interface degradation (Figure 2.19i). Also, the photovoltaic performance (Figure 2.19 g & 2.19h) has enhanced in both cases with respect to reference devices delivering efficiencies more than 20%. The deposition of $(p\text{-}FPEA)_2PbI_4$ on the top of 3D perovskite film also found to be able to improve the performance and stability of the solar cells.[225] The devices with stabilized PCE of 20.26% maintained 99% of their initial performance after 864 h upon exposure to dry air with RH 10-30%. Cho et al. passivated the interfacial trap sites in the device by depositing a 2D/3D perovskite layer at the perovskite/hole transport layer interface.[226] They spin coated a solution containing mixture of bulky organic ammonium iodide, iso-butylammonium iodide (iBAI) and formamidinium iodide (FAI) on the top of 3D perovskite ($(FAPbI_3)_{0.85}(MAPbBr_3)_{0.15}$) film, which led to the formation of a 2D/3D perovskite phase at top of the film. The passivation of non-radiative recombination pathways resulted in improvement in both V_{oc} and FF, producing stabilized PCE of 21.7%. Kelvin probe force microscopy (KPFM), a powerful tool to study charge-carrier concentration, ionic defects, impurities on the perovskite films by analyzing spatial surface potential or contact potential difference (CPD) revealed the properties of passivated perovskite surface.[182,227]

Under applied voltage bias, passivated sample showed a smaller change in CPD due to reduced number of ionic defects at the surface, within and underneath the 2D/3D passivation layer (Figure 2.20a-2.20c). Consequently, devices with passivation layer have displayed reduced J-V hysteresis with respect to solar cells using non-passivated perovskite layer since surface defects play a huge role in device hysteresis. The 2D/3D passivation layer also helped to resist moisture

infiltration to the 3D perovskite layer (passivation layer shown in Figure 2.20d). The devices with passivation layer showed superior stability compared to non-passivated devices stored in RH 75 ± 20% humidity conditions (Figure 2.20e). Cao et al. found post-treatment of the $MAPBI_3$ film with tetra-ammonium zinc phthalocyanine (ZnPc) produces 2D $(ZnPc)_{0.5}MA_{n-1}Pb_nI_{3n+1}$ perovskites at the grain boundaries of perovskite which passivated the defects in the perovskite film (Figure 2.21a- 2.21c).[228] Elongated PL decay time from 44 to 57 ns have shown the reduction of trap-assisted recombination with modification of $MAPbI_3$ grain boundaries. The devices employing passivated perovskite film showed an increase in the average PCE from 18.1% to 19.4%. More importantly, moisture and heat stability of these devices improved, as shown in Figure 2.21d-2.21g. Devices using modified perovskite retained over 90% of their original performance after 1000 h test at 85℃ with a humidity of 45% RH. All-inorganic halide perovskites are alternative to organic-inorganic halide perovskites, which largely avoid the stability issues associated with the moisture-sensitive organic component. α-$CsPbI_3$ is the most suitable inorganic perovskite with a band gap of ~1.73 eV.[204,229] But the α-phase of $CsPbI_3$ is structurally unstable and easily converts into photo-inactive δ-phase under ambient conditions. The α-phase could be structurally stabilized by incorporating a small amount of bulkier organic cations, thus producing 2D/3D inorganic perovskites.[230,231] Inclusion of a small amount of 2D perovskite $EDAPbI_4$ into $CsPbI_3$ produced highly robust α-$CsPbI_3$ films, stable at room temperature for several months.[230] Interestingly, authors found that if a monofunctional ethylamine (EA) or a longer chain alkylamine, such as BA, was used instead of a bication ethylenediamine (EDA), the stability of formed 2D/3D $CsPbI_3$ was on par with that of the pure α-$CsPbI_3$. The solar cells based on the $CsPbI_3$ photoactive layer containing the optimum amount of $EDAPbI_4$ showed an average PCE of 10.42% vs. 5.56% in pure $CsPbI_3$ devices. The most relevant works on 2D/3D PSCs are listed in **Table 2.3.**

Table 2.3 Photovoltaic performance and stability of 2D/3D PSCs.

Compound	Device configuration	Average PCE (%) *	Notes	Stability
$(BA)_2(MA)_{49}Pb_{50}Br_{151}$	FTO/TiO_2/perovskite/Spiro-OMeTAD/Au[221]	8.8 (9.5)	Active area of 0.04 cm^2	Devices maintained ~60% of initial performance under 1 sun illumination, 90 ℃ and RH 50% humidity conditions
$(PEA)_2(MA)_{59}Pb_{60}I_{181}$	FTO/c-TiO_2/perovskite/spiro-OMeTAD/Au[186]	18.40	Active area of 0.049 cm^2	Devices retained more than 74% initial performance stored in RH 55% for 14 days.
$(PEA)_2(MA)_{49}Pb_{50}Br_{151}$	FTO/TiO_2/perovskite/Spiro-OMeTAD/Au[221]	7.5 (8.6)	Active area of 0.04 cm^2	Devices maintained ~78% of initial performance under 1 sun illumination, 90 ℃ and 50% RH conditions
$(AVA)_{0.3}(MA)_{0.7}PbI_3$	FTO/c-TiO_2/meso-TiO_2/perovskite/meso-ZrO_2/Carbon	10.1	10×10 cm^2 solar modules with 46.7 cm^2 active area	Encapsulated devices displayed no loss of initial performance under ambient air with 1 Sun illumination kept at 55℃
$BA_{0.05}(FA_{0.83}Cs_{0.17})_{0.91}Pb(I_{0.8}Br_{0.2})_3$	FTO/SnO_2/$PC_{61}BM$/perovskite/spiro-OMeTAD/Au.[223]	18.1	Active area of 0.09 cm^2	N/A
$BA_{0.09}(FA_{0.83}Cs_{0.17})_{0.91}Pb(I_{0.6}Br_{0.4})_3$	FTO/SnO_2/$PC_{61}BM$/perovskite/spiro-OMeTAD/Au.[223]	15.5	Active area of 0.09 cm^2	Encapsulated devices retained 80% of initial efficiency after 1680h under AM1.5 irradiance with temperature in between 50-60℃ and humidity in between RH 40-50%.
$CsPbI_3 \cdot 0.025EDAPbI_4$	FTO/c-TiO_2/perovskite/spiro-OMeTAD/Ag[230]	14.05 (14.53)	Active area of 0.12 cm^2	Devices retained more than 80% of initial efficiency stored in a dark dry box for 1 month.
$Cs_{0.1}FA_{0.74}MA_{0.13}PbI_{2.48}Br_{0.39}$/$(A43)_2PbI_4$ and $(A43)_2MAPb_2I_7$	FTO/c-TiO_2/meso-TiO_2/perovskite/spiro-OMeTAD/Au[224]	20.0	Active area of 0.16 cm^2	Encapsulated devices retained more than 65% of initial efficiency after 250h under ambient atmosphere.
$(FAPbI_3)_{0.85}(MAPbBr_3)_{0.15}$/ 50% nBAI/50% FAI mixture	FTO/c-TiO_2/meso-TiO_2/perovskite/spiro-OMeTAD/Au[224]	21.7	Active area of 0.16 cm^2	Devices retained more than 85% of initial efficiency after 38 days of storage in RH 75±20%.
$MAPBI_3/(ZnPc)_{0.5}MA_{n-1}Pb_nI_{3n+1}$	FTO/c-TiO_2/meso-TiO_2/perovskite/co-porphyrin/Au[228]	19.4 (19.8)	Active area of 0.10 cm^2	Devices maintained 95% of their original efficiency after 2000 h under humidity of RH 45%.

Table 2.3 Photovoltaic performance and stability of 2D/3D PSCs. (Continued)

Compound	Device configuration	Average PCE (%) *	Notes	Stability
$Cs_{0.1}(FA_{0.83}MA_{0.17})_{0.9}Pb(I_{0.83}Br_{0.17})_3$/ $(p\text{-}FPEA)_2PbI_4$	FTO/c-TiO_2/meso-TiO_2/perovskite/spiro-OMeTAD/Au[225]	20.26 (20.54)	Active area of 0.06 cm^2	Devices maintained 99% of their initial performance after 864 h upon exposure to dry air with 10-30 RH %.

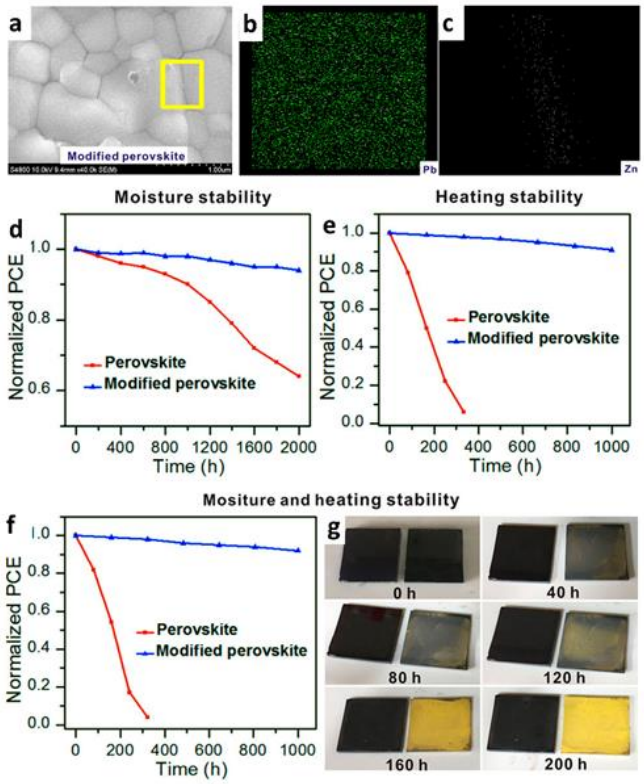

Figure 2.21 (a) SEM images of perovskite film with modified grain boundaries, and elemental map of (b) perovskite film surface, (c) grain boundary, (d) moisture (e) heat, and (f) moisture+heat stability of solar cells employing modified perovskite films, and (g) photographs of degraded perovskite films. Reprinted from ref. 229 with permission from the American Chemical Society.

2.5 Design principles of 2D/quasi-2D and 2D/3D PSCs

2.5.1 Perovskite film thickness

The film thickness of layered perovskites, especially 2D/quasi-2D perovskites in planar solar cells, is critical in determining the photovoltaic performance of the devices. In contrast to 3D perovskites, 2D/quasi-2D PSCs operate in the Langevin-Type charge carrier recombination regime, where the excitonic nature of charge carriers imposes the limit on the thickness of the solar absorber layer.[232–234] Although, an increase in 2D/quasi-2D perovskites film thickness will improve the optical absorption, it reduces the carrier transport, which in turn decreases the PCE of solar cells. As an example, the PCE, J_{sc} and V_{oc} values of $(BA)_2(MA)_3Pb_3I_{10}$ perovskite devices are plotted in Figure 2.22a- 2.22c as a function of film thickness. The PCE of solar cells is thus defined by the competition between photogeneration (absorption) and carrier transport through the film (Figure 2.22d).[56] Different from 2D/quasi-2D PSCs, mixed 2D/3D PSCs are similar to 3D perovskite devices in the sense that their photovoltaic performance is less sensitive to film thickness in the 300-500 nm range as the optical excitation generates free charge carriers, instead of excitons, at room temperature. In a solar cell, a nearly vertical steep slope at the open circuit (OC) condition in a J-V curve indicates that current collection is efficient at low internal electric field and deviation from the ideal slope implies the loss of photocurrent. on the contrary, at the short circuit condition (SC) when the field attains the maximum, a flat slope is anticipated for the efficient charge transport and collection, whereas a steep slope at SC alludes that charge collection is field dependent. As illustrated in Figure 2.22d & 2.22e, when a 2D perovskite film thickness is >375 nm, a sharp fall in the slope value at OC was observed, suggesting that the charge collection efficiency of 2D PSCs is more sensitive at OC than 3D PSCs. The slope of 2D PSCs at SC largely deviated from the ideal value when the film thickness was more than 400 nm. These results explicitly state that charge collection strongly depends on the internal electric field in the absorber layer.[234,235] Simulations on the band diagram provided further details about the internal electric field in 2D PSCs (Figure 2.23a & 2.23b).

A uniformly strong internal field throughout the film is present for a thin absorber layer device, while the field becomes non-uniform for a thicker film, in particular with the considerably reduced field at the center. The recombination profiles obtained through device simulation (Figure 2.23c & 2.23d) disclose that the major recombination takes place at the proximity of the interface for a thin film since it is fully depleted.

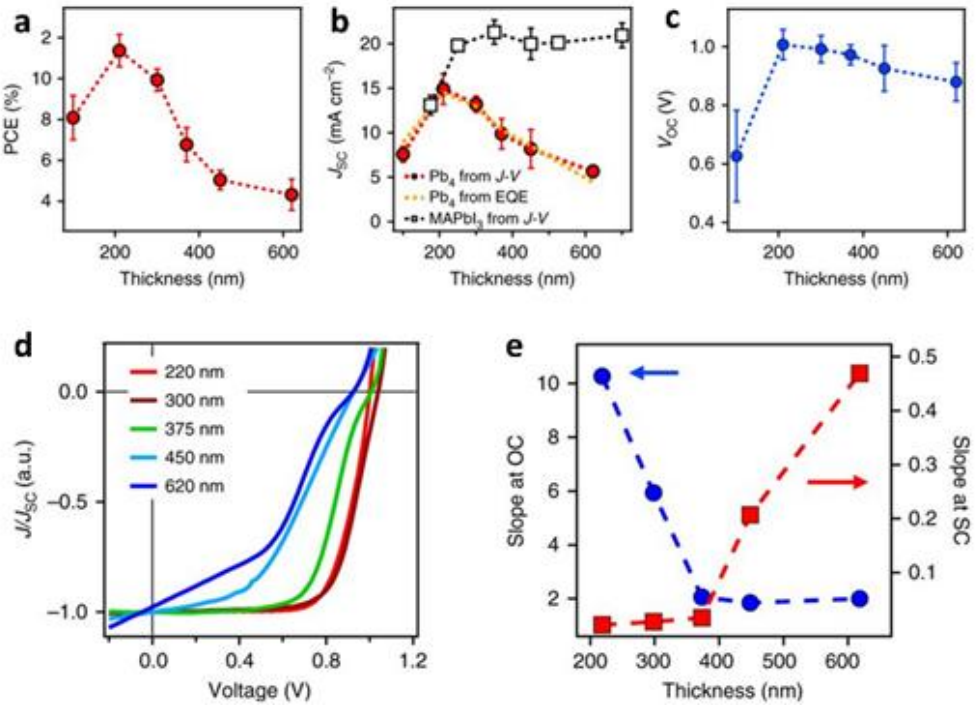

Figure 2.22 (a-c) Average PCE, J_{SC} and V_{OC} as a function of film thickness, (d) J–V curves for devices with various film thickness, and (e) J–V slope obtained for devices with various film thickness. Reprinted from ref. 234 with permission from Springer Nature Publishing AG.

In the thicker absorber layer, recombination occurs both at the bulk and near the interface due to the faded internal field near the center. A schematic of recombination processes in thin and thick films is displayed in Figure 2.23e & 2.23f. It was proposed that a slight mismatch and imperfect crystal packing in thin films (Figure 2.23g) compared to single crystals, can act as potential barriers, which are generated in part by organic spacers between conducting inorganic or perovskite slabs.[234] Consequently, two types of charge carriers can be envisioned in layered perovskite devices, the quasi-bound charge carriers localized in inorganic or perovskite layer regions and free delocalized carriers outside the potential barriers.

The electrons and holes are recurrently trapped into and released from the quasi-bound states as they move toward their respective selective contacts (Figure 2.23h). The devices with a thick absorber layer suffer from increased recombination process prompted by organic potential barriers compared to thin films, which regulates the performance of 2D PSCs. Most recent reports on 2D PSCs adopt the strategy to control the orientation and packing of perovskite layers with additives such as NH_4SCN and MACl to enhance the performance of solar cells.

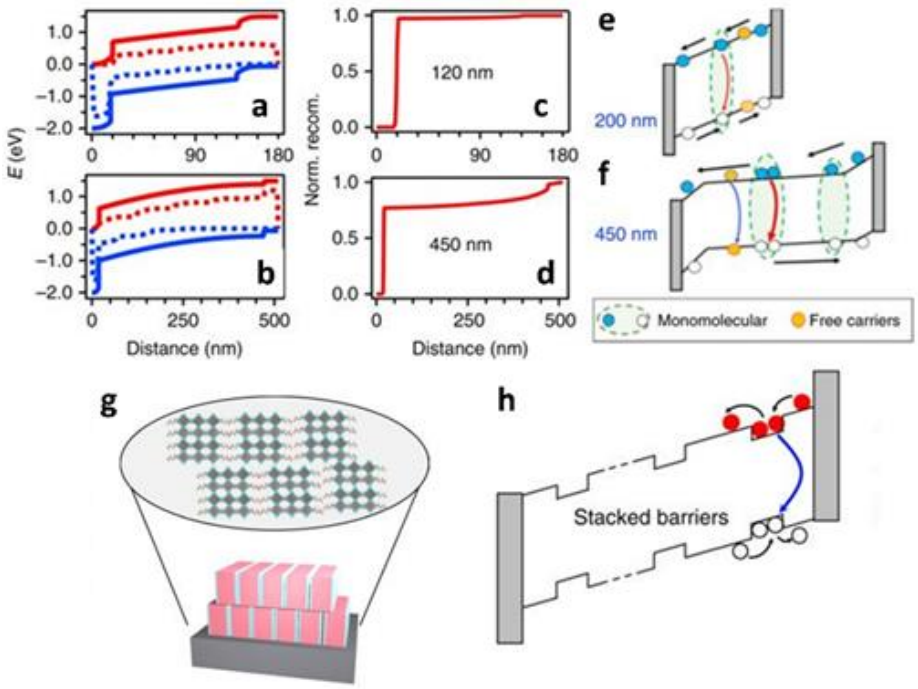

Figure 2.23 (a and b) calculated band energy as a function of 2D perovskite film thickness, (c and d) normalized recombination profile as a function of 2D perovskite film thickness, Illustration of the carrier recombination processes in (e) thin and (f) thick layered perovskite film, and (g) schematic of vertically packed perovskite layers with misalignment in molecular structures. Reprinted from ref. 234 with permission from Springer Nature Publishing AG.

Well oriented-perovskite quantum wells with perfect crystal packing reduce the number of potential barriers, enabling efficient charge carrier transport to selective contacts. Alternatively, use of organic spacers with high conductivity or doped organic spacer cations in 2D perovskites can lower the potential barriers for efficient charge transport.

2.5.2 Crystal growth orientation

A proper crystal growth orientation is vital in the layered perovskite system to ensure efficient charge transport to selective contacts. Orientation is a unique, yet important requirement for high performance 2D perovskite-based PSCs. For illustrating this concept, a schematic of orientations of $(BA)_2(MA)_{n-1}Pb_nI_{3n+1}$ 2D perovskite on the substrate is shown in Figure 2.24a.[236] The perovskite layers oriented along the (0k0) direction (horizontal growth) are undesired whereas those oriented along the (202) direction, known as vertically oriented with respect to the plane of the substrate, are highly desired for solar cell application. The crystal orientation can be characterized using powder XRD (PXRD) and Grazing-Incidence X-Ray Scattering (GIXS) method.

2.5.2.1 PXRD pattern method

The March–Dollase can calculate the degree of preferential orientation for the layered 2D perovskites or the alignment of the perovskite slabs relative to the substrate.[237,238] Kanatzidis *et al*. simulated PXRD patterns of the $(BA)_2(MA)_4Pb_5I_{16}$ (n = 5) material (Figure 2.24b) as a function of the degree of orientation along (101).[195] In an ideal case of $(BA)_2(MA)_{n-1}Pb_nI_{3n+1}$ film with perfect alignment along (202), the March–Dollase parameter is zero, and only the (202) peak is observed in the film PXRD. As the vertical growth starts to weaken, the (111) peak appears. The ratio of (111) to (202) peaks can be used to determine the orientation of perovskite slabs on the substrate. Also, the correlation between layer thickness and crystal growth orientation can be elucidated from film PXRD. Figure 2.24c shows the difference in the ratio of (111) and (202) peaks when n goes from n=3 to n=5; it demonstrates an increase in the (111)-to (202) ratios with increasing n.

2.5.2.2 GIXS Methods

Grazing-Incidence Scattering (GIXS) is a powerful tool in investigating crystal growth, morphology, and degradation of perovskites. In general, the GIXS method can probe a large sample volume on scales relevant for typical solar cell devices while being nondestructive. There are two types of GIXS, Grazing-Incidence Small-Angle X-Ray Scattering (GISXAS) and Wide-Angle X-Ray Scattering (GIWXAS).

In a GIXS measurement, the sample reference frame is typically positioned onto the sample surface where z is normal to the surface and x pointing into the direction of the X-ray beam as depicted in Figure 2.24d. The x-ray beam with the momentum $\overrightarrow{k_i}$ impinges at a shallow angle α_i. The emergent scattering waves with the momentum $\overrightarrow{k_f}$ are expressed by the in-plane exit angle α_f and out-of-plane angle Ψ.

The scattering vector, $\vec{q}$ is given by [239]

$$\vec{q} = \overrightarrow{k_f} - \overrightarrow{k_i} \qquad (2.5)$$

In GISAXS, the detector-sample distance is > 2m. Crystal morphology and domain/grain sizes with length scale in the range of several nanometers up to micrometers can be probed using GISAXS.

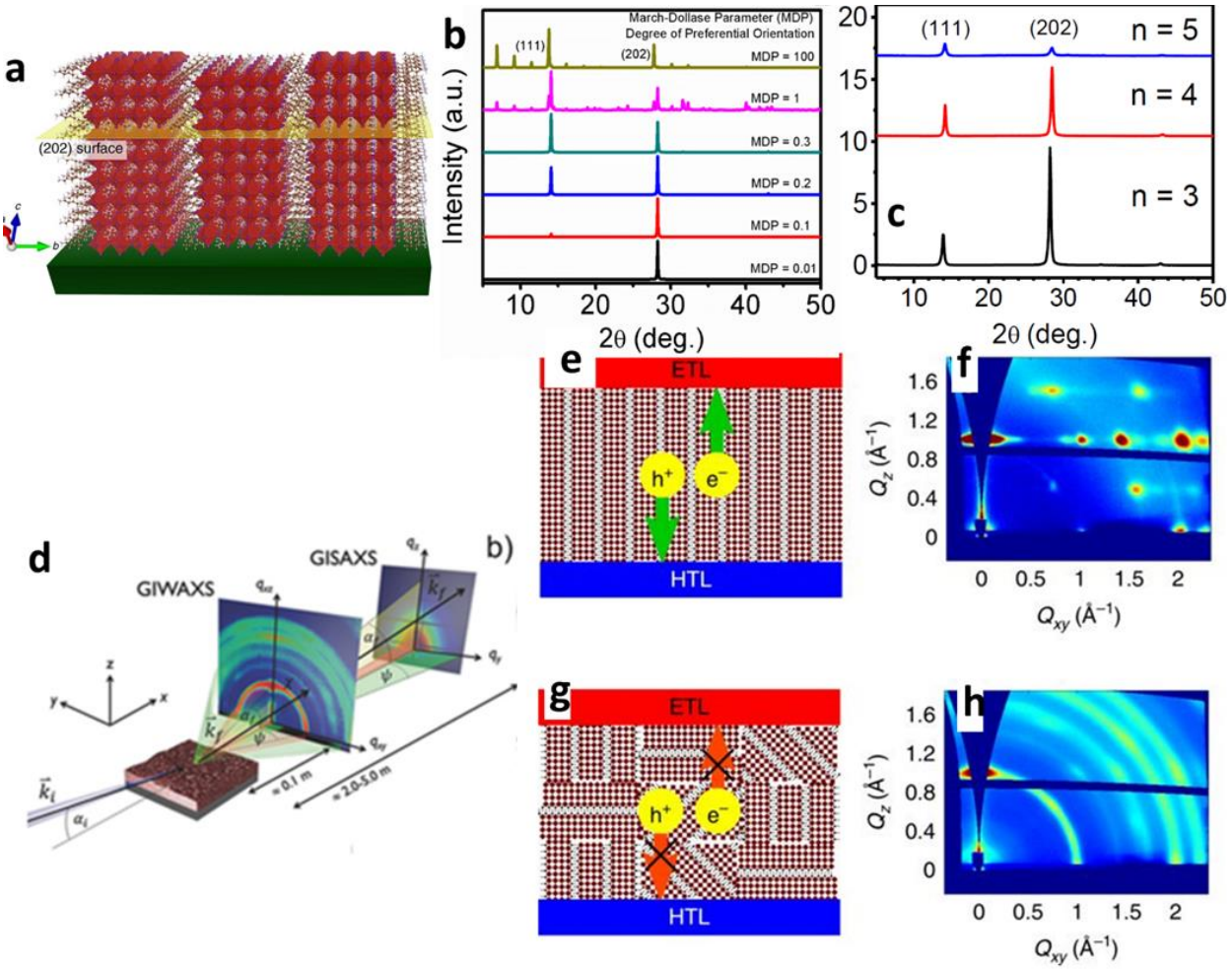

Figure 2.24 (a) Schematic of an orthorhombic (101) vertically oriented 2D perovskite structure, with (202) planes parallel to the substrate. Reprinted from ref. 236 with permission from Springer Nature Publishing AG. (b) Simulation of XRD pattern of $BA_2(MA)_2Pb_5I_{16}$ as the degree of preferential orientation changes along the (202) direction, (c) PXRD patterns of a series of $BA_2MA_{n-1}Pb_nI_{3n+1}$ (n = 3, 4, 5). Reprinted from ref. 195 with permission from John Wiley & Sons, Inc. (d) Illustration of the scattering geometry of GIXS methods. Reprinted from ref. 239 with permission from John Wiley & Sons, Inc. (e) Charge transport and (f) GIWAXS with preferential layer orientation, and (g) charge transport and (h) GIWAXS with random layer orientation. Reprinted from ref. 236 with permission from Springer Nature Publishing AG.

Conversely, GIWAXS investigates length scales down to the atomic range and therefore bears crystallographic information about the crystalline component of the material. The scattering pattern produced in GIWAXS measurements originates from crystal planes in the reciprocal space and provides information about crystalline phase as well as crystal orientation with respect to normal to the surface of the substrate.

The azimuthal angle χ describes the crystal orientation in the sample to the normal component q_z of the scattering vector. The random orientation in the sample produces Debye–Scherrer rings

with homogeneous intensity distribution. The scattered waves, k_f, depict an Ewald sphere (a sphere in the reciprocal space). According to the Laue condition, only the points of reciprocal lattice, which overlap with the surface of the Ewald's sphere, are detectable in the GIWAXS map. Thus, intense Bragg spots are observed for the samples containing highly oriented crystalline phase (Figure 2.24e-2.24h). In short, GIWAXS is complementary to specular XRD, which examines a small part of reciprocal space along the normal of the surface of the substrate ($q_r \approx 0$). In 2D/quasi-2D PSCs, the orientation of perovskite slabs with respect to substrate is a key factor to achieving high performance.[207] The orientation of perovskite slabs parallel to the substrate impedes charge transport to the respective electrodes due to the encountering of charge carriers with insulating organic spacer cations in their transport paths (Figure 2.24g).[236,240] Therefore, the knowledge of perovskite crystal orientation obtained through GIWAXS is essential to understand, design and optimize 2D perovskite absorber films. As seen in the previous section, most recent reports on 2D/quasi-2D PSCs tried to alter the perovskite layer orientation by using additives and modifying film deposition parameters and the GIWAXS technique has been almost exclusively utilized in these efforts.[56,185,212]

2.6 Conclusion and Future Perspectives

2D perovskites are an attractive alternative to 3D perovskites for solar cell application as they directly address a critical issue of stability of 3D PSCs, while achieving a similarly high PCE (now close to 20%). The impressive accomplishment sprouted from the developments in scientific understanding of the materials and the advancements in the fabrication and synthetic chemistry skills of 2D perovskites and solar cells as well as the exploration of relevant, top-notch characterization tools. Their unique layered structural design enables structural flexibility and grants functional material design. Physical and chemical nature of spacer cations, choice of metal cations and halides, variation of perovskite slab thickness even external stress can be used to tune optoelectronic properties of 2D perovskites. To date, RP phase 2D perovskites are intensely studied and utilized in solar cell investigations, but layered perovskites are not only limited to the RP phase. For example, DJ phase and newly discovered ACI phase perovskites were tested as solar absorbers to produce a PCE more than 15%. We anticipate that a more fundamental understanding of structure-property relationships of different 2D perovskite phases can lead to the further development of impressively stable, high-performing photovoltaic materials. On the synthetic chemistry front, 2D perovskites containing bifunctional organoammonium cations such as $Y(CH_2)_2NH_3^+$ (Y = F, Cl, Br, I, CN), will open the door for a new class of band gap tunable photovoltaic materials, although they have not been widely employed for solar cell applications

yet. Recent reports on fluorination of aromatic organic spacer cations to improve charge transport in 2D perovskites are very encouraging. A detailed investigation on changes in structural and intermolecular electronic coupling between neighboring organic cations in organic gallery upon fluorination could lead to employing a wide variety of bifunctional organic molecules in layered perovskites to improve photovoltaic performance of the solar cells. A phase-pure, high member ($n \geq 5$) of layered perovskites is still challenging to synthesize and advancement in synthetic chemistry is expected to provide a leap forward in 2D perovskite semiconductors research. So far, we have limited understanding about the nature of excitonic properties of charge carriers and conversion of excitons to free charge carries in the RP phase 2D perovskites. Current experimental results are not convincing enough to categorize excitons into one of the regimes of excitons, namely Wannier and Frenkel. Another plausible scenario is that the excitons in 2D perovskites may belong to an intermediate state between the Wannier and Frenkel regimes. Recently, mixed 2D/3D PSCs have also generated great interest due to their long-term stability without much compromising the photovoltaic properties. Thus far, a strong theoretical framework is not developed for the enhanced long-term stability of 2D/3D perovskites, but the preliminary experimental and theoretical findings suggest that the incorporation of 2D phases modifies the defect chemistry.

We foresee a breakthrough in 2D perovskite research in the coming years, which could potentially replace 3D perovskites and become a ‘next big thing’ in semiconductor materials for solar cell applications.

3 AROMATIC ALKYLAMMONIUM SPACER CATIONS FOR EFFICIENT TWO-DIMENSIONAL PEROVSKITE SOLAR CELLS

Title of the article: Aromatic Alkylammonium Spacer Cations for Efficient Two-Dimensional Perovskite Solar Cells with Enhanced Moisture and Thermal Stability

French translation: Cations Spaceurs d'Alkylammonium pour une Efficacité Accrue des Cellules solaires à Base de Pérovskites à Deux Dimensions avec une Amélioration de la Stabilité Thermique et contre l'Humidité

Authors:

Authors' names: Deepak Thrithamarassery Gangadharan, Yujie Han, Ashish Dubey, Xinyu Gao, Baoquan Sun, Qiquan Qiao, Ricardo Izquierdo, and Dongling Ma

Title of the journal or book:

Solar RRL, Manuscript submitted on 27 November 2017, Accepted on 06 February 2018, DOI:10.1002/solr.201700215

Contribution of the authors:

Deepak Thrithamarassery Gangadharan and Dongling Ma conceived the experiments. Yujie Han, Xinyu Gao conducted the synchrotron experiments. Deepak Thrithamarassery Gangadharan conducted material synthesis, material characterizations, solar cell fabrication and device characterizations. Deepak Thrithamarassery Gangadharan wrote original draft of the manuscript. Dongling Ma supervised the project. Ashish Dubey, Baoquan Sun, Qiquan Qiao, Ricardo Izquierdo provided advise and expertise. All authors contributed to the final version of the manuscript.

Link between the previous article or articles and the following:

From chapter 2, it is clear that stability of halide perovskites is a pressing issue in the process of commercializing this photovoltaic technology and employing 2D perovskites is one of the best solutions to achieve stable PSCs. Here, aromatic organic spacer cation, PEA, was chosen to design 2D perovskites. The reasoning behind opting aromatic organic cation is their better hydrophobicity and larger ionic size compared to aliphatic organic cations, which can lead to

better moisture and thermal stability. The major issue with the 2D perovskite is subpar photovoltaic efficiency compared to 3D perovskites due to their distinct optoelectronic properties and perovskite layer orientation on the substrate. This article explores modifying the crystal orientation by modifying perovskite thin layer deposition and their application in solar cells. Furthermore, moisture and thermal stability of the 2D perovskites are investigated using various characterization techniques.

3.1 Introduction

Recent photovoltaic research has mainly been dominated by the hybrid organic-inorganic perovskites because of their remarkable photophysical and optoelectronic properties as well as their broad tunability in material properties, highly relying on the nature and content of inorganic and organic components.[12,14,17,45,241–245] Within a few years of development, an impressive certified power conversion efficiency (PCE) of 22.7% has been achieved by perovskite solar cells, challenging the matured inorganic semiconductor technologies. Unfortunately, the poor chemical stability of perovskite hinders the commercialization prospect of this exciting new technology. For instance, moisture and heat exposure can cause rapid decomposition of three-dimensional (3D) perovskite films.[246–250]

Hybrid perovskite materials follow a general formula ABX_3 and adopt a 3D structural framework, where organic cations occupy the 'A' sites, group IV cations occupy the 'B' sites, and the group VII anions occupy the 'X' sites.[96,251] In a prototypical 3D hybrid perovskite such as methylammonium lead triiodide ($MAPbI_3$), 'A' sites are occupied by methylammonium (MA) cations, 'B' sites are occupied by lead cations (Pb^{2+}) and 'X' sites are occupied by iodide anions (I^-). The 3D perovskite framework involves a corner-shared network of $[BX_6]^-$ octahedra with 'A' cations occupying 12-fold coordinated cavities counterbalancing the charge of BX_3. Goldschmidt's tolerance factor (t) dictates whether a particular set of 'A,' 'B' or 'X' ions may adopt the perovskite framework, which is formulated based on space-filling constraints of ions, viz., $t = \frac{(R_A+R_B)}{\sqrt{2}(R_B+R_X)}$, where R_A, R_B and R_X, are ionic radii of corresponding ions. The Goldschmidt's tolerance factor must satisfy $t \approx 1$ to form the 3D perovskite framework.[41]

One of the immediate concerns of 3D perovskite is its poor moisture stability. Water molecules can complex with perovskite and form a hydrate similar to $(CH_3NH_3)_4PbI_6{\cdot}2H_2O$.[248] More rapid decomposition of hybrid perovskite has been observed under ambient conditions in the presence of light, where photogenerated electrons in the perovskite conduction band react with adsorbed oxygen, forming superoxide anions that deprotonate the MA cations. [252] Another concern is thermal robustness of the perovskite. Substantial degradation of perovskite has been observed even at temperature ≤100 °C.[253] The exact mechanism behind the thermal degradation of hybrid perovskite is not entirely understood, but several mechanisms have been proposed such as phase transition at relatively modest temperature, the breakage of weak lead-iodide bonds and its reaction with charge carrier selective layers, *etc*.[254–256] Hygroscopic MA cations have been identified as a primary source of instability in hybrid perovskites, so replacing the MA cations with

more suitable (*i.e.*, less hygroscopic) cations is one of the promising ways to address this issue. Regardless of several successful attempts to replace MA cations with small organic cations (such as formamidinium), inorganic cations (such as cesium) and a mixture of cations (formamidinium, cesium, and MA), the stability of the hybrid perovskite solar cells is still well below the industry standards for commercial applications.[45,203,257] In another approach, considerably larger hydrophobic organic cations are introduced into the perovskite framework resulting in layered or two-dimensional (2D) hybrid perovskite structures with good moisture stability.[37,58,59,186,258,259] The 2D perovskites have a generic formula of $(RNH_3)_2(A)_{n-1}BX_{3n+1}$ (n is an integer which represents the number of perovskite layers), where RNH_3 is a primary aromatic or aliphatic alkylammonium cation functioning as a spacer between the perovskite layer, the A and B cations and X anions form the perovskite framework.[61,259] There have been a few successful attempts to synthesize multilayered hybrid perovskites for the solar cell applications.[36,37,260] Recently, Tsai *et al.* reported the highest PCE (12.52%) for lower dimensional perovskite (n=4) solar cells by modifying thin film deposition method, where BA was used as a spacer cation.[260] Even though PCE was significantly improved in those devices, moisture stability was still not satisfactory retaining only 20% of original PCE for over 24 hours stored in 65% relative humidity (RH). We believe that it is mainly because of hygroscopic nature of relatively smaller sized BA molecules. Zhang *et al*. further improved the PCE of BA-based 2D perovskite solar cells by cesium doping reporting a record PCE of 13.7% for the lower dimensional perovskite devices.[200] In another example, Kanatzidis *et al*. designed a new type of 2D perovskites with alternating cations (MA and guanidinium) in the interlayer space (named as ACI perovskites). [85] The devices fabricated using ACI perovskites yielded a PCE of 7.23%, but the device stability data are not available at present. There have been several attempts to synthesize 2D perovskites using different ammonium spacer cations such as histammonium, benzylammonium, and hexylammonium ions, *etc.*[79,261,262] Unfortunately, solar cells fabricated using these materials showed deficient photovoltaic performance.

The first report on 2D perovskite solar cells using $(C_6H_5(CH_2)_2NH_3)_2(CH_3NH_3)_2Pb_3I_{10}$ ($(PEA)_2(MA)_2Pb_3I_{10}$) as light absorber showed a low efficiency (4.73%) with large hysteresis.[36] Here, we prepared high quality $(PEA)_2(MA)_{n-1}Pb_n\ I_{3n+1}$ perovskite films (n= 3, 4) by modifying the deposition method and device architecture. We chose conductive organic materials as charge carrier selective layers in a planar solar cell configuration that can be easily scaled up for roll-to-roll fabrication of solar cells.[263–266] The excitonic nature of charge carriers in 2D perovskite limits the thickness of $(PEA)_2(MA)_{n-1}Pb_nI_{3n+1}$ film for the solar cell application. The optimization of solar absorber layer thickness was found to be critical in obtaining highly efficient 2D perovskite devices with very low hysteresis. We also investigated the superior stability of PEA-based 2D perovskite

through a series of characterizations, such as X-ray diffraction (XRD) analysis, absorption measurements, charge-carrier lifetime measurements and thermogravimetric analysis (TGA).

3.2 Results and Discussion

3.2.1 Film Fabrication and Characterization

High-quality perovskite films were obtained by hot cast method (Figure 3.S1).[260,267] Scanning electron micrograph (SEM) of hot cast 2D perovskite films (n = 3, 4) show that pin-hole free films with large crystalline grains are formed (Figure 3.1a and 3.1b). The quality of perovskite films starts to deteriorate as the number of perovskite layers increases to n=5. Figure 3.1c shows a poor coverage of $(PEA)_2(MA)_4Pb_5I_{16}$ (n=5) on the substrate, which would potentially deteriorate device performance. The previous studies show that a simple one-step spin coating of DMF-based 3D perovskite precursors did not yield a homogenous perovskite film.[192,268,269] The crystallization direction largely depends on the type of organic cations present in the precursor as well as the solvent used to prepare the precursor solution. For example, the presence of MAI in the perovskite precursor prepared in dimethylformamide (DMF) encourages a rapid crystal growth along the c-crystallographic axis, leading to formation of inhomogeneous perovskite film. On the other hand, the 2D perovskites (n=1, 2, 3, 4) crystalize as plates on the top of the glass substrate with good surface coverage because the crystallization along a-b crystallographic axes occurs more rapidly than the c axis, unlike 3D perovskites.[36] In short, the organic species in $(PEA)_2(MA)_4Pb_5I_{16}$ (n=5) mostly composed of MAI (MAI: 66% and PEAI: 34%) led to the formation of less homogeneous perovskite film, which is evident from SEM and AFM images (Figure 3.1c and Figure 3.S1f). With conventional room temperature spin coating, smaller crystalline grains are formed because of quick evaporation of DMF before the crystallization of the perovskites, which also leads to the incomplete coverage of perovskite on the substrate. It has been hypothesized that, when a substrate is maintained above the crystallization temperature of perovskite during spin coating, a prolonged crystal growth is promoted due to the presence of an excess solvent during the crystallization.[267] In conventional spin coating, not fully crystallized intermediate perovskite phase is deposited, and complete perovskite crystallization only occurs during the post-annealing step. The perovskite crystal growth is thus limited in the conventional post-annealing step of perovskite film due to nearly total evaporation of the solvent before complete perovskite crystallization. On the other hand, the presence of excess solvent during the crystallization offers more time for larger crystal growth in the hot cast method. Here, we kept the substrate at a temperature (140 ℃) well below the boiling temperature of DMF (152-154℃) to

avoid any significant evaporation of solvent, which is yet high enough to favor the perovskite crystal growth. Schematic representation of the crystal structure of 2D perovskites (n = 3, 4, 5) is shown in the inset of Figure 3.1a-3.1c. The crystal structure of 2D perovskite film is investigated by grazing incidence X-ray diffraction (GIXRD) technique. The major diffraction peaks were observed at 14.10° and 28.76°, corresponding to diffraction planes (111) and (202), respectively (Figure 3.1d, 3.1e and 3.1f). More diffraction peaks emerge at 24.45°, 31.78°, 40.48° and 42.92° in the XRD pattern (Figure 3.1f) of the $(PEA)_2(MA)_4Pb_5I_{16}$ film, similar to the diffraction pattern of the 3D perovskite.[270] The hot cast 2D perovskite films $(PEA)_2(MA)_3Pb_4I_{13}$ and $(PEA)_2(MA)_4Pb_5I_{16}$) exhibit more intense (111) diffraction peaks than the conventional, spin-coated films, indicative of the formation of a preferential oriented crystalline grains in $(PEA)_2(MA)_3Pb_4I_{13}$ and $(PEA)_2(MA)_4Pb_5I_{16}$) films on the glass substrate.[267] Highly oriented perovskite layers are beneficial for 2D perovskite solar cells because 2D perovskite films with random crystal structure orientation would reduce the charge carrier mobility in the film due to the presence of non-conductive spacer layers. The full-width at half-maximum (FWHM) of the (111) crystalline plane is considerably reduced from 0.58° to 0.34° and 0.61° to 0.41° for the $(PEA)_2(MA)_3Pb_4I_{13}$ and $(PEA)_2(MA)_4Pb_5I_{16}$ films, respectively, when the hot cast method was employed. It suggests that the crystals in hot cast (n=4, 5) films are larger than those in conventional spin coated films.

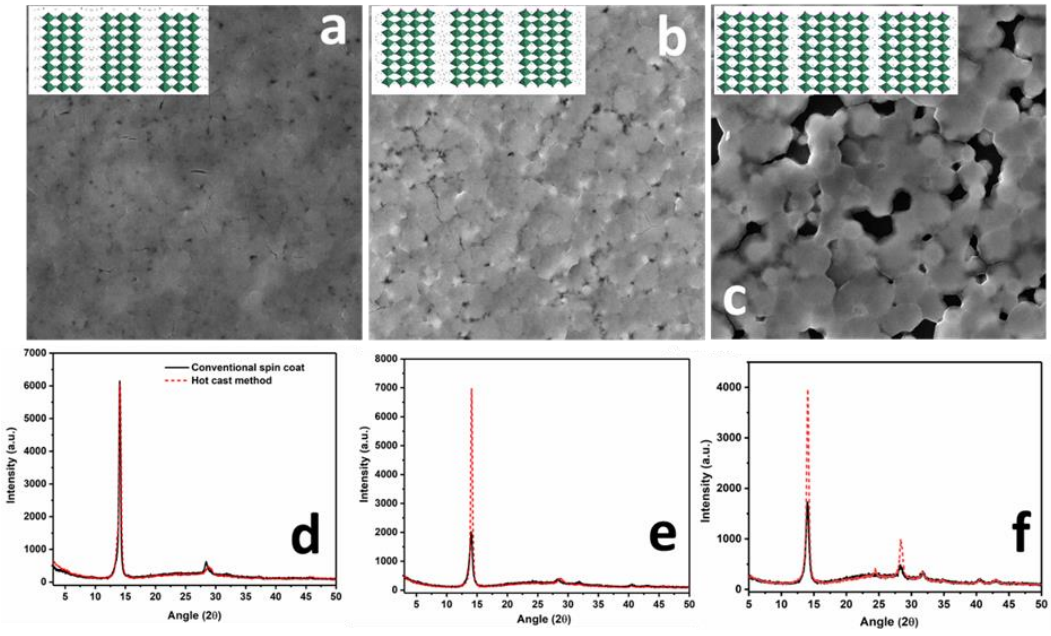

Figure 3.1 SEM micrographs of hot cast a) $(PEA)_2(MA)_2Pb_3I_{10}$, b) $(PEA)_2(MA)_3Pb_4I_{13}$ and c) $(PEA)_2(MA)_4Pb_5I_{16}$ films (schematic representation of the crystal structures of 2D perovskites are shown in the inset) and GIXRD analysis of d) $(PEA)_2(MA)_2Pb_3I_{10}$, e) $(PEA)_2(MA)_3Pb_4I_{13}$ and f) $(PEA)_2(MA)_4Pb_5I_{16}$ films.

Interestingly, we did not observe any changes in the intensity or FWHM of the (111) crystalline plane for the hot cast $(PEA)_2(MA)_2Pb_3I_{10}$ (n=3) film compared to conventional spin coated film (Figure 3.1d). These results indicate that stoichiometric ratio of organic species present in the perovskite precursor influences the crystal growth direction.[37] The crystal structure of 2D perovskite film is investigated by grazing incidence X-ray diffraction (GIXRD) technique. The major diffraction peaks were observed at 14.10° and 28.76°, corresponding to diffraction planes (111) and (202), respectively (Figure 3.1d, 3.1e and 3.1f). More diffraction peaks emerge at 24.45°, 31.78°, 40.48° and 42.92° in the XRD pattern (Figure 3.1f) of the $(PEA)_2(MA)_4Pb_5I_{16}$ film, similar to the diffraction pattern of the 3D perovskite.[270] The hot cast 2D perovskite films $(PEA)_2(MA)_3Pb_4I_{13}$ and $(PEA)_2(MA)_4Pb_5I_{16}$) exhibit more intense (111) diffraction peaks than the conventional, spin-coated films, indicative of the formation of a preferential oriented crystalline grains in $(PEA)_2(MA)_3Pb_4I_{13}$ and $(PEA)_2(MA)_4Pb_5I_{16}$) films on the glass substrate.[267] Highly oriented perovskite layers are beneficial for 2D perovskite solar cells because 2D perovskite films with random crystal structure orientation would reduce the charge carrier mobility in the film due to the presence of non-conductive spacer layers. The full-width at half-maximum (FWHM) of the (111) crystalline plane is considerably reduced from 0.58° to 0.34° and 0.61° to 0.41° for the $(PEA)_2(MA)_3Pb_4I_{13}$ and $(PEA)_2(MA)_4Pb_5I_{16}$ films, respectively, when the hot cast method was employed. It suggests that the crystals in hot cast (n=4, 5) films are larger than those in conventional spin coated films. Interestingly, we did not observe any changes in the intensity or FWHM of the (111) crystalline plane for the hot cast $(PEA)_2(MA)_2Pb_3I_{10}$ (n=3) film compared to conventional spin coated film (Figure 3.1d). These results indicate that stoichiometric ratio of organic species present in the perovskite precursor influences the crystal growth direction.[37] An in-depth crystallography measurement using 2D grazing incidence wide-angle X-ray scattering (2D-GIWAXS) imaging provides more understanding about the crystalline orientation as well as crystallization process of 2D perovskites (Figure 3.2).[260] For example, the hot cast $(PEA)_2(MA)_2Pb_3I_{10}$ (n=3) film displays sharp and discrete Bragg spots compared to Debye−Scherrer rings with an isotropic intensity distribution observed in conventional spin coated film (Figure 3.2a and 3.2b). Sharp and discrete Bragg spots at $q_z \approx 10$ nm^{-1} indicate that (111) crystalline planes are parallel to the substrate. With further increasing n (>3), preferential orientation of the crystalline plane becomes weaker (Figure 3.2d and 3.2f). Interestingly, 2D-GIWAXS images show that crystallization is not complete in the conventional spin coated 2D perovskite films. In general, a simple thermal annealing at 100 ℃ for 20 min results in the high purity halide perovskite crystalline phase. The bright streaks located at $q_z \approx 9$ nm^{-1} and 11 nm^{-1} in Figure 3.2a, 3.2c and 3.2e represent diffraction from the PbI_2 and crystalline precursor

(crystallized mixture of PEA(I), MAI and PbI_2) respectively.[254,271] In contrast, a complete crystallization of 2D perovskite has occurred in hot cast films evident from the absence of any diffraction spots at $q_z \approx 9$ nm^{-1} and 11 nm^{-1}. The GIWAXS crystallography measurement suggests that crystallization kinetics are very different, depending on the film deposition process.

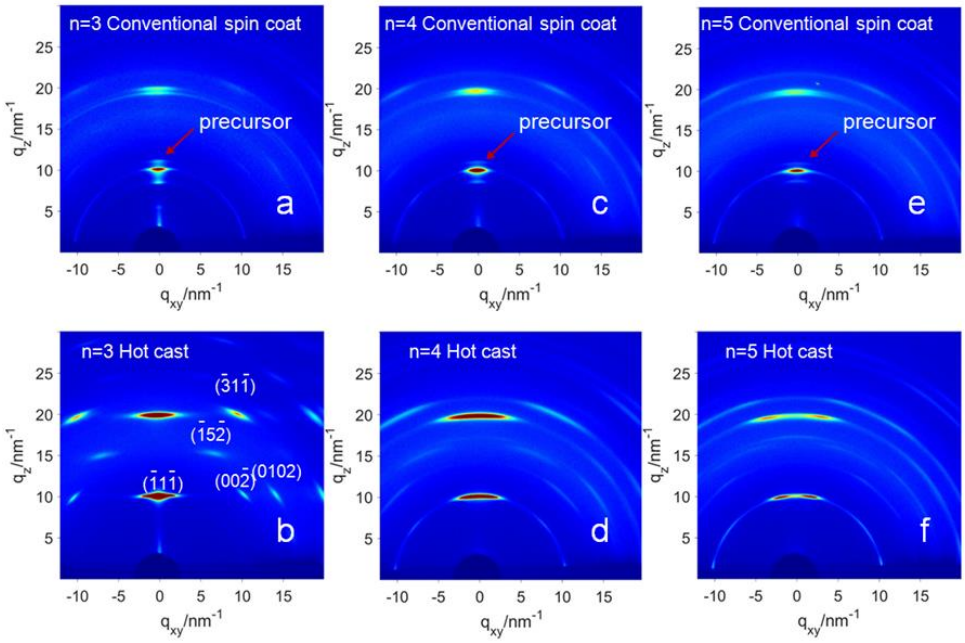

Figure 3.2 GIXWAS images of a) conventional spin coated $(PEA)_2(MA)_2Pb_3I_{10}$ film, b) hot cast $(PEA)_2(MA)_2Pb_3I_{10}$ c) conventional spin coated $(PEA)_2(MA)_3Pb_4I_{13}$ d) hot cast $(PEA)_2(MA)_3Pb_4I_{13}$ e) conventional spin coated $(PEA)_2(MA)_4Pb_5I_{16}$ and f) hot cast $(PEA)_2(MA)_4Pb_5I_{16}$.

The absorption onset and steady-state photoluminescence (PL) peaks of hot cast $(PEA)_2(MA)_2Pb_3I_{10}$ (n=3), $(PEA)_2(MA)_3Pb_4I_{13}$ (n=4) and $(PEA)_2(MA)_4Pb_5I_{16}$ (n=5) films coincide at 1.65 eV, 1.64 eV and 1.63 eV, respectively, representing the optical band gaps of these semiconductors (Figure 3.3 a-3.3b). In addition to the primary absorption peak, we also observed two additional peaks at 2.05 eV and 2.18 eV, which gradually subside as the number of perovskite layers increases.[37] These secondary absorption peaks are ascribed to small-n phases present in 2D perovskites.[272] We also noticed that the absorbance had been considerably enhanced when precursor solution was allowed to crystallize at a higher temperature (Figure 3.S2), highly likely due to the formation of high purity crystalline phase as revealed by 2D-GIWXAS measurements.[273]

Time-resolved PL spectroscopy is used to monitor the decay of photo-excited charge carriers to understand charge carrier recombination processes (interband relaxation, radiative bimolecular recombination, and trap-assisted recombination) in the 2D perovskite films (Figure 3.3c).[267] The

PL lifetime is significantly extended for all the hot cast 2D perovskite films compared to conventional spin coated films, which may be correlated to the reduction of recombination processes (Figure 3.S3).[161] More specifically, the PL average lifetime is increased from 24 ns to 43 ns for $(PEA)_2(MA)_2Pb_3I_{10}$ film, 11 ns to 21 ns for $(PEA)_2(MA)_3Pb_4I_{13}$ film and 5 ns to 14 ns for $(PEA)_2(MA)_4Pb_5I_{16}$ film with the use of the hot cast method. The elongation in the PL lifetime can be attributed to the reduction of defects and disorders at grain boundaries. We also noticed that reduction in PL lifetime as the number of perovskite layers is increased (from 43 ns to 14 ns). The less homogeneous perovskite film coverage on glass substrates results in an increased charge carrier recombination rate that causes a reduction in PL lifetime.

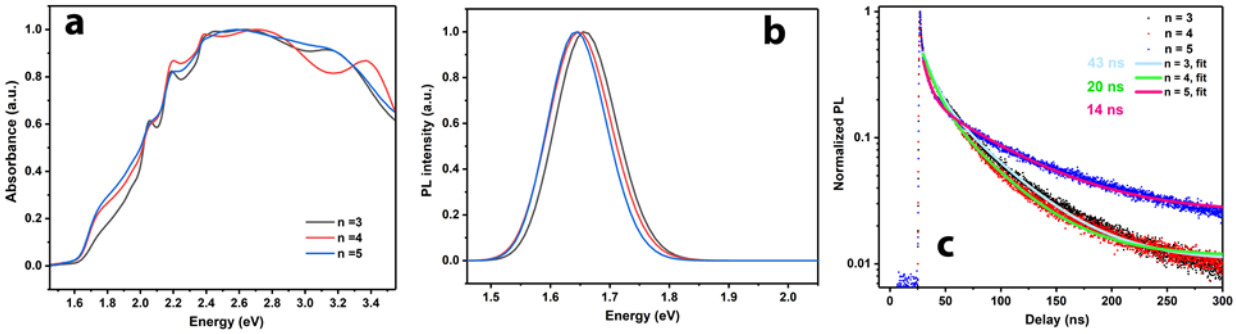

Figure 3.3 a) Absorbance and b) PL of 2D perovskite films, c) time-resolved PL of hot cast 2D perovskite films.

3.2.2 Device Performance

PCE of lower dimensional perovskite devices is significantly improved when the hot cast method was employed. The optimization of perovskite absorber layer thickness is crucial in accomplishing high efficiency in planar 2D perovskite devices (Figure 3.S4), and optimum thickness was found to be around 240-260 nm. Table 2.1 compares the photovoltaic parameters of 2D perovskite devices fabricated by both hot cast method and conventional spin coating method. Short-circuit current density (J_{sc}) has greatly enhanced for all the hot cast 2D perovskite devices as a result of enhanced absorption of photons and the orientation of perovskite crystals (n=4, 5). The large crystals along with good surface coverage in hot cast film led to reduced interfacial charge trapping and fewer bulk defects, resulting in an improvement in fill factor (FF) and open-circuit voltage (V_{oc}) for the solar cells. For example, atomic force microscopy (AFM) image (Figure 3.S1e) shows small grains with poor film coverage for the conventional spin coated $(PEA)_2(MA)_4Pb_5I_{16}$ (n=5) film. The corresponding device showed low FF (47.88%) whereas it is improved by 14.22% to 55.82% when the hot cast method is used. In the case of

$(PEA)_2(MA)_3Pb_4I_{13}$ devices, FF is improved from 54.40% to 56.50% (by 3.7%) and V_{oc} from 0.91 V to 1.02 V (by 10.78%).

Among all the lower dimensional perovskites, $(PEA)_2(MA)_3Pb_4I_{13}$ devices showed the best photovoltaic performance. All the photovoltaic parameters are better in the hot cast $(PEA)_2(MA)_3Pb_4I_{13}$ devices, which exhibit an improved average PCE of 5.50% vs. 3.92% for the conventional spin coated $(PEA)_2(MA)_3Pb_4I_{13}$ devices. We performed J-V measurements at different scan directions (Figure 3.4a), and scan rates (Figure 3.4b) and low J-V hysteresis was observed for $(PEA)_2(MA)_3Pb_4I_{13}$ devices, suggesting photovoltaic operation reliability of these devices. We also calculated J_{SC} from external quantum efficiency (EQE) measurements of $(PEA)_2(MA)_3Pb_4I_{13}$ device (Figure 3.4c), which is correlated with J_{SC} obtained from the J-V curve. Perovskite film quality, such as trap density, surface coverage, and roughness, plays a very important role in determining PCE of planar perovskite devices. Hot cast $(PEA)_2(MA)_3Pb_4I_{13}$ films result in improved J_{sc}, $V_{oc,}$ and FF for the corresponding devices. Although the $(PEA)_2(MA)_4Pb_5I_{16}$ film has a slightly lower optical band gap, its short-circuit behavior due to the poor surface coverage caused the lower efficiency than that of $(PEA)_2(MA)_3Pb_4I_{13}$ devices. A shorter PL lifetime was observed for the $(PEA)_2(MA)_4Pb_5I_{16}$ film as compared to other 2D perovskite films signifying an its relatively higher charge carrier recombination rate due to its less homogeneous surface coverage. Conversely, the higher optical band gap along with higher excitonic nature of charge carriers in the $(PEA)_2(MA)_2Pb_3I_{10}$ film as compared to $(PEA)_2(MA)_3Pb_4I_{13}$ result in its lower PCE (4.58% vs. 5.5%).

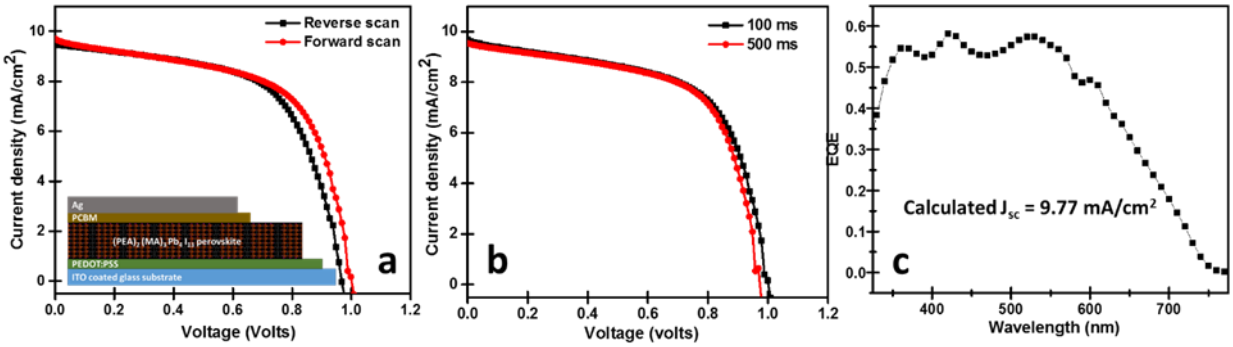

Figure 3.4 J-V measurements of $(PEA)_2(MA)_3Pb_4I_{13}$ device at different a) scan directions and b) scan rates, and c) EQE measurement of $(PEA)_2(MA)_3Pb_4I_{13}$ device.

3.2.3 Stability of 2D perovskites

From hereafter, the $(PEA)_2(MA)_3Pb_4I_{13}$ perovskite is designated as 2D perovskite unless otherwise specified. To investigate moisture stability, we stored un-encapsulated 2D perovskite

devices in the dark at 72±2% RH. The half-life of these devices was found to be ~90 hours (Figure 3.5a).

Table 3.1 Average photovoltaic parameters of 2D perovskite solar cells

Number of perovskite layers [n]	Deposition technique	J_{sc} [mA/cm^2]	V_{oc} [Volt]	FF [%]	Average Efficiency [%]
3	Conventional method	6.73	1.04	49.24	3.44
	Hot cast method	8.71	1.02	51.47	4.58
4	Conventional method	7.96	0.91	54.40	3.92
	Hot cast method	9.64	1.02	56.50	5.50
5	Conventional method	8.14	0.87	47.88	3.40
	Hot cast method	8.45	1.00	55.82	4.80

In contrast, the half-life of 3D perovskite devices was found to be much shorter, ~ 10 hours. Interestingly, the PCE of 2D perovskite devices is initially increased by 10% after moisture exposure. Figure 3.5b shows thermal stability of 3D and 2D perovskite devices kept at 100℃ in the inert atmosphere (N_2). In the case of 3D perovskite devices, PCE drops to less than 20% of the initial performance after 24 hours. 2D perovskite solar cells show excellent thermal stability, retaining 65% of the initial PCE after 70 hours.

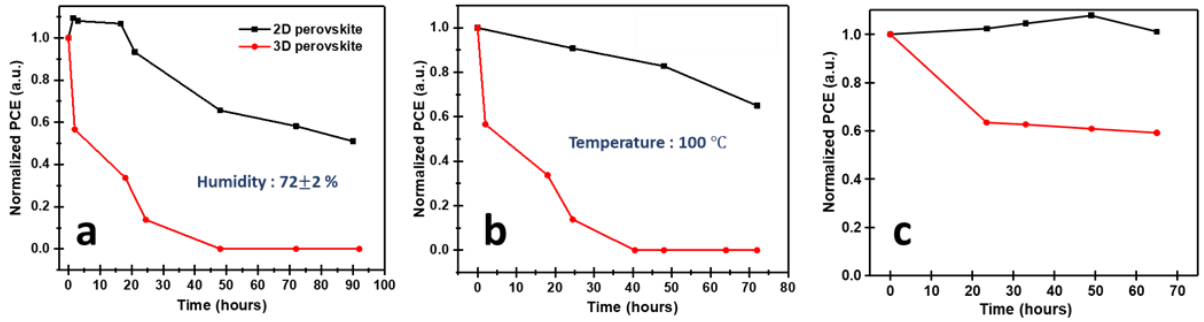

Figure 3.5 a) Moisture stability testing at 72±2% RH, b) thermal stability testing at 100℃ and c) photostability testing under constant AM 1.5G illumination of unencapsulated $(PEA)_2(MA)_3 Pb_4 I_{13}$ and 3D perovskite solar cells.

Figure 3.5c demonstrates the photostability of perovskite devices tested for 65 hours in the inert atmosphere and PCE remains almost constant for 2D perovskite while 3D perovskite retains only

60% of the initial PCE. Figure 3.S5 shows changes in photovoltaic parameters with respect to time under different harsh environmental conditions. To understand the moisture stability of 2D perovskite, we analyzed changes in the XRD pattern of perovskite films stored in 72±2% RH (Figure 3.6a). A peak corresponding to PbI_2 at 12.7° starts to emerge in the 2D perovskite film after ten days of intense moisture exposure. In contrast, 3D perovskite starts to show the sign of degradation after three days (Figure 3.S6). Moreover, we did not observe any obvious declination in the absorbance of the 2D perovskite film even after 23 days in 72±2% RH (Figure 3.6b). On the other hand, consistently absorbance of the 3D perovskite film is significantly reduced especially in the visible region of the solar spectrum after four days in 72±2% RH, indicating major degradation of the material (Figure 3.S6). We have also observed relatively unchanged absorption in the wavelength range of 400-425 nm, where PbI_2 absorbs, for the 3D perovskite film.

To understand the distinctive feature of the PCE enhancement after few hours of humidity exposure shown by 2D perovskite devices, we monitored changes in the PL lifetime of 2D perovskite films deposited on the glass substrate. It was observed that PL lifetime of the 2D perovskite film is significantly increased with moisture exposure (Figure 3.6c). The PL lifetime is improved from 21 ns to 49 ns after 24h hours of moisture exposure. Further, the perovskite film stored in the moisture shows a monoexponential decay curve after 24 hours indicating that only trap-assisted recombination is dictating the recombination process in the perovskite film. It is hypothesized that with the help of humidity defects and disorders at the grain boundaries in the perovskite films are passivated resulting in an improvement in efficiency. This study of moisture effects on recombination processes points out that moisture may be used in the fabrication of 2D perovskite solar cells smartly to enhance their photovoltaic performance. It has been reported that hydrogen bonding between water molecules and the MA cations leads to transformation of 3D perovskite structure into 2D sheets separated by water molecules and, finally, into isolated PbI_6^{4-} octahedra.[248,274,275] We propose that in the current investigation PEA cations intercalated in between perovskite layers can prevent direct exposure of the MA cations to water molecules; so, perovskite layers are nanoencapsulated that accounts for stability enhancement. Nonetheless, even though the PEA cations are less hygroscopic than MA cations, they are still susceptible to water molecules which eventually lead to the slow degradation of 2D perovskites. This is evident from the emergence of a peak, corresponding to PbI_2, in the XRD pattern after exposure to the moisture. But absorbance measurements show that material degradation is very minimal and doesn't primarily affect photovoltaic performance as in the case of 3D perovskites. The degradation of perovskites in the device is much more complicated. For example, interfacial layers

can accelerate the degradation of the perovskite in the device, and metal electrodes can corrode upon aging causing device failure.[276,277]

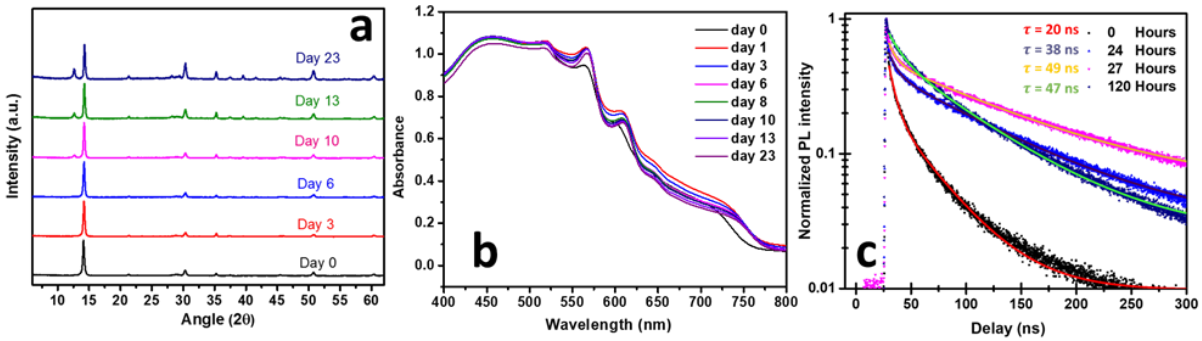

Figure 3.6 a) XRD pattern, b) absorption spectra and c) PL decay of $(PEA)_2$ $(MA)_3$ Pb_4I_{13} film stored in 72±2% RH.

The exceptional thermal stability of the 2D perovskite was uncovered by investigating the thermal behavior of precursors and perovskites using TGA. We initially anticipated superior thermal behavior for PEAI compared to MAI, resulting in an excellent thermal stability for $(PEA)_2(MA)_3Pb_4I_{13}$. But TGA plots reveal that the thermal behavior of PEAI is similar to that of MAI (Figure 3.7a, 3.7b, and inset of Figure 3.7c). We determined the enthalpy of sublimation (ΔH_{sub}) and sublimation temperature (T_{sub}) from a linear least-squares fitting of the TGA isotherm data (Equation S1). The calculated ΔH_{sub} and T_{sub} values from log ($m\ T^{1/2}$) vs. 1/T plot are listed in Table 3.2, where m is the slope of the mass loss obtained from each isotherm at constant temperature (T) (Figure 3.S7). Figure 3.7c shows the TGA curves for the 3D and 2D perovskite powder. The two mass loss steps observed in the first derivative of the TGA curves for perovskite (Figure 3.7d) correspond to the liberation of organic and inorganic species, respectively.[249,278] The inset of Figure 3.7c shows a comparison of TGA heating curves of organic species (MAI and PEAI) and perovskite powders, where mass loss step of MAI occurs more quickly when it is inside the 3D perovskite matrix. But in the presence of PEAI in the perovskite matrix, a noticeable delay has been observed in the sublimation of organic species. TGA curves of the perovskites confirm that different decomposition pathways occur when the PEA cation is incorporated into the perovskite structure that essentially points to the superior thermal behavior of the 2D perovskite.

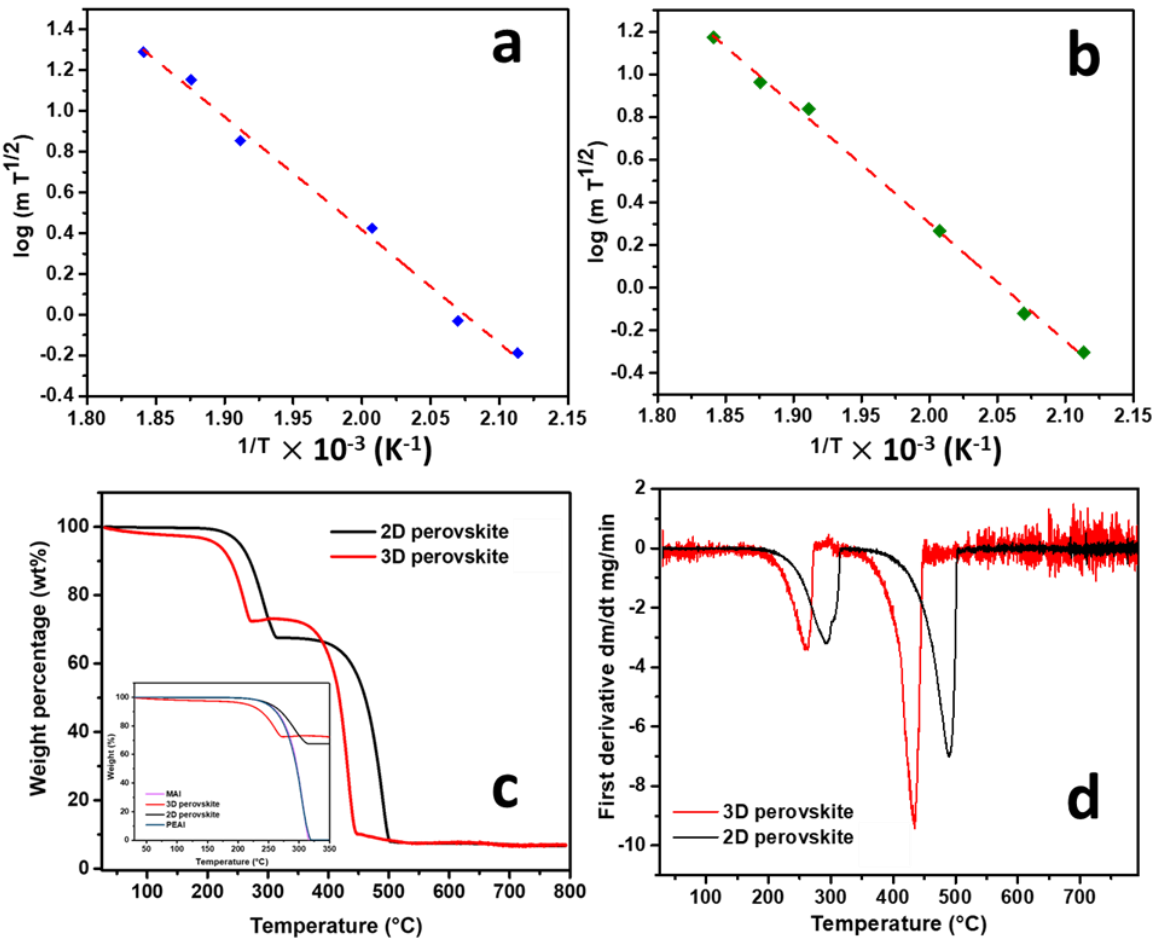

Figure 3.7 Calculated log (m $T^{1/2}$) vs. 1/T for a) MAI and b) PEAI used to determine ΔH_{sub} and T_{sub} from TGA isotherms, c) TGA heating curves for perovskite powders (a comparison of TGA heating curves of organic species and perovskite powders is shown in the inset) and d) corresponding first derivatives for the perovskite powders.

Table 3.2 ΔH_{sub} and T_{sub} of MAI and PEAI estimated from a linear least-squares fitting of the TGA isotherms

Precursor	**ΔH_{sub} [kJ mol^{-1}]**	**T_{sub} [℃]**
MAI	106±4	220±8
PEAI	105±3	217±5

3.3 Conclusions

In this work, we demonstrate that large aromatic alkylammonium halide based 2D perovskite solar cells with an average PCE of 5.5% show high tolerance against heat and moisture. The incorporation of larger organic PEA cations into the perovskite framework can largely influence not only the photovoltaic properties but also the stability of the perovskites. Highly crystalline 2D perovskite films without any detectable, un-reacted precursors are achieved by employing hot cast method as compared to conventional spin coating technique, resulting in an enhanced efficiency. 2D-GIWAXS measurements show a complete conversion of precursors into 2D perovskites when the hot cast method is employed. The number of perovskite layers of 2D perovskites was optimized to achieve the highest PCE solar cells. Moreover, the $(PEA)_2(MA)_3Pb_4I_{13}$ device demonstrates excellent stability under harsh environmental conditions. For instance, these devices show excellent tolerance against moisture, maintaining more than 50% of their initial performance for over 90 hours in 72±2% relative humidity. In contrast, the efficiency of 3D perovskite devices drops to less than 10% of the initial performance after 24 hours. Time-resolved PL measurements indicate that oxygen or water molecules can help passivating defects at grain boundaries of the PEA-based 2D perovskite when the device is operated under moisture environment. The device is also capable of retaining 65% of their initial performance for over 70 hours at 100℃, while 3D perovskites wholly degrade after 40 hours under heat stress. Also, these 2D perovskites show no noticeable degradation for over 70 hours under constant AM 1.5G illumination in an inert atmosphere. The work provides physical insights into the further development of highly stable 2D perovskite solar cells.

3.4 Experimental section

Materials: Methylammonium iodide (CH_3NH_3I) and phenylethylammonium iodide ($C_6H_5(CH_2)_2NH_3I$) were purchased from Dyesol. Dimethylformamide (DMF), γ-butyrolactone (GBL), dimethyl sulfoxide (DMSO) and toluene were purchased from Sigma Aldrich. Lead iodide (PbI_2) was bought from Acros Organics. Phenyl-C61-butyric acid methyl ester ($PC_{61}BM$) and poly(3, 4-ethylenedioxythiophene)-poly(styrene sulfonate) (PEDOT:PSS; Clevios™ P VP AI 4083) were obtained from 1-Materials and Heraeus respectively. All chemicals were used as received.

Perovskite Precursor Solution Preparation: 2D perovskite (n= 3, 4, 5) precursor solutions were prepared by mixing stoichiometric ratios of methylammonium iodide (MAI), phenylethylammonium iodide (PEAI) and PbI_2 in DMF. For n=3 precursor solution, MAI, PEAI, and PbI_2 were mixed in a molar ratio of 2:2:3 in DMF. For n=4 and n=5 precursor solutions, MAI, PEAI, and PbI_2 were mixed

with molar ratios of 3:2:4 and 4:2:5, respectively, in DMF. The 3D perovskite (n=∞) precursor solution was prepared by mixing PbI_2 with MAI in a molar ratio of 1:1 in GBL: DMSO (7:3) mixture with a PbI_2 concentration of 1.26 M. All precursor solutions were stirred overnight at 70℃ before spin coating on a glass substrate. 2D perovskite solutions were prepared at different PbI_2 concentrations varying from 0.15 M to 0.40 M to optimize the solar absorber film thickness.

Device Fabrication: Patterned ITO-coated glasses were cleaned by sonication in detergent followed by sequential washing with deionized water, acetone, and isopropanol. After drying under air flow, the substrate surface was cleaned by oxygen plasma for 10 min under rough vacuum. The PEDOT: PSS solution was spin-coated on top of an ITO-coated glass substrate at 5000 rpm for 60 s; PEDOT: PSS performs as the hole transporting layer. The PEDOT: PSS film was then dried in air on a hot plate (set at 150 °C) for 15 min. After drying, the substrate is transferred to a nitrogen-filled glovebox for further use. The perovskite absorber layer was spin coated on the top of PEDOT: PSS film. In the conventional spin coating method, the 2D perovskite precursor solution was spin-coated at 4000 rpm for 45s on the substrate at room temperature. In the hot cast method, the substrate was preheated at 140℃ for 10 min; subsequently, the hot substrate was immediately transferred to the spin coater chuck, and the 2D perovskite precursor solution was spin-coated at 5000 rpm for 20s on it [260]. To deposit 3D perovskite films, previously reported solvent engineering method was employed [192]. Then the $PC_{61}BM$ solution (20 mg/mL in chlorobenzene) was spin-coated on top of the perovskite film at 1000 rpm for 45 s to form a 20 nm thick electron transporting layer. Finally, the whole device was transferred to a thermal evaporation chamber inside the nitrogen filled glove box. The chamber was pumped down to 1×10^{-7} Torr for silver deposition. The 100 nm thick silver top electrode was deposited through a shadow mask that defines the active device area as 0.06 cm^2 for the solar cells.

Perovskite Film Characterization: Topography of perovskite film surface was obtained by using Bruker MultiMode8 AFM. SEM micrographs were acquired using a Jeol JSM-6300FSEM. The absorption spectra were collected by using a Lambda 750, UV-Visible-NIR spectrometer (Perkin Elmer). Steady-state PL spectra were obtained from a Fluorolog®-3 system (Horiba Jobin Yvon). The PL lifetime was measured using the Time-correlated single-photon counting (TCSPC) mode with a 444 nm laser as an excitation source. GIXRD measurements were carried out using a Panalytical X-Pert PRO MRD X-Ray diffractometer. The grazing incidence wide angle X-ray scattering (GIWAXS) measurements were carried out at the BL14B1 beamline of Shanghai Synchrotron Radiation Facility (SSRF). The 2D-GIWAXS patterns were collected by a MarCCD detector which is mounted vertically at a distance of around 194 mm from the sample, the

exposure time is less than 50 sec and a grazing incidence angle with respect to the surface plane is 1°. The 2D-GIWAXS patterns were analyzed afterward using the Fit 2D software and displayed in scattering vector q coordinates with $q = 4\pi\sin\theta/\lambda$, where θ is half of the diffraction angle, and λ is the incident X-ray (0.124 nm) wavelengths.

Solar cell characterization: Solar cell performance was measured using a class ABA LED solar simulator which was calibrated to deliver simulated AM 1.5 sunlight at an irradiance of 100 mW/cm^2 (The irradiance was calibrated using an NREL-calibrated KG5 filtered silicon reference cell). Current–voltage curves were recorded using a source meter (Keithley 2400, USA). External quantum efficiency (EQE) measurement was conducted by using an IQE200B system (Newport Corporation).

Device stability tests: The stability of 2D and 3D perovskites devices was tested in the same device configuration without any encapsulation. For moisture stability tests, the 2D and 3D perovskite devices were placed inside a desiccator and humidity was controlled by saturated NaCl solution. The relative humidity was measured with a digital humidity sensor. For photo stability tests, the 2D and 3D perovskite devices were placed under constant AM1.5G illumination inside the N_2 filled glovebox. Thermal stability of devices was tested by placing samples on a hot plate set at 100℃ inside the N_2 filled glovebox.

Thermal Analysis: The thermal behavior of the organic materials and perovskite powder was recorded using a TGA (Q500) (TA Instruments). To prepare the perovskite powder, the precursor solution was spin coated onto glass substrates. The perovskite powder was scratched off the substrate and used directly for the thermal analysis. In order to determine decomposition pathway of perovskite and precursors, TGA was performed at a heating rate of 5℃ min^{-1} under a constant 20 mL min^{-1} He gas flow. The investigated temperature interval was between 30 °C, and 800 °C. Approximately 10−25 mg of sample was employed for each TGA measurement.

Supporting Information

Supporting Information is available from the Wiley Online Library or from the author.

Acknowledgements

Financial support from the Natural Sciences and Engineering Research Council (NSERC) of Canada, in the context of a NSREC Discovery Grant and a NSERC Strategic Grant (Industry

partner: Canadian Solar Inc.) is greatly appreciated. D. Ma is also grateful for the financial support from Quebec Center for Functional Materials (CQMF), Canada. D.T.G acknowledges scholarship support from the Fonds de recherche du Québec—Nature et technologies (FRQNT) under the Programme de Bourses d'Excellence (Merit Scholarship Program for Foreign Students). The authors thank beamline BL14B1 at Shanghai Synchrotron Radiation Facility (SSRF) for providing the beam time.

Supporting Information

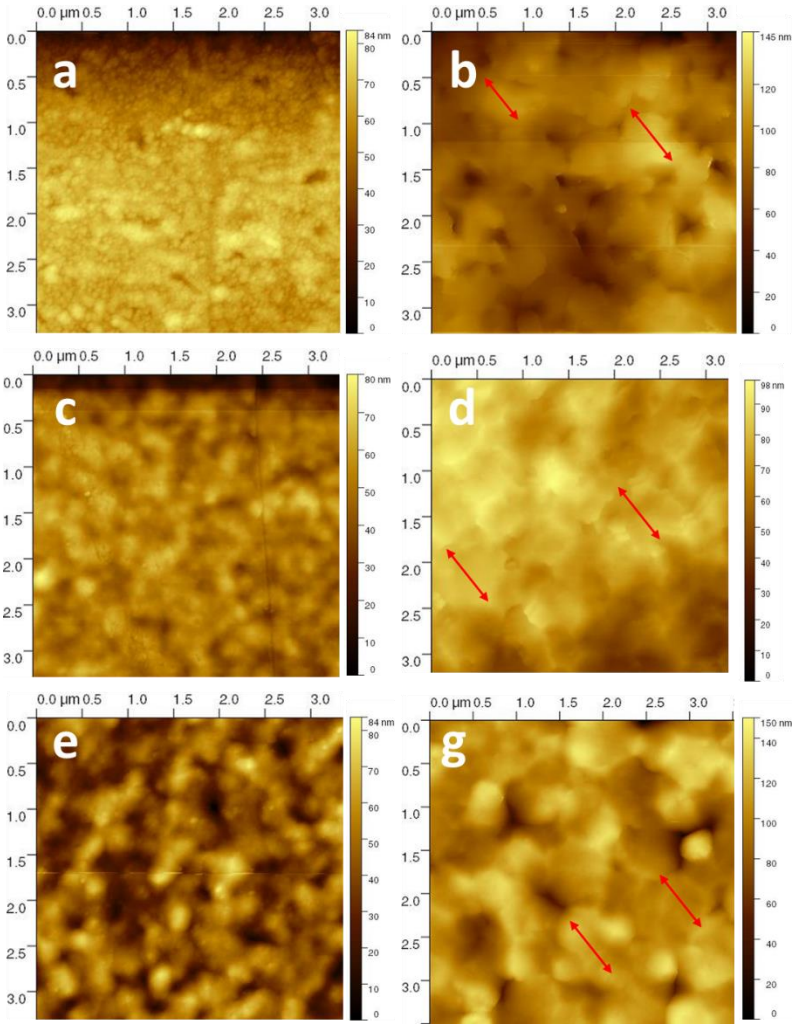

Figure 3.S1 Topography of a) room temperature cast and b) hot cast $(PEA)_2(MA)_2Pb_3I_{10}$ (n=3) films, c) room temperature cast and d) hot cast $(PEA)_2(MA)_3Pb_4I_{13}$ (n=4) films, and e) room temperature cast and f) hot cast $(PEA)_2(MA)_4Pb_5I_{16}$ (n=5) films. The large crystalline grains are marked in the figures.

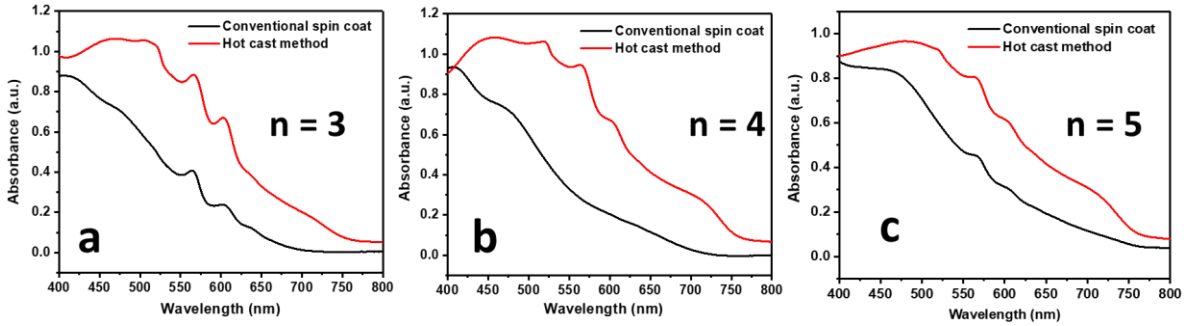

Figure 3.S2 Comparison of absorption spectra of conventional spin coated and hot cast 2D a) $(PEA)_2(MA)_4Pb_5I_{16}$ (n=3), b) $(PEA)_2(MA)_3Pb_4I_{13}$ (n=4) and c) $(PEA)_2(MA)_4Pb_5I_{16}$ (n=5) films.

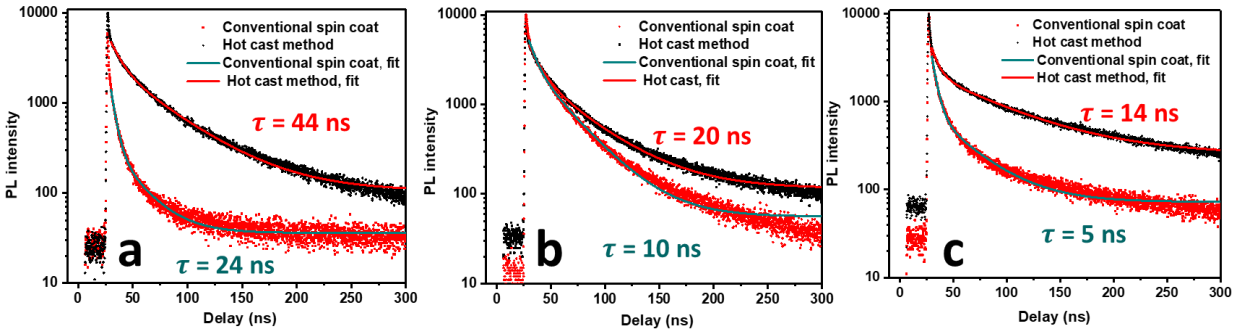

Figure 3.S3 Comparison of time-resolved PL of the hot cast and conventional spin coated a) $(PEA)_2(MA)_4Pb_5I_{16}$, b) $(PEA)_2(MA)_3Pb_4I_{13}$ and c) $(PEA)_2(MA)_4Pb_5I_{16}$ films.

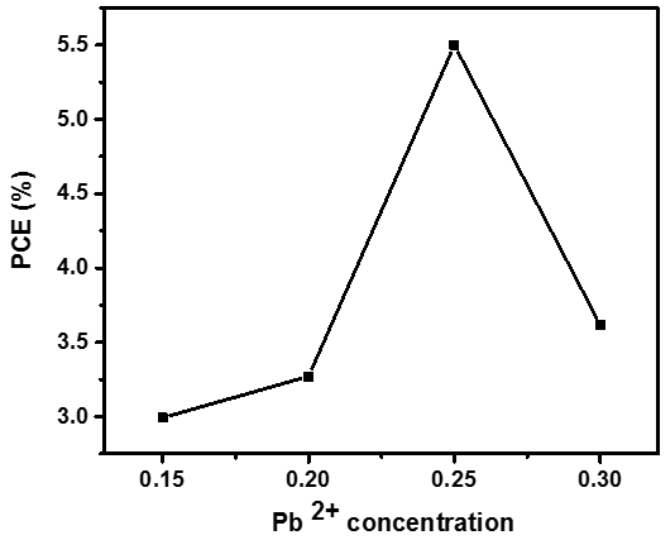

Figure 3.S4 Device PCE as a function of precursor concentration for the $(PEA)_2(MA)_3Pb_4I_{13}$ perovskite solar cells.

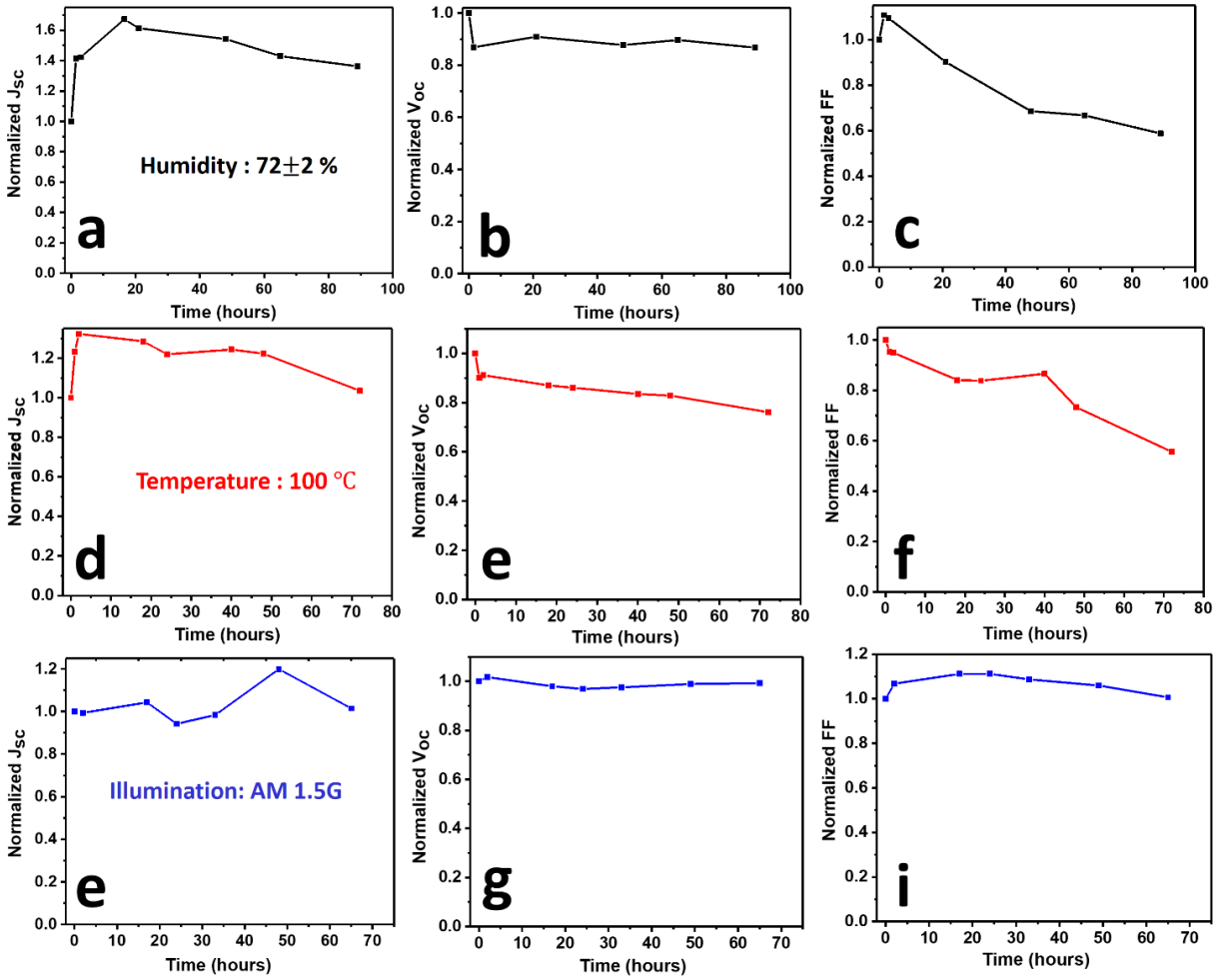

Figure 3.S5 Stability of unencapsulated $(PEA)_2(MA)_3Pb_4I_{13}$ devices: a) current density b) open-circuit voltage c) fill factor at 72±2% RH, d) current density e) open-circuit voltage f) fill factor at 100℃, and e) current density g) open-circuit voltage i) fill factor under constant AM 1.5G illumination.

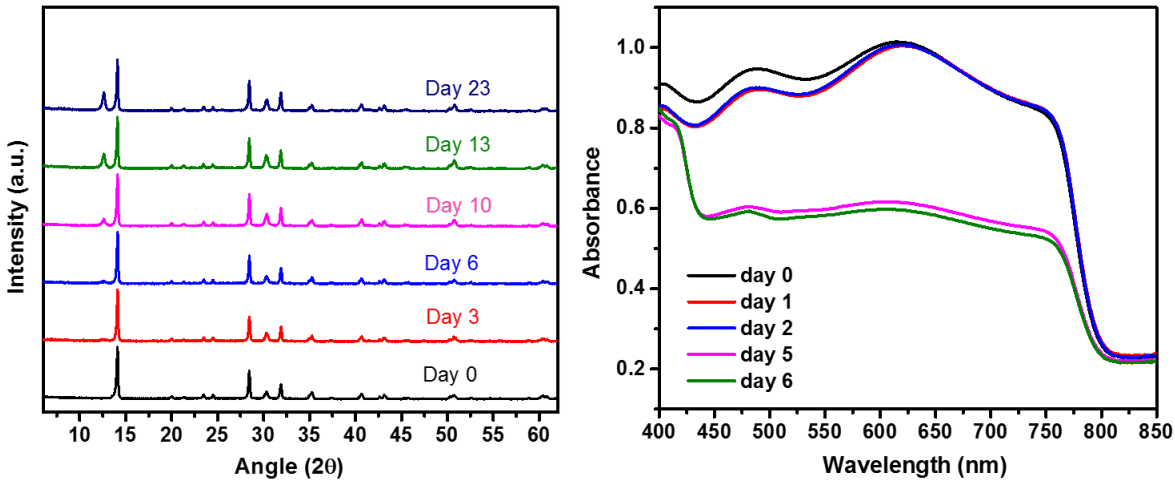

Figure 3.S6 a) XRD pattern and b) absorption spectra of 3D perovskite film stored in 72±2% RH.

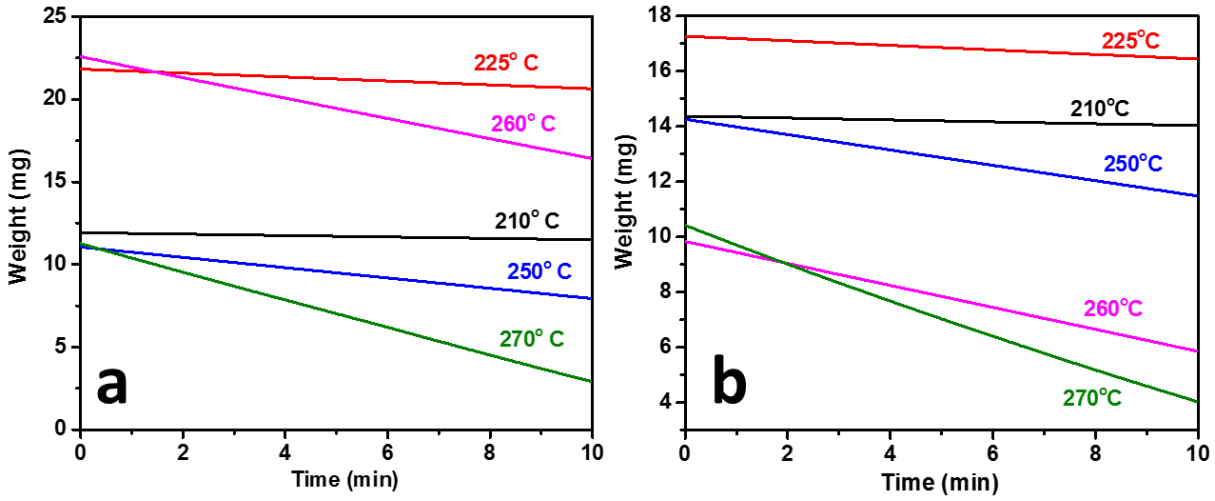

Figure 3.S7 Multiple isotherms for 10 min of a) PEAI and b) MAI.

Thermal analysis of precursors: Figure 3.S7 shows the mass loss as a function of time at different isotherm regions for PEAI and MAI. For each isotherm, the slope of the mass loss (m) is determined.

The enthalpy of sublimation (ΔH_{sub}) and sublimation temperature (T_{sub}) are calculated from log (m $T^{1/2}$) vs. 1/T plot. The linear slope of

$$log\ (m\ T^{1/2}) = -\frac{-0.0522\ (\Delta Hsub)}{T} + \left[\frac{0.0522\ (\Delta Hsub)}{Tsub} - \frac{1}{2} log\ (\frac{1306}{Mw})\right] \qquad \textit{(Equation S1)}$$

log (mT $^{1/2}$) vs. 1/T plot yields H_{sub}. In addition, the y-intercept of such a plot provides a value for T_{sub}.

4 EFFECTS OF AROMATIC ALKYLAMMONIUM SPACER CATIONS IN HALIDE ALLOYED PEROVSKITES

Title of the article: Reducing non-radiative recombination in Pb-less halide perovskite films by incorporating bulky phenylethylammonium cations

French translation: Réduction de la recombinaison non radiative dans les couches de pérovskite sans halogénure de Pb en incorporant des cations phényléthylammonium volumineux

Authors:

Authors' names: Deepak Thrithamarassery Gangadharan, Pandeng Li, Qingzhe Zhang, Fan Yang, Ricardo Izquierdo, Baoquan Sun, Maurizia Palummo, Giacomo Giorgi, Dongling Ma

Title of the journal or book:

ACS Applied Energy Materials, Manuscript submitted on 07 November 2019.

Contribution of the authors:

Deepak Thrithamarassery Gangadharan and Dongling Ma conceived the experiments. Deepak Thrithamarassery Gangadharan conducted material synthesis, material characterizations, solar cell fabrication and device characterizations. Pandeng Li conducted the synchrotron and surface potential experiments. Qingzhe Zhang conducted XPS measurements. Fan Yang conducted PL measurements. Deepak Thrithamarassery Gangadharan wrote original draft of the manuscript. Dongling Ma supervised the project. Giacomo Giorgi did the theoretical calculations. Maurizia Palummo, Baoquan Sun, Ricardo Izquierdo provided advise and expertise. All authors contributed to the final version of the manuscript.

Link between the previous article or articles and the following:

The previous chapter has shown that 2D perovskites employing bulky cations are resistant against moisture and oxygen, but at the expense of PCE of the solar cell. This chapter explores the effects of substituting a small amount of A-site organic cations in Sn-Pb alloyed perovskites with PEA cations. The amount of added PEA was optimized to increase both PCE and stability simultaneously. Here, a variety of alloyed Sn-Pb perovskites was used to reduce the amount of toxic Pb in the device. The incorporation of PEA in Sn-Pb perovskites contributed to the increase

in crystallinity and reduction of non-radiative recombination by lowering the number of defects associated with Sn vacancies.

4.1 Introduction

Halide perovskites adopt the ABX_3 general stoichiometric relation, where A = methylammonium ($MA=CH_3NH_3^+$), formamidinium ($FA={}^+HC(NH_2)_2$), caesium (Cs) and/or rubidium (Rb); B= lead (Pb) and/or tin (Sn); X= chlorine (Cl), bromine (Br) and/or iodine (I).[279] In recent years, halide perovskites (hereafter simply *perovskites*), mainly the hybrid organic-inorganic peorvskites [2] but also the all-inorganic perovskites,have attracted the major research interest in the photovoltaic community mainly because of their simple solution deposition fabrication process, rapidly increasing and high power conversion efficiencies (PCEs) and fascinating optical and electronic properties, including tunable bandgap from 1.15 to 3.06 eV by swapping different cations and halides in the perovskite structure.[194,197,280,281]

The state-of-the-art perovskite solar cells (PSCs) involve water-soluble Pb species, which hamper the commercialization of this technology.[21] Once in contact with water or moisture, Pb perovskites easily form water-soluble by-products of Pb, which can accumulate within the food chain and so human body.[23] It is thus highly necessary to restrict the use of Pb by replacing it partially or completely with less toxic or, even better, non-toxic metals. Most likely, appropriate candidates for Pb replacement without compromising too much photovoltaic properties are elements in the same group (group 4) as Pb. The immediate candidates then appear as Sn and Ge, both of which, however, can be more easily oxidized from the 2^+ to 4^+ oxidation states than Pb. Computational studies have shown that the electronic configuration of Pb^{2+} in the ABX_3 perovskite structure is crucial for its remarkable photovoltaic behavior.[24,25,282,283] Therefore, although Sn-based perovskites are highest-performing lead-free solar cells in terms of PCE,[26,27] the fact that Sn is more stable in the 4^+ oxidation state causes critical stability issues.[284] Meanwhile, they still show much lower photovoltaic performances than Pb perovskites because of the formation of Sn vacancies associated with the oxidation of Sn^{2+} to Sn^{4+}. These vacancies act as nonradiative recombination centers in Sn-based perovskites.[284,285] Sn-based PSCs thus demonstrate subpar open-circuit voltage (V_{oc}) mainly due to severe trap-assisted recombination triggered by Sn vacancy-mediated unintentional doping/defects.[286] Different approaches including morphological control of the Sn perovskites, minimization of oxygen exposure during the device preparation, and the addition of Sn salts, have been explored and found to be useful in improving the performance of Sn-based PSCs. Recently, Wang *et al.* reported one of the Sn PSCs with an efficiency of 9.41% by employing quasi-two-dimensional (2D) Sn perovskites, which however is still falling far short of Pb PSCs.[28] On the other hand, alloying Pb with Sn perovskites seems to be a promising, balanced strategy towards achieving stable, less toxic solar cells without much compromising the

photovoltaic performance.[287] Moreover, alloyed Sn-Pb perovskites bring an added advantage, extended absorption of photons to the near-infrared (NIR) spectral range (up to 1050 nm with an optical bandgap of 1.18 eV). In contrast, typical hybrid organic-inorganic halide perovskites such as $MAPbI_3$, $FAPbI_3$ and $FASnI_3$ lack absorption in the NIR range because of their relatively higher optical bandgaps of 1.55 eV (up to 800 nm), 1.48 eV (up to 838 nm) and 1.30 eV (up to 950 nm), respectively.[204] Unfortunately, the performance of Sn-Pb perovskites is limited by the mentioned $Sn^{2+} \rightarrow Sn^{4+}$ oxidation. The most successful strategy for inhibiting such detrimental process has been the incorporation of SnF_2 into Sn-based perovskites. However, even with an optimum amount of SnF_2, the trap-assisted recombination coefficient, which is defined as a specific rate at which oppositely charged ions combine at traps, is ~ 70 times higher than those in Pb-based ones.[288] It suggests a prospect of improving the performance of Sn-Pb alloyed PSCs by reducing the defects associated with oxidation of Sn^{2+} to Sn^{4+} and/or Sn vacancy formation.

More recently, several groups including ours have shown that 2D perovskites employing bulky cations are resistant against moisture and oxygen, but at the expense of PCE of the solar cell.[37,39,171,200] Herein, we explore the suppression of defects formation through substituting small organic cations in alloyed perovskites with bulky organic cations for the first time with the purpose of increasing both PCE and stability simultaneously. To be more specific, different compositions of Sn-Pb alloyed perovskites are realized by stoichiometrically mixing $FASnI_3$ and $MAPbI_3$ (labelled as FA/MA alloyed perovskites).[287] By substituting FA/MA with bulkier PEA cations in alloyed perovskites (labelled as PEA-FA/MA alloyed perovskites), we suppressed the oxidation of Sn^{2+} during the thin film preparation. By employing them as a solar absorber, a significant reduction of trap-assisted recombination was achieved in the device, therefore, a dramatic improvement of 40% in photovoltaic performance for Sn-rich PSCs. Notably, theoretical calculations suggest that the formation energy of Sn vacancies (under Sn-rich conditions, same as our experimental conditions) in Sn-based PEA containing perovskites (PEA_2SnI_4) is quantitatively larger than the formation energy for Sn vacancies in FA containing Sn-based perovskites ($FASnI_3$). More intriguing is the fact that hypothetical mixed $(PEA_{1-x}FA_x)_2SnI_4$ perovskites we assembled and optimized have shown an even lower tendency of Sn vacancy formation. Thus, assuming a reduced impact of the metal ion nature on the B-site vacancy formation energy for PEA- and FA-based perovskites and PEA/FA mixed ones, our results support the fact that less defects are likely to form in those Sn-Pb perovskite films characterized by the co-presence of both short (FA) hydrophilic and long (PEA) hydrophobic organic cations. The reduction in the number of defects and also increase of the crystallinity in PEA-FA/MA perovskites were supported by X-ray diffraction (XRD) and synchrotron radiation techniques,

photoluminescence measurements and elemental composition analysis by X-ray photoelectron spectroscopy (XPS) of the perovskite materials. It is worth noting that, we did not detect any 2D perovskite formation in the material after incorporating bulky PEA in the alloyed perovskites, as evidenced by XRD and synchrotron-based structural characterization, either due to the very low concentration of PEA we added herein or PEA might just act as an additive in the perovskite at lower concentration without forming any 2D perovskite phases in the material. During the preparation of this manuscript, we found few reports using different bulkier organic cations to improve performance and stability of alloyed perovskites. But these reports rely on altering the crystal orientation of perovskite layers through in-situ growth of 2D perovskite phases to improve the solar cell performance. On the other hand, our work provides new physical insight about the reduction of Sn defect formation upon incorporation of PEA molecules in Sn-Pb perovskites which is strongly supported by experimental results and theoretical calculations. We tested photovoltaic properties of a series of $(PEA)_y$ $(FA_x\ MA_{1-x})_{1-y}\ Sn_x\ Pb_{1-x}\ I_3$ (y= 0, 0.05 and 0.1, x=0.3, 0.5, and 0.7) compositions and found that the highest average PCE of $13.60 \pm 0.69\%$ was obtained for $PEA_{0.05}FA_{0.3}MA_{0.7}Sn_{0.3}Pb_{0.7}I_3$ devices. Our strategy simultaneously addresses another major drawback of Sn-based perovskites, i.e., the inferior stability under ambient environment. The PEA-FA/MA alloyed PSCs showed better stability (half-life, $t_{1/2}$ = 200 h) under $28 \pm 2\%$ RH humidity compared to that of control FA/MA alloyed PSCs ($t_{1/2}$ = 80h). The defects formed in the course of perovskite film preparation can be detrimental to the stability of the PSCs. So, minimizing the defects in Sn-Pb perovskites improves the stability. The defects also play a detrimental role in current density-voltage (J-V) curve hysteresis in PSCs through defect migration at grain boundaries (GBs) and perovskite film interfaces. By reducing the number of defects in PEA-FA/MA perovskite films as verified by surface potential measurements, we eliminated the J-V hysteresis in the derived PSCs whereas FA/MA PSCs exhibited significant J-V hysteresis.

4.2 Results and discussion

The optical absorption onsets of $(FASnI_3)_x$ $(MAPbI_3)_{1-x}$ and $(PEA)_y$ $(FA_x\ MA_{1-x})_{1-y}\ Sn_x\ Pb_{1-x}\ I_3$ (x= 0, 0.3, 0.5, 0.7 and 1) were determined from ultraviolet-visible (UV-Vis) absorption measurements (Figure 4.1a and 4.S1).

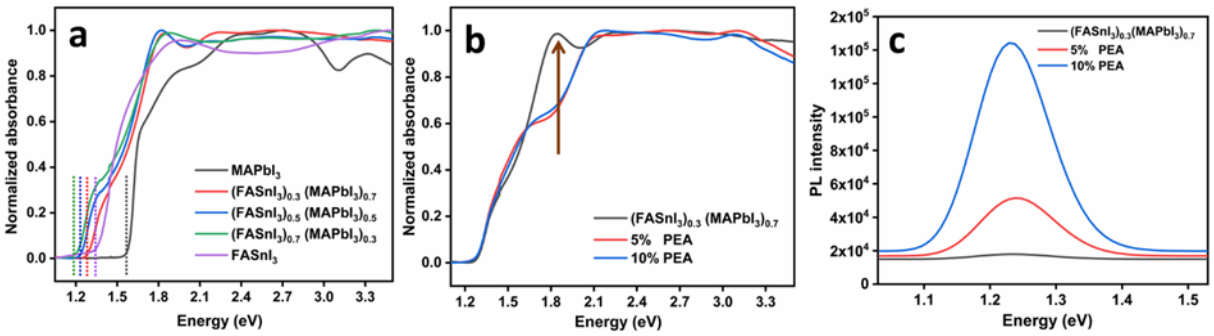

Figure 4.1. a) UV-vis absorption spectra of FA/MA perovskite films and comparison of b) absorption spectra and c) steady-state photoluminescence (PL) spectra of FA/MA perovskite vs. PEA-FA/MA perovskite films, $(PEA)_y\ (FA_{0.3}\ MA_{0.7})_{1-y}\ Sn_{0.3}\ Pb_{0.7}\ I_3$. Dotted lines in a) denote absorption onsets of perovskites.

Mixed Sn-Pb perovskites show the shift of the absorption onset to the NIR region compared to pure Pb (x=0) or Sn (*x*=1) perovskites. The lowest was 1.18 eV for $(FASnI_3)_{0.7}\ (MAPbI_3)_{0.3}$, followed by 1.22 eV for $(FASnI_3)_{0.5}\ (MAPbI_3)_{0.5}$ and 1.26 eV for $(FASnI_3)_{0.3}\ (MAPbI_3)_{0.7}$, as marked by dotted lines in Figure 4.1a. Substituting FA/MA with small amount of PEA does not change optical absorption onset considerably (Figures 4.1b and 4.S1). But we noticed a change in the shape of the optical absorption spectra as well as optical absorption intensity. Interestingly, the peak located at ~1.85 eV (marked with an arrow in the absorption spectrum) of FA/MA alloyed perovskites disappeared for PEA-FA/MA alloyed perovskites.[289] In general, the peak close to the optical absorption edge is ascribed to the bound excitonic state due to the Columbic attraction of electrons and holes (the hydrogenic absorption peak). In our case the peak is located (at 1.85 eV) significantly distant from the absorption onsets (at 1.18 eV, 1.22 eV, 1.26 eV), which basically excludes the hydrogenic absorption origin of the peak. The change in the shape of absorption spectra could be associated with excitonic properties of PEA-FA/MA alloyed perovskites and more detailed studies focusing on photogenerated species in low bandgap, alloyed perovskites are needed to understand this peculiar feature.[290]

The optical bandgaps obtained from PL measurements match well with the absorption onsets observed in the absorption spectra, indicative of the direct bandgap nature in $(PEA)_y\ (FA_x\ MA_{1-x})_{1-y}\ Sn_x\ Pb_{1-x}\ I_3$ materials (Figure 4.S2a). Further, we compared the PL intensity of FA/MA alloyed perovskites with PEA-FA/MA alloyed perovskites in Figure 4.1c and Figure 4.S2 (b-c). A noticeable enhancement in PL intensity was observed after stoichiometrically replacing FA/MA partially with PEA in alloyed perovskites. Essentially, the more PEA is introduced, the higher the PL intensity. Such an observation indicates the decrease of defects in the PEA-FA/MA alloyed perovskites, which otherwise serve as charge recombination sites. This finding is also consistent

with previously theoretical results that clearly show the integration of bulky cations in perovskite structure caused the increase of PL of perovskites.

The topography of alloyed perovskite films obtained by atomic force microscopy (AFM) is shown in Figure 4.2. Essentially pin-hole free, dense alloyed perovskite films were formed in all the samples. However, a gradual increase in crystal grain size was noticed as the Sn content in alloyed perovskites increased. With the incorporation of PEA, the alloyed perovskite film surface showed a plate-like feature, being more evident at a higher PEA concentration (10%). Consistently, a noticeable reduction in the root mean square (RMS) roughness was observed with respect to control samples. Our observation is in line with previous reports, which showed that incorporation of PEA would encourage perovskites to crystallize as plates because the crystallization along *a-b* crystallographic axes occurs more rapidly than that along the c-axis.[171]

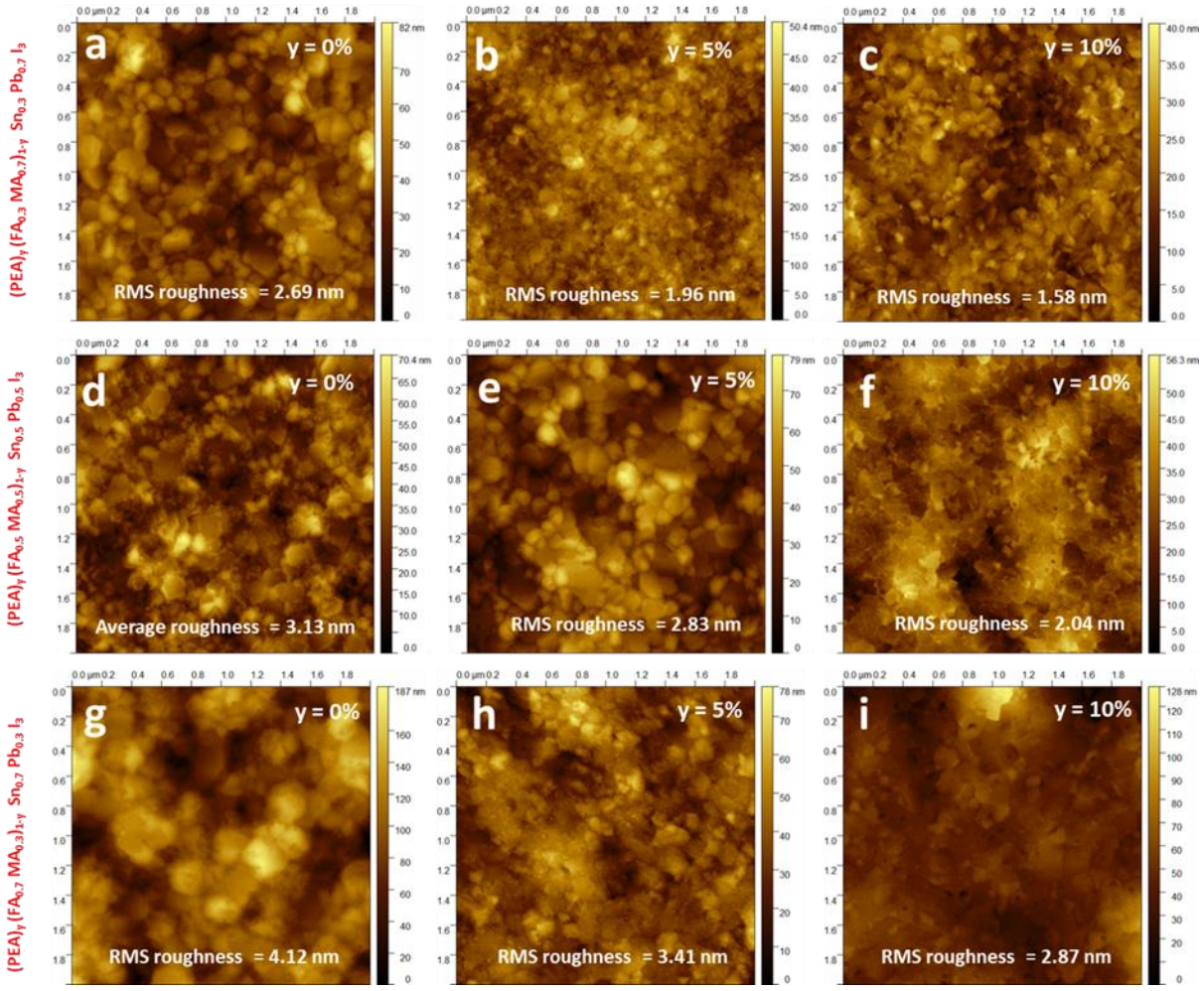

Figure 4.2. AFM height topographical images of (a-c) $(PEA)_y$ $(FA_{0.3}MA_{0.7})_{1-y}$ $Sn_{0.3}$ $Pb_{0.7}$ I_3 (y=0% (a), 5% (b) and 10% (c)), (d-f) (PEA)y $(FA_{0.5}MA_{0.5})_{1-y}$ $Sn_{0.5}$ $Pb_{0.5}$ I_3 (y=0% (a), 5% (b) and 10% (c)), (g-f) (PEA)y $(FA_{0.7}MA_{0.3})_{1-y}$ $Sn_{0.7}$ $Pb_{0.3}$ I_3 (y=0% (a), 5% (b) and 10% (c)).

Energy-dispersive X-ray spectroscopy (EDS) studies reveal that Sn and Pb are homogenously distributed throughout the alloyed perovskite films and there is no observable phase separation in these films (Figures 4.S3 and 4.S4).

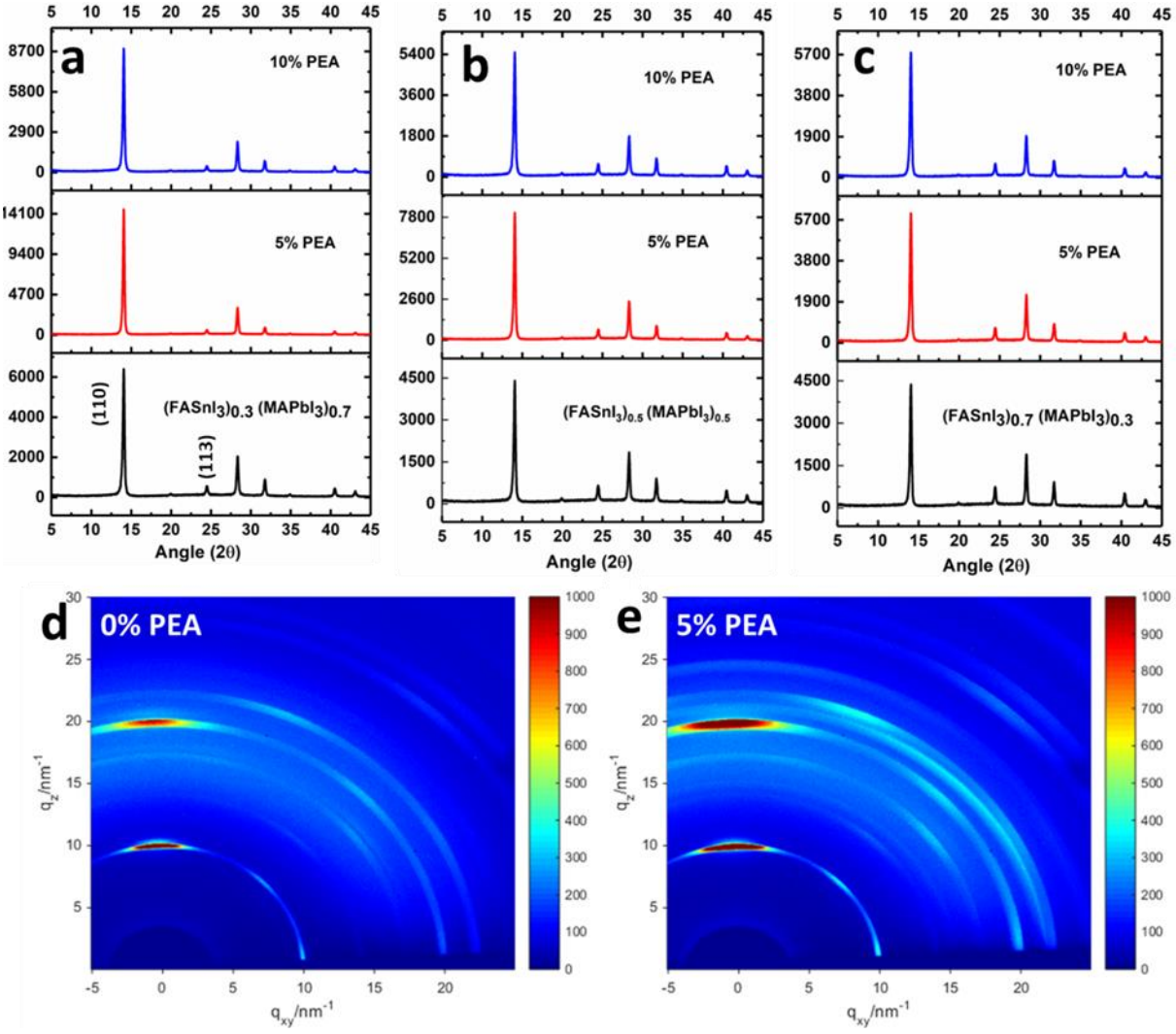

Figure 4.3. θ-2θ XRD spectra of different compositions of FA/MA and PEA-FA/MA perovskites: a) $(PEA)_y$ $(FA_{0.3}MA_{0.7})_{1-y}$ $Sn_{0.3}$ $Pb_{0.7}$ I_3, b) $(PEA)_y$ $(FA_{0.5}MA_{0.5})_{1-y}$ $Sn_{0.5}$ $Pb_{0.5}$ I_3 and c) $(PEA)_y$ $(FA_{0.7}MA_{0.3})_{1-y}$ $Sn_{0.7}$ $Pb_{0.3}$ I_3, and GIWAXS patterns of d) $(FASnI_3)_{0.3}$ $(MAPbI_3)_{0.7}$ and e) $(PEA)_{0.05}$ $(FA_{0.3}MA_{0.7})_{0.95}$ $Sn_{0.3}$ $Pb_{0.7}$ I_3 films.

We characterized the crystalline structure of alloyed perovskites by θ-2θ XRD. As shown in Figure 4.S5, $FASnI_3$ has only one peak, within the 2θ range of 22°-25° , indexed to the (113) plane in the orthorhombic A*mm*2 space group whereas $MAPbI_3$ exhibits two peaks in the same range indexed to the (211) and (202) planes in the tetragonal (*I4 cm*) space group.[291] The θ-2θ XRD spectra of alloyed perovskites (Figure 4.3a-4.3c) display only one peak within the 2θ range of 22°-25°, which

strongly suggests that alloyed perovskites adopt the orthorhombic crystal structure.[292] Moreover, it seems that Sn and Pb atoms randomly occupy the metal sites of corner-sharing ($[Sn_{1-x}Pb_xI_6]^{-4}$) octahedra.[293] The crystal structure is unchanged after replacing a small quantity of FA/MA cations by PEA cations in PEA-FA/MA alloyed perovskites. The bulky organic cations like PEA are typically used to synthesis 2D perovskites, but we did not observe any low angle peaks (2θ <10°) corresponding to low dimensional perovskites as well as absorption onsets, so we can reasonably conclude that there is no experimentally observable 2D perovskite phase formation when a low amount of PEA incorporated in the material. The intensity of the XRD peaks, in particular the (110) peak at 14.1°, notably increased for all the alloyed perovskites with the introduction of PEA, which could be due to a higher crystallinity of the alloyed perovskite and/or better film coverage on the substrate.

We further probed the change in the crystal size by tracking the variation in the full width at full width at half maximum (FWHM) of the θ-2θ XRD peak located at 14°corresponding to the (110) crystalline plane (Figure 4.S6). The FWHM dropped from 0.239° to 0.214° and from 0.246° to 0.230° in $(FASnI_3)_{0.3}$ $(MAPbI_3)_{0.7}$ and $(FASnI_3)_{0.5}$ $(MAPbI_3)_{0.5}$ when FA/MA were substituted with 5% of PEA, respectively. The change in FWHM correlates to local strain and crystallinity. The decrease of FWHM implies increase in the crystallinity as well as reduced lattice strain. Especially, reduction of FWHM of XRD peak located at (110) signifies lowering lattice strain along the inorganic bonding direction of I-Pb-I, I-Sn-I. But further integration of PEA to 10% caused an increase of the FWHM, which however was still below that of PEA-free sample. It is clear that 5% PEA integration can produce highly crystalline alloyed perovskites among $(PEA)_y$ $(FA_{0.3}MA_{0.7})_{1-y}$ $Sn_{0.3}Pb_{0.7}I_3$, $(PEA)_y$ $(FA_{0.5}MA_{0.5})_{1-y}$ $Sn_{0.5}Pb_{0.5}I_3$ (y=0%, 5%, and 10%) compositions. On the contrary, the Sn-rich composition showed a different trend. The FWHM gradually increased with the amount of PEA (5 and 10%) in $(FASnI_3)_{0.7}$ $(MAPbI_3)_{0.3,}$ suggesting in this case PEA introduction led to decrease in the crystallinity.

Grazing-incidence wide-angle X-ray scattering (GIWAXS) measurements were also conducted. GIWAXS further confirms that the 5% PEA incorporation improves the crystallinity. The GIWAXS pattern of $(FASnI_3)_{0.3}$ $(MAPbI_3)_{0.7}$ and $(PEA)_{0.05}$ $(FA_{0.3}MA_{0.7})_{0.95}$ $Sn_{0.3}Pb_{0.7}I_3$ films are illustrated in Figure 4.3d and 4.3e, respectively. The latter exhibits more intense Bragg reflection at q = 10.0 nm^{-1} and 20 nm^{-1} with respect to the former, implying enhanced crystallinity for PEA-FA/MA alloyed perovskites and consistent with XRD results (Figure 4.3a-4.3c). An additional Bragg reflection at 21.5 $nm^{-1,}$ observed only for PEA-FA/MA alloyed perovskites, corresponds to the crystalline phase of SnF_2.[294] We assume that overall enhancement of the crystallinity in PEA-

FA/MA alloyed perovskites also accentuated the Bragg reflection related to the SnF_2 crystalline phase.

To investigate the role of PEA cations in preventing the oxidation of Sn^{2+} in alloyed perovskites, XPS measurements were carried out (Figure 4.S7, Figure 4.4a and 4.4b). For the $(FASnI_3)_{0.3}$ $(MAPbI_3)_{0.7,}$ the Sn $3d_{5/2}$ peak (located at 486.08 eV) could be well deconvoluted into two peaks located at 485.75 eV and 486.3 eV, corresponding to Sn^{2+} and Sn^{4+} oxidation states (Figure 4.4a). Likewise, the Sn $3d_{3/2}$ peak (located at 495.41 eV) comprised of two peaks located at 494.27 eV and 494.71 eV, associated with Sn^{2+} and Sn^{4+} oxidation states.[285] In contrast, the $(PEA)_{0.05}$ $(FA_{0.3}$ $MA_{0.7})_{0.95}$ $Sn_{0.3}$ $Pb_{0.7}$ I_3 only shows two sharp, non-deconvolutable peaks, with no Sn^{4+} peaks. The XPS spectra of $(PEA)_{0.05}$ $(FA_{0.7}$ $MA_{0.3})_{0.95}$ $Sn_{0.7}$ $Pb_{0.3}$ I_3 perovskites also showed similar behavior compared to their control samples (Figure 4.S7). The oxidation of Sn^{2+} to Sn^{4+} is a strong indication of the formation of Sn vacancies in Sn-based perovskites, which are the dominant defects in Sn-based perovskites due to their low defect formation energy among all the point defects.[295–297]

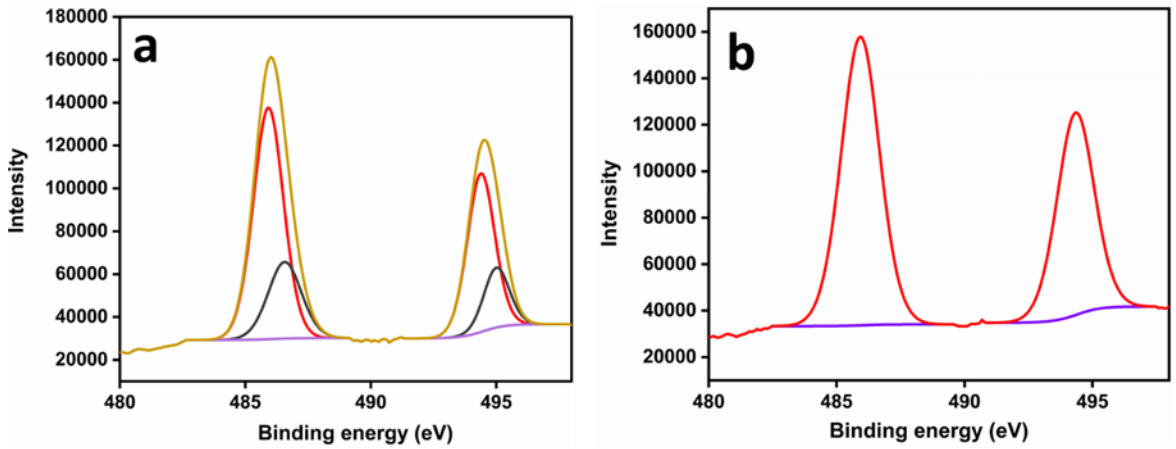

Figure 4.4. High resolution XPS spectra of Sn 3d in a) $(FASnI_3)_{0.3}$ $(MAPbI_3)_{0.7}$ and b) $(PEA)_{0.05}$ $(FA_{0.3}$ $MA_{0.7})_{0.95}$ $Sn_{0.3}$ $Pb_{0.7}$ I_3, (yellow line: measured XPS spectrum; red and black lines: deconvoluted peaks; violet line: background).

The resultant defects can stimulate nonradiative (or trap-assisted) recombination processes, which is detrimental to photovoltaic performance. The PEA-FA/MA alloyed perovskites do not show any detectable signals of Sn^{4+}, enhanced photovoltaic performance and stability are expected. We also note that there is no detectable interaction between PEA molecules and Sn^{2+} cations in the perovskite as evidenced by no shift in XPS peaks corresponding to Sn^{2+}.

First principle calculations have shown that the size of organic cations could play a vital role in governing the formation energy of Sn vacancies in Sn-based perovskites.[286] The larger ionic size could reduce the Sn 5s–I 5p antibonding coupling, leading to higher Sn vacancy formation energies. To establish the effect of organic cations on the formation energy of Sn vacancies in our specific case, we performed DFT calculations taking into account the van der Waals (vdW) interactions (see the Computational Details in the "Experimental and Theoretical Procedures" section) by means of the electron exchange-correlation functional of Perdew-Burke-Ernzerhof (PBE).[298] In particular, we have initially optimized the PEA_2SnI_4 structure along with that of $FASnI_3$ and compared the Sn vacancy formation energy of these two systems (Figure 4.5).

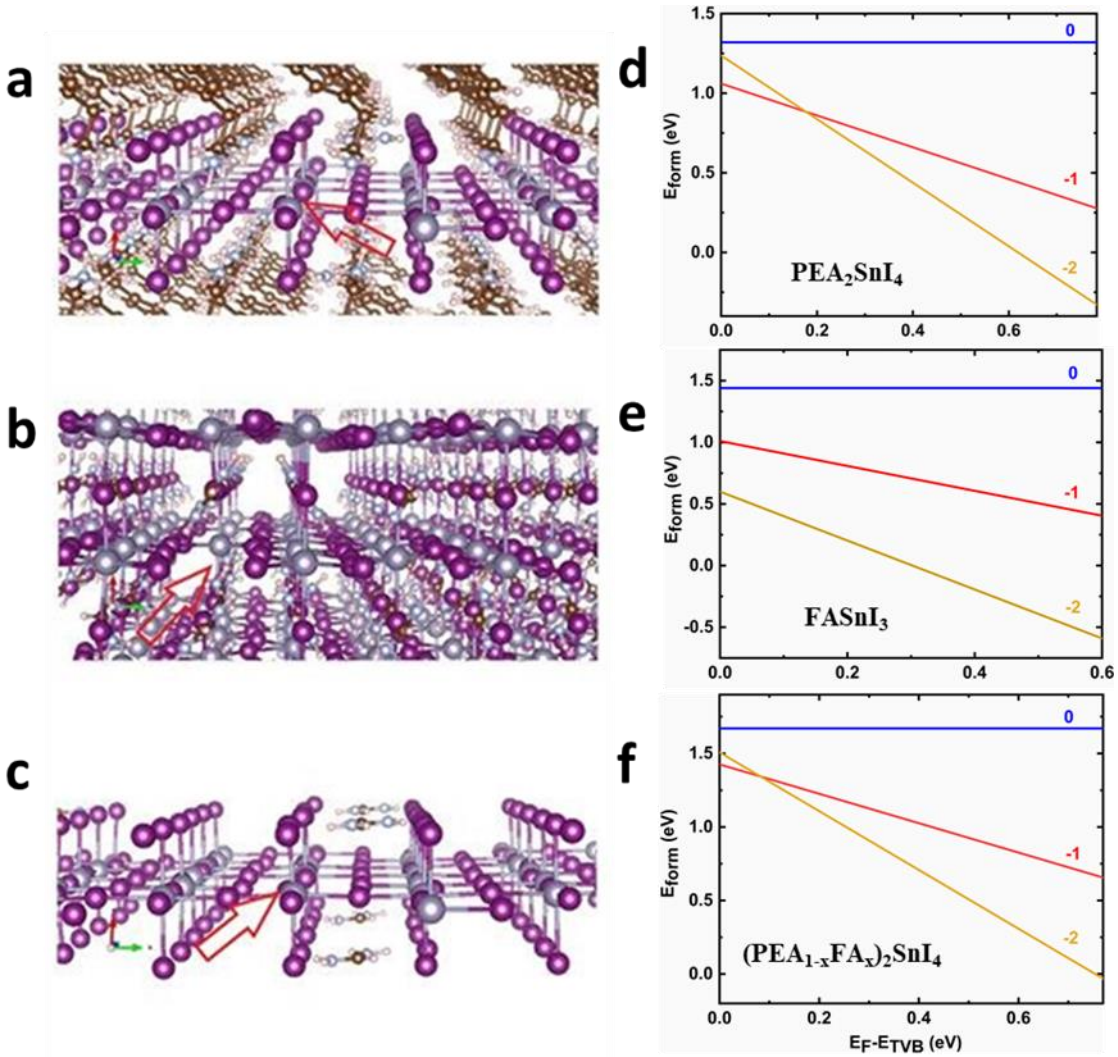

Figure 4.5. Optimized neutral V_{Sn} defective structure of a) PEA_2SnI_4, b) $FASnI_3$, and c) mixed $(PEA_{1-x}FA_x)_2SnI_4$ (x=0.056) perovskite. An in-plane replica of the initially optimized supercells is reported for the three cases. The red arrow shows the V_{Sn} positions. For the sake of clarity, in c) only FA cations are reported, while PEA ones are removed [Large mauve: Sn; purple: I; cyan: N; brown: C; white: H atoms]. The corresponding

formation energy plots in the Sn-rich conditions for the three cases are reported in (d-f) where the electron chemical potential is referred to the top of the valence band.

For the former we considered a 1×3×3 supercell, while for the latter structure a 3×2×2 one (Figure 4.5a and 4.5b). The formation energy of the Sn vacancy (V_{Sn}) was calculated via the following equation:

$$E_{form}=E_{tot}(V_{Sn}^{q}) - E_{tot} + \mu_{Sn} + q(\varepsilon_{VBM}+E_F+\Delta V), \qquad (4.1)$$

where $E_{tot}(V_{Sn}^{q})$ is the energy of the defective system in its charged state (q=0, 1, 2), E_{tot} is the energy of the neutral non-defective structure, μ_{Sn} is the chemical potential of Sn, ε_{VBM} represents the Kohn-Sham eigenvalue (top of the valence band, TVB), E_F is the electron chemical potential (referenced to the TVB of the pristine, non-defective, crystal), while ΔV is the correction due to the potential alignment. The chemical potentials of PEA_2SnI_4 constituents were estimated by imposing thermodynamic equilibrium of PEA_2SnI_4 with the SnI_2 phase. The equilibrium with SnI_4 and its formation is excluded because of the reduced tendency of Sn oxidation in these systems.[180] We thus apply the two constraints:

$$4\mu_I + \mu_{Sn} + 2\mu_{PEA} = \Delta H(PEA_2SnI_4), \qquad (4.2)$$

$$2\mu_I + \mu_{Sn} = \Delta H(SnI_2), \qquad (4.3)$$

where μ_I and μ_{PEA} are chemical potentials of iodine and PEA respectively and $\Delta H(PEA_2SnI_4)$ and $\Delta H(SnI_2)$ are formation enthalpies of PEA_2SnI_4 and SnI_2 respectively. Here the chemical potentials of Sn and I have been referenced to the value of the I_2 molecule and Sn bulk metal (β-tin, I4(1)/amd, Z=4), respectively.[299] We applied an additional constraint of Sn-rich condition (*i.e.* μ_{Sn} = 0) for realistic representation of our alloyed perovskite systems, which contain surplus of Sn through the addition of 10 mol% of SnF_2. Thus, the formation energy of V_{Sn} in Sn-rich condition was calculated (Figure 4.5d). The bandgap employed here was obtained by means of PBE calculations with the inclusion of the van der Waals (vdW) interactions. We are aware of the intrinsic underestimation of the bandgap of semiconductors at the PBE level due to the presence of the so-called self-interaction error; at the same time the huge number of atoms in our systems (~700) prevents us to use more accurate post-DFT approaches. We are anyway confident of the reliability of our results for what regards the trend in the vacancy formation energy at the band

edges (see Figure 4.5d) mainly because we are consistently treating similar systems at the same level of theory. Although the formation of the Sn vacancy defect is energetically favored at the bottom of the conduction band minimum (CBM), interestingly the calculated formation energy in PEA_2SnI_4 is always higher than the same vacancy formation energy in $FASnI_3$. As previously reported in the text such latter crystal has an orthorhombic A*mm*2 space *polar* group,[291,300] a feature relevant to determine the vacancy formation energy. The neutral optimized defective structures for both PEA_2SnI_4 and $FASnI_3$ are reported in Figures 4.5a-4.5b, respectively. The bandgap energy for the polar $FASnI_3$ supercell is 0.64 eV. According to the Eq.(4.1) and also considering, as in the PEA_2SnI_4 case, only the equilibrium with SnI_2 (as said the co-presence of PEA in the final compounds is expected to reduce the presence of oxidized Sn^{+4} species) we obtain that the V_{Sn} formation energy in $FASnI_3$ is a process always thermodynamically more favored (than in PEA_2SnI_4) in each range of the electron chemical potential. In particular, it is three times easier to be formed at *p*-type conditions (low values of the electron chemical potential) and twice at *n*-type ones (opposite conditions, bottom of the Conduction Band, CBM) as observed by comparing Figures 4.5d-4.5e, respectively.

This result is consistent with the data reported by Shi *et al.,*[286] where no vdW interactions are included in the calculations with thus an expected larger bandgap as consequence of a reduced contraction of the $FASnI_3$ crystal. It is worth mentioning that calculations (not reported here) in the less stable, *non-polar* (a metastable structure obtained by rotating FA cations “by hand” in order to have zero dipole along the [001] direction), $FASnI_3$ show a massively more exothermic formation energy of V_{Sn} further confirming that the occurrence of such defect is definitely more favored in $FASnI_3$. To provide an even stronger evidence of the reduced tendency of V_{Sn} formation in mixed PEA-FA/MA perovskites, we have replaced in the initial PEA_2SnI_4 supercell two PEA cations with two FAs, thus obtaining a mixed $(PEA_{1-x}FA_x)_2SnI_4$ perovskite (x=0.056) where, after the optimization, we calculated still by means of Eq. (4.1) the V_{Sn} formation energy. The defective $(PEA_{1-x}FA_x)_2SnI_4$ structure is reported in Figure 4.5c. Strikingly, results clearly show an even reduced tendency of V_{Sn} formation for the mixed case (shown in Figure 4.5f) which corresponds to our experimental findings, i.e. the V_{Sn} formation becomes an endothermic process in the whole electron chemical potential range (only at *n*-type conditions it turns to be slightly favored, E_{form}=-0.035 eV). It is worth stressing that anyway this latter structure is only a hypothetical structure (whose thermodynamic stability is anyway manifestly confirmed by calculations) and that a modeling closer to the complex experimental situation should involve an interface of a very thick $FASnI_3$ slab with a very small 2D-PEA slab or a $FASnI_3$ surface where only one (or few, up to the experimental concentrations) PEA cation replaces a FA one. In this way we could probably better

test the effect of PEA_2SnI_4 small domains and PEA positioning at the interface/grain boundaries. It is highly likely indeed that bulkier (than FA) cations, not fitting the 3D semiconductor cage, tend to locate at the grain boundaries. As matter of fact, calculating the formation energy of Sn-vacancies in such kind of more realistic models would be computationally very expensive even if not feasible at all. The mixed PEA/FA system may provide an indication about the impact of the presence of FA and PEA near a Sn vacancy and the way it can influence its formation energy with respect to the other two extreme cases, i.e. $FASnI_3$ and PEA_2SnI_4.

We thus reasonably conclude that the introduction of bulkier organic cations (PEA) increases the formation energy of Sn vacancies in PEA-containing alloyed perovskites under our Sn rich conditions. Less Sn-vacancies in PEA-FA/MA Sn-Pb perovskites are highly encouraging for the photovoltaic applications. We anticipate that the optimum PEA-containing alloyed perovskites would exhibit superior PCE and stability compared to control samples.

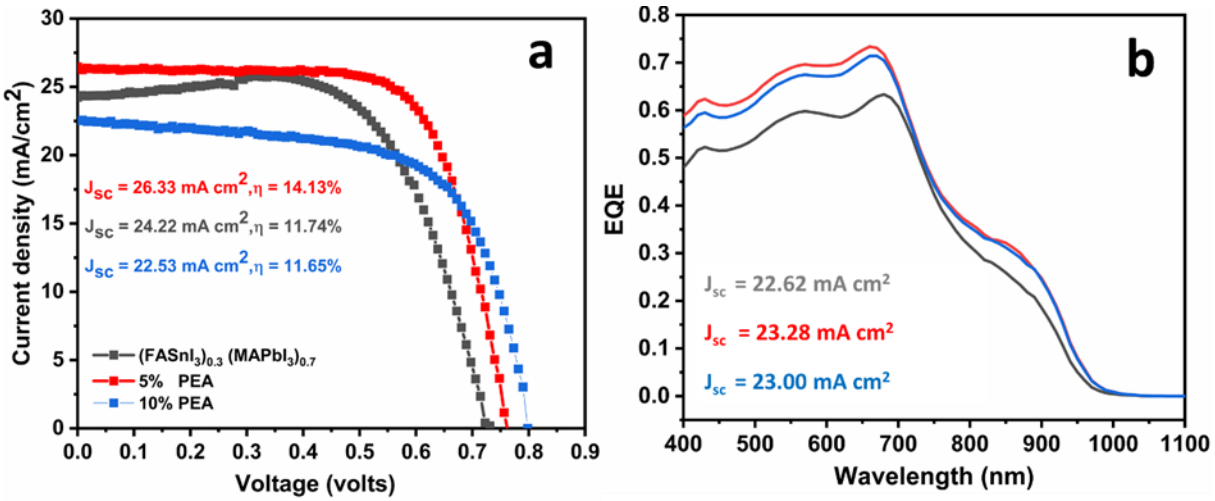

Figure 4.6. J-V curves of a) $(PEA)_y$ $(FA_{0.3}MA_{0.7})_{1-y}$ $Sn_{0.3}Pb_{0.7}I_3$, and b) corresponding EQE spectra of the devices (y = 0 (gray), 5% (red) and 10% (blue)).

To test the photovoltaic properties of alloyed FA/MA and PEA-FA/MA perovskites, we employed a solar cell architecture of indium doped tin oxide (ITO)/ poly (3, 4-ethylene dioxythiophene)-poly (styrene sulfonate) (PEDOT:PSS)/perovskite/phenyl-C_{61}-butyric acid methyl ester (PCBM)/silver (Ag). Among the FA/MA alloyed perovskites, $(FASnI_3)_{0.3}$ $(MAPbI_3)_{0.7}$ showed the highest PCE followed by $(FASnI_3)_{0.5}$ $(MAPbI_3)_{0.5}$ and then $(FASnI_3)_{0.7}$ $(MAsPbI_3)_{0.3}$. Both V_{oc} and fill factor (FF) reduced as the Sn content increased (Table 4.1), with Sn-rich ($(FASnI_3)_{0.7}$ $(MAPbI_3)_{0.3}$) showing the lowest V_{oc} and FF amongst all the compositions. As V_{oc} and FF are strongly dependent on charge carrier recombination in the solar cell, Sn-rich perovskites are highly likely to contain a higher number of defects limiting the V_{oc} and FF of their devices. Specifically, the defects in the

bandgap would attract electrons/holes and act as nonradiative recombination centers, which largely impacts the V_{oc} of corresponding solar cells.[301]

Table 4.1. Photovoltaic parameters of the PSCs based on FA/MA and PEA-FA/MA alloyed perovskites.

Compositions	**V_{oc} (V)**	**J_{sc} (mA/cm^2)**	**FF (%)**	**PCE (%)**
$(FASnI_3)_{0.3}$ $(MAPbI_3)_{0.7}$	0.722±0.015	23.54±1.42	67.60±2.97	11.49±0.73
$(PEA)_{0.05}(FA_{0.3}MA_{0.7})_{0.95}(Sn_{0.3}Pb_{0.7})I_3$	0.768±0.015	25.79±1.14	68.61±1.32	13.60±0.69
$(PEA)_{0.1}(FA_{0.3}MA_{0.7})_{0.90}(Sn_{0.3}Pb_{0.7})I_3$	0.800±0.01	22.36±1.98	64.07±2.72	11.43±0.75
$(FASnI_3)_{0.5}$ $(MAPbI_3)_{0.5}$	0.626±0.03	23.28±2.08	59.58±1.75	8.63±1.17
$(PEA)_{0.05}(FA_{0.5}MA_{0.5})_{0.95}(Sn_{0.5}Pb_{0.5})I_3$	0.725±0.03	23.71±2.38	64.37±3.24	11.05±1.20
$(PEA)_{0.1}(FA_{0.5}MA_{0.5})_{0.90}(Sn_{0.5}Pb_{0.5})I_3$	0.774±0.01	23.83±0.51	64.19±0.70	11.84±0.26
$(FASnI_3)_{0.7}$ $(MAPbI_3)_{0.3}$	0.395±0.05	25.76±2.40	45.55±1.73	4.68±0.93
$(PEA)_{0.05}(FA_{0.7}MA_{0.3})_{0.95}(Sn_{0.7}Pb_{0.3})I_3$	0.581±0.03	22.85±2.48	57.78±4.06	7.66±0.93
$(PEA)_{0.1}(FA_{0.7}MA_{0.3})_{0.90}(Sn_{0.7}Pb_{0.3})I_3$	0.624±0.09	13.01±3.01	58.69±2.89	4.78±0.53

By partially substituting FA/MA with PEA in alloyed perovskites, V_{oc} was significantly improved. In particular, with 10% PEA, the V_{oc} of $(FASnI_3)_{0.3}$ $(MAPbI_3)_{0.7}$ PSCs was boosted from 0.72 V to 0.80 V. The highest V_{oc} enhancement (of 0.23V) was observed for $(PEA)_{0.1}$ $(FA_{0.7}MA_{0.3})_{0.90}$ $Sn_{0.7}$ $Pb_{0.3}$ I_3, followed by $(PEA)_{0.1}$ $(FA_{0.5}$ $MA_{0.5})_{0.90}$ $Sn_{0.5}$ $Pb_{0.5}$ I_3 (with an improvement of 0.15 V). It can be easily understood in a such a way that "Sn-rich" alloyed perovskites contain more defects, so the effect of defect reduction with PEA on V_{oc} is more evident. On the other hand, FF reached its maximum for the samples with 5% PEA. With the further increase to 10%, FF remained almost unchanged or slightly declined. As we have seen in the XRD discussion, the increase in PEA content in the perovskites change the orientation of semiconducting perovskite layers on the

substrate or lattice strain along inorganic bonding direction I-Pb-I, I-Sn-I, which could negatively affect charge carrier diffusion length and reduce the FF.[161] Overall, elimination of Sn^{2+} oxidation (see XPS analysis discussion) thereby reduction of defects (see PL and DFT calculation discussion) in the $(PEA)_{0.05}$ $(FA_x$ $MA_{1-x})_{0.95}$ Sn_x Pb_{1-x} I_3 reduced the trap-assisted recombination, which resulted in improved V_{oc} and FF in the PEA-FA/MA alloyed perovskite devices.

As for $J_{sc,}$ there is no clear trend of variation with incorporating PEA among various alloyed perovskite compositions. But in a particular alloyed perovskite compositional group, the J_{sc} in the devices follows a similar trend as observed in XRD data, especially in Sn-rich perovskites, where reduction of crystallinity with higher amount of PEA lowered the J_{sc}. By and large, the PSCs employing Sn-Pb alloyed perovskites with 5% bulkier PEA cations produced the highest PCE. We hypothesis this is due to a trade-off between local lattice strain or/and crystallinity and number of defects in the alloyed perovskites. Figures 4.S8-4.S10 shows the statistical distribution of efficiency of 20-30 devices in each compositional group.

J-V curves and corresponding external quantum efficiency (EQE) spectra of solar cells are shown in Figures 4.6 and 4.S11. It can be seen from the EQE measurements that the photoresponse of all the solar cells reach up to the near infrared (NIR) region. The calculated J_{sc} values from EQE basically matched with those obtained from the J-V curves, except for $(FASnI_3)_{0.7}$ $(MAPbI_3)_{0.3}$. Since EQE was measured after J-V curve measurements and the larger mismatch

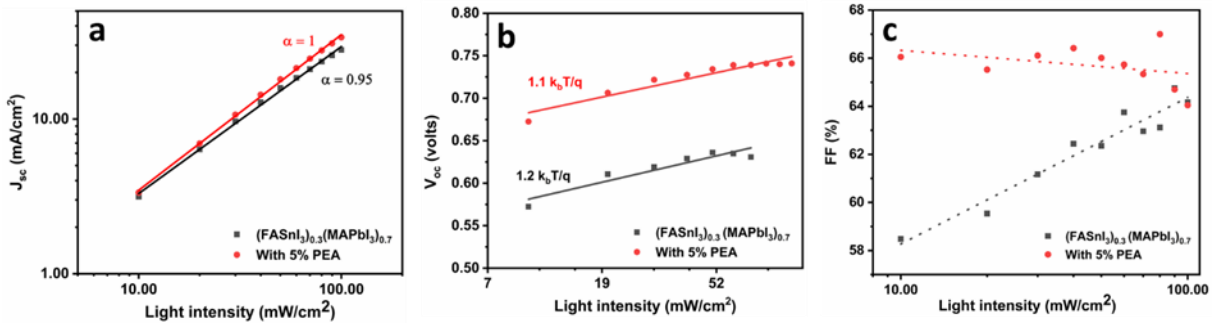

Figure 4.7. Dependence of a) J_{sc}, b) V_{oc} and c) FF against the incident light intensity of the FA/MA PSCs and PEA-FA/MA PSCs.

was observed only in the Sn-rich FA/MA perovskites, we speculate it is due to the serious degradation of Sn-rich samples, which led to lower calculated photocurrents.

Figure 4.7a shows the dependence of J_{sc} on incident light intensity by fitting to a power law ($I \propto J_{sc}{}^{\alpha}$).[302] The fitting parameter (α = 0.95) deviated from the linear dependence in FA/MA alloyed perovskite devices compared to that (α = 1) of PEA-FA/MA perovskite devices, which implies that photogenerated charge carriers in FA/MA alloyed perovskite devices are not as efficiently

transported to the electrodes as in PEA-FA/MA perovskite devices.[303] To investigate the recombination of photogenerated carriers during solar cell operation near V_{oc}, we plotted V_{oc} versus logarithmically scaled light intensity (Figure 4.7b).

By linearly fitting the plot using

$$V_{oc} \propto (nk_bT/q) \ln (I), \qquad (4.4)$$

where q is the elementary charge, n is the ideality factor, k_b is the Boltzmann's constant and T is the absolute temperature, we obtained a slope of 1.1 k_bT/q (n is close to unity) for PEA-FA/MA perovskite devices, which strongly suggests that bimolecular recombination process dominates close to the V_{oc} of the solar cells. The larger deviation of the slope (1.2 k_bT/q) of FA/MA perovskite devices from k_bT/q means trap-assisted recombination plays a larger role in the FA/MA system with respect to the PEA-FA/MA system.[234] FF is a more significant parameter as the solar cell is operated near a maximum power point. The dependence of FF on incident light intensity unravels the nature of the recombination process in the solar cell during the device operation. In the pure bimolecular recombination process, recombination rate is proportional to the product of charge carrier densities.[304] Therefore, at a low light intensity (i.e., low charge carrier densities), the recombination rate reduces and a better FF is obtained. This is basically the trend that was observed for the PEA-FA/MA alloyed PSCs (Figure 4.7c), which is in line with the dominance of the bimolecular recombination in these devices. On the other hand, FF clearly decreased with decreasing light intensity in FA/MA alloyed perovskite devices, which unambiguously supports the dominance of the trap-assisted recombination in these devices.[304] Since the number of traps does not change with lowering light intensity, it can be easily understood that the rate of recombination of photo-generated charge carriers with trapped charges increases with decreasing light intensity, and therefore results in a lower FF. The study clearly shows that the introduction of PEA effectively changed the dominant charge carrier recombination process in our PSCs.

The photovoltaic performance degradation of unencapsulated, best-performing (in term of PCE) 5% PEA-containing alloyed perovskite devices was monitored under different environmental conditions to evaluate their stability and compare with that of their control samples. Here, we define $t_{1/2}$ as a time for the PCE of the device to drop to 50% of its initial value for standardizing the comparison between different devices.

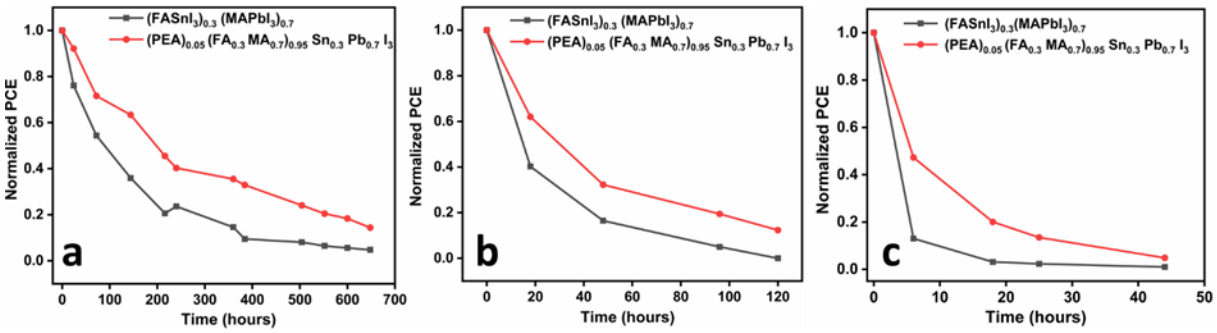

Figure 4.8. Comparison of the stability of PEA-FA/MA perovskite devices vs. FA/MA perovskite devices: a) under 28±2% RH humidity in the dark, b) under N_2 at 1.5G AM solar illumination and c) under 28±2% RH humidity at 1.5G AM sun illumination.

Figure 4.8a shows degradation of devices under modest moisture environment (28±2% RH humidity) in the dark. The degradation was significantly slowed down by substituting FA/MA with 5% of PEA in $(FASnI_3)_{0.3}$ $(MAPbI_3)_{0.7}$. The $t_{1/2}$ for $(PEA)_{0.05}$ $(FA_{0.3}$ $MA_{0.7})_{0.95}$ $Sn_{0.3}$ $Pb_{0.7}$ I_3 was found to be 200h appreciably better than that ($t_{1/2}$ = 87 h) of corresponding FA/MA perovskite devices.

Figure 4.8b displays the degradation of devices under AM1.5G illumination in an inert atmosphere. The $(PEA)_{0.05}$ $(FA_{0.3}$ $MA_{0.7})_{0.95}$ $Sn_{0.3}$ $Pb_{0.7}$ I_3 devices exhibited better photostability compared to FA/MA perovskite devices ($t_{1/2}$ = 30h vs. $t_{1/2}$ = 15h). Light seems to be more harmful to alloyed perovskite devices than moisture. Figure 4.8c shows that the degradation of alloyed perovskite devices became faster in the co-presence of light and modest moisture. However, PEA-FA/MA perovskite devices were still more resistant to the degradation, retaining 20% of initial performance after 24h whereas FA/MA perovskite devices wholly degraded during the same period. The defects in Sn-Pb perovskites induced by Sn vacancies not only play key role in determining photovoltaic performance (PCE and J-V hysteresis) but also the stability of the devices. The defects in perovskites are vulnerable to oxygen or moisture filtration and accelerate the degradation of devices under ambient conditions.[223] Reduced defects (see DFT calculations and PL discussion) and enhanced crystallinity (see XRD and GIWAXS discussion) with the incorporation of 5% PEA in Sn-Pb perovskites contribute to enhanced stability of the PEA-FA/MA Sn-Pb PSCs.

Based on all the above described characterizations on materials (PL, AFM, SEM, XPS, XRD, GIWAXS) and devices (J-V and EQE measurements, light intensity dependent analyses of the solar cell performance parameters) , a reasonable conclusion can be made: i) more defects are present in the FA/MA alloyed PSCs, and the trap-assisted recombination indeed dominates their performance and ii) by replacing FA/MA cations with a small quantity of PEA cations, the number

of defects can be considerably reduced and thereby there is a significant drop in the trap-assisted recombination in the alloyed perovskites. This conclusion is further supported by a large decrease in J-V hysteresis observed in PEA-FA/MA alloyed perovskite devices compared to that of FA/MA alloyed perovskite devices (Figure 4.S12). Among the several suggested possible reasons for the detrimental phenomenon of the hysteresis of the J-V curve, the defect migration in PSCs is considered the main responsible.[305,306] It has been previously shown that charged defects such as MA/FA and Pb/Sn vacancies close to the charge selective layers obstruct the charge extraction at selective contacts, causing the solar cell hysteresis.[307] By reducing the number of charged defects, we believe the defect migration has been substantially reduced in PEA-containing Sn-Pb perovskites and therefore lowering the J-V hysteresis in the devices. As noted, defects close to the interfacial region between perovskite and charge selective layers predominately influence the J-V hysteresis.[308]

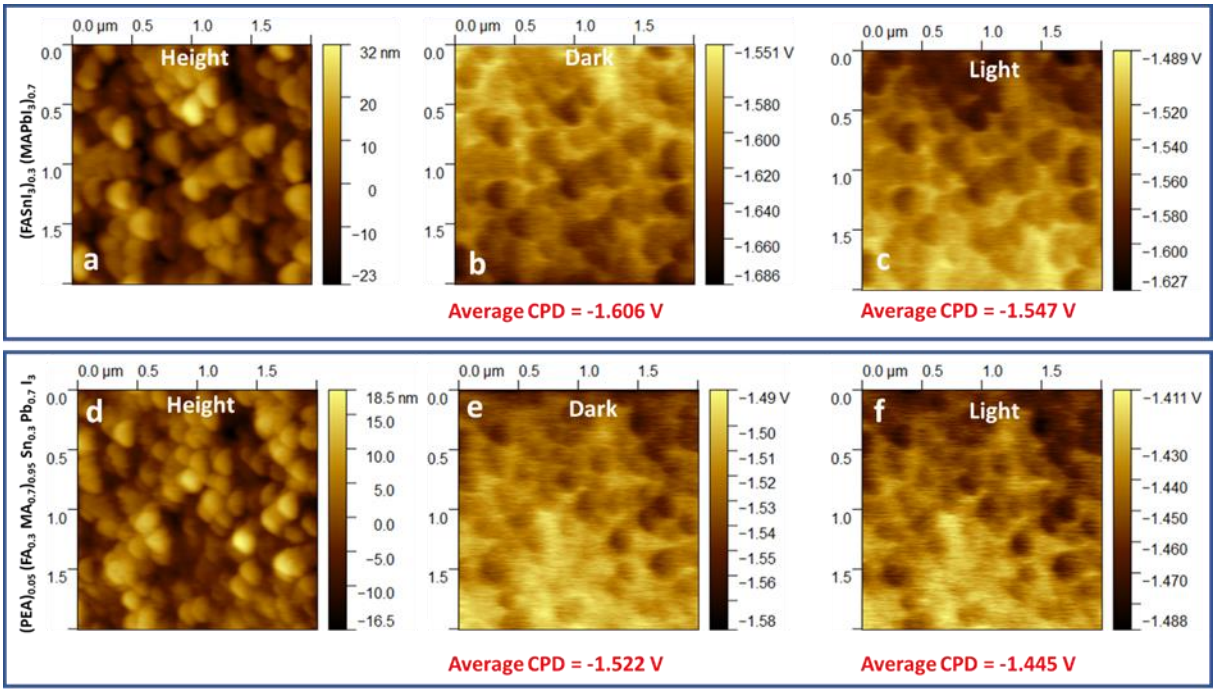

Figure 4.9. a) Height topography and b-c) surface potential profile of $(FASnI_3)_{0.3}$ $(MAPbI_3)_{0.7}$, d) topography and e-f) surface potential profile of $(PEA)_{0.05}$ $(FA_{0.3}$ $MA_{0.7})_{0.95}$ $(Sn_{0.3}$ $Pb_{0.7})$ I_3. The average CPD calculated using Gwyddion software also provided at the bottom of each Figure.

To understand defects at perovskite/selective layer interface, contact potential difference (CPD) of the samples was measured in the dark and under illumination by Kelvin probe force microscopy (KPFM), as shown in Figure 4.9. By substituting FA/MA with 5% of PEA in alloyed perovskites, the CPD was reduced at GBs as well as in the grain interior (GI) (Figures 4.9b, 4.9c, 4.9e and 4.9f). The surface photovoltage (SPV) estimated by subtracting the average CPD in the dark from

that measured under illumination, provides the information about photocharge carrier separation at the perovskite/PEDOT:PSS interface.[309,310] Under illumination, the charge-separation process in the complete device is mimicked using the AFM probe in the KPFM measurement and SPV represents the V_{oc} or internal electric field in the solar cell.[227] The SPV increased from 0.059 V to 0.077 V with 5% PEA in alloyed perovskite film, indicating an increase in the internal electric field in PEA-FA/MA perovskite devices, therefore we can reasonably conclude that photogenerated carriers are more efficiently separated in the PEA-FA/MA perovskite film than FA/MA perovskite film.[311,312] The KPFM measurements essentially suggest reduced recombination events for the devices employing PEA-FA/MA perovskite film compared to their control samples. This clearly demonstrate that the number of defects is lowered in Sn-Pb perovskites with inclusion of 5% PEA, which also reduces the defect migration, leading to eradication of J-V hysteresis in resultant PSCs.[313,314] Not secondarily, partly replacing MA/FA with more bulky PEA cations has the advantage of massively reducing the polarizability of the final device,[283,315–317] the other factor which is strongly believed to affect the J-V hysteresis in the FA/MA PSCs, further stressing the great advantages of using PEA-containing alloyed perovskites in PSCs.

4.3 Conclusions

In this work, we have used bulky aromatic cations to improve both the efficiency and stability of Sn-Pb perovskite solar cells. By incorporating PEA cations to Sn-Pb perovskites, we observed key advancements in perovskite semiconductor material quality. The overall crystallinity of the alloyed perovskites was significantly improved as evidenced by XRD and GIWAXS, suggestive of a reduced number of defects that is further confirmed by PL spectroscopy. Consistently, DFT calculations suggested the formation energy for Sn vacancies is twice to three times higher in long-chain organic cation PEA containing Sn-based perovskites (PEA_2SnI_4) than in short-chain FA containing Sn-based perovskites ($FASnI_3$), while calculations in Sn perovskite models with mixed FA/PEA organic moieties show a further reduction of the Sn vacancy formation energy. The advantages of reduction of defects associated with Sn vacancies in Sn-Pb perovskites are threefold: 1) the PCE enhanced by up to ~40% in Sn-rich 5% PEA-containing alloyed PSCs and 15% in Pb-rich alloyed PSCs compared to their control samples due to reduced nonradiative recombination in the alloyed perovskites; 2) eliminated J-V hysteresis in PEA-FA/MA Sn-Pb PSCs attributable to lowered Sn vacancy defect migration and 3) improved device stability due to the reduced number of active defect sites in alloyed perovskites where accelerated material degradation can take place. In short, by modifying defect chemistry in Sn-Pb perovskites realized through incorporating optimum amount of PEA, we improved the photovoltaic performance and

stability of alloyed PSCs. Our work on passivating defects with bulky organic cations in Sn-Pb perovskites opens new opportunities in designing highly efficient, stable Pb-less alloyed perovskite solar cells.

4.4 Materials and Methods

Materials: Methylammonium iodide (CH_3NH_3I), Formamidinium iodide ($CH(NH_2)_2I$) and phenylethylammonium iodide ($C_6H_5(CH_2)_2NH_3I$) were purchased from Dyesol. Tin iodide (SnI_2), tin fluoride (SnF_2), dimethylformamide (DMF) and dimethyl sulfoxide (DMSO) were purchased from Sigma Aldrich. Lead iodide (PbI_2) was bought from Acros Organics. Phenyl-C61-butyric acid methyl ester ($PC_{61}BM$) and poly (3, 4-ethylene dioxythiophene)-poly (styrene sulfonate) (PEDOT: PSS; Clevios™ P VP AI 4083) were obtained from 1-Materials and Heraeus, respectively. All chemicals were used as received.

Alloyed perovskite precursor solution: $FASnI_3$ precursor solution (1.1 M) was prepared by adding equimolar FAI and SnI_2 powders and 20 mol% of SnF_2 into a mixture of DMF: DMSO (4:1 v/v). $MAPbI_3$ precursor solution (1.1 M) was prepared by adding MAI and PbI_2 in a mixture of DMF: DMSO (4:1 v/v). $(FASnI_3)_x$ $(MAPbI_3)_{1-x}$ (x = 0.3, 0.5, 0.7) solutions were prepared by stoichiometrically mixing $FASnI_3$ and $MAPbI_3$ solutions. The PEA-FA/MA alloyed perovskite precursor solutions were prepared by stoichiometrically substituting FAI/MAI with 5% and 10% PEAI in $(FASnI_3)_x$ $(MAPbI_3)_{1-x}$ precursor solution.

Solar cell fabrication: Patterned ITO-coated glasses were cleaned by sonication in detergent followed by sequential washing with deionized water, acetone, and isopropanol. After drying under air flow, the substrate surface was cleaned by oxygen plasma for 10 min under rough vacuum. PEDOT: PSS solution was spin-coated on top of the ITO-coated glass substrate at 4500 rpm for 45 s; PEDOT: PSS performs as the hole transporting layer. The PEDOT: PSS film was then dried in air on a hot plate (set at 170 °C) for 10 min. After drying, the substrate was transferred to a nitrogen-filled glovebox for further use. The FA/MA and PEA-FA/MA alloyed perovskite absorber layer were spin-coated on the PEDOT: PSS film at 5000 rpm for 60 s. Diethyl ether was dropped onto the spinning substrate. The spin coated films were annealed at 60℃ for 5 minutes. Then the $PC_{61}BM$ solution (20 mg/mL in chlorobenzene) was spin-coated on top of the perovskite film at 2000 rpm for 60 s to form a 20 nm thick electron transporting layer. Finally, the film was transferred to a thermal evaporation chamber inside the nitrogen filled glove box. The chamber was pumped down to 1×10^{-6} Torr for silver deposition. The 100 nm thick silver top electrode was

deposited through a shadow mask that defines the active device area as 0.06 cm^2 for the solar cells.

Perovskite Film Characterization: Topography of perovskite film surface was obtained by using a Bruker MultiMode8 AFM. Absorption spectra were collected by using a UV-Visible-NIR spectrometer Lambda 750 (Perkin Elmer). Steady-state PL spectra were obtained from a Fluorolog®-3 system (Horiba Jobin Yvon) using a 444 nm laser. XRD measurements were carried out using a Panalytical X-Pert PRO MRD X-Ray diffractometer. The oxidation of tin element was probed by an XPS spectrometer (ESCALAB 220I-XL) equipped with an Al Kα (1486.6 eV) monochromatic source. The grazing incidence wide angle X-ray scattering (GIWAXS) measurements were done at the BL14B1 beamline of Shanghai Synchrotron Radiation Facility (SSRF). The GIWAXS patterns were collected by a MarCCD detector which is mounted vertically at around 194 mm from the sample. The exposure time was less than 50 s and a grazing incidence angle with respect to the surface plane is 1°. The GIWAXS patterns were examined afterward using the Fit 2D software and displayed in scattering vector q coordinates with $q=4\pi\sin\theta/\lambda$, where θ is half of the diffraction angle, and λ is the incident X-ray wavelength (0.124 nm). KPFM measurements were done using the tapping mode in a Cypher AFM (Model: Cypher S) under ambient conditions. KPFM measurements were performed using a Platinum-coated Silicon tip. A white LED lamp was used to carry out KPFM measurements under illumination.

Solar cell characterization: Solar cell performance was measured using a class ABA LED solar simulator, which was calibrated to deliver simulated AM 1.5 sunlight at an irradiance of 100 mW/cm^2. The irradiance was calibrated using an NREL-calibrated KG5 filtered silicon reference cell. Current density-voltage (J-V) curves were recorded using a source meter (Keithley 2400, USA). External quantum efficiency (EQE) measurements were conducted by using an IQE200B system (Newport Corporation).

Device stability tests: The stability of devices was tested without any device encapsulation. For moisture stability tests, the PEA-FA/MA and FA/MA perovskite devices were placed inside a desiccator under ambient environment. The relative humidity ($28 \pm 2\%$ RH humidity) was continuously monitored with a digital humidity sensor. For photostability tests, the perovskite devices were placed under constant AM1.5G illumination inside a N_2 filled glovebox. Devices were also tested under constant AM1.5G illumination at $28 \pm 2\%$ RH humidity.

Computational details: We performed DFT calculations by means of the electron exchange-correlation functional of Perdew–Burke–Ernzerhof (PBE)[298] as implemented in the VASP code.[318] The projector augmented wave (PAW) method [319,320] has been similarly adopted. Van der Waals

corrections to the potential energy were included by means of the DFT-D3 method of Becke and Johnson (BJ).[321,322] The cutoff energy for the plane-wave basis set was set to 600 eV, while residual forces were all lower than 0.02 eV/Å.

A 2x4x4 Γ-centered *k*-point sampling of the Brillouin Zone (BZ) was used for the structural optimizations of PEA_2SnI_4 and of $(PEA_{1-x}FA_x)_2SnI_4$ (x=0.056). The PEA_2SnI_4 structure we optimized has the following lattice parameters: a=32.38 Å; b=18.05 Å; c=18.55 Å, in very close agreement with previously reported experimental data.[323]

Following previous literature, we used the Γ–point for sampling the BZ in the structural optimization of the $FASnI_3$ supercell (a= 18.57 Å; b=18.30 Å; c=17.32 Å) and derived defective structures.

AUTHOR INFORMATION

Corresponding Author

E-mail: ma@emt.inrs.ca

Author Contributions

The manuscript was written through contributions of all authors. All authors have given approval to the final version of the manuscript.

ACKNOWLEDGMENT

Financial support from the Natural Sciences and Engineering Research Council (NSERC) of Canada, in the context of a NSREC Discovery Grant and a NSERC Strategic Grant (Industry partner: Canadian Solar Inc.) is greatly appreciated. D.M is also grateful for the financial support from Quebec Center for Functional Materials (CQMF), Canada. D.T.G acknowledges scholarship support from the Fonds de recherche du Québec–Nature et technologies (FRQNT) under the Programme de Bourses d'Excellence (Merit Scholarship Program for Foreign Students). M.P. thanks INFN for financial support through the National project Nemesys and for allocated computational resources at CINECA. G. G. acknowledges PRACE (Grant No. Pra17_4466 “DECONVOLVES”) and ISCRA (“2D-OIHPs” HP10BGUJ6X) for awarding access to resource Marconi based in Italy at CINECA. The authors thank beamline BL14B1 at Shanghai Synchrotron Radiation Facility (SSRF) for providing the beam time.

Supplementary information

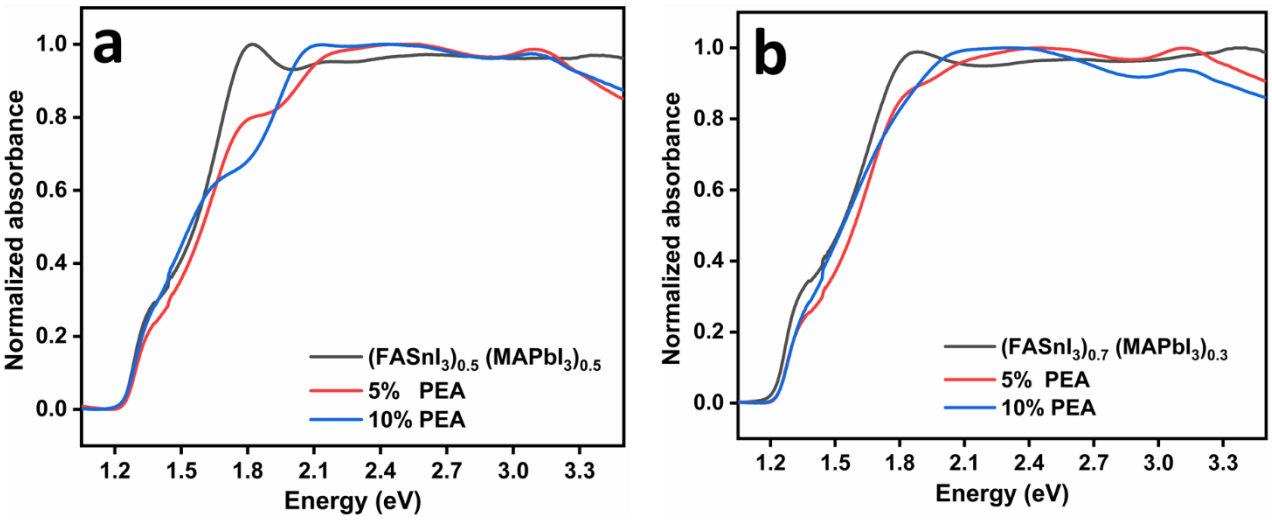

Figure 4.S1. Comparison of absorption pattern: a) $(PEA)_y (FA_{0.5} MA_{0.5})_{1-y} Sn_{0.5} Pb_{0.5} I_3$ and b) $(PEA)_y (FA_{0.7} MA_{0.3})_{1-y} Sn_{0.7} Pb_{0.3} I_3$.

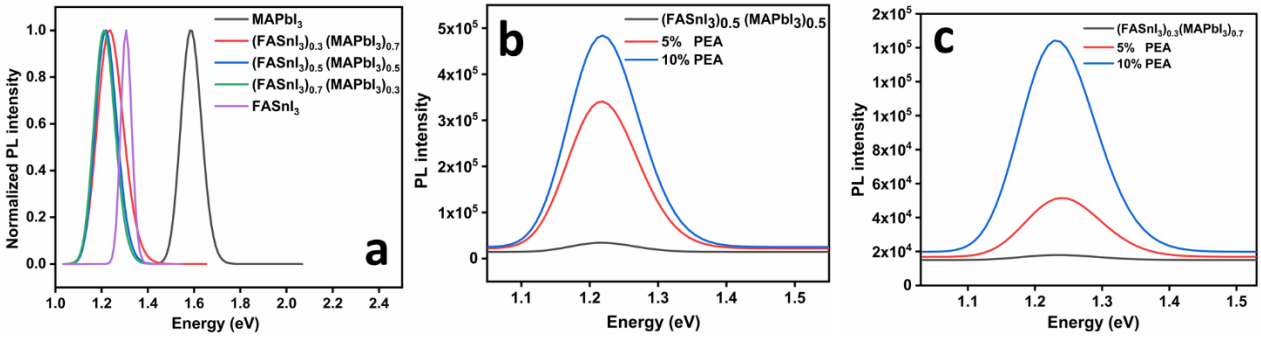

Figure 4.S2. a) Steady-state PL spectra of 3D perovskite films and comparison of steady-state PL spectra of 3D perovskites vs. 2D/3D perovskites: b) $(PEA)_y (FA_{0.5} MA_{0.5})_{1-y} Sn_{0.5} Pb_{0.5} I_3$ and c) $(PEA)_y (FA_{0.7} MA_{0.3})_{1-y} Sn_{0.7} Pb_{0.3} I_3$. y=0, 5% and 10%.

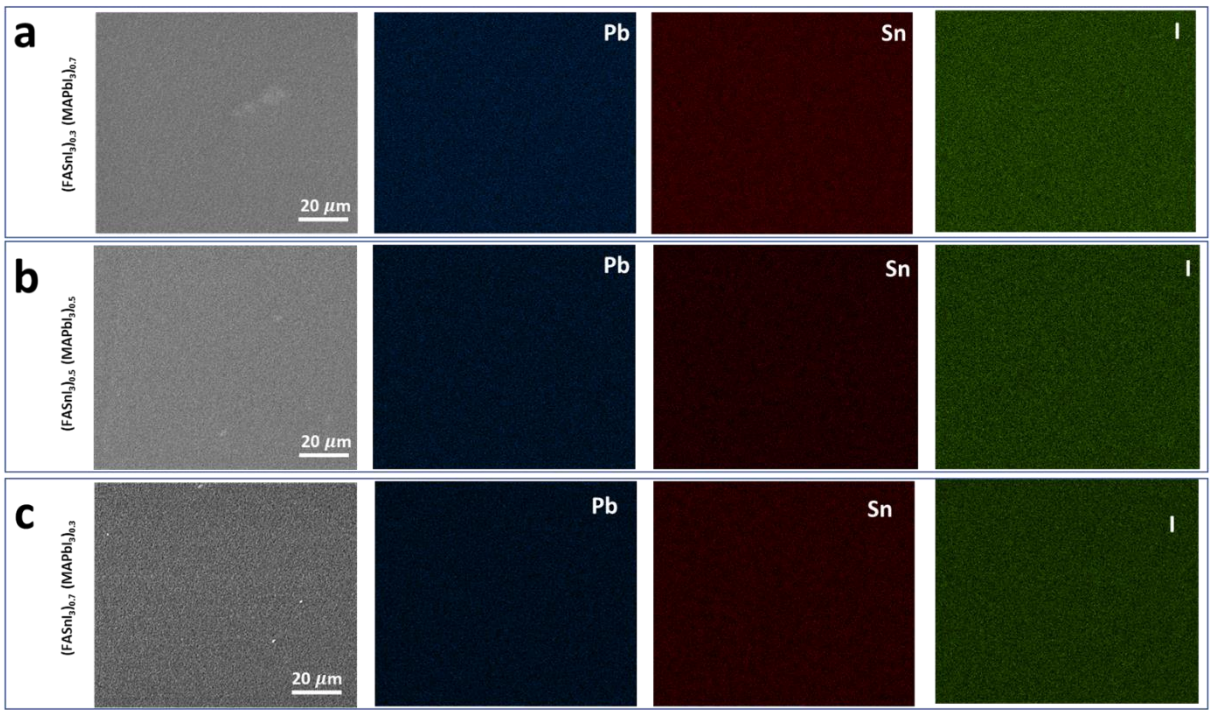

Figure 4.S3. SEM images and elemental mapping of Pb, Sn and I of a) $(FASnI_3)_{0.3}$ $(MAPbI_3)_{0.7}$, b) $(FASnI_3)_{0.5}$ $(MAPbI_3)_{0.5}$, c) $(FASnI_3)_{0.7}$ $(MAPbI_3)_{0.3}$.

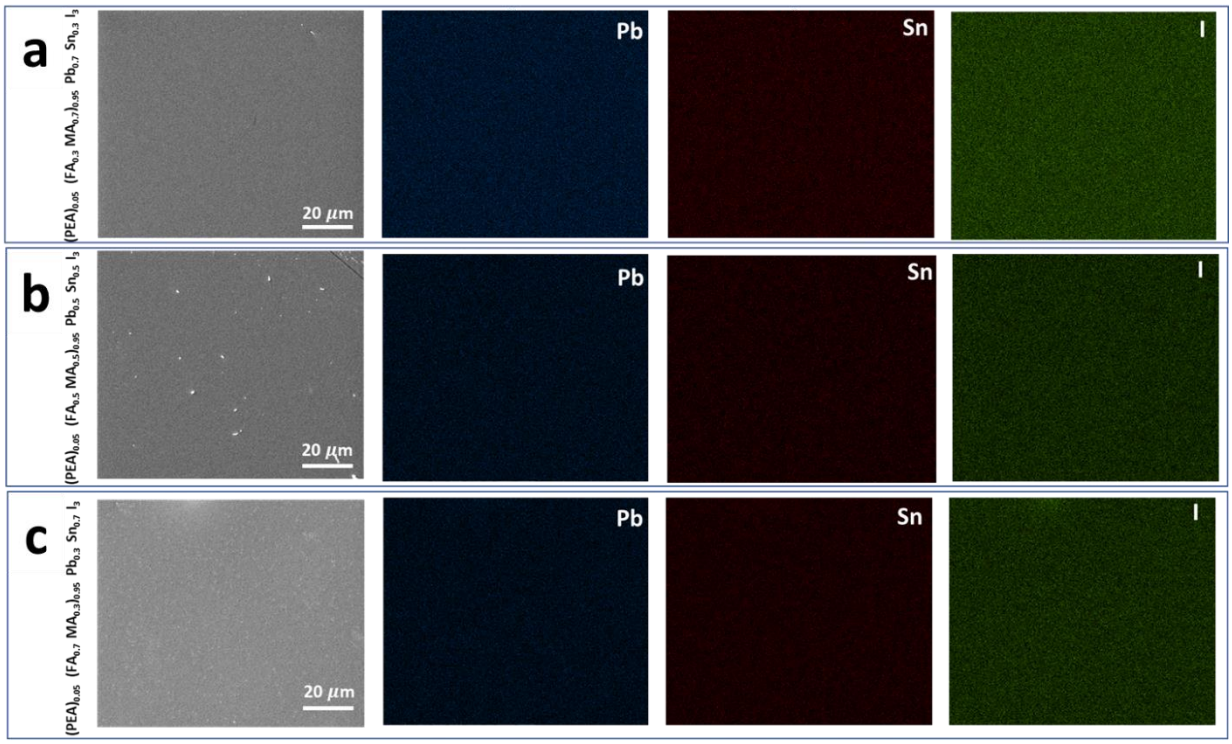

Figure 4.S4. SEM images and elemental mapping of Pb, Sn and I of a) $(PEA)_{0.05}(FA_{0.3}MA_{0.7})_{0.95}Pb_{0.7}Sn_{0.3}I_3$, b) $(PEA)_{0.05}(FA_{0.5}MA_{0.5})_{0.95}Pb_{0.5}Sn_{0.5}I_3$, and c) $(PEA)_{0.05}(FA_{0.7}MA_{0.3})_{0.95}Pb_{0.3}Sn_{0.7}I_3$.

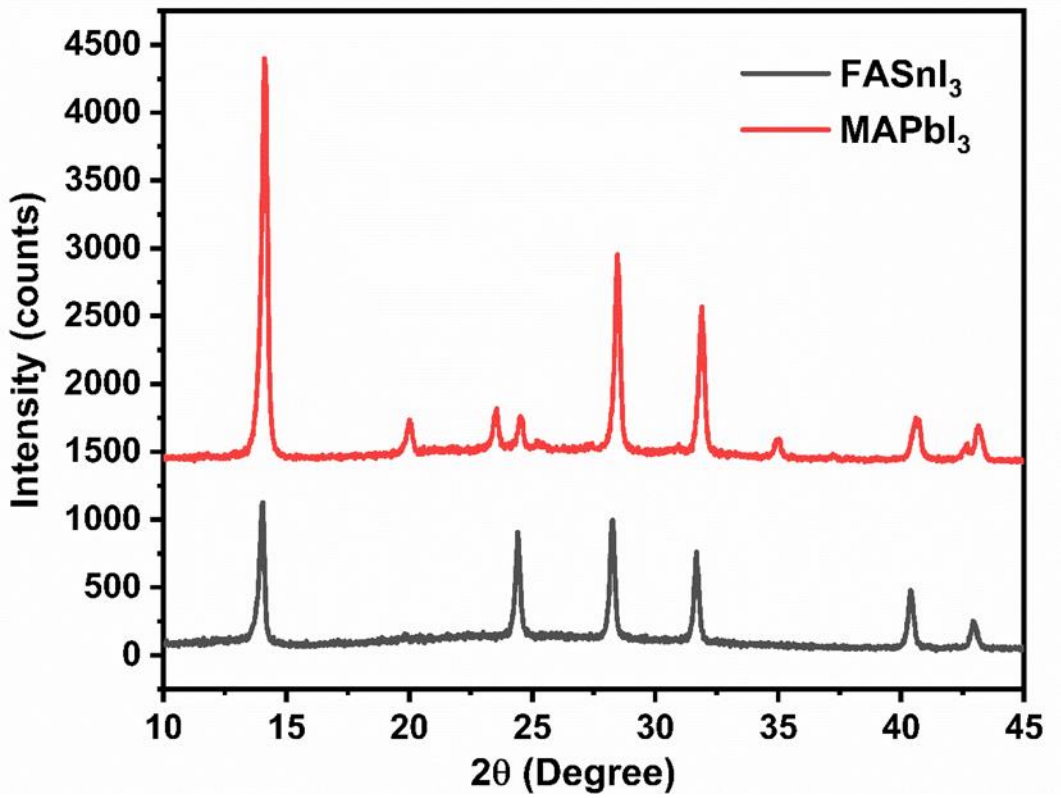

Figure 4.S5. XRD of $FASnI_3$ and $MAPbI_3$ perovskite films.

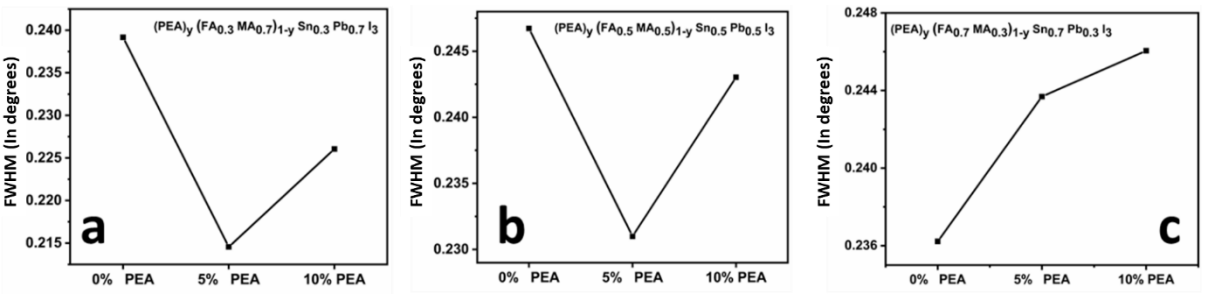

Figure 4.S6. Variation of FWHM of the (110) diffraction peak of a) $(PEA)_y(FA_{0.3}MA_{0.7})_{1-y}Sn_{0.3}Pb_{0.7}I_3$, b) $(PEA)_y(FA_{0.5}MA_{0.5})_{1-y}Sn_{0.5}Pb_{0.5}I_3$ and c) $(PEA)_y(FA_{0.7}MA_{0.3})_{1-y}Sn_{0.7}Pb_{0.3}I_3$. y=0, 5% and 10%.

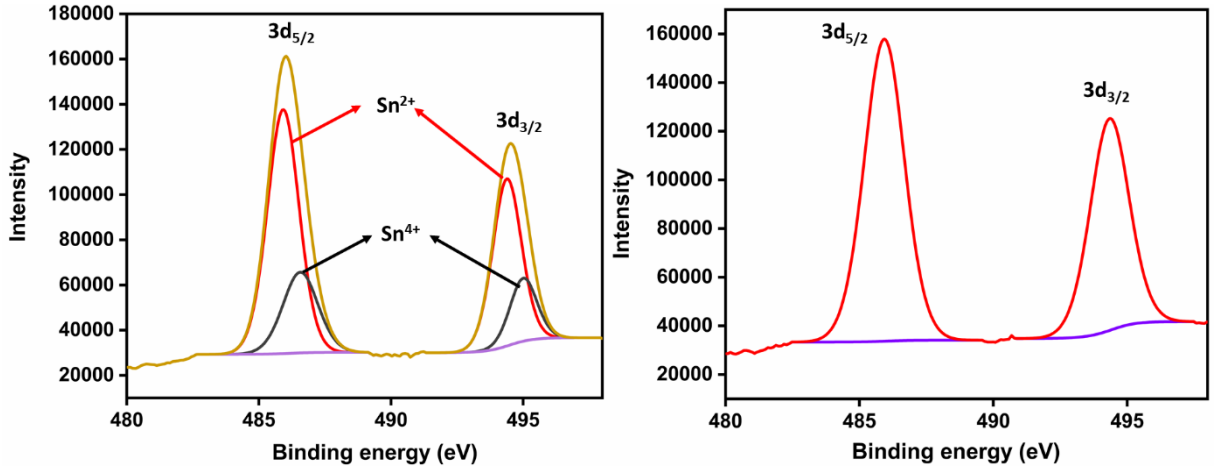

Figure 4.S7. XPS survey spectra of $(FASnI_3)_{0.7}$ $(MAPbI_3)_{0.3}$ and $(PEA)_{0.05}$ $(FA_{0.7}$ $MA_{0.3})_{0.95}$ $Sn_{0.7}$ $Pb_{0.3}$ I_3.

(brown line: measured XPS spectrum; red and black lines: deconvoluted peaks; violet line: background)

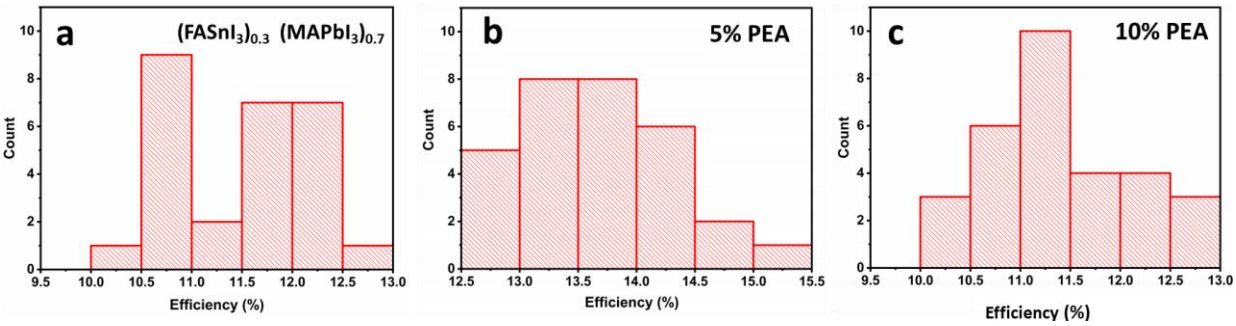

Figure 4.S8. Statistical distribution of PCEs of a) $(FASnI_3)_{0.3}$ $(MAPbI_3)_{0.7}$, b) $(PEA)_{0.05}$ $(FA_{0.3}$ $MA_{0.7})_{0.95}$ $Sn_{0.3}$ $Pb_{0.7}$ I_3 and c) $(PEA)_{0.1}$ $(FA_{0.3}$ $MA_{0.7})_{0.95}$ $Sn_{0.3}$ $Pb_{0.7}$ I_3 devices.

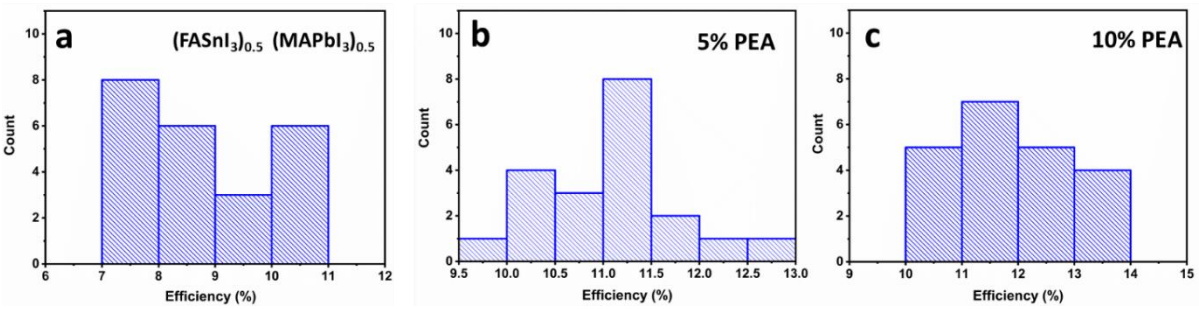

Figure 4.S9. Statistical distribution of PCEs of a) $(FASnI_3)_{0.5}$ $(MAPbI_3)_{0.5}$, b) $(PEA)_{0.05}$ $(FA_{0.5}$ $MA_{0.5})_{0.95}$ $Sn_{0.5}$ $Pb_{0.5}$ I_3 and c) $(PEA)_{0.1}$ $(FA_{0.5}$ $MA_{0.5})_{0.95}$ $Sn_{0.5}$ $Pb_{0.5}$ I_3 devices.

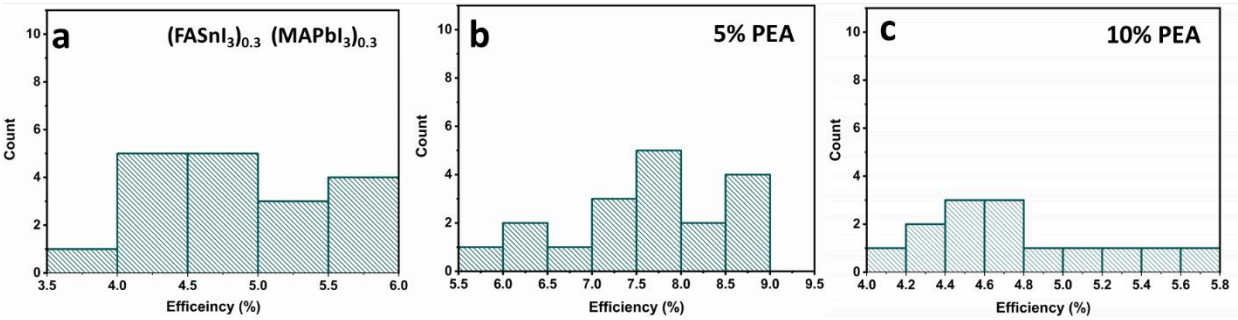

Figure 4.S10. Statistical distribution of PCEs of a) $(FASnI_3)_{0.7}$ $(MAPbI_3)_{0.3}$, b) $(PEA)_{0.05}$ $(FA_{0.7}$ $MA_{0.3})_{0.95}$ $Sn_{0.7}$ $Pb_{0.3}$ I_3 and c) $(PEA)_{0.1}$ $(FA_{0.7}$ $MA_{0.3})_{0.95}$ $Sn_{0.7}$ $Pb_{0.3}$ I_3 devices.

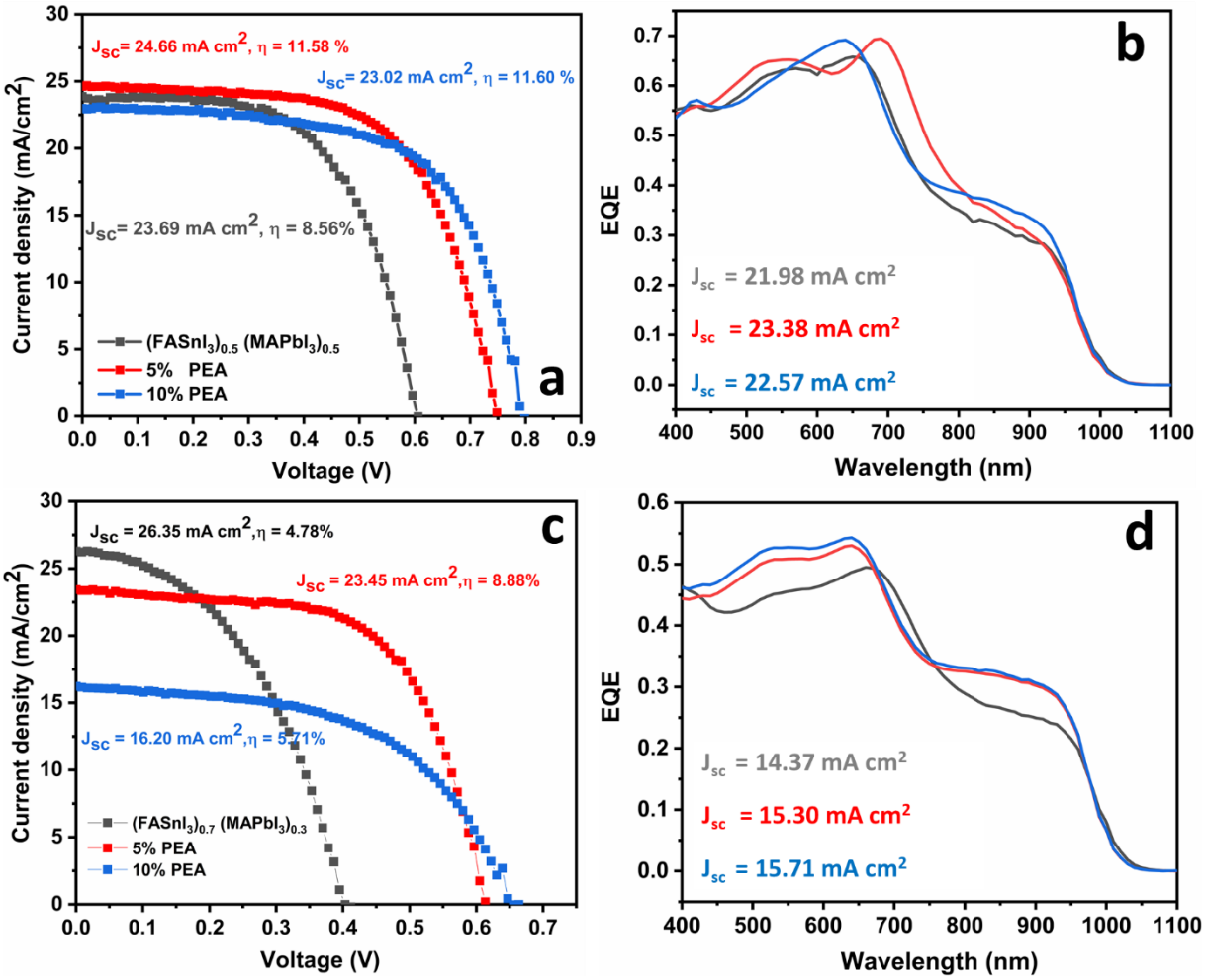

Figure 4.S11. J-V curves and corresponding EQE spectra of a-b) $(PEA)_y$ $(FA_{0.5}$ $MA_{0.5})_{1-y}$ $Sn_{0.5}$ $Pb_{0.5}$ I_3 and c-d) $(PEA)_y$ $(FA_{0.7}$ $MA_{0.3})_{1-y}$ $Sn_{0.7}$ $Pb_{0.3}$ I_3 devices, (y = 0 (gray), 5% (red) and 10% (blue)).

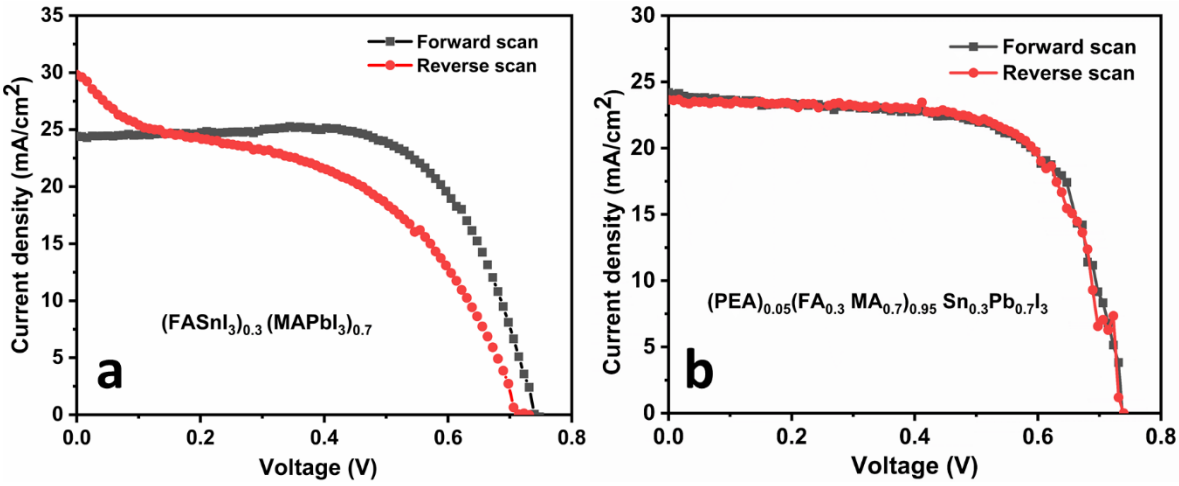

Figure 4.S12. J-V hysteresis of a) $(FASnI_3)_{0.3}$ $(MAPbI_3)_{0.7}$ and b) $(PEA)_{0.05}$ $(FA_{0.3}$ $MA_{0.7})_{0.95}$ $Sn_{0.3}$ $Pb_{0.7}$ I_3 devices.

5 EFFECTS OF AROMATIC ALKYLAMMONIUM SPACER CATIONS IN MIXED HALIDE ALLOYED PEROVSKITES

Title of the article: Bulky cations improve band alignment and efficiency in Sn-based perovskite solar cells

French translation: Les cations volumineux améliorent l'alignement des bandes et l'efficacité des cellules solaires de pérovskites à base de Sn

Authors:

Authors' names: Deepak Thrithamarassery Gangadharan, David A Valverde-Chávez, Ricardo Izquierdo, Carlos Silva, Dongling Ma, Juan-Pablo Correa-Baena

Title of the journal or book:

Manuscript submitted to ACS Energy Letters, 09 February 2020.

Contribution of the authors:

Deepak Thrithamarassery Gangadharan, Juan-Pablo Correa-Baena and Dongling Ma conceived the experiments. Deepak Thrithamarassery Gangadharan conducted material synthesis, material characterizations, solar cell fabrication and device characterizations. David A Valverde-Chávez conducted the transient absorption measurements. Deepak Thrithamarassery Gangadharan wrote original draft of the manuscript. Dongling Ma and Juan-Pablo Correa Baena supervised the project. Carlos Silva and Ricardo Izquierdo provided advise and expertise. All authors contributed to the final version of the manuscript.

Link between the previous article or articles and the following:

The previous chapter has shown that a small quantity of PEA cations in iodide-based alloyed perovskites can improve PCE of the solar cell. This chapter explores the effects of substituting a small number of A-site organic cations in mixed halide Sn-Pb alloyed perovskites with PEA cations. The amount of PEA added was optimized to increase both PCE and stability simultaneously. Here, mixed halide alloyed Sn-Pb perovskites were used by mixing $FASnI_3$ and $MAPbBr_3$ perovskite precursors. The incorporation of PEA in mixed halide Sn-Pb perovskites led to homogenization of metals and halides in the perovskite film, thereby achieved a favorable band alignment at perovskite/electron selective layer interface.

With the recently certified power conversion efficiency (PCE) of 25.3%, halide perovskite solar cells (PSCs) are ready to match the performance of silicon (Si) and gallium arsenide (GaAs) thin-film photovoltaic technologies.[16] Nevertheless, the use of toxic lead (Pb) in state-of-the-art ABX_3 perovskites (where A = methylammonium (MA), formamidinium (FA), caesium (Cs) and/or rubidium (Rb); B = Pb and/or tin (Sn); X = chlorine (Cl), bromine (Br) and/or iodine (I)) is challenging in kickstarting large scale production and commercialization of this new technology. Recent reports have shown the bioavailability of Pb from perovskites and their detrimental effects on plants.[324] On the other hand, Sn/Germanium (Ge)-based perovskites, double perovskites such as $Cs_2AgBiBr_6$, $Cs_2AgBiCl_6$, $AgBi_2I_7$, and Bismuth (Bi)/Antimony (Sb)-based perovskite-like structures are some viable alternatives to the Pb-based perovskites.[291,325–333]

Among the Pb-free alternatives, Sn-based perovskites are the most attractive candidates due to their similar optoelectronic properties of the Pb-based counterparts.[173,174,177,334–336] With bandgaps ranging from 1.15 to 3.55 eV, long-lived charge carriers, and high optical density, Sn-based perovskites should, in principle, be able to exhibit similar efficiencies to those of Pb-based perovskites. However, their performance is mainly limited by low open-circuit voltage (V_{oc}) due to high defect concentration in the material.[337,338] One of the main reasons for the poor V_{oc} is unwanted oxidation of Sn^{2+} to Sn^{4+}, which acts as a p-type dopant in the material.[339] To circumvent full oxidation of the perovskites, alloying of Sn with Pb has been used as a promising strategy towards achieving less toxic PSCs with device performances that approach those of the Pb-based counterparts. So far, halide Sn-Pb perovskites with ≤60% Sn of total B-site metal content deliver the highest efficiencies.[340–342] The performance of halide Sn-Pb perovskites with ≥60% Sn is partly limited by oxidization of Sn^{2+} to Sn^{4+}, which generally reduces the V_{oc} of PSCs.[343,344] In addition to being less toxic, the bandgaps of Sn-based perovskites make them ideal for building perovskite-perovskite tandem solar cells.[345]

The band gap of the perovskite can be tuned by using fractional mixtures of I and Br in the composition, known as mixed halide perovskites.[203,204] However, these mixtures are known to induce segregation of halides,[346–348] which is in turn responsible for low photovoltaic performance and stability of the devices.[349–353] The halide segregation involves many different processes, including light-induced halide ion migration, which leads to the formation of I-rich and Br-rich domains.[347] Recently, we found Br-rich aggregates in the mixed halide perovskite films even at dark affect the performance of PSCs, but halide distribution becomes homogenized upon partial substitution of A-site cations with inorganic cations.[354] In another report, we explored partial substitution of A-site cations with large organic cations, which are typically used to synthesize

lower-dimensional perovskites and have been shown as advantageous in lowering the defects in the alloyed perovskites. Recent record efficiency reports suggest that addition of bulky organic cations (such as phenylethyl ammonium (PEA), butylammonium (BA), and guanidinium thiocyanate (GuSCN)) in the perovskites lead to surface passivation, improved charge carrier lifetimes, and reduced ionic transport.[196,340,355–358]

In this work, we employ a mixed halide Sn-rich alloyed perovskite (with 70% Sn and 30% Pb of total B-site metal content) with a band gap of 1.4 eV rather than the widely used narrow band gap iodide-based alloyed perovskites. The mixed halide Sn-Pb alloyed perovskite thin films, $(FASnI_3)_{0.7}$ $(MAPbBr_3)_{0.3}$ (FA/MA/SnPb/I/Br) are prepared by mixing $FASnI_3$ and $MAPbBr_3$ perovskite precursors. The 1.4 eV band gap of FA/MA/SnPb/I/Br is very close to the optimal band gap for achieving maximum theoretical efficiency in a single junction solar cell.[345] This material showed poor solar cell performance mainly due to inferior photocurrent, despite its impressive V_{oc}. The photoelectron spectroscopy revealed the metal halide inhomogeneity in FA/MA/SnPb/I/Br perovskite and their unfavorable band alignment with the electron selective layer, phenyl-C61-butyric acid methyl ester (PCBM). The recombination dynamics in alloyed perovskites were investigated through transient absorption (TA) measurements. A prolonged laser exposure on FA/MA/SnPb/I/Br perovskite during the TA measurement led to a redshift of photobleach near the band gap, indicating photo-induced halide segregation in the samples. Here, we investigate the effects of adding bulky PEA cations in a perovskite composition in solution on the homogenization of metals and halides throughout the film, thereby achieving favorable band alignment with PCBM and reducing the photo-induced halide segregation in mixed halide Sn-Pb alloyed perovskites. The FA/MA(SnPb)I/Br precursor solution is prepared by mixing $FASnI_3$ and $MAPbBr_3$ solutions (in DMF and DMSO) at a 2.33:1 ratio. A 5% of PEA with respect to FA/MA added to produce PEA/FA/MA(SnPb)I/Br precursor solution. A schematic of PEA/FA/MA(SnPb)I/Br precursor solution preparation is presented in Figure 5.1a. We prepared films of FA/MA(SnPb)I/Br and PEA/FA/MA(SnPb)I/Br using the commonly-used antisolvent approach for Sn perovskites (Figure 5.1b).[287,342] The thin films were prepared on a glass substrate for optical characterization. The absorption spectra of these films were measured, and the band gap was extracted for the FA/MA(SnPb)I/Br and PEA/FA/MA(SnPb)I/Br perovskites as shown in Figure1c and d. Generally, Sn-Pb alloyed perovskites are narrow band gap semiconductors (~1.2 eV).[287,340,359]

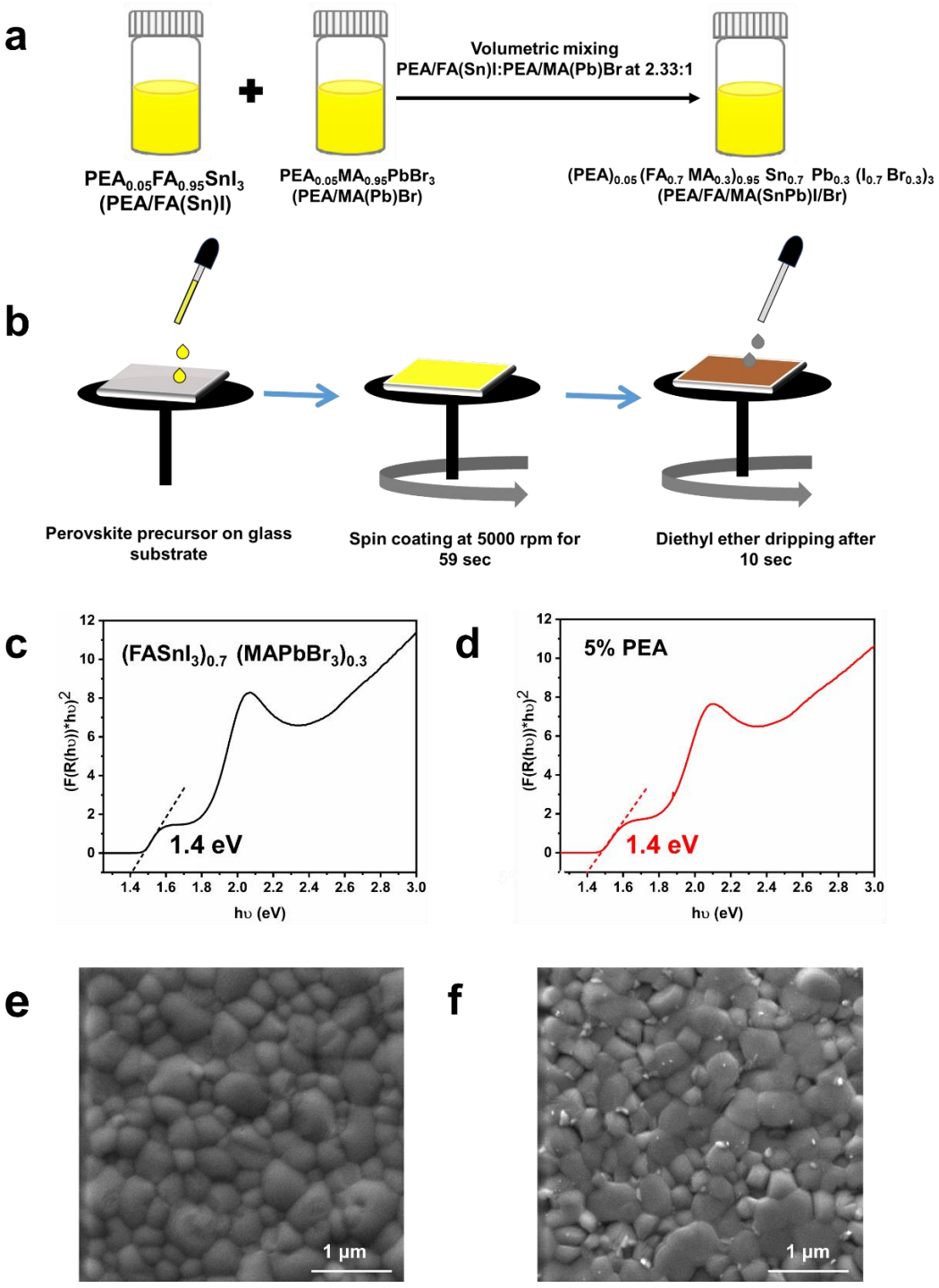

Figure 5.1 Perovskite thin film deposition and their optical properties: a) Schematic of preparation of PEA/FA/MA(SnPb)I/Br perovskite precursor, b) schematic of perovskite thin film fabrication, Tauc plots showing bandgaps of c) FA/MA(SnPb)I/Br and d) PEA/FA/MA(SnPb)I/Br, SEM images of e) FA/MA(SnPb)I/Br and f) PEA/FA/MA(SnPb)I/Br.

The presence of both Pb and Br in the mixed halide Sn-Pb perovskites resulted in a wider band gap of 1.4 eV. Adding 5% of PEA to the FA/MA(SnPb)I/Br perovskite solution did not change the band gap of the perovskite thin film (Figure1d). We characterized the morphology by imaging the top view of the perovskite films prepared on glass /poly (3, 4-ethylene dioxythiophene)-poly (styrene sulfonate) (PEDOT: PSS) substrate by scanning electron microscopy (SEM; Figure 5.1 e and f). The images show pinhole-free perovskite films with crystal grain sizes between 100 nm to 500 nm. Pinhole-free films with large grain sizes are highly desirable for efficient, hysteresis-free, reproducible solar cells.[267,360] No significant changes in grain sizes were observed upon the addition of PEA. Both films showed a relatively broad distribution of grain sizes, which is not ideal for optoelectronic applications and we anticipate a further optimization of solvent and antisolvent engineering could result in larger grains with more uniform distribution.[361,362]

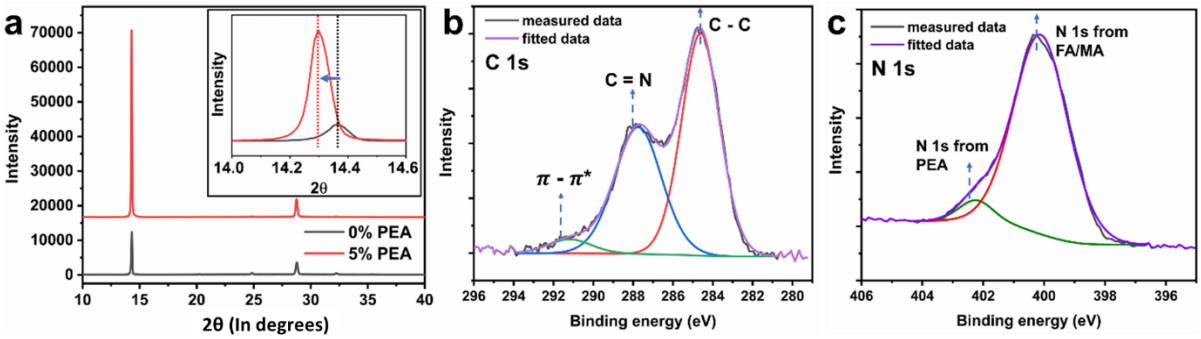

Figure 5.2 Structural properties and elemental composition of perovskite thin film: a) Comparison of XRD spectra of FA/MA(SnPb)I/Br and PEA/FA/MA(SnPb)I/Br (Inset: shift in major XRD peak), high-resolution XPS spectra of (b) C 1s, (c) N 1s of PEA/FA/MA(SnPb)I/Br perovskite.

To understand structural changes to the perovskite films upon the addition of PEA, we performed X-ray diffraction (XRD) measurements. XRD results are presented in Figure 5.2a. A significant increase in XRD peak intensity was observed for PEA/FA/MA(SnPb)I/Br samples compared to FA/MA(SnPb)I/Br showing that PEA/FA/MA(SnPb)I/Br perovskites exhibit increased preferential orientation in the (110) plane than the counterparts without PEA. Interestingly, we observed a shift in XRD peaks in these alloyed perovskites when we incorporated PEA, indicating an increase in lattice constants. The major peak located at 14.365° corresponding (110) crystal plane shifted to 14.297° when PEAI was added (see inset of Figure 5.2a). Generally, incorporation of a cation with a large ionic radius in the structure increases the lattice constants. However, due to its larger size, we would not expect the PEA to be able to be integrated within the perovskite structure.[363] In mixed halide perovskites, adding more iodine in the composition or homogenization of bromine w.r.t iodine increases the lattice constant as iodine expands the lattice. Peak profile analysis has

shown that the addition of PEAI led to a slight decrease in the full width at half maximum (FWHM) (Figure 5.S1). The decrease in the FWHM implies less strained lattice upon addition of 5% PEA. The reduction of FWHM of the (110), (200) peaks shows a lowering of lattice strain along the inorganic bonding direction of I-Sn (or/and Pb)-I, Br-Pb (or/and Sn)-Br or I-Pb (or/and Sn)-Br.[354]

The elemental composition of perovskite films was probed by using X-ray photoemission spectroscopy (XPS). The high-resolution spectra of various elements in perovskites are shown in Figure 5.2b, Figure 5.2c, Figure 5.S2 and Figure 5.S3. Presence of PEA in PEA/FA/MA(SnPb)I/Br confirmed by analyzing C 1s and N 1s peaks (Figure 5.2b and 5.2c). The $\pi - \pi*$ satellite peak observed at 291.2 eV around 6.4 eV from the main C 1s peak corresponds to the aromatic rings of PEA molecule (Figure 5.2b). The N 1s peak of PEA/FA/MA(SnPb)I/Br perovskite (Figure 5.2c) can be deconvoluted into two peaks: (1) located at 402.2 eV correspond to N 1s peak from PEA, and (2) located at 400.1 eV correspond to N 1s peak from FA/MA. Further, we analyzed chemical compositional differences between samples by quantifying XPS signal intensity ratios between different elements. The estimated intensity ratios from XPS compared to the ratios obtained from chemical formula to investigate chemical compositions of thin films. Table 5.1 presents the Sn/Pb and I/Br ratios estimated from high-resolution XPS for the perovskites. The estimated Sn/Pb ratio from XPS for FA/MA(SnPb)I/Br perovskite is 3.90, which deviates from the theoretical value of 2.33. Because XPS is a surface-sensitive technique (less than 3 nm), a large deviation in Sn/Pb ratio suggests a Sn-rich perovskite surface in FA/MA(SnPb)I/Br perovskite thin film. The estimated I/Br ratio, 2.06 for FA/MA(SnPb)I/Br perovskite also differs from the theoretical value (3.00), obtained from chemical formula suggesting I-poor perovskite surface. In short, the FA/MA(SnPb)I/Br perovskite film has a Sn-rich and I-poor surface. This may be due to inhomogeneous distribution of elements throughout the FA/MA(SnPb)I/Br perovskite thin film. Addition of PEA changes the chemical composition of the perovskite film at the surface. The Sn/Pb and I/Br ratios for PEA/FA/MA(SnPb)I/Br are close to the theoretical values, in agreement with the chemical formula (Table 5.1). This suggests that a more homogenous elemental distribution is present throughout the PEA/FA/MA(SnPb)I/Br perovskite film. The more homogeneous nature of the PEA-containing samples is expected to influence its charge carrier recombination in the perovskites since Br-rich/I-rich domains in the perovskite film act as recombination centers, and its interfacial charge transfer. In order to understand the recombination dynamics in mixed halide alloyed perovskites, we studied the photophysical dynamics through transient absorption spectroscopy (TAS), as shown in Figure 5.3.

Table 5.1 Intensity ratios between elements calculated from XPS spectra from perovskites.

Composition	**Sn/Pb (theoretical:2.33)**	**I/Br (theoretical:3)**
FA/MA(SnPb)I/Br	3.90	2.06
PEA/FA/MA(SnPb)I/Br	2.29	3.21

TAS measurements were performed on perovskite/glass substrate to study carrier dynamics and effects of prolonged photo-irradiation in the neat mixed halide alloyed perovskite films. In this scenario, we do not expect any quenching of the TA signal as the glass substrate does not act as a quencher. Pump pulses of 2.70 eV, ~220 fs with fluences of ~500 nJ/cm² were used to photoexcite into the conduction band of the perovskites. The two-dimensional transient absorption maps for FA/MA(SnPb)I/Br and PEA/FA/MA(SnPb)I/Br (Figure 5.3a and 5.3b respectively) present subtle differences. The dominant characteristic of the TAS spectra located around 1.5 eV can be assigned to long-lived ground-state bleaching (GSB) and stimulated emission (SE).[364–368] Another weak GSB+SE region observed above 2.2 eV. The presence of two distinct GSB+SE regions in halide perovskites has been attributed to electronic transitions stem from the perovskite's dual valence band composition. There is an ultrafast photoinduced absorption process that occurs at ~1.4 eV, this can be attributed to hot carrier cooling and bandgap renormalization.[369] Finally a short-lived (~1 ps), weak photoinduced absorption spanning from ~1.9 - 2.2 eV can be attributed to photo-induced refractive index changes and/or to transitions of free carriers from the conduction band (CB) edge to higher states within the CB and/or from lower valence bands (VBs) to the VB edge.[369,370] Figure 5.3c shows the TAS spectra at 0.1 ps normalized to the 1.5 eV peak for both perovskites. Although the spectral shape look similar, the GSB+SE near band gap is slightly red-shifted upon PEA addition and it is in line with the study of Shao *et al.*[182]

The time-dependent behavior of the normalized GSB+SE signal at 1.5 eV is shown in Figure 5.3d. The GSB+SE recovery of the PEA/FA/MA(SnPb)I/Br sample is slightly slower compared to FA/MA(SnPb)I/Br sample suggesting a slower charge carrier depopulation in PEA-containing samples. Slow GSB+SE signal recovery in TAS implies a long-lived charge carrier population and

longer diffusion length in the perovskite semiconductor. Compositional inhomogeneity and lattice strain can instigate non-radiative losses in these mixed halide perovskite films.[371]

Further measurements were performed in order to study the evolution under light exposure, where both pump light and probe light were continuously impinging the sample for over 30 min in a new spot. The FA/MA(SnPb)I/Br sample presents both a decrease and a redshift of bleach near the bandgap (Figure 5.3e). Light-induced redshift often attributed to phase segregation in the mixed halide perovskite.[353,372–374] The dynamics (Figure 5.3g) show a decrease in the GSB+SE intensity, mainly due to phase segregation as well as degradation of the material, the dynamics are reduced from hundreds of ps at the beginning of the measurement to only tens of ps after 30 min exposure to light.

The incorporation of PEA into the perovskite presents a different scenario after 30 minutes of light exposure (Figure 5.3f), there is no evident peak shift of the 1.5 eV feature, and there is only a slight degradation of the GSB+SE peaks. Furthermore, the dynamics become slower but still in the hundreds of ps range (Figure 5.3h). This is a piece of clear evidence that the addition of PEA makes the perovskite structure more robust and less prone to degradation. The photovoltaic properties of FA/MA(SnPb)I/Br and PEA/FA/MA(SnPb)I/Br perovskites were evaluated in a planar solar cell architecture consisting of indium doped tin oxide (ITO)/ poly (3, 4-ethylene dioxythiophene)-poly (styrene sulfonate) (PEDOT:PSS)/perovskite/phenyl-C61-butyric acid methyl ester (PCBM)/Bathocuproine (BCP)/silver (Ag) (Figure 5.4a). The current density-voltage (J-V) curves and external quantum efficiencies (EQEs) of champion devices are shown in Figure 5.4 (b-c) and Figure 5.4d, respectively. FA/MA(SnPb)I/Br devices exhibited an average PCE of 7.03$\pm$0.70 % with open-circuit voltage (V_{oc}) of 0.72$\pm$0.03 V, a short-circuit current density (J_{sc}) of 15.03$\pm$1.35 mAcm^{-2} and a fill factor (FF) of 64.73$\pm$1.36%. It should be mentioned that the V_{oc} reported here for FA/MA(SnPb)I/Br devices is among the highest for a Sn-rich alloyed perovskite solar cell. Our previous report on alloyed perovskite solar cells employing $(FASnI_3)_{0.7}(MAPbI_3)_{0.3}$ perovskite (an iodide-based alloyed perovskite) showed a lower V_{oc} of 0.395±0.05 V. The high V_{oc} in mixed halide-based alloyed perovskite system (FA/MA(SnPb)I/Br) is as a result of wider band gap (1.4 eV) and reduced recombination dynamics of this material. We are aware of only one report with similar V_{oc} (0.76 V) for Sn-rich perovskite composition ($FA_{0.8}Cs_{0.2}Sn_{0.7}Pb_{0.3}I_3$), where authors used Cs to tune the band gap of the material *via* octahedral tilting.[294]

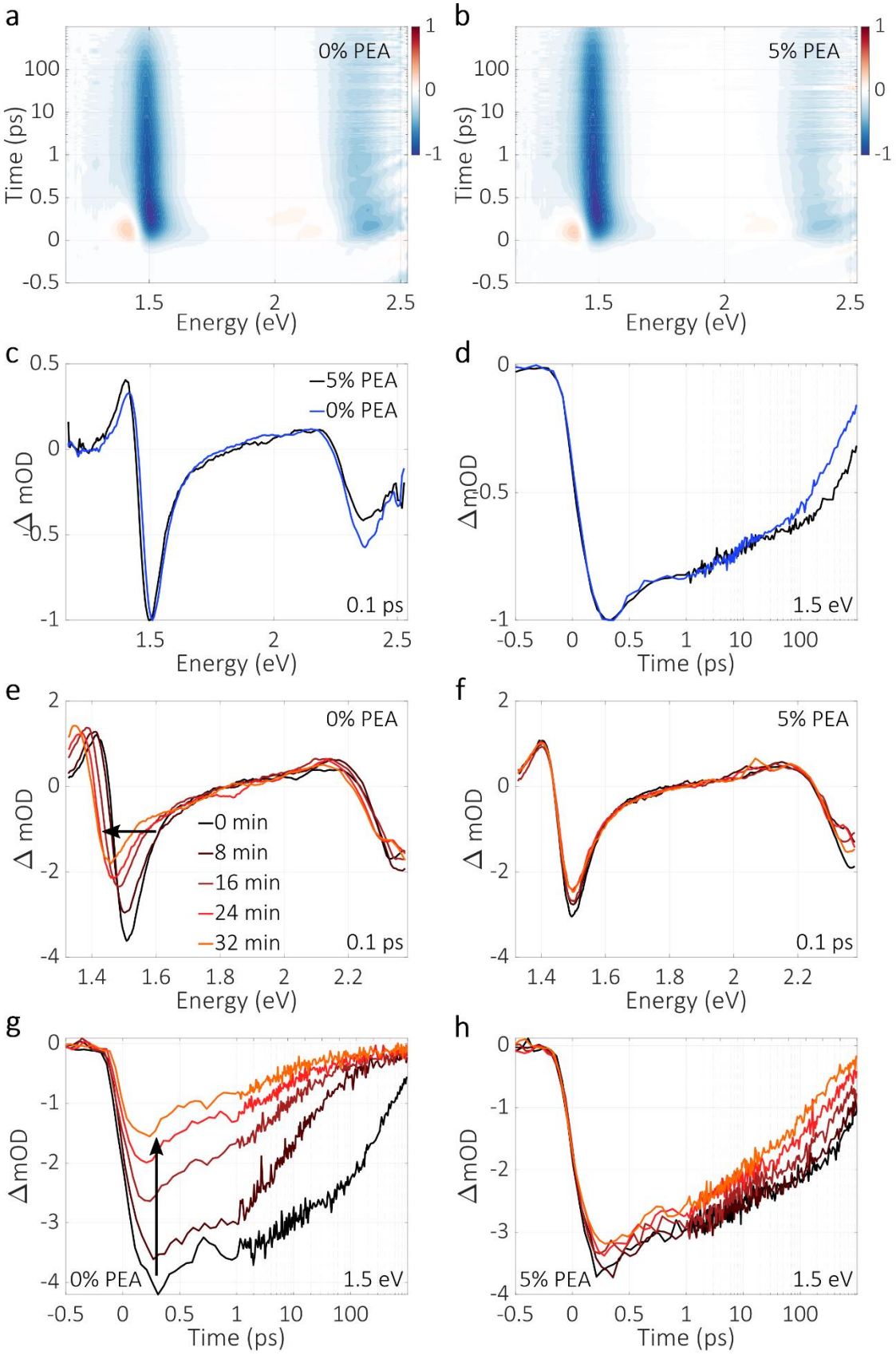
a
0% PEA
Time (ps)
Energy (eV)
b
5% PEA
Time (ps)
Energy (eV)
c
5% PEA
0% PEA
Δ mOD
0.1 ps
Energy (eV)
d
Δ mOD
1.5 eV
Time (ps)
e
0% PEA
0 min
8 min
16 min
24 min
32 min
Δ mOD
0.1 ps
Energy (eV)
f
5% PEA
Δ mOD
0.1 ps
Energy (eV)
g
ΔmOD
0% PEA
1.5 eV
Time (ps)
h
ΔmOD
5% PEA
1.5 eV
Time (ps)

Figure 5.3 Charge carrier dynamics and optical properties of perovskite thin films a) Transient absorption 2D maps of a) FA/MA(SnPb)I/Br perovskite and b) PEA/FA/MA(SnPb)I/Br perovskite, c) comparison of normalized TAS of FA/MA(SnPb)I/Br perovskite and PEA/FA/MA(SnPb)I/Br perovskite at 0.1 ps after excitation with a 2.7 eV laser pulse, and d) comparison of time-dependent behavior of the normalized GSB+SE signals at 1.5 eV. e) Evolution of TAS at 0.1 ps after pump excitation and white light (WL) probe exposure for FA/MA(SnPb)I/Br and f) PEA/ FA/MA(SnPb)I/Br perovskites g) Evolution of TAS dynamics at 1.5 eV after pump excitation and WL probe exposure for FA/MA(SnPb)I/Br and h) PEA/ FA/MA(SnPb)I/Br perovskites.

The addition of PEA yields a significant enhancement in the overall device performance. PEA/FA/MA(SnPb)I/Br devices exhibited an average PCE of 12.06±0.62% with V_{oc} of 0.76±0.01 V, J_{sc} of 22.61±1.06 mAcm^{-2} and FF of 69.42±0.78%. Figure 5.4 (d-g) shows a box plot of summarizing the photovoltaic parameters obtained for FA/MA(SnPb)I/Br and PEA/FA/MA(SnPb)I/Br devices from 21 devices per perovskite compound.

All the photovoltaic parameters were improved in PEA/FA/MA(SnPb)I/Br devices compared to FA/MA(SnPb)I/Br devices, with the J_{sc} showing the most substantial enhancement. The enhancement in J_{sc} was also reflected in the EQE, which is the ratio of the number of photons to the number of generated charge carriers in a solar cell. The increase in V_{oc} in PEA/FA/MA(SnPb)I/Br devices correlates to the less halide segregation in perovskite films, as seen by TAS. Halide segregation under illumination causes the formation of Br-rich (I-poor) or I-rich (Br-poor) domains in mixed halide perovskites which facilitates recombination and limits the V_{oc} of the solar cells.[375] The FF depends in part on the band alignment at perovskite/PEDOT:PSS and perovskite/PCBM interfaces. An increased conductivity in PEA/FA/MA(SnPb)I/Br film as a result of reduced recombination might be partly responsible for increased FF in the PEA-containing devices. The devices exhibited improved J-V hysteresis for the PEA/FA/MA(SnPb)I/Br materials. The Hysteresis-Index (H-index) = ($PCE_{forward}$ - $PCE_{reverse}$/$PCE_{reverse}$)×100, a metric to measure the severity of J-V hysteresis is used to compare both systems. The FA/MA(SnPb)I/Br device shows a high H-index of 21% while PEA/FA/MA(SnPb)I/Br device shows an H-index of 8%. The substantial increase in J_{sc} in PEA/FA/MA(SnPb)I/Br devices motivated to investigate band alignment of perovskites with charge selective layers, as this has been observed to influence the photocurrent of devices heavily.[376]

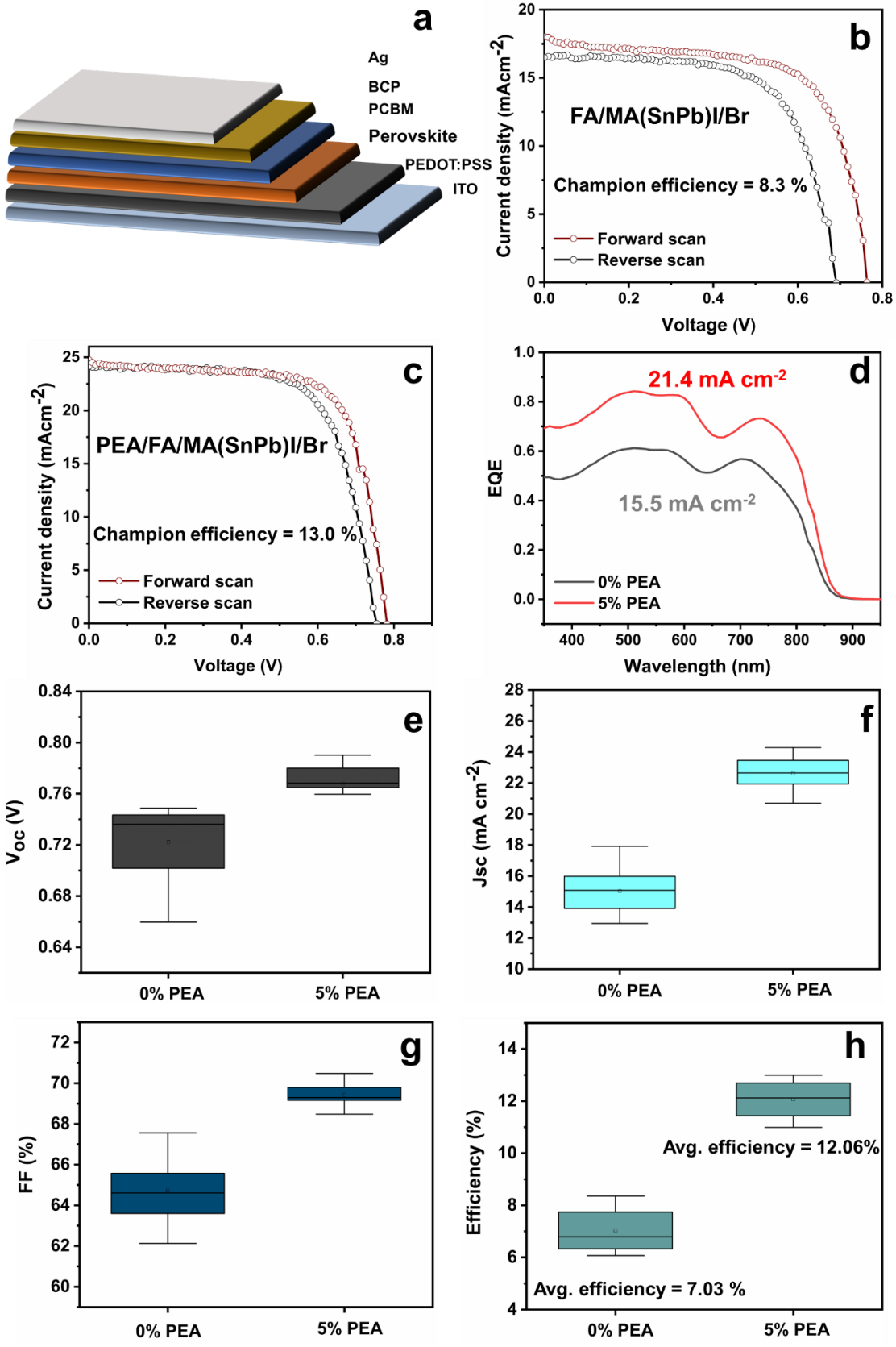
a
Ag
BCP
PCBM
Perovskite
PEDOT:PSS
ITO
b
FA/MA(SnPb)I/Br
Champion efficiency = 8.3 %
Forward scan
Reverse scan
Current density (mAcm-2)
Voltage (V)
c
PEA/FA/MA(SnPb)I/Br
Champion efficiency = 13.0 %
Forward scan
Reverse scan
Current density (mAcm-2)
Voltage (V)
d
21.4 mA cm-2
15.5 mA cm-2
0% PEA
5% PEA
EQE
Wavelength (nm)
e
Voc (V)
0% PEA
5% PEA
f
Jsc (mA cm-2)
0% PEA
5% PEA
g
FF (%)
0% PEA
5% PEA
h
Avg. efficiency = 12.06%
Avg. efficiency = 7.03 %
Efficiency (%)
0% PEA
5% PEA

Figure 5.4 Solar cell configuration and characterization a) Schematic of the perovskite solar cells b) J-V curves of solar cells employing FA/MA(SnPb)I/Br and c) PEA/FA/MA(SnPb)I/Br in PEDOT: PSS/Perovskite/PCBM/BCP/Ag device configuration, d) comparison of EQE spectra of FA/MA(SnPb)I/Br and PEA/FA/MA(SnPb)I/Br devices (calculated J_{sc} from EQE presented in the graph), statistical values for e) V_{oc}, f) J_{sc}, g) FF, and h) efficiency from 21 devices per perovskite composition. (In box plot, median is the line drawn in the box, small square dot in the box is the average value and maximum and minimum values are represented by top and bottom horizontal lines)

Ultraviolet photoemission spectroscopy (UPS) was performed on FA/MA(SnPb)I/Br and PEA/FA/MA(SnPb)I/Br perovskites to understand the ionization energy (with respect to vacuum), and therefore the valence band maximum (VBM) of these compounds (Figure 5.5(a-d)). The PEA/FA/MA(SnPb)I/Br showed lower ionization energy compared to that of FA/MA(SnPb)I/Br (-5.66 eV vs. -6.04 eV, respectively). As we have noted in the XPS discussion, the precise chemical composition may be different in PEA/FA/MA(SnPb)I/Br compared to FA/MA(SnPb)I/Br which may result in changes in VBM position of the material. We reason that I-poor (and potentially Br-rich) perovskite surfaces of FA/MA(SnPb)I/Br influence the energetic position of the VBM as Br-perovskites exhibit a significantly higher ionization energy (and therefore deeper VBMs).[377] Our observation is in line with DFT calculations done by Beljonne *et al.*, where authors have shown that perovskite film surface termination plays critical role in determining VBM and conduction band minima (CBM) energy levels.[378] Besides, Wang *et al.* recently reported a similar effect on mixed halide Pb perovskites upon addition of n-propylammonium (PA) spacer cations, showing a CBM upshift of 0.16 eV.[379] To construct a conduction band alignment with the electron selective contact we added the optical bandgap to the ionization energy of the compounds and the known energy levels of PCBM [380] and PEDOT:PSS [381] and sketched it in Figure 5.5e and 5.5f. Due to a deeper VBM, the CBM of FA/MA(SnPb)I/Br has an unfavorable band alignment with PCBM creating an energy barrier of approximately 0.3 eV for the electron transport across perovskite/PCBM interface. In contrast, the CBM of PEA/FA/MA(SnPb)I/Br aligns well with that of PCBM with no apparent barrier across the perovskite/PCBM interface. Energetic barriers at the electron selective contact/perovskite interface have been shown to cause low J_{sc} and increased hysteresis index in perovskite solar cells.[376] While the favorable band alignment across perovskite/PCBM boosts the J_{sc} in PEA/FA/MA(SnPb)I/Br solar cells, the CBM misalignment with PCBM inhibits interfacial charge transfer in FA/MA(SnPb)I/Br solar cells which in turn reduces the J_{sc} in the devices.

The efficiency of interfacial charge transfer also affects the J-V hysteretic behavior in the device. The energy barrier at perovskite/PCBM interface leads to the accumulation of charges at the interface inducing a high electric field and/or dipole formation causing a large J-V hysteresis in the device.[376] Improved J–V hysteretic behavior in PEA/FA/MA(SnPb)I/Br solar cells can be linked to efficient charge collection at the perovskite/PCBM interface.

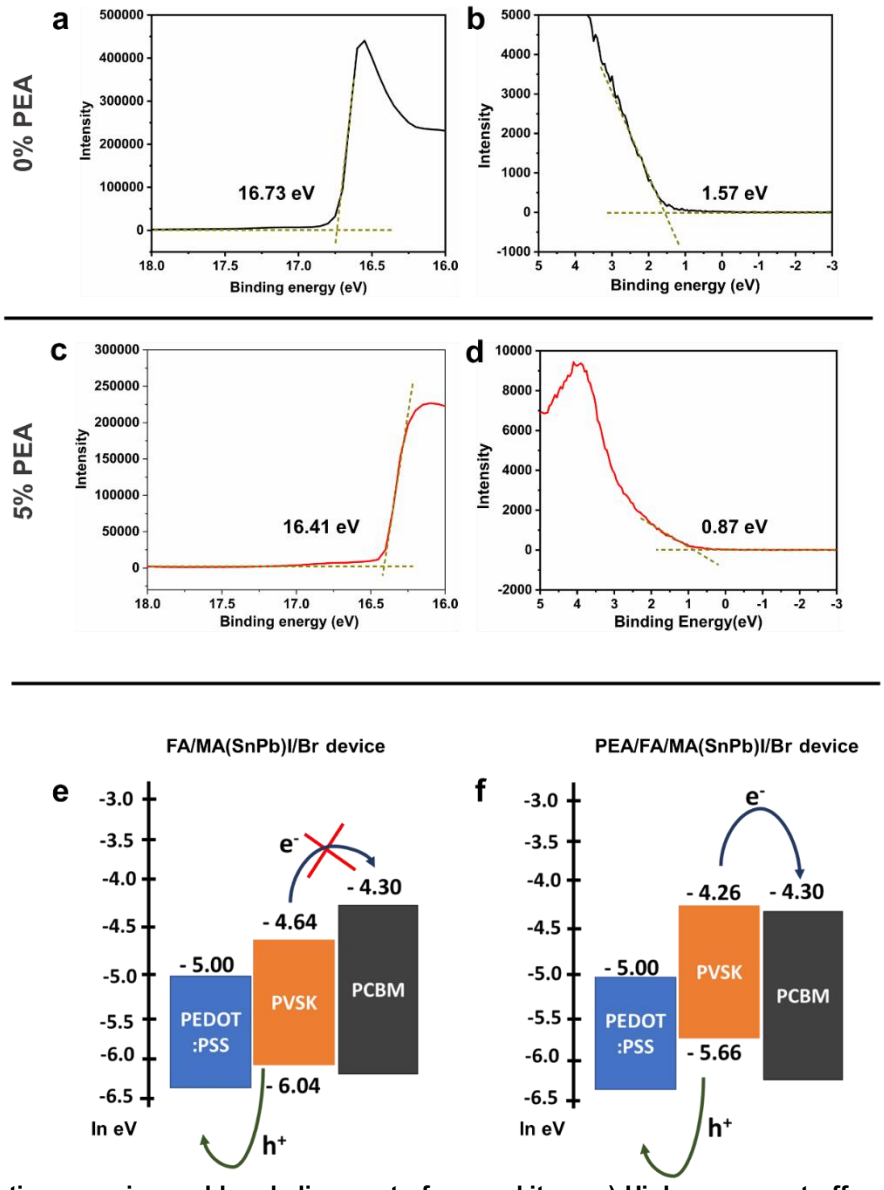

Figure 5.5 Ionization energies and band alignment of perovskites. a) High energy cut-off and b) low energy cut-off of UPS spectra for the FA/MA(SnPb)I/Br perovskite, c) High energy cut-off and d) low energy cut-off of UPS spectra for the PEA/FA/MA(SnPb)I/Br perovskite, and band alignment diagrams of e) FA/MA(SnPb)I/Br device and f) PEA/FA/MA(SnPb)I/Br device.

In this work, we found that compositional inhomogeneities and light-induced halide segregation in mixed halide Sn-Pb perovskite films are mainly responsible for their lower solar cell performance and stability. Photoelectron spectroscopy and TA results reveal that the addition of bulky PEA cations in mixed halide Sn-Pb perovskites homogenizes the metals and halides and reduces the light-induced halide segregation in the material. Compositional homogenization in PEA-containing mixed halide Sn-Pb perovskites presents a favorable band alignment across perovskite/PCBM improving the photocurrent, FF, and J-V hysteretic behavior in the solar cells. While the suppression of light-induced halide segregation lowers the recombination, which results in improved V_{oc} in the PEA/FA/MA(SnPb)I/Br devices. In summary, we investigated the beneficial effects of incorporating bulky organic cations in mixed halide Sn-Pb perovskites and their impact on the performance of Sn-based mixed halide perovskite solar cells.

ASSOCIATED CONTENT

Supporting Information

Experimental methods and various characterization results including X-ray diffraction, X-ray photoelectron spectroscopy, and transient absorption. (PDF)

AUTHOR INFORMATION

Corresponding Authors

* Juan-Pablo Correa-Baena, E-mail: jpcorrea@gatech.edu, Twitter: @jpcorreabaena

* Dongling Ma, E-mail: ma@emt.inrs.ca

First Author

Deepak Thrithamarassery Gangadharan, E-mail: deepak.thrithamarassery@emt.inrs.ca, Twitter: @wavefuncollaps

Notes

The authors declare no competing financial interest.

ACKNOWLEDGMENT

Financial support from the Natural Sciences and Engineering Research Council (NSERC) of Canada, in the context of a NSREC Discovery Grant and a NSERC Strategic Grant (Industry partner: Canadian Solar Inc.) is greatly appreciated. D.M is also grateful for the financial support from Quebec Center for Functional Materials (CQMF), Canada. D.T.G acknowledges scholarship support from the Fonds de recherche du Québec–Nature et technologies (FRQNT) for the Bourses de recherche en énergie / Doctorat (PhD Energy Research Scholarship) and Stages internationaux -Énergie-Numérique-Aérospatiale (International internship Scholarship-Energy-Digital-Aerospace).

Supplementary Information

Materials and Methods

Materials: All chemicals were used as received. Methylammonium iodide (CH_3NH_3I), Formamidinium iodide ($CH(NH_2)_2I$) and phenylethylammonium iodide ($C_6H_5(CH_2)_2NH_3I$) were purchased from Dyesol. Tin iodide (SnI_2), tin fluoride (SnF_2), dimethylformamide (DMF) and dimethyl sulfoxide (DMSO), Bathocuproine (BCP) were purchased from Sigma Aldrich. Lead iodide (PbI_2) was bought from Acros Organics. Phenyl-C61-butyric acid methyl ester ($PC_{61}BM$) and poly (3, 4-ethylene dioxythiophene)-poly (styrene sulfonate) (PEDOT: PSS; Clevios™ P VP AI 4083) were obtained from 1-Materials and Heraeus, respectively.

Alloyed perovskite precursor solution: $FASnI_3$ precursor solution (1.45 M) was prepared by adding equimolar FAI and SnI_2 powders and 20 mol% of SnF_2 into a mixture of DMF: DMSO (4:1 v/v). $MAPbBr_3$ precursor solution (1.45 M) was prepared by adding MAI and $PbBr_2$ in a mixture of DMF: DMSO (4:1 v/v). $(FASnI_3)_{0.7}(MAPbBr_3)_{0.3}$ solution was prepared by stoichiometrically mixing $FASnI_3$ and $MAPbI_3$ solutions. The PEA-FA/MA alloyed perovskite precursor solutions were prepared by stoichiometrically substituting FAI/MAI with 5% PEAI in $(FASnI_3)_{0.7}(MAPbBr_3)_{0.3}$ precursor solution.

Solar cell fabrication: Patterned ITO-coated glasses were cleaned by sonication in detergent followed by sequential washing with deionized water, acetone, and isopropanol. After drying under air flow, the substrate surface was cleaned by oxygen plasma for 10 min under rough vacuum. PEDOT: PSS solution was spin-coated on top of the ITO-coated glass substrate at 4500 rpm for 45 s; PEDOT: PSS performs as the hole transporting layer. The PEDOT: PSS film was then dried in air on a hot plate (set at 170 °C) for 10 min. After drying, the substrate was transferred to a nitrogen-filled glovebox for further use. The FA/MA(SnPb)I/Br and PEA/FA/MA(SnPb)I/Br

alloyed perovskite absorber layers were spin-coated on the PEDOT: PSS film at 5000 rpm for 60 s. Diethyl ether was dropped onto the spinning substrate. The spin coated films were annealed at 100℃ for 10 minutes. Then the $PC_{61}BM$ solution (20 mg/mL in chlorobenzene) was spin-coated on top of the perovskite film at 2000 rpm for 60 s to form a 20 nm thick electron transporting layer. Subsequently, a thin film of BCP solution in 2-propanol was spin coated onto PCBM film at 2000 rpm. Finally, the film was transferred to a thermal evaporation chamber inside the nitrogen filled glove box. The chamber was pumped down to 1×10^{-6} Torr for silver deposition. The 100 nm thick silver top electrode was deposited through a shadow mask that defines the active device area as 0.06 cm^2 for the solar cells.

Perovskite Film Characterization: Topography of perovskite film surface was obtained by using LYRA3 TESCAN SEM instrument. Absorption spectra were collected by using a UV-Visible-NIR spectrometer Lambda 750 (Perkin Elmer). XRD measurements were carried out using a Panalytical X-Pert PRO MRD X-Ray diffractometer. The chemical states of elements were probed by an XPS spectrometer (ESCALAB 220I-XL) equipped with an Al Kα (1486.6 eV) monochromatic source.

Solar cell characterization: Solar cell performance was measured using a class ABA LED solar simulator, which was calibrated to deliver simulated AM 1.5 sunlight at an irradiance of 100 mW/cm^2. The irradiance was calibrated using an NREL-calibrated KG5 filtered silicon reference cell. Current density-voltage (J-V) curves were recorded using a source meter (Keithley 2400, USA). External quantum efficiency (EQE) measurements were conducted by using an IQE200B system (Newport Corporation).

Transient absorption spectroscopy (TAS): TAS measurements were performed by a commercial system from Light Conversion similar to HARPIA transient absorption spectrometer. Laser pulses of 1030 nm, ~220 fs are generated in an ultrafast laser system at 100 kHz repetition rate (PHAROS Model PH1-20-0200-02-10, Light Conversion). The output laser beam is split, where one portion is sent into a commercial optical parametric amplifier (ORPHEUS, Light Conversion) to obtain the 2.7 eV pump excitation pulse, typical fluences used in the experiment were around 500 nJ/cm^2. The remaining of the laser beam is used to generate a probe beam by focusing the laser pulses into a sapphire crystal to obtain a white light continuum spanning 480 - 1100 nm. The probe beam is transmitted through the sample and is modulated by the pump beam. The probe beam is finally sent to an imaging spectrograph (Shamrock 193i, Andor Technology) and then detected with a multichannel detector (256 pixels, 200–1100 nm wavelength sensitivity range). The transient absorption data was taken at two different central wavelengths and were

later merged and corrected for the chirp with the CarpetView software provided by Light Conversion.

We noticed a significant degradation of FA/MA(SnPb)I/Br perovskite upon transient absorption measurement. These perovskites are prone to photoinduced degradation; exposure to the powerful laser or white light continuum during the transient absorption measurement damage the perovskite film. As show in the main text, PEA/FA/MA(SnPb)I/Br samples only show slight degradation indicating better photostability of the material. The perovskites are also sensitive to the ambient air humidity, to avoid degradation both samples were loaded into an argon filled optical chamber, all TAS measurements were carried out in this chamber.

Analysis of XRD peak profile:

The lattice constant was calculated from major (110) peak in XRD measurements. The addition of PEA increases the lattice from 6.16 Å to 6.19 Å. Peak profile analysis of shows a slight reduction full width at half maximum (FWHM) of peaks corresponding to (110) and (200) crystal planes upon the incorporation of PEA (Figure 5.S1). The addition of PEA in mixed halide alloyed perovskites led to reduction of FWHM from 0.09865±0.00124 to 0.0920±0.000419 and 0.20442±0.01541 to 0.1873±0.0424 for (110) and (200) peaks respectively.

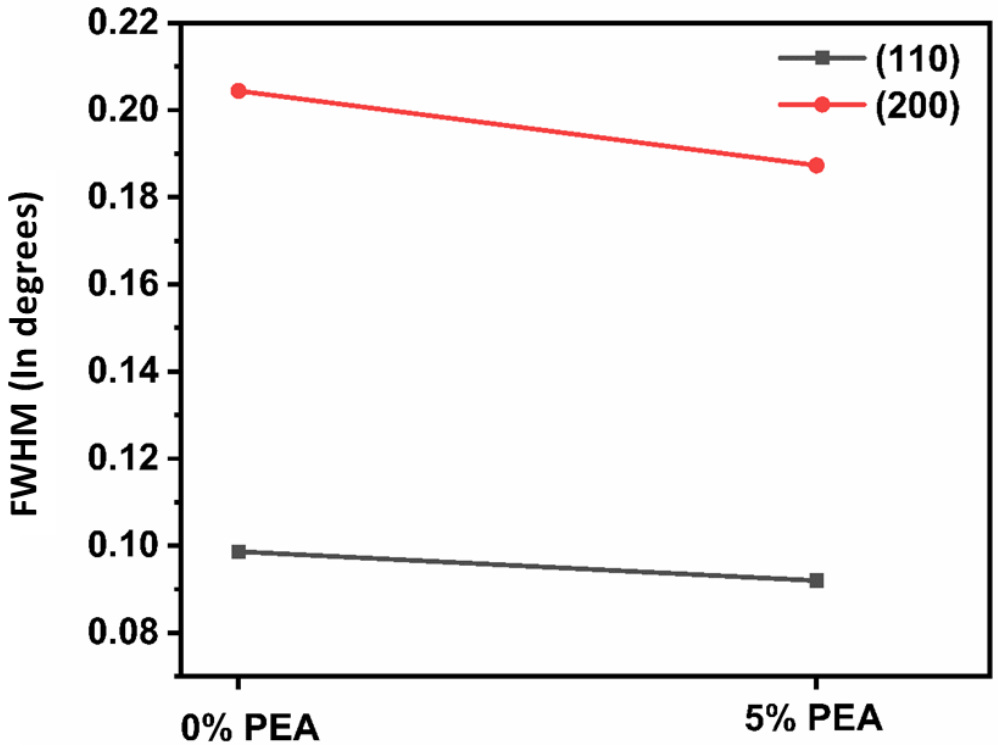

Figure 5.S1 Variation in FWHM of peaks corresponding to (110) and (200) crystal planes of FA/MA(SnPb)I/Br and PEA/FA/MA(SnPb)I/Br perovskites.

Quantification of elements using XPS spectra:

The high-resolution spectra of elements in FA/MA(SnPb)I/Br and PEA/FA/MA(SnPb)I/Br perovskites shown in Figure 5.S2 and Figure 5.S3 respectively.

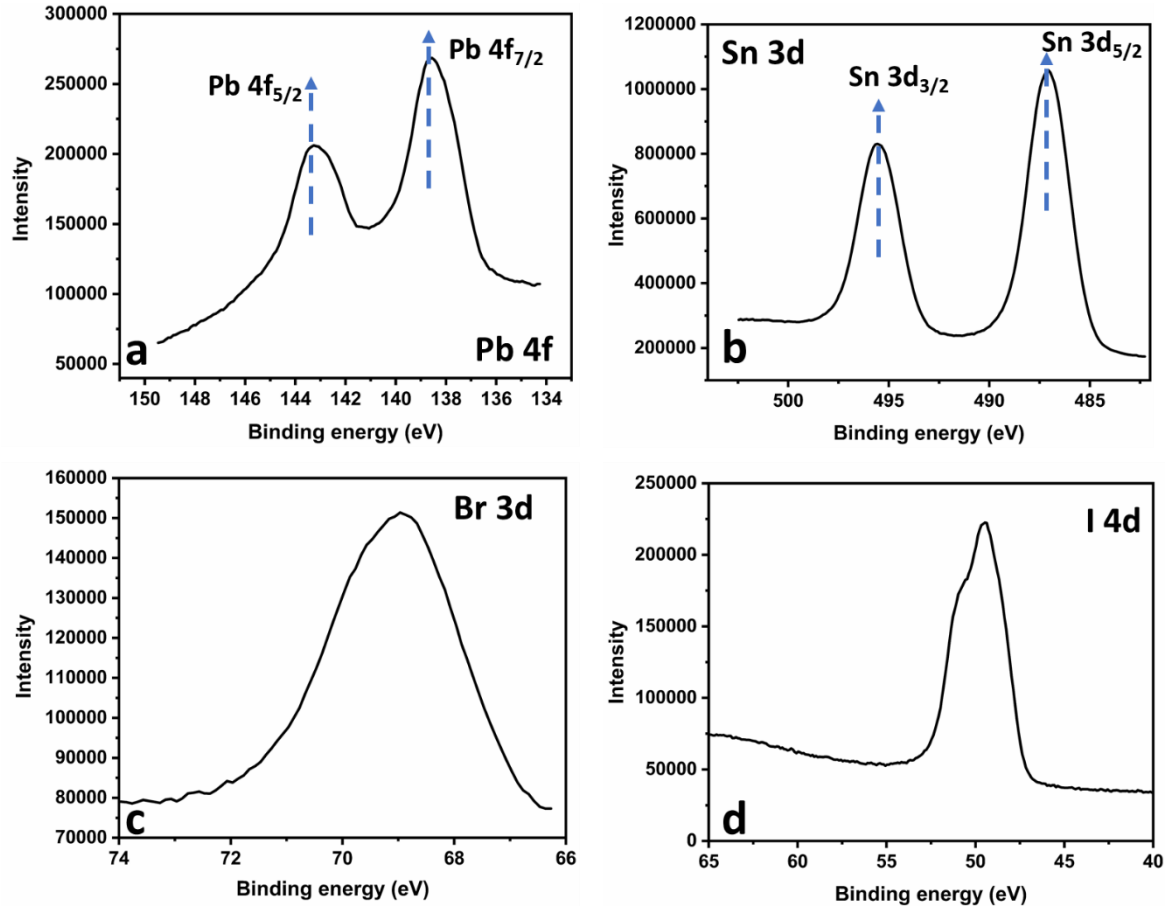

Figure 5.S2. High-resolution XPS spectra of **(a)** Pb 4f, **(b)** Sn 3d, **(c)** Br 3d, and **(d)** I 4d in FA/MA(SnPb)I/Br perovskite film.

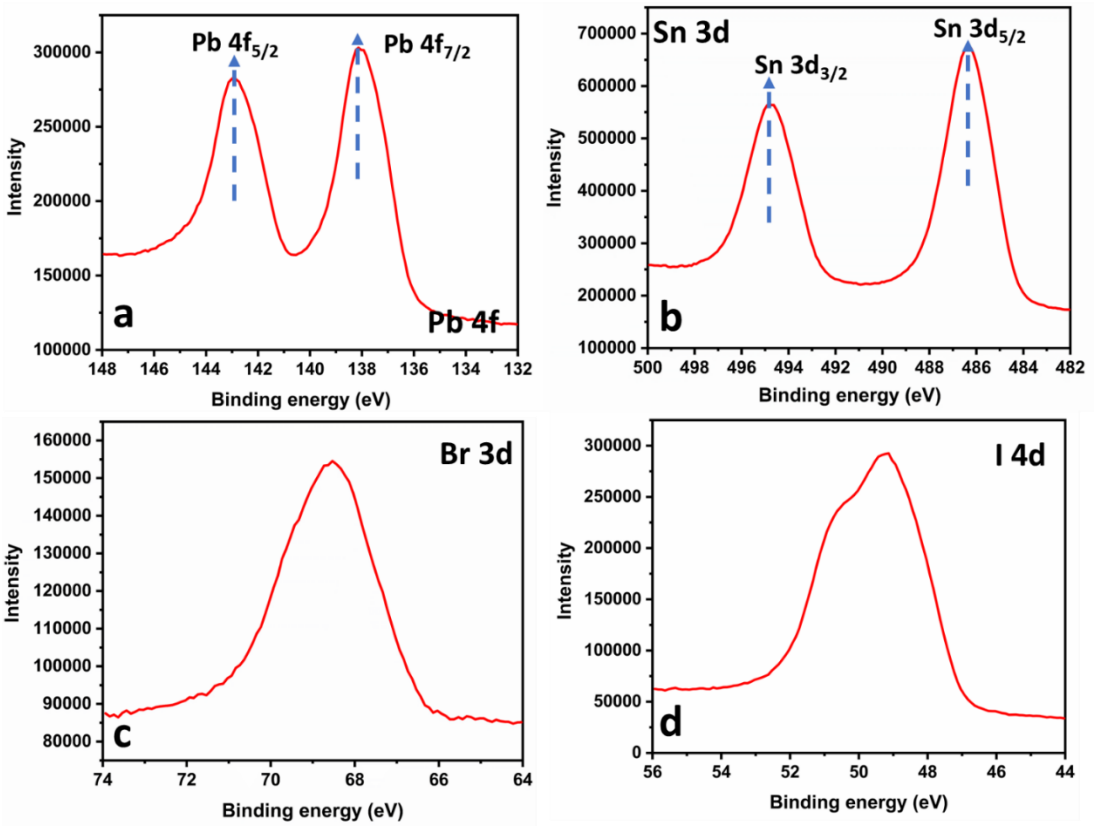

Figure 5.S3. High-resolution XPS spectra of **(a)** Pb 4f, **(b)** Sn 3d, **(c)** Br 3d, and **(d)** I 4d in PEA/FA/MA(SnPb)I/Br perovskite film.

6 GENERAL DISCUSSION AND CONCLUSION

This Ph.D. thesis addresses two greatest concerns in the state-of-the-art 3D halide perovskites, namely, improving chemical stability and realizing efficient Pb-less perovskites.

6.1 Conclusions

Even though halide perovskites are promising photovoltaic materials, the presence of toxic lead (Pb) (B-site cations) in the state-of-the-art halide PSCs hampers the marketability of this technology. Pb-based halide perovskites in contact with water or humid air form water-soluble by-products of Pb, which can accumulate within the food chain and reach the human body. Therefore, countries around the world adhere to lead-free directives which set a maximum amount of lead in electronic devices. These directives generally restricted to 0.1% in weight the maximum concentration of lead in each homogeneous material contained in any electronic devices, i.e., the perovskite material within a perovskite solar cell. Meanwhile, it should be noted that highly efficient PSCs contain more than 10% lead in weight. And so, the real-world applications using state-of-the-art Pb perovskites are unfeasible.

However, the electronic configuration of divalent Pb^{2+} in the ABX_3 perovskite structure is crucial for the photovoltaic behavior of the solar cell. Alternatively, alloying or partially replacing Pb with other divalent metals is a promising strategy to adhere to the Pb-free directives for restricting Pb in electronic devices to 0.1% in weight without much compromising the photovoltaic performance. In my Ph.D., it has been shown that alloying Pb with Sn perovskites is a promising strategy for achieving less toxic solar cells with respectable photovoltaic performance, alloying metals also provide compositional space for additional bandgap tuning of perovskites; the bandgap in alloyed perovskites demonstrates bowing behavior, where alloys display lower bandgaps than either of the “parent” compositions. But they are highly unstable under ambient conditions mainly due to oxidation of Sn^{2+} to Sn^{4+}. This work explores use of bulky organic cations to modify defect chemistry and compositional homogeneity in alloyed perovskites. PEA can have different effects on halide perovskites depending on quantity of PEA and composition of the perovskite. The addition of PEA in iodide-based alloyed perovskites mainly alter defect chemistry of the material resulting in inhibiting Sn vacancy formation. It is well known that mixed halide perovskites (for example partially substituting iodide with bromide) have greater structural stability than halide perovskites. Additionally, Br substitution allows to tune the band gap of perovskites. The maximum efficiency of a single-junction solar cell calculated by the Shockley-Queisser model as

a function of bandgap predicts ~1.4 eV as an ideal bandgap. Here, an ideal bandgap of Pb-less perovskites was obtained by partial substitution of X-site anion, I with Br. Even though they showed an impressive V_{oc} of 0.72±0.03 V for a Sn-rich alloyed perovskite, it did not translate into good solar cell performance mainly due to inferior photocurrent. The UPS studies revealed an unfavorable band alignment at perovskite/PCBM interface is mainly responsible for lower photocurrent in mixed halide Sn-Pb alloyed perovskite devices, and therefore the efficiency. Further, the effects of PEA incorporation in homogenizing halides and metals in mixed halide alloyed perovskites were explored. The XPS results revealed homogenization of Br and Sn upon addition of PEA in the perovskites. Importantly, the homogenization of Br and Sn led to favorable band alignment at perovskite/PCBM interface which resulted in significant improvement in J_{sc} and efficiency.

6.2 Perspectives

So far, Sn and Ge-based perovskites are the highest-performing Pb-free solar cells, but the fact that Sn and Ge are more stable in the 4+ oxidation state causes critical stability issues. This Ph.D. work would be an excellent guideline to develop other Pb-free/ alloyed perovskites. Theoretical studies have shown that divalent alkaline-earth metals such as Ba^{2+} and Ca^{2+} can also form the ABX_3 perovskite structure. Ba and Ca metals have an exclusive oxidation state of +2, as the Ba^{2+} and Ca^{2+} ions respectively make them promising Pb alternatives. Thus, the use of divalent alkaline-earth metals like Ba or Ca as B-site cations solve the critical issue of stability related to oxidation of mostly used Pb-free, B-site cations such as Sn and Ge. Unfortunately, Ba and Ca-based perovskites exhibit relatively larger bandgaps (2.95-3.3 eV), which are unsuitable for single-junction solar cell applications. Following the protocols established in Pb-Sn alloy project, design of Pb-free perovskite materials with the bandgap of 1.4 eV by alloying Ba or Ca with Sn is proposed. Further, defect chemistry and compositional homogeneity can be fine-tuned by partial substation of A-site cations with bulky organic cations like PEA, BA or other bifunctional organic molecules to improve photovoltaic performance and stability.

The experimental viewpoints discussed above highlights the prominent role played by nature of divalent metals, and defects in the optoelectronic properties of perovskites. For a vivid grasp of observed phenomena, a computational modelling of the material is necessary. Density functional theory (DFT) calculations are very useful in predicting cation and anion vacancies, and band gap of halide perovskites. In this regard, experimental observations together with DFT predictions is essential to design and understand the Pb-free/Pb-less perovskites.

In summary, developing Pb-free/Pb-less perovskites by alloying metals and study of their optoelectronic properties are technologically relevant topic and relatively new in the perovskite field.

7 BIBLIOGRAPHY

1. Reddy, K. G.; Deepak, T. G.; Anjusree, G.S.; Thomas, S.; Vadukumpully, S.; Subramanian, K. R. V; Nair, S. V; Nair, A S. On Global Energy Scenario, Dye-Sensitized Solar Cells and the Promise of Nanotechnology. *Phys. Chem. Chem. Phys.,* **2014**, 16, 6838–6858.
2. NSERC Energy Maps, https://www.nrcan.gc.ca/maps-tools-and publications/maps /energymaps/16872. (accessed Apr 9, 2020).
3. New Energy Outlook 2019. https://about.bnef.com/new-energy-outlook/.
4. PVinsights. http://pvinsights.com/RetailerPrice.php (accessed Feb 9, 2020).
5. Cao, G.; Wang, D. Nanomaterials for Energy Conversion and Storage, **2017**.
6. Alternative Energy Tutorials. Solar Cell I-V Characteristic and the Solar Cell I-V Curve,http://www.alternative-energy-tutorials.com/energy-articles/solar-cell-i-v characteristic.html.
7. Alsema, E. A.; De Wild-Scholten, M. J. Environmental Impacts of Crystalline Silicon Photovoltaic Module Production. In Materials Research Society Symposium Proceedings. **2006**.
8. Tyagi, V. V.; Rahim, N. A. A.; Rahim, N. A.; Selvaraj, J. A. L. Progress in Solar PV Technology: Research and Achievement. *Renew. Sustain. Energy Rev.,* **2013**, 20, 443-461.
9. Fthenakis, V. Sustainability of Photovoltaics: The Case for Thin-Film Solar Cells. *Renew. Sustain. Energy Rev.,* **2009**, 13, 2746-2750.
10. Hardin, B. E.; Snaith, H. J.; McGehee, M. D. The Renaissance of Dye-Sensitized Solar Cells. *Nat. Photonics,* **2012**, 6, 162–169.
11. O'Regan, B.; Grätzel, M. A Low-Cost, High-Efficiency Solar Cell Based on Dye-Sensitized Colloidal TiO2 Films. *Nature*, **1991**, 353, 737–740.
12. Sivaram, V.; Stranks, S. D.; Snaith, H. J. Outshining Silicon. *Sci. Am.* **2015**, 313, 54–59.
13. Kojima, A.; Teshima, K.; Shirai, Y.; Miyasaka, T. Organometal Halide Perovskites as Visible-Light Sensitizers for Photovoltaic Cells. *J. Am. Chem. Soc.,* **2009**, 131, 6050–6051.
14. Green, M. A.; Ho-Baillie, A.; Snaith, H. J. The Emergence of Perovskite Solar Cells. *Nat. Photonics*, **2014**, 8, 506–514.
15. Grätzel, M. The Light and Shade of Perovskite Solar Cells. *Nat. Mater.,* **2014**, 13, 838–842.
16. NREL Solar cell efficiency chart https://www.nrel.gov/pv/assets/pdfs/pv-efficiency-

chart.20190103.pdf (accessed Jan 23, 2020).

17. Manser, J. S.; Christians, J. A.; Kamat, P. V. Intriguing Optoelectronic Properties of Metal Halide Perovskites. *Chem. Rev.,* **2016**, 116, 12956–13008.

18. McMeekin, D. P.; Sadoughi, G.; Rehman, W.; Eperon, G. E.; Saliba, M.; Hörantner, M. T.; Haghighirad, A.; Sakai, N.; Korte, L.; Rech, B.; et al. A Mixed-Cation Lead Mixed-Halide Perovskite Absorber for Tandem Solar Cells. *Science*, **2016**, 351, 151-155.

19. Brivio, F.; Butler, K. T.; Walsh, A.; Van Schilfgaarde, M. Relativistic Quasiparticle Self-Consistent Electronic Structure of Hybrid Halide Perovskite Photovoltaic Absorbers. *Phys. Rev. B. Phys.,* **2014**. 89, 155204.

20. Kepenekian, M.; Robles, R.; Katan, C.; Sapori, D.; Pedesseau, L.; Even, J. Rashba and Dresselhaus Effects in Hybrid Organic-Inorganic Perovskites: From Basics to Devices. *ACS Nano*, **2015**, 9, 11557-11567.

21. Wang, D.; Wright, M.; Elumalai, N. K.; Uddin, A. Stability of Perovskite Solar Cells. *Sol. Energy Mater. Sol. Cells*, **2016**, 147, 255–275.

22. Meng, L.; You, J.; Yang, Y. Addressing the Stability Issue of Perovskite Solar Cells for Commercial Applications. *Nat. Commun.,* **2018**, 9, Article number: 5265.

23. Lyu, M.; Yun, J. H.; Chen, P.; Hao, M.; Wang, L. Addressing Toxicity of Lead: Progress and Applications of Low-Toxic Metal Halide Perovskites and Their Derivatives. *Adv. Energy Mater.,* **2017**, 7, 1602512.

24. Frolova, L. A.; Anokhin, D. V; Gerasimov, K. L.; Dremova, N. N.; Troshin, P. A. Exploring the Effects of the Pb^{2+} Substitution in $MAPbI_3$ on the Photovoltaic Performance of the Hybrid Perovskite Solar Cells. *J. Phys. Chem. Lett.,* **2016**, 7, 4353-4357.

25. Ray, D.; Clark, C.; Pham, H. Q.; Borycz, J.; Holmes, R. J.; Aydil, E. S.; Gagliardi, L. Computational Study of Structural and Electronic Properties of Lead-Free $CsMI_3$ Perovskites (M = Ge, Sn, Pb, Mg, Ca, Sr, and Ba). *J. Phys. Chem. C.,* **2018**. 122, 7838-7848.

26. Hao, F.; Stoumpos, C. C.; Cao, D. H.; Chang, R. P. H.; Kanatzidis, M. G. Lead-Free Solid-State Organic-Inorganic Halide Perovskite Solar Cells. *Nat. Photonics*, **2014**, 8, 489–494.

27. Zhao, Z.; Gu, F.; Li, Y.; Sun, W.; Ye, S.; Rao, H.; Liu, Z.; Bian, Z.; Huang, C. Mixed-Organic-Cation Tin Iodide for Lead-Free Perovskite Solar Cells with an Efficiency of 8.12%. *Adv. Sci.,* **2017**, 4, 1700204.

28. Wang, F.; Jiang, X.; Chen, H.; Shang, Y.; Liu, H.; Wei, J.; Zhou, W.; He, H.; Liu, W.; Ning, Z. 2D-Quasi-2D-3D Hierarchy Structure for Tin Perovskite Solar Cells with Enhanced Efficiency and Stability. *Joule*, **2018**, 2, 2732-2743.

29. Docampo, P.; Bein, T. A Long-Term View on Perovskite Optoelectronics. *Acc. Chem. Res.*, **2016**, 49, 339-346.

30. Leguy, A. M. A.; Hu, Y.; Campoy-Quiles, M.; Alonso, M. I.; Weber, O. J.; Azarhoosh, P.; Van Schilfgaarde, M.; Weller, M. T.; Bein, T.; Nelson, J.; et al. Reversible Hydration of $CH_3NH_3PbI_3$ in Films, Single Crystals, and Solar Cells. *Chem. Mater.,* **2015**, 27, 3397-3407.

31. Niu, G.; Guo, X.; Wang, L. Review of Recent Progress in Chemical Stability of Perovskite Solar Cells. *J. Mater. Chem. A*, **2015**, 3, 8970–8980.

32. Juarez-Perez, E. J.; Ono, L. K.; Maeda, M.; Jiang, Y.; Hawash, Z.; Qi, Y. Photodecomposition and Thermal Decomposition in Methylammonium Halide Lead Perovskites and Inferred Design Principles to Increase Photovoltaic Device Stability. *J. Mater. Chem. A*, **2018**, 6, 9604-9612.

33. Aristidou, N.; Eames, C.; Sanchez-Molina, I.; Bu, X.; Kosco, J.; Saiful Islam, M.; Haque, S. A. Fast Oxygen Diffusion and Iodide Defects Mediate Oxygen-Induced Degradation of Perovskite Solar Cells. *Nat. Commun.*, **2017**, 8, Article number: 15218.

34. Xiang, Y.; Zhang, F.; He, J.; Lian, J.; Zeng, P.; Song, J.; Qu, J. Light-Current-Induced Acceleration of Degradation of Methylammonium Lead Iodide Perovskite Solar Cells. *J. Power Sources*, **2018**, 384, 303-311.

35. Jodlowski, A. D.; Rodríguez-Padrón, D.; Luque, R.; de Miguel, G. Alternative Perovskites for Photovoltaics. *Adv. Energy Mater.,* **2018**, 8, 1703120.

36. Smith, I. C.; Hoke, E. T.; Solis-Ibarra, D.; McGehee, M. D.; Karunadasa, H. I. A Layered Hybrid Perovskite Solar-Cell Absorber with Enhanced Moisture Stability. *Angew. Chem. Int.,* **2014**, 53, 11232–11235.

37. Cao, D. H.; Stoumpos, C. C.; Farha, O. K.; Hupp, J. T.; Kanatzidis, M. G. 2D Homologous Perovskites as Light-Absorbing Materials for Solar Cell Applications. *J. Am. Chem. Soc.,* **2015**, 137, 7843–7850.

38. Chen, P.; Bai, Y.; Wang, S.; Lyu, M.; Yun, J. H.; Wang, L. In Situ Growth of 2D Perovskite Capping Layer for Stable and Efficient Perovskite Solar Cells. *Adv. Funct. Mater.*, **2018**, 28, 1706923.

39. Stoumpos, C. C.; Cao, D. H.; Clark, D. J.; Young, J.; Rondinelli, J. M.; Jang, J. I.; Hupp, J. T.; Kanatzidis, M. G. Ruddlesden-Popper Hybrid Lead Iodide Perovskite 2D Homologous Semiconductors. *Chem. Mater.*, **2016**, 28, 2852–2867.

40. Li, X.; Hoffman, J.; Ke, W.; Chen, M.; Tsai, H.; Nie, W.; Mohite, A. D.; Kepenekian, M.; Katan, C.; Even, J.; et al. Two-Dimensional Halide Perovskites Incorporating Straight

Chain Symmetric Diammonium Ions, $(NH_3C_mH_{2m}NH_3)(CH_3NH_3)_{n-1}Pb_nI_{3n+1}$ (m = 4–9; n = 1–4). *J. Am. Chem. Soc.*, **2018**. 140, 12226-12238.

41. Saparov, B.; Mitzi, D. B. Organic-Inorganic Perovskites: Structural Versatility for Functional Materials Design. *Chem. Rev.,* **2016**, 116, 4558–4596.

42. Mao, L.; Stoumpos, C. C.; Kanatzidis, M. G. Two-Dimensional Hybrid Halide Perovskites: Principles and Promises. *J. Am. Chem. Soc.,* **2019**, 141, 1171-1190.

43. Zhang, R.; Liu, D.; Wang, Y.; Zhang, T.; Gu, X.; Zhang, P.; Wu, J.; Chen, Z. D.; Zhao, Y.; Li, S. Theoretical Lifetime Extraction and Experimental Demonstration of Stable Cesium-Containing Tri-Cation Perovskite Solar Cells with High Efficiency. *Electrochim. Acta*, **2018**, 265, 98-106.

44. Singh, T.; Miyasaka, T. Stabilizing the Efficiency Beyond 20% with a Mixed Cation Perovskite Solar Cell Fabricated in Ambient Air under Controlled Humidity. *Adv. Energy Mater.*, **2018**, 8, 1700677.

45. Saliba, M.; Matsui, T.; Seo, J.-Y.; Domanski, K.; Correa-Baena, J.-P.; Nazeeruddin, M. K.; Zakeeruddin, S. M.; Tress, W.; Abate, A.; Hagfeldt, A.; et al. Cesium-Containing Triple Cation Perovskite Solar Cells: Improved Stability, Reproducibility and High Efficiency. *Energy Environ. Sci.*, **2016**, 9, 1989–1997.

46. Manser, J. S.; Saidaminov, M. I.; Christians, J. A.; Bakr, O. M.; Kamat, P. V. Making and Breaking of Lead Halide Perovskites. *Acc. Chem. Res.,* **2016**, 49, 330-338.

47. Frost, J. M.; Butler, K. T.; Brivio, F.; Hendon, C. H.; Van Schilfgaarde, M.; Walsh, A. Atomistic Origins of High-Performance in Hybrid Halide Perovskite Solar Cells. *Nano Lett.*, **2014**, 14, 2584-2590.

48. Jong, U. G.; Yu, C. J.; Ri, G. C.; McMahon, A. P.; Harrison, N. M.; Barnes, P. R. F.; Walsh, A. Influence of Water Intercalation and Hydration on Chemical Decomposition and Ion Transport in Methylammonium Lead Halide Perovskites. *J. Mater. Chem. A*, **2018**, 6, 1067-1074.

49. Huang, W.; Manser, J. S.; Kamat, P. V.; Ptasinska, S. Evolution of Chemical Composition, Morphology, and Photovoltaic Efficiency of $CH_3NH_3PbI_3$ Perovskite under Ambient Conditions. *Chem. Mater.*, **2016**, 28, 303-311.

50. Bryant, D.; Aristidou, N.; Pont, S.; Sanchez-Molina, I.; Chotchunangatchaval, T.; Wheeler, S.; Durrant, J. R.; Haque, S. A. Light and Oxygen Induced Degradation Limits the Operational Stability of Methylammonium Lead Triiodide Perovskite Solar Cells. *Energy Environ. Sci.*, **2016**, 9, 1655-1660.

51. Xiao, Z.; Wang, D.; Dong, Q.; Wang, Q.; Wei, W.; Dai, J.; Zeng, X.; Huang, J. Unraveling

the Hidden Function of a Stabilizer in a Precursor in Improving Hybrid Perovskite Film Morphology for High Efficiency Solar Cells. *Energy Environ. Sci.*, **2016**, 9, 867-872.

52. Ko, H. S.; Lee, J. W.; Park, N. G. 15.76% Efficiency Perovskite Solar Cells Prepared under High Relative Humidity: Importance of PbI_2 Morphology in Two-Step Deposition of $CH_3NH_3PbI_3$. *J. Mater. Chem. A*, **2015**, 3, 8808-8815.

53. Breternitz, J.; Schorr, S. What Defines a Perovskite? *Adv. Energy Mater.*, **2018**, 8, 1802366.

54. Koh, T. M.; Thirumal, K.; Soo, H. Sen; Mathews, N. Multidimensional Perovskites: A Mixed Cation Approach Towards Ambient Stable and Tunable Perovskite Photovoltaics. *ChemSusChem.,* **2016**, 9, 2541-2558.

55. Yang, S.; Wang, Y.; Liu, P.; Cheng, Y. B.; Zhao, H. J.; Yang, H. G. Functionalization of Perovskite Thin Films with Moisture-Tolerant Molecules. *Nat. Energy*, **2016**, 1, Article number: 15016.

56. Tsai, H.; Nie, W.; Blancon, J. C.; Stoumpos, C. C.; Asadpour, R.; Harutyunyan, B.; Neukirch, A. J.; Verduzco, R.; Crochet, J. J.; Tretiak, S.; et al. High-Efficiency Two-Dimensional Ruddlesden-Popper Perovskite Solar Cells. *Nature*, **2016**, 536, 312–316.

57. Stoumpos, C. C.; Mao, L.; Malliakas, C. D.; Kanatzidis, M. G. Structure-Band Gap Relationships in Hexagonal Polytypes and Low-Dimensional Structures of Hybrid Tin Iodide Perovskites. *Inorg. Chem.,* **2017**, 56, 1, 56-73.

58. Liu, Y.; Xiao, H.; Goddard, W. A. Two-Dimensional Halide Perovskites: Tuning Electronic Activities of Defects. *Nano Lett.,* **2016**, 16, 3335–3340.

59. Dou, L.; Wong, A. B.; Yu, Y.; Lai, M.; Kornienko, N.; Eaton, S. W.; Fu, A.; Bischak, C. G.; Ma, J.; Ding, T.; et al. Atomically Thin Two-Dimensional Organic-Inorganic Hybrid Perovskites. *Science*, **2015**, 349, 1518–1521.

60. Huo, C.; Cai, B.; Yuan, Z.; Ma, B.; Zeng, H. Two-Dimensional Metal Halide Perovskites: Theory, Synthesis, and Optoelectronics. Small Methods, **2017**, 1, 1600018.

61. Mitzi, D. B. Templating and Structural Engineering in Organic-Inorganic Perovskites. *J. Chem. Soc. Dalt. Trans.,* **2001**, 1, 1–12.

62. Nazarenko, O.; Kotyrba, M. R.; Yakunin, S.; Aebli, M.; Rainò, G.; Benin, B. M.; Wörle, M.; Kovalenko, M. V. Guanidinium-Formamidinium Lead Iodide: A Layered Perovskite-Related Compound with Red Luminescence at Room Temperature. *J. Am. Chem. Soc.,* **2018**, 140, 3850-3853.

63. Cao, D. H.; Stoumpos, C. C.; Farha, O. K.; Hupp, J. T.; Kanatzidis, M. G. Two-Dimensional Homologous Perovskites as Light Absorbing Materials for Solar Cell Applications. *J. Am.*

Chem. Soc., **2015**, 137, 7843-7850.

64. Ruddlesden, S. N.; Popper, P. The Compound $Sr_3Ti_2O_7$ and Its Structure. *Acta Crystallogr.,***1958**, 11, 54-55.

65. Ruddlesden, S. N.; Popper, P. New Compounds of the K_2NIF_4 Type. *Acta Crystallogr.*, **1957**, 10, 538-539.

66. Jacobson, A. J.; Johnson, J. W.; Lewandowski, J. T. Interlayer Chemistry between Thick Transition-Metal Oxide Layers: Synthesis and Intercalation Reactions of $K[Ca_2Na_{n-3}Nb_nO_{3n+1}]$ ($3 \leq n \leq 7$). *Inorg. Chem.,* **1985**, 24, 3727-3729.

67. Aurivillius, B. Mixed Bismuth Oxides with Layer Lattices. II. Structure of $Bi_4Ti_3O_{12}$. *Ark. Kemi*,**1949**, 7, 217-224.

68. Hervoches, C. H.; Lightfoot, P. A Variable-Temperature Powder Neutron Diffraction Study of Ferroelectric $Bi_4Ti_3O_{12}$. *Chem. Mater.*, **1999**, 11, 3359-3364.

69. Kendall, K. R.; Navas, C.; Thomas, J. K.; Zur Loye, H. C. Recent Developments in Oxide Ion Conductors: Aurivillius Phases. *Chem. Mater.,* **1996**, 8, 642-649.

70. Mao, L.; Ke, W.; Pedesseau, L.; Wu, Y.; Katan, C.; Even, J.; Wasielewski, M. R.; Stoumpos, C. C.; Kanatzidis, M. G. Hybrid Dion-Jacobson 2D Lead Iodide Perovskites. *J. Am. Chem. Soc.*, **2018**, 140, 3775-3783.

71. Sajjad Ahmad, Ping Fu, Shuwen Yu, Qing Yang, Xuan Liu, Xuchao Wang, Xiuli Wang, Xin Guo, and C. L. *Joule,* **2019**, 3, 794–806

72. Calabrese, J.; Jones, N.; Harlow, R.; Herron, N.; Thorn, D.; Wang, Y. Preparation and Characterization of Layered Lead Halide Compounds. *J. Am. Chem. Soc.*, **1991**, 113, 2328–2330.

73. Mitzi, D. B.; Feild, C. a.; Harrison, W. T. a.; Guloy, a. M. Conducting Tin Halides with a Layered Organic-Based Perovskite Structure. *Nature*, **1994**, 369, 467–469.

74. Papavassiliou, G. C.; Mousdis, G. A.; Raptopoulou, C. P.; Terzis, A. Some New Luminescent Compounds Based on 4-Methylbenzylamine and Lead Halides. *Z. Naturforsch. B,* **2000**, 55.

75. Zhu, X. H.; Mercier, N.; Riou, A.; Blanchard, P.; Frère, P. $(C_4H_3CH_2NH_3)_2(CH_3NH_3)Pb_2I_7$: Non-Centrosymmetrical Crystal Structure of a Bilayer Hybrid Perovskite. *Chem. Commun.*, **2002**, 18, 2160-2161.

76. Mercier, N. $(HO_2C(CH_2)_3NH_3)_2(CH_3NH_3)Pb_2I_7$: A Predicted Noncentrosymmetrical Structure Built up from Carboxylic Acid Supramolecular Synthons and Bilayer Perovskite Sheets. *CrystEngComm*, **2005**, 7, 429-432.

77. Stoumpos, C. C.; Soe, C. M. M.; Tsai, H.; Nie, W.; Blancon, J. C.; Cao, D. H.; Liu, F.;

Traoré, B.; Katan, C.; Even, J.; et al. High Members of the 2D Ruddlesden-Popper Halide Perovskites: Synthesis, Optical Properties, and Solar Cells of $(CH_3(CH_2)_3NH_3)_2(CH_3NH_3)_4Pb_5I_{16}$. *Chem*, **2017**, 2, 427-440.

78. Soe, C. M. M.; Nagabhushana, G. P.; Shivaramaiah, R.; Tsai, H.; Nie, W.; Blancon, J.-C.; Melkonyan, F.; Cao, D. H.; Traoré, B.; Pedesseau, L.; et al. Structural and Thermodynamic Limits of Layer Thickness in 2D Halide Perovskites. *Proc. Natl. Acad. Sci.*, **2019**, 116, 58–66.

79. Mao, L.; Tsai, H.; Nie, W.; Ma, L.; Im, J.; Stoumpos, C. C.; Malliakas, C. D.; Hao, F.; Wasielewski, M. R.; Mohite, A. D.; et al. Role of Organic Counterion in Lead- and Tin-Based Two-Dimensional Semiconducting Iodide Perovskites and Application in Planar Solar Cells. *Chem. Mater.*, **2016**, 28, 7781–7792.

80. Yu, Y.; Zhang, D.; Yang, P. Ruddlesden-Popper Phase in Two-Dimensional Inorganic Halide Perovskites: A Plausible Model and the Supporting Observations. *Nano Lett.,* **2017**, 17, 5489–5494.

81. Yu, Y.; Zhang, D.; Kisielowski, C.; Dou, L.; Kornienko, N.; Bekenstein, Y.; Wong, A. B.; Alivisatos, A. P.; Yang, P. Atomic Resolution Imaging of Halide Perovskites. *Nano Lett.,* **2016**, 16, 7530–7535.

82. Li, J.; Yu, Q.; He, Y.; Stoumpos, C. C.; Niu, G.; Trimarchi, G. G.; Guo, H.; Dong, G.; Wang, D.; Wang, L.; et al. $Cs_2PbI_2Cl_2$, All-Inorganic Two-Dimensional Ruddlesden–Popper Mixed Halide Perovskite with Optoelectronic Response. *J. Am. Chem. Soc.*, **2018**, 140, 11085-11090.

83. Li, J.; Stoumpos, C. C.; Trimarchi, G. G.; Chung, I.; Mao, L.; Chen, M.; Wasielewski, M. R.; Wang, L.; Kanatzidis, M. G. Air-Stable Direct Bandgap Perovskite Semiconductors: All-Inorganic Tin-Based Heteroleptic Halides $A_xSnCl_yI_z$(A = Cs, Rb). *Chem. Mater.* **2018**, 30, 4847-4856.

84. Daub, M.; Hillebrecht, H. Synthesis, Single-Crystal Structure and Characterization of $(CH_3NH_3)_2Pb(SCN)_2I_2$. *Angew. Chem. Int. Ed*., **2015**, 54, 11016-11017.

85. Soe, C. M. M.; Stoumpos, C. C.; Kepenekian, M.; Traoré, B.; Tsai, H.; Nie, W.; Wang, B.; Katan, C.; Seshadri, R.; Mohite, A. D.; et al. New Type of 2D Perovskites with Alternating Cations in the Interlayer Space, $(C(NH_2)_3)(CH_3NH_3)_nPb_nI_{3n+1}$: Structure, Properties, and Photovoltaic Performance. *J. Am. Chem. Soc.,* **2017**, 139, 16297–16309.

86. Ma, C.; Shen, D.; Ng, T. W.; Lo, M. F.; Lee, C. S. 2D Perovskites with Short Interlayer Distance for High-Performance Solar Cell Application. *Adv. Mater.,* **2018**, 30, 1800710.

87. Mitzi, D. B.; Chondroudis, K. Crystal Structure and Properties of Dye-Containing Organic-

Inorganic Perovskites. In Molecular Crystals and Liquid Crystals Science and Technology, Section A: Molecular Crystals and Liquid Crystals, **2001**, 356, 549-558.

88. Mitzi, D. B.; Chondroudis, K.; Kagan, C. R. Design, Structure, and Optical Properties of Organic−Inorganic Perovskites Containing an Oligothiophene Chromophore. *Inorg. Chem.,* **1999**, 38, 6246-6256.

89. Ema, K.; Inomata, M.; Kato, Y.; Kunugita, H.; Era, M. Nearly Perfect Triplet-Triplet Energy Transfer from Wannier Excitons to Naphthalene in Organic-Inorganic Hybrid Quantum-Well Materials. *Phys. Rev. Lett.*, **2008**, 100, 257401.

90. Kikuchi, K.; Takeoka, Y.; Rikukawa, M.; Sanui, K. Fabrication and Characterization of Organic-Inorganic Perovskite Films Containing Fullerene Derivatives. *Colloids Surf. A Physicochem. Eng. Asp.*, **2005**, 257, 199-202.

91. Passarelli, J. V.; Fairfield, D. J.; Sather, N. A.; Hendricks, M. P.; Sai, H.; Stern, C. L.; Stupp, S. I. Enhanced Out-of-Plane Conductivity and Photovoltaic Performance in n = 1 Layered Perovskites through Organic Cation Design. *J. Am. Chem. Soc.,* **2018**, 140, 7313-7323.

92. Leveillee, J.; Katan, C.; Zhou, L.; Mohite, A. D.; Even, J.; Tretiak, S.; Schleife, A.; Neukirch, A. J. Influence of π -Conjugated Cations and Halogen Substitution on the Optoelectronic and Excitonic Properties of Layered Hybrid Perovskites. *Phys. Rev. Mater.*, **2018**, 2, 105406.

93. Jemli, K.; Audebert, P.; Galmiche, L.; Trippé-Allard, G.; Garrot, D.; Lauret, J. S.; Deleporte, E. Two-Dimensional Perovskite Activation with an Organic Luminophore. *ACS Appl. Mater. Interfaces*, **2015**, 7, 21763-21769.

94. Van Gompel, W. T. M.; Herckens, R.; Van Hecke, K.; Ruttens, B.; D'Haen, J.; Lutsen, L.; Vanderzande, D. Towards 2D Layered Hybrid Perovskites with Enhanced Functionality: Introducing Charge-Transfer Complexes: Via Self-Assembly. *Chem. Commun.,* **2019**, 55, 2481-2484.

95. Hu, J.; Oswald, I. W. H.; Stuard, S. J.; Nahid, M. M.; Zhou, N.; Williams, O. F.; Guo, Z.; Yan, L.; Hu, H.; Chen, Z.; et al. Synthetic Control over Orientational Degeneracy of Spacer Cations Enhances Solar Cell Efficiency in Two-Dimensional Perovskites. *Nat. Commun.*, **2019**, 10, Article number: 1276.

96. Mitzi, D. B.; Dimitrakopoulos, C. D.; Kosbar, L. L. Structurally Tailored Organic-Inorganic Perovskites: Optical Properties and Solution-Processed Channel Materials for Thin-Film Transistors. *Chem. Mater.,* **2001**, 13, 3728–3740.

97. Kikuchi, K.; Takeoka, Y.; Rikukawa, M.; Sanui, K. Structure and Optical Properties of Lead

Iodide Based Two-Dimensional Perovskite Compounds Containing Fluorophenethylamines. *Curr. Appl. Phys.,* **2004**, 4 , 599–602.

98. Dohner, E. R.; Hoke, E. T.; Karunadasa, H. I. Self-Assembly of Broadband White-Light Emitters. *J. Am. Chem. Soc.,* **2014**, 136, 1718-1721.

99. Mitzi, D. B. Synthesis, Crystal Structure, and Optical and Thermal Properties of $(C_4H_9NH_3)_2MI_4$ (M = Ge, Sn, Pb). *Chem. Mater.,* **1996**, 8, 3, 791-800.

100. Tabuchi, Y.; Asai, K.; Rikukawa, M.; Sanui, K.; Ishigure, K. Preparation and Characterization of Natural Lower Dimensional Layered Perovskite-Type Compounds. *J. Phys. Chem. Solids,* **2000**, 61, 837-845.

101. Oswald, I. W. H.; Koegel, A. A.; Neilson, J. R. General Synthesis Principles for Ruddlesden-Popper Hybrid Perovskite Halides from a Dynamic Equilibrium. *Chem. Mater.*, **2018**, 30, 8606-8614.

102. Umari, P.; Mosconi, E.; Angelis, F. De. Relativistic GW Calculations on Perovskites for Solar Cell Applications. *Sci. Rep.*, **2014**, 4 . 1–7.

103. Borriello, I.; Cantele, G.; Ninno, D. Ab Initio Investigation of Hybrid Organic-Inorganic Perovskites Based on Tin Halides. *Phys. Rev. B.*, **2008**, 77, 235214.

104. Horzum, S.; Torun, E.; Serin, T.; Peeters, F. M. Structural, Electronic and Optical Properties of Cu-Doped ZnO: Experimental and Theoretical Investigation. *Philos. Mag.*, **2016**, 96, 1743–1756.

105. Castelli, I. E.; Olsen, T.; Datta, S.; Landis, D. D.; Dahl, S.; Thygesen, K. S.; Jacobsen, K. W. Computational Screening of Perovskite Metal Oxides for Optimal Solar Light Capture. *Energy Environ. Sci.,* **2012**, 5, 5814–5819.

106. Li, X.; Hoffman, J.; Ke, W.; Chen, M.; Tsai, H.; Nie, W.; Mohite, A. D.; Kepenekian, M.; Katan, C.; Even, J.; et al. Two-Dimensional Halide Perovskites Incorporating Straight Chain Symmetric Diammonium Ions, $(NH_3C_mH_2NH_3)(CH_3NH_3)_{n-1}Pb_nI_{3n+1}$(m = 4-9; n = 1-4). *J. Am. Chem. Soc.*, **2018**, 140, 12226-12238.

107. Labram, J. G.; Venkatesan, N. R.; Takacs, C. J.; Evans, H. A.; Perry, E. E.; Wudl, F.; Chabinyc, M. L. Charge Transport in a Two-Dimensional Hybrid Metal Halide Thiocyanate Compound. *J. Mater. Chem. C*, **2017**, 5, 5930-5938.

108. Umeyama, D.; Lin, Y.; Karunadasa, H. I. Red-to-Black Piezochromism in a Compressible Pb-I-SCN Layered Perovskite. *Chem. Mater.*, **2016**, 28, 3241-3244.

109. Liu, G.; Kong, L.; Guo, P.; Stoumpos, C. C.; Hu, Q.; Liu, Z.; Cai, Z.; Gosztola, D. J.; Mao, H. K.; Kanatzidis, M. G.; et al. Two Regimes of Bandgap Red Shift and Partial Ambient Retention in Pressure-Treated Two-Dimensional Perovskites. *ACS Energy Lett.,* **2017**, 2,

2518-2524.

110. Liu, G.; Gong, J.; Kong, L.; Schaller, R. D.; Hu, Q.; Liu, Z.; Yan, S.; Yang, W.; Stoumpos, C. C.; Kanatzidis, M. G.; et al. Isothermal Pressure-Derived Metastable States in 2D Hybrid Perovskites Showing Enduring Bandgap Narrowing. *Proc. Natl. Acad. Sci.,* **2018**, 115, 8076-8081.

111. Wei, Y.; Lauret, J. S.; Galmiche, L.; Audebert, P.; Deleporte, E. Strong Exciton-Photon Coupling in Microcavities Containing New Fluorophenethylamine Based Perovskite Compounds. *Opt. Express,* **2012**, 20, 10399.

112. Wang, Z.; Ganose, A. M.; Niu, C.; Scanlon, D. O. First-Principles Insights into Tin-Based Two-Dimensional Hybrid Halide Perovskites for Photovoltaics*. J. Mater. Chem. A*, **2018**, 6, 5652–5660.

113. Yu, Z. G. The Rashba Effect and Indirect Electron-Hole Recombination in Hybrid Organic-Inorganic Perovskites. *Phys. Chem. Chem. Phys.*, **2017**, 19, 14907-14912.

114. Zhang, X.; Shen, J. X.; Van De Walle, C. G. Three-Dimensional Spin Texture in Hybrid Perovskites and Its Impact on Optical Transitions. *J. Phys. Chem. Lett.,* **2018**, 9, 2903-2908.

115. Becker, M. A.; Vaxenburg, R.; Nedelcu, G.; Sercel, P. C.; Shabaev, A.; Mehl, M. J.; Michopoulos, J. G.; Lambrakos, S. G.; Bernstein, N.; Lyons, J. L.; et al. Bright Triplet Excitons in Caesium Lead Halide Perovskites. *Nature*, **2018**, 553, 189–193.

116. Hsiao, Y. C.; Wu, T.; Li, M.; Hu, B. Magneto-Optical Studies on Spin-Dependent Charge Recombination and Dissociation in Perovskite Solar Cells. *Adv. Mater.,* **2015**, 27, 2899-2906.

117. Etienne, T.; Mosconi, E.; De Angelis, F. Dynamical Origin of the Rashba Effect in Organohalide Lead Perovskites: A Key to Suppressed Carrier Recombination in Perovskite Solar Cells? *J. Phys. Chem. Lett.*, **2016**, 7, 1638-1645.

118. Zhai, Y.; Baniya, S.; Zhang, C.; Li, J.; Haney, P.; Sheng, C. X.; Ehrenfreund, E.; Vardeny, Z. V. Giant Rashba Splitting in 2D Organic-Inorganic Halide Perovskites Measured by Transient Spectroscopies. *Sci. Adv.,* **2017**, 3, e1700704.

119. Yin, J.; Maity, P.; Xu, L.; El-Zohry, A. M.; Li, H.; Bakr, O. M.; Brédas, J.-L.; Mohammed, O. F. Layer-Dependent Rashba Band Splitting in 2D Hybrid Perovskites. *Chem. Mater.*, **2018**, 30, 8538-8545.

120. Im, J.; Stoumpos, C. C.; Jin, H.; Freeman, A. J.; Kanatzidis, M. G. Antagonism between Spin-Orbit Coupling and Steric Effects Causes Anomalous Band Gap Evolution in the Perovskite Photovoltaic Materials $CH_3NH_3Sn_{1-x}Pb_xI_3$. *J. Phys. Chem. Lett.*, **2015**, 6, 3503-

3509.

121. Mitzi, D. B.; Chondroudis, K.; Kagan, C. R. Organic-Inorganic Electronics. *IBM J. Res. Dev.*, **2001**, 45, 29–45.

122. Even, J.; Pedesseau, L.; Katan, C. Understanding Quantum Confinement of Charge Carriers in Layered 2D Hybrid Perovskites. *ChemPhysChem*, **2014**, 15, 3733–3741.

123. He, X. F. Excitons in Anisotropic Solids: The Model of Fractional-Dimensional Space. *Phys. Rev. B,* **1991**, 43, 2063–2069.

124. Mathieu, H.; Lefebvre, P.; Christol, P. Simple Analytical Method for Calculating Exciton Binding Energies in Semiconductor Quantum Wells. *Phys. Rev. B*, **1992**, 46, 4092–4101.

125. Sapori, D.; Kepenekian, M.; Pedesseau, L.; Katan, C.; Even, J. Quantum Confinement and Dielectric Profiles of Colloidal Nanoplatelets of Halide Inorganic and Hybrid Organic-Inorganic Perovskites. *Nanoscale*, **2016**, 8, 6369–6378.

126. Dohner, E. R.; Jaffe, A.; Bradshaw, L. R.; Karunadasa, H. I. Intrinsic White-Light Emission from Layered Hybrid Perovskites. *J. Am. Chem. Soc.*, **2014**, 136, 13154–13157.

127. Lanty, G.; Bréhier, A.; Parashkov, R.; Lauret, J. S.; Deleporte, E. Strong Exciton-Photon Coupling at Room Temperature in Microcavities Containing Two-Dimensional Layered Perovskite Compounds. *New J. Phys.*, **2008**, 10, 065007.

128. Pedesseau, L.; Sapori, D.; Traore, B.; Robles, R.; Fang, H. H.; Loi, M. A.; Tsai, H.; Nie, W.; Blancon, J. C.; Neukirch, A.; et al. Advances and Promises of Layered Halide Hybrid Perovskite Semiconductors. *ACS Nano,* **2016**,10, 9776–9786.

129. Kumagai, M.; Takagahara, T. Excitonic and Nonlinear-Optical Properties of Dielectric Quantum-Well Structures. *Phys. Rev. B*, **1989**, 40, 12359–12381.

130. Muljarov, E. A.; Tikhodeev, S. G.; Gippius, N. A.; Ishihara, T. Excitons in Self-Organized Semiconductor/Insulator Superlattices: PbI-Based Perovskite Compounds. *Phys. Rev. B*, **1995**, 51, 14370–14378.

131. Traore, B.; Pedesseau, L.; Assam, L.; Che, X.; Blancon, J. C.; Tsai, H.; Nie, W.; Stoumpos, C. C.; Kanatzidis, M. G.; Tretiak, S.; et al. Composite Nature of Layered Hybrid Perovskites: Assessment on Quantum and Dielectric Confinements and Band Alignment. *ACS Nano,* **2018**, 12, 3321-3332.

132. Keldysh, L. V. Coulomb Interaction in Thin Semiconductor and Semimetal Films. *Soviet Physics JETP*, **1979**, 658–660.

133. Cudazzo, P.; Tokatly, I. V.; Rubio, A. Dielectric Screening in Two-Dimensional Insulators: Implications for Excitonic and Impurity States in Graphane. *Phys. Rev. B. Phys.*, **2011**, 84, 085406.

134. Chernikov, A.; Berkelbach, T. C.; Hill, H. M.; Rigosi, A.; Li, Y.; Aslan, O. B.; Reichman, D. R.; Hybertsen, M. S.; Heinz, T. F. Exciton Binding Energy and Nonhydrogenic Rydberg Series in Monolayer WS_2. *Phys. Rev. Lett.*, **2014**, 113, 076802.

135. Berkelbach, T. C.; Hybertsen, M. S.; Reichman, D. R. Theory of Neutral and Charged Excitons in Monolayer Transition Metal Dichalcogenides. Phys. Rev. B, **2013**, 88, 045318.

136. Agranovich, V. M.; Basko, D. M.; La Rocca, G. C.; Bassani, F. Excitons and Optical Nonlinearities in Hybrid Organic-Inorganic Nanostructures. *J. Condens.,***1998**, 10, 9369–9400.

137. Blancon, J. C.; Stier, A. V.; Tsai, H.; Nie, W.; Stoumpos, C. C.; Traoré, B.; Pedesseau, L.; Kepenekian, M.; Katsutani, F.; Noe, G. T.; et al. Scaling Law for Excitons in 2D Perovskite Quantum Wells. *Nat. Commun.*, **2018**, 9, Article number: 2254.

138. Gélvez-Rueda, M. C.; Hutter, E. M.; Cao, D. H.; Renaud, N.; Stoumpos, C. C.; Hupp, J. T.; Savenije, T. J.; Kanatzidis, M. G.; Grozema, F. C. Interconversion between Free Charges and Bound Excitons in 2D Hybrid Lead Halide Perovskites. *J. Phys. Chem. C*, **2017**, 121, 26566–26574..

139. Straus, D. B.; Kagan, C. R. Electrons, Excitons, and Phonons in Two-Dimensional Hybrid Perovskites: Connecting Structural, Optical, and Electronic Properties. *J. Phys. Chem. Lett.,* **2018**, 9, 1434-1447

140. Hong, X.; Ishihara, T.; Nurmikko, A. V. Dielectric Confinement Effect on Excitons in PbI4-Based Layered Semiconductors. *Phys. Rev. B*, **1992**, 45, 6961–6964.

141. Xu, Z.; Mitzi, D. B. SnI42--Based Hybrid Perovskites Templated by Multiple Organic Cations: Combining Organic Functionalities through Noncovalent Interactions. *Chem. Mater.*, **2003**, 15, 3632–3637.

142. Younts, R.; Duan, H. S.; Gautam, B.; Saparov, B.; Liu, J.; Mongin, C.; Castellano, F. N.; Mitzi, D. B.; Gundogdu, K. Efficient Generation of Long-Lived Triplet Excitons in 2D Hybrid Perovskite. *Adv. Mater.*, **2017**, 29, 1604278.

143. Miyata, A.; Mitioglu, A.; Plochocka, P.; Portugall, O.; Wang, J. T. W.; Stranks, S. D.; Snaith, H. J.; Nicholas, R. J. Direct Measurement of the Exciton Binding Energy and Effective Masses for Charge Carriers in Organic-Inorganic Tri-Halide Perovskites. *Nat. Phys.*, **2015**, 11, 582–587.

144. Tanaka, K.; Takahashi, T.; Ban, T.; Kondo, T.; Uchida, K.; Miura, N. Comparative Study in the Excitons in Lead halide based Perovskite-Type Crystals $CH_3NH_3PbBr_3$,$CH_3NH_3PbI_3$. *Solid State Commun.,* **2003**, 127, 619–623.

145. Koutselas, I. B.; Ducasse, L.; Papavassiliou, G. C. Electronic Properties of Three- and

Low-Dimensional Semiconducting Materials with Pb Halide and Sn Halide Units. *J. Phys. Condens. Matter*, **1996**, 8, 1217–1227.

146. Kittel, C. Introduction to Solid State Physics, **2010**.

147. Neukirch, A. J.; Nie, W.; Blancon, J. C.; Appavoo, K.; Tsai, H.; Sfeir, M. Y.; Katan, C.; Pedesseau, L.; Even, J.; Crochet, J. J.; et al. Polaron Stabilization by Cooperative Lattice Distortion and Cation Rotations in Hybrid Perovskite Materials. *Nano Lett.*, **2016**, 16, 3809-3816.

148. Miyata, K.; Meggiolaro, D.; Tuan Trinh, M.; Joshi, P. P.; Mosconi, E.; Jones, S. C.; De Angelis, F.; Zhu, X. Y. Large Polarons in Lead Halide Perovskites. *Sci. Adv.*, **2017**, 3, e1701217.

149. Thouin, F.; Valverde-Chávez, D. A.; Quarti, C.; Cortecchia, D.; Bargigia, I.; Beljonne, D.; Petrozza, A.; Silva, C.; Srimath Kandada, A. R. Phonon Coherences Reveal the Polaronic Character of Excitons in Two-Dimensional Lead Halide Perovskites. *Nat. Mater.,* **2019**, 18, 349–356.

150. Guo, Z.; Wu, X.; Zhu, T.; Zhu, X.; Huang, L. Electron-Phonon Scattering in Atomically Thin 2D Perovskites. *ACS Nano***, 2016**, 10, 9992–9998.

151. Chen, Y.; Sun, Y.; Peng, J.; Tang, J.; Zheng, K.; Liang, Z. 2D Ruddlesden–Popper Perovskites for Optoelectronics. *Adv. Mater.,* **2018**, 30, 1703487.

152. Yin, J.; Li, H.; Cortecchia, D.; Soci, C.; Brédas, J. L. Excitonic and Polaronic Properties of 2D Hybrid Organic-Inorganic Perovskites. *ACS Energy Lett*., **2017**, 2, 417–423.

153. Straus, D. B.; Hurtado Parra, S.; Iotov, N.; Gebhardt, J.; Rappe, A. M.; Subotnik, J. E.; Kikkawa, J. M.; Kagan, C. R. Direct Observation of Electron-Phonon Coupling and Slow Vibrational Relaxation in Organic-Inorganic Hybrid Perovskites. *J. Am. Chem. Soc.*, **2016**, 138, 13798–13801.

154. Hu, T.; Smith, M. D.; Dohner, E. R.; Sher, M. J.; Wu, X.; Trinh, M. T.; Fisher, A.; Corbett, J.; Zhu, X. Y.; Karunadasa, H. I.; et al. Mechanism for Broadband White-Light Emission from Two-Dimensional (110) Hybrid Perovskites. *J. Phys. Chem. Lett.*, **2016**, 7, 2258-2263.

155. Smith, M. D.; Crace, E. J.; Jaffe, A.; Karunadasa, H. I. The Diversity of Layered Halide Perovskites. *Annu. Rev. Mater. Res.*, **2018**, 48, 111-136.

156. Smith, M. D.; Karunadasa, H. I. White-Light Emission from Layered Halide Perovskites. *Acc. Chem. Res.*, **2018**, 3, 619-627.

157. Thirumal, K.; Chong, W. K.; Xie, W.; Ganguly, R.; Muduli, S. K.; Sherburne, M.; Asta, M.; Mhaisalkar, S.; Sum, T. C.; Soo, H. Sen; et al. Morphology-Independent Stable White-

Light Emission from Self-Assembled Two-Dimensional Perovskites Driven by Strong Exciton-Phonon Coupling to the Organic Framework. *Chem. Mater.,* **2017**, 9, 3947-3953.

158. Blancon, J. C.; Tsai, H.; Nie, W.; Stoumpos, C. C.; Pedesseau, L.; Katan, C.; Kepenekian, M.; Soe, C. M. M.; Appavoo, K.; Sfeir, M. Y.; et al. Extremely Efficient Internal Exciton Dissociation through Edge States in Layered 2D Perovskites. *Science*, **2017**, 355, 1288–1292.

159. Kepenekian, M.; Traore, B.; Blancon, J. C.; Pedesseau, L.; Tsai, H.; Nie, W.; Stoumpos, C. C.; Kanatzidis, M. G.; Even, J.; Mohite, A. D.; et al. Concept of Lattice Mismatch and Emergence of Surface States in Two-Dimensional Hybrid Perovskite Quantum Wells. *Nano Lett.,* 2018, 9, 5603-5609.

160. Vurgaftman, I.; Meyer, J. R.; Ram-Mohan, L. R. Band Parameters for III-V Compound Semiconductors and Their Alloys. *J. Appl. Phys.*, **2001**, 89, 5815.

161. Milot, R. L.; Sutton, R. J.; Eperon, G. E.; Haghighirad, A. A.; Martinez Hardigree, J.; Miranda, L.; Snaith, H. J.; Johnston, M. B.; Herz, L. M. Charge-Carrier Dynamics in 2D Hybrid Metal-Halide Perovskites. *Nano Lett.,* **2016**, 16, 7001–7007.

162. Mikhnenko, O. V.; Blom, P. W. M.; Nguyen, T.-Q. Exciton Diffusion in Organic Semiconductors. *Energy Environ. Sci.***, 2015**, 8, 1867–1888.

163. Shao, Y.; Fang, Y.; Li, T.; Wang, Q.; Dong, Q.; Deng, Y.; Yuan, Y.; Wei, H.; Wang, M.; Gruverman, A.; et al. Grain Boundary Dominated Ion Migration in Polycrystalline Organic-Inorganic Halide Perovskite Films. *Energy Environ. Sci.,* **2016**, 9, 1752-1759.

164. Li, D.; Wu, H.; Cheng, H. C.; Wang, G.; Huang, Y.; Duan, X. Electronic and Ionic Transport Dynamics in Organolead Halide Perovskites. *ACS Nano,* **2016**, 7, 6933-6941.

165. Xiao, X.; Dai, J.; Fang, Y.; Zhao, J.; Zheng, X.; Tang, S.; Rudd, P. N.; Zeng, X. C.; Huang, J. Suppressed Ion Migration along the In-Plane Direction in Layered Perovskites. *ACS Energy Lett.,* **2018**, 3, 684-688.

166. Lin, Y.; Bai, Y.; Fang, Y.; Wang, Q.; Deng, Y.; Huang, J. Suppressed Ion Migration in Low-Dimensional Perovskites. *ACS Energy Lett.*, **2017**, 2, 1571-1572.

167. Yuan, Y.; Wang, Q.; Huang, J. Organic-Inorganic Halide Perovskite Photovoltaics: From Fundamentals to Device Architectures, **2016**, 137-162.

168. Yuan, Y.; Huang, J. Ion Migration in Organometal Trihalide Perovskite and Its Impact on Photovoltaic Efficiency and Stability. *Acc. Chem. Res.*, **2016**, 49, 286-293.

169. Levine, I.; Nayak, P. K.; Wang, J. T. W.; Sakai, N.; Van Reenen, S.; Brenner, T. M.; Mukhopadhyay, S.; Snaith, H. J.; Hodes, G.; Cahen, D. Interface-Dependent Ion Migration/Accumulation Controls Hysteresis in $MAPbI_3$ solar Cells. *J. Phys. Chem. C,*

2016, 120, 16399-16411.

170. Xing, J.; Wang, Q.; Dong, Q.; Yuan, Y.; Fang, Y.; Huang, J. Ultrafast Ion Migration in Hybrid Perovskite Polycrystalline Thin Films under Light and Suppression in Single Crystals. *Phys. Chem. Chem. Phys.*, **2016**, 18, 30484-30490.

171. Thrithamarassery Gangadharan, D.; Han, Y.; Dubey, A.; Gao, X.; Sun, B.; Qiao, Q.; Izquierdo, R.; Ma, D. Aromatic Alkylammonium Spacer Cations for Efficient Two-Dimensional Perovskite Solar Cells with Enhanced Moisture and Thermal Stability. *Sol. RRL,* **2018**, 2, 1700215.

172. Kamat, P. V.; Bisquert, J.; Buriak, J. Lead-Free Perovskite Solar Cells. *ACS Energy Lett.,* **2017**. 2, 904-905.

173. Noel, N. K.; Stranks, S. D.; Abate, A.; Wehrenfennig, C.; Guarnera, S.; Haghighirad, A. A.; Sadhanala, A.; Eperon, G. E.; Pathak, S. K.; Johnston, M. B.; et al. Lead-Free Organic-Inorganic Tin Halide Perovskites for Photovoltaic Applications. *Energy Environ. Sci.*, **2014**, 7, 3061-3068.

174. Giustino, F.; Snaith, H. J. Toward Lead-Free Perovskite Solar Cells. *ACS Energy Lett*., **2016**, 1, 1233-1240.

175. Shi, Z.; Guo, J.; Chen, Y.; Li, Q.; Pan, Y.; Zhang, H.; Xia, Y.; Huang, W. Lead-Free Organic–Inorganic Hybrid Perovskites for Photovoltaic Applications: Recent Advances and Perspectives. *Adv.Mater*., **2017**, 29, 1605005.

176. Zhao, X. G.; Yang, J. H.; Fu, Y.; Yang, D.; Xu, Q.; Yu, L.; Wei, S. H.; Zhang, L. Design of Lead-Free Inorganic Halide Perovskites for Solar Cells via Cation-Transmutation. *J. Am. Chem. Soc.,* **2017**, 139, 2630-2638.

177. Abate, A. Perovskite Solar Cells Go Lead Free. *Joule*, **2017**, 1, 659-664.

178. Hong, F.; Saparov, B.; Meng, W.; Xiao, Z.; Mitzi, D. B.; Yan, Y. Viability of Lead-Free Perovskites with Mixed Chalcogen and Halogen Anions for Photovoltaic Applications. *J. Phys. Chem. C*, **2016**, 120, 6435-6441.

179. Yang, S.; Fu, W.; Zhang, Z.; Chen, H.; Li, C.-Z. Recent Advances in Perovskite Solar Cells: Efficiency, Stability and Lead-Free Perovskite. *J. Mater. Chem. A,* **2017**, 5, 11462-11482.

180. Liao, Y.; Liu, H.; Zhou, W.; Yang, D.; Shang, Y.; Shi, Z.; Li, B.; Jiang, X.; Zhang, L.; Quan, L. N.; et al. Highly Oriented Low-Dimensional Tin Halide Perovskites with Enhanced Stability and Photovoltaic Performance. *J. Am. Chem. Soc.,* **2017**, 139, 6693-6699.

181. Liao, W.; Zhao, D.; Yu, Y.; Grice, C. R.; Wang, C.; Cimaroli, A. J.; Schulz, P.; Meng, W.; Zhu, K.; Xiong, R. G.; et al. Lead-Free Inverted Planar Formamidinium Tin Triiodide

Perovskite Solar Cells Achieving Power Conversion Efficiencies up to 6.22%. *Adv. Mater.*, **2016**, 28, 9333-9340.

182. Shao, S.; Liu, J.; Portale, G.; Fang, H. H.; Blake, G. R.; ten Brink, G. H.; Koster, L. J. A.; Loi, M. A. Highly Reproducible Sn-Based Hybrid Perovskite Solar Cells with 9% Efficiency. *Adv. Energy Mater.,* **2018**, 8, 1702019.

183. Lee, S. J.; Shin, S. S.; Kim, Y. C.; Kim, D.; Ahn, T. K.; Noh, J. H.; Seo, J.; Seok, S. Il. Fabrication of Efficient Formamidinium Tin Iodide Perovskite Solar Cells through SnF2-Pyrazine Complex. *J. Am. Chem. Soc.,* **2016**, 138, 3974–3977.

184. Fu, W.; Wang, J.; Zuo, L.; Gao, K.; Liu, F.; Ginger, D. S.; Jen, A. K.-Y. Two-Dimensional Perovskite Solar Cells with 14.1% Power Conversion Efficiency and 0.68% External Radiative Efficiency. *ACS Energy Lett.,* **2018**, 3, 2086-2093.

185. Zhang, X.; Wu, G.; Fu, W.; Qin, M.; Yang, W.; Yan, J.; Zhang, Z.; Lu, X.; Chen, H. Orientation Regulation of Phenylethylammonium Cation Based 2D Perovskite Solar Cell with Efficiency Higher Than 11%. *Adv. Energy Mater.*, **2018**, 8, 1702498.

186. Quan, L. N.; Yuan, M.; Comin, R.; Voznyy, O.; Beauregard, E. M.; Hoogland, S.; Buin, A.; Kirmani, A. R.; Zhao, K.; Amassian, A.; et al. Ligand-Stabilized Reduced-Dimensionality Perovskites. *J. Am. Chem. Soc.,* **2016**, 138 , 2649–2655.

187. Koh, T. M.; Febriansyah, B.; Mathews, N. Ruddlesden-Popper Perovskite Solar Cells. *Chem,* **2017**, 2, 326-327.

188. Zhang, F.; Kim, D. H.; Lu, H.; Park, J. S.; Larson, B. W.; Hu, J.; Gao, L.; Xiao, C.; Reid, O. G.; Chen, X.; et al. Enhanced Charge Transport in 2D Perovskites via Fluorination of Organic Cation. *J. Am. Chem. Soc.*, **2019**, 141, 5972-5979.

189. Williams, O. F.; Guo, Z.; Hu, J.; Yan, L.; You, W.; Moran, A. M. Energy Transfer Mechanisms in Layered 2D Perovskites. *J. Chem. Phys.*, **2018**,148, 134706.

190. Chen, Y.; Sun, Y.; Peng, J.; Zhang, W.; Su, X.; Zheng, K.; Pullerits, T.; Liang, Z. Tailoring Organic Cation of 2D Air-Stable Organometal Halide Perovskites for Highly Efficient Planar Solar Cells. *Adv. Energy Mater.,* **2017**, 7, 1700162.

191. Hao, F.; Stoumpos, C. C.; Guo, P.; Zhou, N.; Marks, T. J.; Chang, R. P. H.; Kanatzidis, M. G. Solvent-Mediated Crystallization of $CH_3NH_3SnI_3$ Films for Heterojunction Depleted Perovskite Solar Cells. *J. Am. Chem. Soc.,* **2015**, 137, 11445-11452.

192. Jeon, N. J.; Noh, J. H.; Kim, Y. C.; Yang, W. S.; Ryu, S.; Seok, S. Il. Solvent Engineering for High-Performance Inorganic-Organic Hybrid Perovskite Solar Cells. *Nat. Mater.,* **2014**, 13, 897–903.

193. Ahn, N.; Son, D. Y.; Jang, I. H.; Kang, S. M.; Choi, M.; Park, N. G. Highly Reproducible

Perovskite Solar Cells with Average Efficiency of 18.3% and Best Efficiency of 19.7% Fabricated via Lewis Base Adduct of Lead(II) Iodide. *J. Am. Chem. Soc.*, **2015**,137, 8696-8699.

194. Yang, W. S.; Noh, J. H.; Jeon, N. J.; Kim, Y. C.; Ryu, S.; Seo, J.; Seok, S. Il. High-Performance Photovoltaic Perovskite Layers Fabricated through Intramolecular Exchange. *Science*, **2015**, 348, 1234-1237.

195. Soe, C. M. M.; Nie, W.; Stoumpos, C. C.; Tsai, H.; Blancon, J. C.; Liu, F.; Even, J.; Marks, T. J.; Mohite, A. D.; Kanatzidis, M. G. Understanding Film Formation Morphology and Orientation in High Member 2D Ruddlesden–Popper Perovskites for High-Efficiency Solar Cells. *Adv. Energy Mater.*, **2018**, 8, 1700979.

196. Zhang, M.; Yun, J. S.; Ma, Q.; Zheng, J.; Lau, C. F. J.; Deng, X.; Kim, J.; Kim, D.; Seidel, J.; Green, M. A.; et al. High-Efficiency Rubidium-Incorporated Perovskite Solar Cells by Gas Quenching. *ACS Energy Lett.* **2017**, 2, 438-444.

197. Edri, E.; Kirmayer, S.; Cahen, D.; Hodes, G. High Open-Circuit Voltage Solar Cells Based on Organic-Inorganic Lead Bromide Perovskite. J. Phys. Chem. Lett. 2013, 4, 897–902.

198. Sadhanala, A.; Deschler, F.; Thomas, T. H.; Dutton, S. E.; Goedel, K. C.; Hanusch, F. C.; Lai, M. L.; Steiner, U.; Bein, T.; Docampo, P.; et al. Preparation of Single Phase Films of CH3 NH3 Pb(I1-x Br x)3 with Sharp Optical Band Edges. *J. Phys. Chem. Lett.,* **2014**, 5, 2501-2505.

199. Hanusch, F. C.; Wiesenmayer, E.; Mankel, E.; Binek, A.; Angloher, P.; Fraunhofer, C.; Giesbrecht, N.; Feckl, J. M.; Jaegermann, W.; Johrendt, D.; et al. Efficient Planar Heterojunction Perovskite Solar Cells Based on Formamidinium Lead Bromide. *J. Phys. Chem. Lett.,* **2014**, 5, 2791-2795.

200. Zhang, X.; Ren, X.; Liu, B.; Munir, R.; Zhu, X.; Yang, D.; Li, J.; Liu, Y.; Smilgies, D.; Li, R.; et al. Stable High Efficiency Two-Dimensional Perovskite Solar Cells via Cesium Doping. *Energy Environ. Sci.,* **2017**, 10, 2095-2102.

201. Zhang, X.; Wu, G.; Yang, S.; Fu, W.; Zhang, Z.; Chen, C.; Liu, W.; Yan, J.; Yang, W.; Chen, H. Vertically Oriented 2D Layered Perovskite Solar Cells with Enhanced Efficiency and Good Stability, *Small,* **2017**, 13, 1700611.

202. Yan, J.; Fu, W.; Zhang, X.; Chen, J.; Yang, W.; Qiu, W.; wang, mang; Liu, F.; Heremans, P.; Chen, H. Highly Oriented Two-Dimensional Formamidinium Lead Iodide Perovskite with a Small Bandgap of 1.51 eV. *Mater. Chem. Front.* **2017**, 2, 121-128.

203. Jeon, N. J.; Noh, J. H.; Yang, W. S.; Kim, Y. C.; Ryu, S.; Seo, J.; Seok, S. Il. Compositional Engineering of Perovskite Materials for High-Performance Solar Cells. *Nature,* **2015**, 517,

476–480.

204. Eperon, G. E.; Stranks, S. D.; Menelaou, C.; Johnston, M. B.; Herz, L. M.; Snaith, H. J. Formamidinium Lead Trihalide: A Broadly Tunable Perovskite for Efficient Planar Heterojunction Solar Cells. *Energy Environ. Sci.,* **2014**, 7, 982-988.

205. Lee, J. W.; Kim, H. S.; Park, N. G. Lewis Acid-Base Adduct Approach for High Efficiency Perovskite Solar Cells. *Acc. Chem. Res.,* **2016**, 49, 311-319.

206. Wang, S.; Ma, Z.; Liu, B.; Wu, W.; Zhu, Y.; Ma, R.; Wang, C. High-Performance Perovskite Solar Cells with Large Grain-Size Obtained by Using the Lewis Acid-Base Adduct of Thiourea. Sol. RRL, **2018**, 2, 1800034.

207. Zhou, N.; Shen, Y.; Li, L.; Tan, S.; Liu, N.; Zheng, G.; Chen, Q.; Zhou, H. Exploration of Crystallization Kinetics in Quasi Two-Dimensional Perovskite and High Performance Solar Cells. *J. Am. Chem. Soc.*, **2018**, 140, 459-465.

208. Cao, D. H.; Stoumpos, C. C.; Yokoyama, T.; Logsdon, J. L.; Song, T.-B.; Farha, O. K.; Wasielewski, M. R.; Hupp, J. T.; Kanatzidis, M. G. Thin Films and Solar Cells Based on Semiconducting Two-Dimensional Ruddlesden–Popper $(CH_3(CH_2)_3NH_3)_2(CH_3NH_3)_{n-1}Sn_nI_{3n+1}$ Perovskites. *ACS Energy Lett.,* **2017**, 2, 982-990.

209. Ramirez, D.; Schutt, K.; Wang, Z.; Pearson, A. J.; Ruggeri, E.; Snaith, H. J.; Stranks, S. D.; Jaramillo, F. Layered Mixed Tin-Lead Hybrid Perovskite Solar Cells with High Stability. *ACS Energy Lett.,* **2018**, 3, 2246-2251.

210. Yang, R.; Li, R.; Cao, Y.; Wei, Y.; Miao, Y.; Tan, W. L.; Jiao, X.; Chen, H.; Zhang, L.; Chen, Q.; et al. Oriented Quasi-2D Perovskites for High Performance Optoelectronic Devices. *Adv. Mater.,* **2018**, 30, 1804771.

211. Cheng, P.; Xu, Z.; Li, J.; Liu, Y.; Fan, Y.; Yu, L.; Smilgies, D.-M.; Müller, C.; Zhao, K.; Liu, S. F. Highly Efficient Ruddlesden–Popper Halide Perovskite $PA_2MA_4Pb_5I_{16}$ Solar Cells. *ACS Energy Lett.*, **2018**, 3, 1975-1982.

212. Lai, H.; Kan, B.; Liu, T.; Zheng, N.; Xie, Z.; Zhou, T.; Wan, X.; Zhang, X.; Liu, Y.; Chen, Y. Two-Dimensional Ruddlesden-Popper Perovskite with Nanorod-like Morphology for Solar Cells with Efficiency Exceeding 15%. *J. Am. Chem. Soc.,* **2018**, 140, 11639-11646.

213. Yao, K.; Wang, X.; Xu, Y. X.; Li, F.; Zhou, L. Multilayered Perovskite Materials Based on Polymeric-Ammonium Cations for Stable Large-Area Solar Cell. *Chem. Mater.*, **2016**, 28, 3131-3138.

214. Mercier, N.; Riou, A. An Organic-Inorganic Hybrid Perovskite Containing Copper Paddle-Wheel Clusters Linking Perovskite Layers: $[Cu(O_2C\text{-}(CH_2)_3\text{-}NH_3)_2]PbBr_4$. *Chem. Commun.* **2004**, 844-845.

215. Ke, W.; Mao, L.; Stoumpos, C. C.; Hoffman, J.; Spanopoulos, I.; Mohite, A. D.; Kanatzidis, M. G. Compositional and Solvent Engineering in Dion–Jacobson 2D Perovskites Boosts Solar Cell Efficiency and Stability. *Adv. Energy Mater.,* **2019**, 9, 1803384.

216. Chen, M.; Ju, M. G.; Hu, M.; Dai, Z.; Hu, Y.; Rong, Y.; Han, H.; Zeng, X. C.; Zhou, Y.; Padture, N. P. Lead-Free Dion-Jacobson Tin Halide Perovskites for Photovoltaics. *ACS Energy Lett.*, **2019**, 4, 276-277.

217. Ahmad, S.; Fu, P.; Yu, S.; Yang, Q.; Liu, X.; Wang, X.; Wang, X.; Guo, X.; Li, C. Dion-Jacobson Phase 2D Layered Perovskites for Solar Cells with Ultrahigh Stability. *Joule*, **2018**, 3, 794-806.

218. Cohen, B. El; Li, Y.; Meng, Q.; Etgar, L. Dion-Jacobson Two-Dimensional Perovskite Solar Cells Based on Benzene Dimethanammonium Cation. *Nano Lett.,* **2019**, 19, 2588-2597.

219. Zhang, Y.; Wang, P.; Tang, M.-C.; Barrit, D.; Ke, W.; Liu, J.; Luo, T.; Liu, Y.; Niu, T.; Smilgies, D.-M.; et al. Dynamical Transformation of Two-Dimensional Perovskites with Alternating Cations in the Interlayer Space for High-Performance Photovoltaics. *J. Am. Chem. Soc.,* **2019**, 141, 2684-2694.

220. Buin, A.; Pietsch, P.; Xu, J.; Voznyy, O.; Ip, A. H.; Comin, R.; Sargent, E. H. Materials Processing Routes to Trap-Free Halide Perovskites. Nano Lett. 2014, 14, 6281-6286.

221. Cohen, B. El; Wierzbowska, M.; Etgar, L. High Efficiency Quasi 2D Lead Bromide Perovskite Solar Cells Using Various Barrier Molecules. *Sustain. Energy Fuels,* **2017**, 1, 1935-1943.

222. Grancini, G.; Roldán-Carmona, C.; Zimmermann, I.; Mosconi, E.; Lee, X.; Martineau, D.; Narbey, S.; Oswald, F.; De Angelis, F.; Graetzel, M.; et al. One-Year Stable Perovskite Solar Cells by 2D/3D Interface Engineering. *Nat. Commun.*, **2017**, 8, Article number: 15684.

223. Wang, Z.; Lin, Q.; Chmiel, F. P.; Sakai, N.; Herz, L. M.; Snaith, H. J. -Air-Stable Solar Cells with 2D-3D Heterostructured Butylammonium-Caesium-Formamidinium Lead Halide Perovskites. *Nat. Energy,* **2017**, 2, Article number: 17135

224. Cho, K. T.; Zhang, Y.; Orlandi, S.; Cavazzini, M.; Zimmermann, I.; Lesch, A.; Tabet, N.; Pozzi, G.; Grancini, G.; Nazeeruddin, M. K. Water-Repellent Low-Dimensional Fluorous Perovskite as Interfacial Coating for 20% Efficient Solar Cells. *Nano Lett.,* **2018**, 18, 5467-5474.

225. Zhou, Q.; Liang, L.; Hu, J.; Cao, B.; Yang, L.; Wu, T.; Li, X.; Zhang, B.; Gao, P. High-Performance Perovskite Solar Cells with Enhanced Environmental Stability Based on a $(p\text{-}FC_6H_4C_2H_4\ NH_3)_2\ [PbI_4]$ Capping Layer. *Adv. Energy Mater.*, **2019**, 9, 1802595.

226. Cho, Y.; Soufiani, A. M.; Yun, J. S.; Kim, J.; Lee, D. S.; Seidel, J.; Deng, X.; Green, M. A.; Huang, S.; Ho-Baillie, A. W. Y. Mixed 3D–2D Passivation Treatment for Mixed-Cation Lead Mixed-Halide Perovskite Solar Cells for Higher Efficiency and Better Stability. *Adv. Energy Mater.* **2018**, 8, 1703392.

227. Yun, J. S.; Ho-Baillie, A.; Huang, S.; Woo, S. H.; Heo, Y.; Seidel, J.; Huang, F.; Cheng, Y. B.; Green, M. A. Benefit of Grain Boundaries in Organic-Inorganic Halide Planar Perovskite Solar Cells. *J. Phys. Chem. Lett.*, **2015**, 6, 875–880.

228. Zhang, T.; Dar, M. I.; Li, G.; Xu, F.; Guo, N.; Grätzel, M.; Zhao, Y. Bication Lead Iodide 2D Perovskite Component to Stabilize Inorganic α-$CsPbI_3$ perovskite Phase for High-Efficiency Solar Cells. *Sci. Adv.,* **2017**, 3, e1700841.

229. Cao, J.; Li, C.; Lv, X.; Feng, X.; Meng, R.; Wu, Y.; Tang, Y. Efficient Grain Boundary Suture by Low-Cost Tetra-Ammonium Zinc Phthalocyanine for Stable Perovskite Solar Cells with Expanded Photoresponse. *J. Am. Chem. Soc.*, **2018**, 140, 11577-11580.

230. Eperon, G. E.; Paternò, G. M.; Sutton, R. J.; Zampetti, A.; Haghighirad, A. A.; Cacialli, F.; Snaith, H. J. Inorganic Caesium Lead Iodide Perovskite Solar Cells. *J. Mater. Chem. A*, **2015**, 3, 19688-19695.

231. Wang, Y.; Zhang, T.; Kan, M.; Li, Y.; Wang, T.; Zhao, Y. Efficient α-$CsPbI_3$ Photovoltaics with Surface Terminated Organic Cations. *Joule*, **2018**, 2, 2065-2075.

232. Albrecht, U.; Bässler, H. Langevin-Type Charge Carrier Recombination in a Disordered Hopping System. *Phys. status solidi*, **1995**, 131, 455-459.

233. Van Der Holst, J. J. M.; Van Oost, F. W. A.; Coehoorn, R.; Bobbert, P. A. Electron-Hole Recombination in Disordered Organic Semiconductors: Validity of the Langevin Formula. *Phys. Rev. B.,* **2009**, 80, 235202.

234. Tsai, H.; Asadpour, R.; Blancon, J.-C.; Stoumpos, C. C.; Even, J.; Ajayan, P. M.; Kanatzidis, M. G.; Alam, M. A.; Mohite, A. D.; Nie, W. Design Principles for Electronic Charge Transport in Solution-Processed Vertically Stacked 2D Perovskite Quantum Wells. *Nat. Commun.*, **2018**, 9, Article number: 2130.

235. Liu, B.; Soe, C. M. M.; Stoumpos, C. C.; Nie, W.; Tsai, H.; Lim, K.; Mohite, A. D.; Kanatzidis, M. G.; Marks, T. J.; Singer, K. D. Optical Properties and Modeling of 2D Perovskite Solar Cells. *Sol. RRL*, **2017**, 1, 1700062.

236. Chen, A. Z.; Shiu, M.; Ma, J. H.; Alpert, M. R.; Zhang, D.; Foley, B. J.; Smilgies, D. M.; Lee, S. H.; Choi, J. J. Origin of Vertical Orientation in Two-Dimensional Metal Halide Perovskites and Its Effect on Photovoltaic Performance. *Nat. Commun.*, **2018**, 9, Article number: 1336.

237. Zolotoyabko, E. Determination of the Degree of Preferred Orientation within the March-Dollase Approach. *J. Appl. Crystallogr.,* **2009**, 42, 513-518.

238. Zolotoyabko, E. Fast Quantitative Analysis of Strong Uniaxial Texture Using a March-Dollase Approach. J. *Appl. Crystallogr.*, **2013**, 46, 1877-1879.

239. Schlipf, J.; Müller-Buschbaum, P. Structure of Organometal Halide Perovskite Films as Determined with Grazing-Incidence X-Ray Scattering Methods. *Adv. Energy Mater.,* **2017**, 7, 1700131.

240. Chen, A. Z.; Shiu, M.; Deng, X.; Mahmoud, M.; Zhang, D.; Foley, B. J.; Lee, S.-H.; Giri, G.; Choi, J. J. Understanding the Formation of Vertical Orientation in Two-Dimensional Metal Halide Perovskite Thin Films. *Chem. Mater.*, **2019**, 31, 1336-1343.

241. Hassan, Y.; Song, Y.; Pensack, R. D.; Abdelrahman, A. I.; Kobayashi, Y.; Winnik, M. A.; Scholes, G. D. Structure-Tuned Lead Halide Perovskite Nanocrystals. *Adv. Mater.*, **2016**, 28, 566–573.

242. Stranks, S. D.; Snaith, H. J. Metal-Halide Perovskites for Photovoltaic and Light-Emitting Devices. *Nat. Nanotechnol.,* **2015**, 10, 391–402.

243. Sum, T. C.; Mathews, N.; Xing, G.; Lim, S. S.; Chong, W. K.; Giovanni, D.; Dewi, H. A. Spectral Features and Charge Dynamics of Lead Halide Perovskites: Origins and Interpretations. *Acc. Chem. Res.,* **2016**, 49, 294–302.

244. Zhang, X.; Ye, J.; Zhu, L.; Zheng, H.; Liu, G.; Liu, X.; Duan, B.; Pan, X.; Dai, S. High-Efficiency Perovskite Solar Cell Prepared by a Sandwich Structure MAI-PbI2-MAI Precursor Film. *Nanoscale,* **2016**, 9, 4691–4699.

245. Zhang, X.; Li, Z.; Ding, Y.; Hu, L.; Ye, J.; Pan, X.; Dai, S. Highly Efficient and Stable Perovskite Solar Cell Prepared from an in Situ Pre-Wetted PbI_2 Nano-Sheet Array Film. *Sustain. Energy Fuels*, **2017**, 1, 1056–1064.

246. Tiep, N. H.; Ku, Z.; Fan, H. J. Recent Advances in Improving the Stability of Perovskite Solar Cells. *Adv. Energy Mater.*, **2015**, 6, 1501420.

247. Wang, Z.; Shi, Z.; Li, T.; Chen, Y.; Huang, W. Stability of Perovskite Solar Cells: A Prospective on the Substitution of the A Cation and X Anion. *Angew. Chemie Int. Ed.,* **2016**, 56, 1190-1212.

248. Christians, J. A.; Miranda Herrera, P. A.; Kamat, P. V. Transformation of the Excited State and Photovoltaic Efficiency of $CH_3NH_3PbI_3$ Perovskite upon Controlled Exposure to Humidified Air. *J. Am. Chem. Soc.*, **2015**, 137, 1530–1538.

249. Conings, B.; Drijkoningen, J.; Gauquelin, N.; Babayigit, A.; D'Haen, J.; D'Olieslaeger, L.; Ethirajan, A.; Verbeeck, J.; Manca, J.; Mosconi, E.; et al. Intrinsic Thermal Instability of

Methylammonium Lead Trihalide Perovskite. *Adv. Energy Mater.,* **2015**, 5, 1500477

250. Berhe, T. A.; Su, W.-N.; Chen, C.-H.; Pan, C.-J.; Cheng, J.-H.; Chen, H.-M.; Tsai, M.-C.; Chen, L.-Y.; Dubale, A. A.; Hwang, B.-J. Organometal Halide Perovskite Solar Cells: Degradation and Stability. *Energy Environ. Sci.,* **2016**, 9, 323-356.

251. Kagan, C. R.; Mitzi, D. B.; Dimitrakopoulos, C. D.; Brown, a. R.; Pomp, a.; Hart, C. M.; Leeuw, D. M. De; Dimitrakopoulos, C. D.; Brown, a. R.; Pomp, a.; et al. Organic-Inorganic Hybrid Materials as Semiconducting Channels in Thin-Film Field-Effect Transistors. *Science*, **1999**, 286, 945–947.

252. Bryant, D.; Aristidou, N.; Pont, S.; Sanchez-Molina, I.; Chotchunangatchaval, T.; Wheeler, S.; Durrant, J. R.; Haque, S. A. Light and Oxygen Induced Degradation Limits the Operational Stability of Methylammonium Lead Triiodide Perovskite Solar Cells. *Energy Environ. Sci.,* **2016**, 9, 1655-1660.

253. Habisreutinger, S. N.; Leijtens, T.; Eperon, G. E.; Stranks, S. D.; Nicholas, R. J.; Snaith, H. J. Carbon Nanotube/Polymer Composites as a Highly Stable Hole Collection Layer in Perovskite Solar Cells. *Nano Lett.,* **2014**, 14, 5561-5568.

254. Tan, K. W.; Moore, D. T.; Saliba, M.; Sai, H.; Estroff, L. a; Hanrath, T.; Snaith, H. J.; Wiesner, U.; Al, T. a N. E. T. Thermally Induced Structural Evolution and Performance of Mesoporous Block Copolymer- Directed Alumina Perovskite Solar Cells. *ACS Nano,* **2014**, 8, 4730–4739.

255. Kawamura, Y.; Mashiyama, H.; Hasebe, K. Structural Study on Cubic-Tetragonal Transition of $CH_3NH_3PbI_3$. *J. Phys. Soc. Japan*, **2002**, 71, 1694–1697.

256. Cheng, Y.; Yang, Q.-D.; Xiao, J.; Xue, Q.; Li, H.-W.; Guan, Z.; Yip, H.-L.; Tsang, S.-W. Decomposition of Organometal Halide Perovskite Films on Zinc Oxide Nanoparticles. *ACS Appl. Mater. Interfaces*, **2015**, 7, 19986–19993.

257. Lee, J. W.; Kim, D. H.; Kim, H. S.; Seo, S. W.; Cho, S. M.; Park, N. G. Formamidinium and Cesium Hybridization for Photo- and Moisture-Stable Perovskite Solar Cell. *Adv. Energy Mater.*, **2015**, 5, 1501310.

258. Wei, Y.; Audebert, P.; Galmiche, L.; Lauret, J. S.; Deleporte, E. Photostability of 2D Organic-Inorganic Hybrid Perovskites. *Materials (Basel),* **2014**, 7, 4789–4802.

259. Mitzi, D. B. Synthesis, Structure, and Properties of Organic-Inorganic Perovskites and Related Materials, **2007**, 48.

260. Tsai, H.; Nie, W.; Blancon, J.-C.; Stoumpos, C. C.; Asadpour, R.; Harutyunyan, B.; Neukirch, A. J.; Verduzco, R.; Crochet, J. J.; Tretiak, S.; et al. High-Efficiency Two-Dimensional Ruddlesden–Popper Perovskite Solar Cells. *Nature*, **2016**, 536, 312–316..

261. Hamaguchi, R.; Yoshizawa-Fujita, M.; Miyasaka, T.; Kunugita, H.; Ema, K.; Takeoka, Y.; Rikukawa, M. Formamidine and Cesium-Based Quasi-Two-Dimensional Perovskites as Photovoltaic Absorbers. *Chem. Commun.,* **2017**, 53, 4366–4369.

262. Du, K. Z.; Tu, Q.; Zhang, X.; Han, Q.; Liu, J.; Zauscher, S.; Mitzi, D. B. Two-Dimensional Lead(II) Halide-Based Hybrid Perovskites Templated by Acene Alkylamines: Crystal Structures, Optical Properties, and Piezoelectricity. *Inorg. Chem.,* **2017**, 56, 9291–9302.

263. Søndergaard, R.; Hösel, M.; Angmo, D.; Larsen-Olsen, T. T.; Krebs, F. C. Roll-to-Roll Fabrication of Polymer Solar Cells. *Mater. Today*, **2012**, 15, 36-49.

264. Bonthu, S.; Lingamallu, G.; Singh, S. P. Recent Advances in Flexible Perovskite Solar Cells. *Chem. Commun.***, 2015**, 51, 14696–14707.

265. Hodes, G.; Cahen, D. Photovoltaics Perovskite Cells Roll Forward. *Nat. Photonics*, **2014**, 8, 87–88.

266. Li, M.-H.; Yang, Y.-S.; Wang, K.-C.; Chiang, Y.-H.; Shen, P.-S.; Lai, W.-C.; Guo, T.-F.; Chen, P. Robust and Recyclable Substrate Template with Ultrathin Nanoporous Counter Electrode for Organic-Hole-Conductor-Free Monolithic Perovskite Solar Cells. *ACS Appl. Mater. Interfaces*, **2017**, 9, 41845-41854.

267. Nie, W.; Tsai, H.; Asadpour, R.; Blancon, J.-C.; Neukirch, A. J.; Gupta, G.; Crochet, J. J.; Chhowalla, M.; Tretiak, S.; Alam, M. A.; et al. High-Efficiency Solution-Processed Perovskite Solar Cells with Millimeter-Scale Grains. Science, **2015**, 347, 522–525.

268. Ahn, N.; Son, D.-Y.; Jang, I.-H.; Kang, S. M.; Choi, M.; Park, N.-G. Highly Reproducible Perovskite Solar Cells with Average Efficiency of 18.3% and Best Efficiency of 19.7% Fabricated via Lewis Base Adduct of Lead(II) Iodide. *J. Am. Chem. Soc.,* **2015**,137, 8696-8699.

269. Zhang, X. H.; Ye, J. J.; Zhu, L. Z.; Zheng, H. Y.; Liu, X. P.; Pan, X.; Dai, S. Y. High Consistency Perovskite Solar Cell with a Consecutive Compact and Mesoporous TiO_2 Film by One-Step Spin-Coating. *ACS Appl. Mater. Interfaces*., **2016**, 8, 35440–35446.

270. Choi, J. J.; Yang, X.; Norman, Z. M.; Billinge, S. J. L.; Owen, J. S. Structure of Methylammonium Lead Iodide within Mesoporous Titanium Dioxide: Active Material in High-Performance Perovskite Solar Cells. *Nano Lett.,* **2014**, 14, 127–133.

271. Yang, Y.; Feng, S.; Li, M.; Xu, W.; Yin, G.; Wang, Z.; Sun, B.; Gao, X. Annealing Induced Re-Crystallization in $CH_3NH_3PbI_{3-x}Cl_x$ for High Performance Perovskite Solar Cells. *Sci. Rep.,* **2017**, 7, 46724.

272. Liu, J.; Leng, J.; Wu, K.; Zhang, J.; Jin, S. Observation of Internal Photoinduced Electron and Hole Separation in Hybrid Two-Dimentional Perovskite Films. *J. Am. Chem. Soc.*,

2017, 139, 1432–1435.

273. Grancini, G.; Srimath Kandada, A. R.; Frost, J. M.; Barker, A. J.; De Bastiani, M.; Gandini, M.; Marras, S.; Lanzani, G.; Walsh, A.; Petrozza, A. Role of Microstructure in the Electron–Hole Interaction of Hybrid Lead Halide Perovskites. *Nat. Photonics,* **2015**, 9, 695–701.

274. Gangishetty, M. K.; Scott, R. W. J.; Kelly, T. L. Effect of Relative Humidity on Crystal Growth, Device Performance and Hysteresis in Planar Heterojunction Perovskite Solar Cells. *Nanoscale,* **2015**, 8, 6300-6307.

275. Yang, J.; Siempelkamp, B. D.; Liu, D.; Kelly, T. L. Investigation of CH3NH3PbI3 degradation Rates and Mechanisms in Controlled Humidity Environments Using in Situ Techniques. *ACS Nano*, **2015**, 9, 1955–1963.

276. Guerrero, A.; You, J.; Aranda, C.; Kang, Y. S.; Garcia-Belmonte, G.; Zhou, H.; Bisquert, J.; Yang, Y. Interfacial Degradation of Planar Lead Halide Perovskite Solar Cells. *ACS Nano***, 2015**, 10, 218-224.

277. Leijtens, T.; Eperon, G. E.; Pathak, S.; Abate, A.; Lee, M. M.; Snaith, H. J. Overcoming Ultraviolet Light Instability of Sensitized TiO2 with Meso-Superstructured Organometal Tri-Halide Perovskite Solar Cells. *Nat. Commun.,* **2013**, 4, Article number: 2885.

278. Dualeh, A.; Gao, P.; Seok, S. Il; Nazeeruddin, M. K.; Grätzel, M. Thermal Behavior of Methylammonium Lead-Trihalide Perovskite Photovoltaic Light Harvesters. *Chem. Mater.,* **2014**, 26, 6160–6164.

279. Saliba, M.; Correa-Baena, J.-P.; Graetzel, M.; Hagfeldt, A.; Abate, A. Perovskite Solar Cells from the Atomic to the Film Level. *Angew. Chemie Int. Ed.*, **2017**, 57, 2554-2569.

280. Pellet, N.; Gao, P.; Gregori, G.; Yang, T. Y.; Nazeeruddin, M. K.; Maier, J.; Grätzel, M. Mixed-Organic-Cation Perovskite Photovoltaics for Enhanced Solar-Light Harvesting. *Angew. Chemie. Int. Ed.,* **2014**, 53, 3151–3157.

281. Ogomi, Y.; Morita, A.; Tsukamoto, S.; Saitho, T.; Fujikawa, N.; Shen, Q.; Toyoda, T.; Yoshino, K.; Pandey, S. S.; Ma, T.; et al. $CH_3NH_3Sn_xPb_{(1-x)}I_3$ Perovskite Solar Cells Covering up to 1060 Nm. *J. Phys. Chem. Lett.,* **2014**, 5, 1004–1011.

282. Giorgi, G.; Fujisawa, J. I.; Segawa, H.; Yamashita, K. Small Photocarrier Effective Masses Featuring Ambipolar Transport in Methylammonium Lead Iodide Perovskite: A Density Functional Analysis. *J. Phys. Chem. Lett.,* **2013**, 4, 4213-4216.

283. Giorgi, G.; Fujisawa, J. I.; Segawa, H.; Yamashita, K. Organic - Inorganic Hybrid Lead Iodide Perovskite Featuring Zero Dipole Moment Guanidinium Cations: A Theoretical Analysis. *J. Phys. Chem. C,* **2015**,119, 4694-4701.

284. Konstantakou, M.; Stergiopoulos, T. A Critical Review on Tin Halide Perovskite Solar

Cells. *J. Mater. Chem. A*, **2017**, 5, 11518–11549.

285. Gupta, S.; Cahen, D.; Hodes, G. How SnF_2 Impacts the Material Properties of Lead-Free Tin Perovskites. *J. Phys. Chem. C*, **2018**, 25, 13926-13936.

286. Shi, T.; Zhang, H. S.; Meng, W.; Teng, Q.; Liu, M.; Yang, X.; Yan, Y.; Yip, H. L.; Zhao, Y. J. Effects of Organic Cations on the Defect Physics of Tin Halide Perovskites. *J. Mater. Chem. A,* **2017**, 5, 15124–15129.

287. Liao, W.; Zhao, D.; Yu, Y.; Shrestha, N.; Ghimire, K.; Grice, C. R.; Wang, C.; Xiao, Y.; Cimaroli, A. J.; Ellingson, R. J.; et al. Fabrication of Efficient Low-Bandgap Perovskite Solar Cells by Combining Formamidinium Tin Iodide with Methylammonium Lead Iodide. *J. Am. Chem. Soc.,* **2016**, 138, 12360–12363.

288. Xing, G.; Kumar, M. H.; Chong, W. K.; Liu, X.; Cai, Y.; Ding, H.; Asta, M.; Grätzel, M.; Mhaisalkar, S.; Mathews, N.; et al. Solution-Processed Tin-Based Perovskite for Near-Infrared Lasing. *Adv. Mater.,* **2016**, 28, 8191-8196.

289. Davies, C. L.; Filip, M. R.; Patel, J. B.; Crothers, T. W.; Verdi, C.; Wright, A. D.; Milot, R. L.; Giustino, F.; Johnston, M. B.; Herz, L. M. Bimolecular Recombination in Methylammonium Lead Triiodide Perovskite Is an Inverse Absorption Process. *Nat. Commun.,* **2018**, 9, Article number: 293.

290. Galkowski, K.; Surrente, A.; Baranowski, M.; Zhao, B.; Yang, Z.; Sadhanala, A.; Mackowski, S.; Stranks, S. D.; Plochocka, P. Excitonic Properties of Low-Band-Gap Lead–Tin Halide Perovskites. *ACS Energy Lett.*, **2019**, 4, 615-621.

291. Stoumpos, C. C.; Malliakas, C. D.; Kanatzidis, M. G. Semiconducting Tin and Lead Iodide Perovskites with Organic Cations: Phase Transitions, High Mobilities, and near-Infrared Photoluminescent Properties. *Inorg. Chem.*, **2013**, 52, 9019–9038.

292. Tidhar, Y.; Edri, E.; Weissman, H.; Zohar, D.; Hodes, G.; Cahen, D.; Rybtchinski, B.; Kirmayer, S. Crystallization of Methyl Ammonium Lead Halide Perovskites: Implications for Photovoltaic Applications. *J. Am. Chem. Soc.,* **2014**. 136, 13249-13256.

293. Hao, F.; Stoumpos, C. C.; Chang, R. P. H.; Kanatzidis, M. G. Anomalous Band Gap Behavior in Mixed Sn and Pb Perovskites Enables Broadening of Absorption Spectrum in Solar Cells. *J. Am. Chem. Soc.*, **2014**, 136, 8094–8099.

294. Prasanna, R.; Gold-Parker, A.; Leijtens, T.; Conings, B.; Babayigit, A.; Boyen, H. G.; Toney, M. F.; McGehee, M. D. Band Gap Tuning via Lattice Contraction and Octahedral Tilting in Perovskite Materials for Photovoltaics. *J. Am. Chem. Soc.*, **2017**, 139, 11117-11124.

295. Rajendra Kumar, G.; Kim, H. J.; Karupannan, S.; Prabakar, K. Interplay between Iodide

and Tin Vacancies in $CsSnI_3$ Perovskite Solar Cells. *J. Phys. Chem. C*, **2017**, 121, 16447–16453.

296. Kumar, M. H.; Dharani, S.; Leong, W. L.; Boix, P. P.; Prabhakar, R. R.; Baikie, T.; Shi, C.; Ding, H.; Ramesh, R.; Asta, M.; et al. Lead-Free Halide Perovskite Solar Cells with High Photocurrents Realized Through Vacancy Modulation. *Adv. Mater.*, **2014**, 26, 7122–7127.

297. Chung, I.; Song, J. H.; Im, J.; Androulakis, J.; Malliakas, C. D.; Li, H.; Freeman, A. J.; Kenney, J. T.; Kanatzidis, M. G. $CsSnI_3$: Semiconductor or Metal? High Electrical Conductivity and Strong near-Infrared Photoluminescence from a Single Material. High Hole Mobility and Phase-Transitions. *J. Am. Chem. Soc.,* **2012**, 134, 8579–8587.

298. Perdew, J. P.; Burke, K.; Ernzerhof, M. Generalized Gradient Approximation Made Simple. *Phys. Rev. Lett.*, **1996**, 77, 3865.

299. Meggiolaro, D.; Mosconi, E.; De Angelis, F. Modeling the Interaction of Molecular Iodine with $MAPbI_3$: A Probe of Lead-Halide Perovskites Defect Chemistry. *ACS Energy Lett.,* **2018**, 3, 447-451.

300. Ke, W.; Stoumpos, C. C.; Zhu, M.; Mao, L.; Spanopoulos, I.; Liu, J.; Kontsevoi, O. Y.; Chen, M.; Sarma, D.; Zhang, Y.; et al. Enhanced Photovoltaic Performance and Stability with a New Type of Hollow 3D Perovskite {en}$FASnI_3$. *Sci. Adv.,* **2017**, 3, e1701293.

301. Yin, W.-J.; Shi, T.; Yan, Y. Unusual Defect Physics in CH3NH3PbI3 Perovskite Solar Cell Absorber. *Appl. Phys. Lett.,* **2014**, 104, 063903.

302. Mauer, R.; Howard, I. A.; Laquai, F. Effect of Nongeminate Recombination on Fill Factor in Polythiophene/ Methanofullerene Organic Solar Cells. *J. Phys. Chem. Lett.*, **2010**, 1, 3500-3505.

303. Yadav, P.; Alotaibi, M. H.; Arora, N.; Dar, M. I.; Zakeeruddin, S. M.; Grätzel, M. Influence of the Nature of A Cation on Dynamics of Charge Transfer Processes in Perovskite Solar Cells. *Adv. Funct. Mater.,* **2017**, 28, 1706073.

304. Sherkar, T. S.; Momblona, C.; Gil-Escrig, L.; Ávila, J.; Sessolo, M.; Bolink, H. J.; Koster, L. J. A. Recombination in Perovskite Solar Cells: Significance of Grain Boundaries, Interface Traps, and Defect Ions. *ACS Energy Lett.,* **2017**, 2, 1214–1222.

305. Jacobs, D. A.; Wu, Y.; Shen, H.; Barugkin, C.; Beck, F. J.; White, T. P.; Weber, K.; Catchpole, K. R. Hysteresis Phenomena in Perovskite Solar Cells: The Many and Varied Effects of Ionic Accumulation. *Phys. Chem. Chem. Phys.*, **2017**, 19, 3094–3103.

306. Pockett, A.; Carnie, M. J. Ionic Influences on Recombination in Perovskite Solar Cells. *ACS Energy Lett.,* **2017**, 2, 1683–1689.

307. Azpiroz, J. M.; Mosconi, E.; Bisquert, J.; De Angelis, F. Defect Migration in

Methylammonium Lead Iodide and Its Role in Perovskite Solar Cell Operation. *Energy Environ. Sci.*, **2015**, 8, 2118-2127.

308. Yu, H.; Lu, H.; Xie, F.; Zhou, S.; Zhao, N. Native Defect-Induced Hysteresis Behavior in Organolead Iodide Perovskite Solar Cells. *Adv. Funct. Mater.,* **2016**, 26, 1411-1419.

309. Lee, D. S.; Yun, J. S.; Kim, J.; Soufiani, A. M.; Chen, S.; Cho, Y.; Deng, X.; Seidel, J.; Lim, S.; Huang, S.; et al. Passivation of Grain Boundaries by Phenethylammonium in Formamidinium-Methylammonium Lead Halide Perovskite Solar Cells. *ACS Energy Lett.*, **2018**, 3, 647–654.

310. Yun, J. S.; Seidel, J.; Kim, J.; Soufiani, A. M.; Huang, S.; Lau, J.; Jeon, N. J.; Seok, S. Il; Green, M. A.; Ho-Baillie, A. Critical Role of Grain Boundaries for Ion Migration in Formamidinium and Methylammonium Lead Halide Perovskite Solar Cells. *Adv. Energy Mater.*, **2016**, 6, 1600330.

311. Kim, Y. C.; Jeon, N. J.; Noh, J. H.; Yang, W. S.; Seo, J.; Yun, J. S.; Ho-Baillie, A.; Huang, S.; Green, M. A.; Seidel, J.; et al. Beneficial Effects of PbI_2 Incorporated in Organo-Lead Halide Perovskite Solar Cells. *Adv. Energy Mater.*, **2016**, 6, 1502104.

312. Yan, Y.; Jiang, C. S.; Noufi, R.; Wei, S. H.; Moutinho, H. R.; Al-Jassim, M. M. Electrically Benign Behavior of Grain Boundaries in Polycrystalline $CuInSe_2$ Films. *Phys. Rev. Lett.,* **2007**, 99, 235504.

313. Van Reenen, S.; Kemerink, M.; Snaith, H. J. Modeling Anomalous Hysteresis in Perovskite Solar Cells. *J. Phys. Chem. Lett.*, **2015**, 6, 3808-3814.

314. Chen, B.; Yang, M.; Priya, S.; Zhu, K. Origin of J-V Hysteresis in Perovskite Solar Cells. *J. Phys. Chem Lett.*, **2016**, 7, 905-917.

315. Giorgi, G.; Yamashita, K. Zero-Dipole Molecular Organic Cations in Mixed Organic-Inorganic Halide Perovskites: Possible Chemical Solution for the Reported Anomalous Hysteresis in the Current-Voltage Curve Measurements. *Nanotechnology*, **2015**, 26, Number 44.

316. Marco, N. De; Zhou, H.; Chen, Q.; Sun, P.; Liu, Z.; Meng, L.; Yao, E. P.; Liu, Y.; Schiffer, A.; Yang, Y. Guanidinium: A Route to Enhanced Carrier Lifetime and Open-Circuit Voltage in Hybrid Perovskite Solar Cells. *Nano Lett.*, **2016**, 16, 1009-1016.

317. Pham, N. D.; Zhang, C.; Tiong, V. T.; Zhang, S.; Will, G.; Bou, A.; Bisquert, J.; Shaw, P. E.; Du, A.; Wilson, G. J.; et al. Tailoring Crystal Structure of $FA_{0.83}Cs_{0.17}PbI_3$ Perovskite Through Guanidinium Doping for Enhanced Performance and Tunable Hysteresis of Planar Perovskite Solar Cells. *Adv. Funct. Mater.,* **2018**, 29, 1806479.

318. Kresse, G.; Furthmüller, J. Efficient Iterative Schemes for Ab Initio Total-Energy

Calculations Using a Plane-Wave Basis Set. *Phys. Rev. B*, **1996**, 54, 11169.

319. Joubert, D. From Ultrasoft Pseudopotentials to the Projector Augmented-Wave Method. *Phys. Rev. B - Condens. Matter Mater. Phys.*, **1999**, 59, 1758.

320. Blöchl, P. E.; Först, C. J.; Schimpl, J. Projector Augmented Wave Method: Ab Initio Molecular Dynamics with Full Wave Functions. Bull. *Mater. Sci.,* **2003**, 26, 33–41.

321. Grimme, S.; Antony, J.; Ehrlich, S.; Krieg, H. A Consistent and Accurate Ab Initio Parametrization of Density Functional Dispersion Correction (DFT-D) for the 94 Elements H-Pu. *J. Chem. Phys.,* **2010**,132, 154104.

322. Grimme, S.; Ehrlich, S.; Goerigk, L. Effect of the Damping Function in Dispersion Corrected Density Functional Theory. *J. Comput. Chem.,* **2011**, 32, 1456-1465.

323. Papavassiliou, G. C.; Koutselas, I. B.; Terzis, A.; Whangbo, M. H. Structural and Electronic Properties of the Natural Quantum-Well System $(C_6H_5CH_2CH_2NH_3)_2SnI_4$. *Solid State Commun.,***1994**, 91, 695-698.

324. Li, J.; Cao, H.-L.; Jiao, W.-B.; Wang, Q.; Wei, M.; Cantone, I.; Lü, J.; Abate, A. Biological Impact of Lead from Halide Perovskites Reveals the Risk of Introducing a Safe Threshold. *Nat. Commun.,* **2020**, 11, 310.

325. Liang, L.; Gao, P. Lead-Free Hybrid Perovskite Absorbers for Viable Application: Can We Eat the Cake and Have It Too? *Adv. Sci.,* **2018**, 5, 1700331.

326. Ke, W.; Stoumpos, C. C.; Kanatzidis, M. G. “Unleaded” Perovskites: Status Quo and Future Prospects of Tin-Based Perovskite Solar Cells. *Adv. Mater.,* **2018**, 31, 1803230.

327. Igbari, F.; Wang, R.; Wang, Z. K.; Ma, X. J.; Wang, Q.; Wang, K. L.; Zhang, Y.; Liao, L. S.; Yang, Y. Composition Stoichiometry of $Cs_2AgBiBr_6$ Films for Highly Efficient Lead-Free Perovskite Solar Cells. *Nano Lett.*, **2019**, 19, 3, 2066-2073.

328. Connor, B. A.; Leppert, L.; Smith, M. D.; Neaton, J. B.; Karunadasa, H. I. Layered Halide Double Perovskites: Dimensional Reduction of $Cs_2AgBiBr_6$. *J. Am. Chem. Soc.*, **2018**, 140, 5235-5240.

329. McClure, E. T.; Ball, M. R.; Windl, W.; Woodward, P. M. Cs_2AgBiX_6 (X = Br, Cl): New Visible Light Absorbing, Lead-Free Halide Perovskite Semiconductors. *Chem. Mater.,* **2016**, 28, 1348-1354.

330. Sun, S.; Hartono, N. T. P.; Ren, Z. D.; Oviedo, F.; Buscemi, A. M.; Layurova, M.; Chen, D. X.; Ogunfunmi, T.; Thapa, J.; Ramasamy, S.; et al. Accelerated Development of Perovskite-Inspired Materials via High-Throughput Synthesis and Machine-Learning Diagnosis. *Joule*, **2019**, 3, 1437-1451.

331. Hu, Y.; Bai, F.; Liu, X.; Ji, Q.; Miao, X.; Qiu, T.; Zhang, S. Bismuth Incorporation Stabilized

α-$CsPbI_3$ for Fully Inorganic Perovskite Solar Cells. *ACS Energy Lett.,* **2017**, 2, 2219-2227.

332. Ju, D.; Jiang, X.; Xiao, H.; Chen, X.; Hu, X.; Tao, X. Narrow Band Gap and High Mobility of Lead-Free Perovskite Single Crystal Sn-Doped $MA_3Sb_2I_9$. *J. Mater. Chem. A*, **2018**, 6, 20753-20759.

333. Hu, Y.; Qiu, T.; Bai, F.; Ruan, W.; Zhang, S. Highly Efficient and Stable Solar Cells with 2D $MA_3Bi_2I_9$/3D $MAPbI_3$ Heterostructured Perovskites. *Adv. Energy Mater.,* **2018**, 8, 1703620.

334. Ke, W.; Kanatzidis, M. G. Prospects for Low-Toxicity Lead-Free Perovskite Solar Cells. *Nat. Commu.,* **2019**, 10, Article number: 965.

335. Babayigit, A.; Ethirajan, A.; Muller, M.; Conings, B. Toxicity of Organometal Halide Perovskite Solar Cells. *Nat. Mater.,* **2016**, 15, 247–251.

336. Anaya, M.; Correa-Baena, J. P.; Lozano, G.; Saliba, M.; Anguita, P.; Roose, B.; Abate, A.; Steiner, U.; Grätzel, M.; Calvo, M. E.; et al. Optical Analysis of $CH_3NH_3Sn_xPb_{1-x}I_3$ Absorbers: A Roadmap for Perovskite-on-Perovskite Tandem Solar Cells. *J. Mater. Chem. A,* **2016**, 4, 11214-11221.

337. Yokoyama, T.; Song, T. Bin; Cao, D. H.; Stoumpos, C. C.; Aramaki, S.; Kanatzidis, M. G. The Origin of Lower Hole Carrier Concentration in Methylammonium Tin Halide Films Grown by a Vapor-Assisted Solution Process. *ACS Energy Lett.*, **2017**, 2, 1, 22-28.

338. Song, T. Bin; Yokoyama, T.; Logsdon, J.; Wasielewski, M. R.; Aramaki, S.; Kanatzidis, M. G. Piperazine Suppresses Self-Doping in $CsSnI_3$ Perovskite Solar Cells. *ACS Appl. Energy Mater.*, **2018**, 1, 4221-4226.

339. Takahashi, Y.; Obara, R.; Lin, Z. Z.; Takahashi, Y.; Naito, T.; Inabe, T.; Ishibashi, S.; Terakura, K. Charge-Transport in Tin-Iodide Perovskite $CH_3NH_3SnI_3$: Origin of High Conductivity. *Dalt. Trans.,* **2011**, 40, 5563-5568.

340. Tong, J.; Song, Z.; Kim, D. H.; Chen, X.; Chen, C.; Palmstrom, A. F.; Ndione, P. F.; Reese, M. O.; Dunfield, S. P.; Reid, O. G.; et al. Carrier Lifetimes of >1 μs in Sn-Pb Perovskites Enable Efficient All-Perovskite Tandem Solar Cells. *Science*, **2019**, 364, 475-479.

341. Prasanna, R.; Leijtens, T.; Dunfield, S. P.; Raiford, J. A.; Wolf, E. J.; Swifter, S. A.; Werner, J.; Eperon, G. E.; de Paula, C.; Palmstrom, A. F.; et al. Design of Low Bandgap Tin–Lead Halide Perovskite Solar Cells to Achieve Thermal, Atmospheric and Operational Stability. *Nat. Energy*, **2019**, 4, 939–947.

342. Leijtens, T.; Prasanna, R.; Bush, K. A.; Eperon, G. E.; Raiford, J. A.; Gold-Parker, A.; Wolf, E. J.; Swifter, S. A.; Boyd, C. C.; Wang, H. P.; et al. Tin-Lead Halide Perovskites with

Improved Thermal and Air Stability for Efficient All-Perovskite Tandem Solar Cells. *Sustain. Energy Fuels*, **2018**, 2, 2450-2459.

343. Zhao, B.; Abdi-Jalebi, M.; Tabachnyk, M.; Glass, H.; Kamboj, V. S.; Nie, W.; Pearson, A. J.; Puttisong, Y.; Gödel, K. C.; Beere, H. E.; et al. High Open-Circuit Voltages in Tin-Rich Low-Bandgap Perovskite-Based Planar Heterojunction Photovoltaics. *Adv. Mater.*, **2017**, 29, 1604744.

344. Tavakoli, M. M.; Zakeeruddin, S. M.; Grätzel, M.; Fan, Z. Large-Grain Tin-Rich Perovskite Films for Efficient Solar Cells via Metal Alloying Technique. *Adv. Mater.*, **2018**, 30, 1705998.

345. Shockley, W.; Queisser, H. J. Detailed Balance Limit of Efficiency of P-n Junction Solar Cells. *J. Appl. Phys.*, **1961**, 32, 510–519.

346. Barker, A. J.; Sadhanala, A.; Deschler, F.; Gandini, M.; Senanayak, S. P.; Pearce, P. M.; Mosconi, E.; Pearson, A. J.; Wu, Y.; Srimath Kandada, A. R.; et al. Defect-Assisted Photoinduced Halide Segregation in Mixed-Halide Perovskite Thin Films. *ACS Energy Lett.,* **2017**, 2, 1416-1424.

347. Yoon, S. J.; Kuno, M.; Kamat, P. V. Shift Happens. How Halide Ion Defects Influence Photoinduced Segregation in Mixed Halide Perovskites. *ACS Energy Lett.,* **2017**, 2,1507-1514.

348. Knight, A. J.; Wright, A. D.; Patel, J. B.; McMeekin, D. P.; Snaith, H. J.; Johnston, M. B.; Herz, L. M. Electronic Traps and Phase Segregation in Lead Mixed-Halide Perovskite. *ACS Energy Lett.,* **2019**, 4, 75-84.

349. 349. Cappel, U. B.; Svanström, S.; Lanzilotto, V.; Johansson, F. O. L.; Aitola, K.; Philippe, B.; Giangrisostomi, E.; Ovsyannikov, R.; Leitner, T.; Föhlisch, A.; et al. Partially Reversible Photoinduced Chemical Changes in a Mixed-Ion Perovskite Material for Solar Cells. *ACS Appl. Mater. Interfaces*, **2017**, 9, 34970-34978.

350. Balakrishna, R. G.; Kobosko, S. M.; Kamat, P. V. Mixed Halide Perovskite Solar Cells. Consequence of Iodide Treatment on Phase Segregation Recovery. *ACS Energy Lett.*, **2018**, 3, 2267-2272.

351. Yoon, S. J.; Draguta, S.; Manser, J. S.; Sharia, O.; Schneider, W. F.; Kuno, M.; Kamat, P. V. Tracking Iodide and Bromide Ion Segregation in Mixed Halide Lead Perovskites during Photoirradiation. *ACS Energy Lett.,* **2016**, 1, 290-296.

352. Draguta, S.; Sharia, O.; Yoon, S. J.; Brennan, M. C.; Morozov, Y. V.; Manser, J. M.; Kamat, P. V.; Schneider, W. F.; Kuno, M. Rationalizing the Light-Induced Phase Separation of Mixed Halide Organic-Inorganic Perovskites. *Nat. Commun.,* **2017**, 8, Article number: 200.

353. Brennan, M. C.; Draguta, S.; Kamat, P. V.; Kuno, M. Light-Induced Anion Phase Segregation in Mixed Halide Perovskites. *ACS Energy Lett.*, **2018**, 1, 204-213.

354. Correa-Baena, J. P.; Luo, Y.; Brenner, T. M.; Snaider, J.; Sun, S.; Li, X.; Jensen, M. A.; Hartono, N. T. P.; Nienhaus, L.; Wieghold, S.; et al. Homogenized Halides and Alkali Cation Segregation in Alloyed Organic-Inorganic Perovskites. *Science,* **2019**, 363, 627-631.

355. Jiang, Q.; Zhao, Y.; Zhang, X.; Yang, X.; Chen, Y.; Chu, Z.; Ye, Q.; Li, X.; Yin, Z.; You, J. Surface Passivation of Perovskite Film for Efficient Solar Cells. *Nat. Photonics,* **2019**, 13, 460–466.

356. Ferdani, D. W.; Pering, S. R.; Ghosh, D.; Kubiak, P.; Walker, A. B.; Lewis, S. E.; Johnson, A. L.; Baker, P. J.; Islam, M. S.; Cameron, P. J. Partial Cation Substitution Reduces Iodide Ion Transport in Lead Iodide Perovskite Solar Cells. *Energy Environ. Sci.*, **2019**, 12, 2264-2272.

357. Sun, Y.; Peng, J.; Chen, Y.; Yao, Y.; Liang, Z. Triple-Cation Mixed-Halide Perovskites: Towards Efficient, Annealing-Free and Air-Stable Solar Cells Enabled by $Pb(SCN)_2$ Additive. *Sci. Rep.,* **2017**, 7, Article number: 46193.

358. Abdi-Jalebi, M.; Andaji-Garmaroudi, Z.; Cacovich, S.; Stavrakas, C.; Philippe, B.; Richter, J. M.; Alsari, M.; Booker, E. P.; Hutter, E. M.; Pearson, A. J.; et al. Maximizing and Stabilizing Luminescence from Halide Perovskites with Potassium Passivation. *Nature,* **2018**, 555, 497–501.

359. Eperon, G. E.; Leijtens, T.; Bush, K. A.; Prasanna, R.; Green, T.; Wang, J. T. W.; McMeekin, D. P.; Volonakis, G.; Milot, R. L.; May, R.; et al. Perovskite-Perovskite Tandem Photovoltaics with Optimized Band Gaps. *Science*, **2016**, 354, 861-865.

360. Castro-Méndez, A.; Hidalgo, J.; Correa-Baena, J. The Role of Grain Boundaries in Perovskite Solar Cells. *Adv. Energy Mater.* **2019**, 9, 1901489.

361. Wieghold, S.; Correa-Baena, J. P.; Nienhaus, L.; Sun, S.; Shulenberger, K. E.; Liu, Z.; Tresback, J. S.; Shin, S. S.; Bawendi, M. G.; Buonassisi, T. Precursor Concentration Affects Grain Size, Crystal Orientation, and Local Performance in Mixed-Ion Lead Perovskite Solar Cells. *ACS Appl. Energy Mater.,* **2018**, 1, 6801-6808.

362. Muscarella, L. A.; Hutter, E. M.; Sanchez, S.; Dieleman, C. D.; Savenije, T. J.; Hagfeldt, A.; Saliba, M.; Ehrler, B. Crystal Orientation and Grain Size: Do They Determine Optoelectronic Properties of $MAPbI_3$ Perovskite?. *J. Phys. Chem. Lett.,* **2019**, 10, 6010-6018.

363. Wang, Z.; Lin, Q.; Chmiel, F. P.; Sakai, N.; Herz, L. M.; Snaith, H. J. Efficient Ambient-Air-

Stable Solar Cells with 2D-3D Heterostructured Butylammonium-Caesium-Formamidinium Lead Halide Perovskites. *Nat. Energy*, **2017**, 2, Article number: 17135.

364. Thouin, F.; Srimath Kandada, A. R.; Valverde-Chávez, D. A.; Cortecchia, D.; Bargigia, I.; Petrozza, A.; Yang, X.; Bittner, E. R.; Silva, C. Electron-Phonon Couplings Inherent in Polarons Drive Exciton Dynamics in Two-Dimensional Metal-Halide Perovskites. *Chem. Mater.*, **2019**, 31, 7085-7091.

365. Wang, L.; Mccleese, C.; Kovalsky, A.; Zhao, Y.; Burda, C. Femtosecond Time-Resolved Transient Absorption Spectroscopy Of. J. Am. Chem. Soc., **2014**, 136, 12205-12208.

366. Manser, J. S.; Kamat, P. V. Band Filling with Free Charge Carriers in Organometal Halide Perovskites. *Nat. Photonics*, **2014**, 8, 737–743.

367. Yuan, M.; Quan, L. N.; Comin, R.; Walters, G.; Sabatini, R.; Voznyy, O.; Hoogland, S.; Zhao, Y.; Beauregard, E. M.; Kanjanaboos, P.; et al. Perovskite Energy Funnels for Efficient Light-Emitting Diodes. *Nat. Nanotechnol.,* **2016**, 11, 872–877.

368. Jacobsson, T. J.; Correa-Baena, J. P.; Halvani Anaraki, E.; Philippe, B.; Stranks, S. D.; Bouduban, M. E. F.; Tress, W.; Schenk, K.; Teuscher, J.; Moser, J. E.; et al. Unreacted PbI_2 as a Double-Edged Sword for Enhancing the Performance of Perovskite Solar Cells. *J. Am. Chem. Soc.,* **2016**, 138, 10331-10343.

369. Price, M. B.; Butkus, J.; Jellicoe, T. C.; Sadhanala, A.; Briane, A.; Halpert, J. E.; Broch, K.; Hodgkiss, J. M.; Friend, R. H.; Deschler, F. Hot-Carrier Cooling and Photoinduced Refractive Index Changes in Organic-Inorganic Lead Halide Perovskites. *Nat. Commun.,* **2015**, 6, Article number: 8420.

370. Droseros, N.; Dänekamp, B.; Tsokkou, D.; Boix, P. P.; Banerji, N. Charge Injection and Trapping at Perovskite Interfaces with Organic Hole Transporting Materials of Different Ionization Energies. *APL Mater.,* **2019**, 7, 041115.

371. Jones, T. W.; Osherov, A.; Alsari, M.; Sponseller, M.; Duck, B. C.; Jung, Y. K.; Settens, C.; Niroui, F.; Brenes, R.; Stan, C. V.; et al. Lattice Strain Causes Non-Radiative Losses in Halide Perovskites. *Energy Environ. Sci.,* **2019**, 12, 596-606.

372. Zhang, H.; Fu, X.; Tang, Y.; Wang, H.; Zhang, C.; Yu, W. W.; Wang, X.; Zhang, Y.; Xiao, M. Phase Segregation Due to Ion Migration in All-Inorganic Mixed-Halide Perovskite Nanocrystals. *Nat. Commun.,* **2019**, 10, Article number: 1088.

373. Ruan, S.; Surmiak, M. A.; Ruan, Y.; McMeekin, D. P.; Ebendorff-Heidepriem, H.; Cheng, Y. B.; Lu, J.; McNeill, C. R. Light Induced Degradation in Mixed-Halide Perovskites. *J. Mater. Chem. C*, **2019**, 7, 9326-9334.

374. Tor Elmelund, Brian Seger, Masaru Kuno, and P. V. K. How Interplay between Photo and

Thermal Activation Dictates Halide Ion Segregation in Mixed Halide Perovskites. *ACS Energy Lett.* **2020**, 5, 56–63.

375. Beal, R. E.; Hagström, N. Z.; Barrier, J.; Gold-Parker, A.; Prasanna, R.; Bush, K. A.; Passarello, D.; Schelhas, L. T.; Brüning, K.; Tassone, C. J.; et al. Structural Origins of Light-Induced Phase Segregation in Organic-Inorganic Halide Perovskite Photovoltaic Materials. *Matter,* **2020**, 2, 207–219.

376. Correa Baena, J. P.; Steier, L.; Tress, W.; Saliba, M.; Neutzner, S.; Matsui, T.; Giordano, F.; Jacobsson, T. J.; Srimath Kandada, A. R.; Zakeeruddin, S. M.; et al. Highly Efficient Planar Perovskite Solar Cells through Band Alignment Engineering. *Energy Environ. Sci.,* **2015**, 8, 2928-2934.

377. Tao, S.; Schmidt, I.; Brocks, G.; Jiang, J.; Tranca, I.; Meerholz, K.; Olthof, S. Absolute Energy Level Positions in Tin- and Lead-Based Halide Perovskites. *Nat. Commun.* **2019**, 10, Article number: 2560.

378. Quarti, C.; De Angelis, F.; Beljonne, D. Influence of Surface Termination on the Energy Level Alignment at the $CH_3NH_3PbI_3$ Perovskite/C60 Interface. *Chem. Mater.,* **2017**, 29, 958-968.

379. Yao, D.; Zhang, C.; Zhang, S.; Yang, Y.; Du, A.; Waclawik, E.; Yu, X.; Wilson, G. J.; Wang, H. 2D–3D Mixed Organic–Inorganic Perovskite Layers for Solar Cells with Enhanced Efficiency and Stability Induced by n -Propylammonium Iodide Additives . *ACS Appl. Mater. Interfaces,* **2019**, 11, 29753-29764.

380. Ye, M.; He, C.; Iocozzia, J.; Liu, X.; Cui, X.; Meng, X.; Rager, M.; Hong, X.; Liu, X.; Lin, Z. Recent Advances in Interfacial Engineering of Perovskite Solar Cells. *J. Phys. D Appl. Phys.,* **2017**, 50, Number 37.

381. Liu, Z.; Ojima, H.; Hong, Z.; Kido, J.; Tian, W.; Wang, X. F. Solution-Processed Organic Photovoltaics Based on Indoline Dye Molecules Developed in Dye-Sensitized Solar Cells. *Molecules*, **2013**, 18, 3107-3117.